Direct and Indirect Laser Sintering of Metals

By

Montasser Marasy A. Dewidar

A Thesis submitted in accordance with the requirements for the degree of Doctor of Philosophy

The University of Leeds
School of Mechanical Engineering
Leeds UK

May 2002

The candidate confirms that the work submitted is his own and that appropriate credit has been given where reference has been made to the work of others.

ABSTRACT

Manufacturing functional prototypes and tools using conventional methods usually is a time consuming procedure with multiple steps. The pressure to get products to market faster has resulted in the creation of several Rapid Prototyping (RP) techniques. However, potentially one of the most important areas of Rapid Manufacturing (RM) technology lies in the field of Rapid Tooling (RT).

Layer manufacture technologies are gaining increasing attention in the manufacturing sector for the production of polymer mould tooling. Layer manufacture techniques can be used in this potential manufacturing area to produce tooling either indirectly or directly, and powder metal based layer manufacture systems are considered an effective way of producing rapid tooling.

Selective Laser Sintering (SLS) is one of available layer manufacture technologies. SLS is a sintering process in which shaped parts are built up layer by layer from bottom to top of powder material. A laser beam scans the powder layer, filling in the outline of each layers CAD-image, and heats the selected powder to fuse it.

This work reports the results of an experimental study examining the potential of layer manufacturing processes to deliver production metal tooling for manufacture of polymer components. Characterisation of indirect selective laser sintering and direct selective laser sintering to provide the metal tooling is reported. Three main areas were addressed during the study: mechanical strength, accuracy, and build rate. Overviews of the results from the studies are presented. Two materials (RapidSteel 2.0 and special grade of high-speed steel) and also two generations of SLS machines (Sinterstation 2000 and sinterstation research machine, which was constructed in Leeds) were used during this work.

ACKNOWLEDGMENTS

First of all I wish to express my deepest gratitude to Dr. K. W. Dalgarno, for his valuable guidance, supervision, advice, encouragement, and understanding throughout the research period and preparation of the thesis.

I would also like to thank Professor T. H. Childs, for his help through the duration of research.

I would like also to express my thanks to Egyptian Government for the sponsorship of this research and financial support.

I would like to thank the members of the Manufacturing, Strength of Materials and Measurement Laboratories for their support, In particular, Mr. Phillip Wood, Mr. Abbas Ismail, Mr. Tony Wiese and Mr. Alan G. Heald. I would like to thank Dr. Todd Stewart and Mr. M. Haiba.

I would like to thank my friends that I have met at University of Leeds. In addition, I would like to thank my friends outside the Leeds community for their continued support throughout the years. I would like to give special thanks to my parents, my brothers, and my sisters for their valuable emotional support.

Last, but definitely not least, I would like to give very special thanks to my wife Asmaa and my lovely kids, Moamen and Mona for their work related help, understanding, patience, and emotional and endless support.

Montasser M. Dewidar

Leeds, May 2002

Table of Contents

List of Figures

List of Tables

List of Notations

r	Scaling factor
f	Offset value
A_N	Andrew number (J/mm^2)
P	Laser power (W)
v	Scan speed mm/sec
s	Scan spacing mm
K1	Empirical constant (N/J)
E	Total Energy (J)
l	Length of the part (mm)
w	Width of the part (mm)
h	Height of the part (mm)
L_t	Layer thickness (mm)
ΔP	Capillary pressure (N)
γ	Surface energy (J)
D	Pore diameter (mm)
θ	Contact angle between infiltration and solid matrix (°)
TRS	Transverse rupture strength (Pa)
F	Maximum load applied to the specimen (N)
L	Span length (mm)
b	Width of the sample (mm)
d	Depth of the sample (mm)
E	Modulus of Elasticity (GPa)
σ_y	Yield Stress (MPa)
I	Inertia moment (mm^4)
M	Bending moment (N mm)
c	Depth of the sample/2 (mm)
y_{max}	Deflection at midspan (mm)
y_1	Deflection at any point of span (mm)
x	Distance from the support to the point at which the deflection is to be calculated when the specimen is straight (mm)
a	Distance from the support to the load applicator when the specimen is straight (mm)
T_s	Scanning time (sec)
T_o	Total time of one layer (sec)
N_n	Total number of layers
T_d	Delay time (sec)
N_l	Number of lines
T_t	Total time of building (sec)
T_c	Set-up time for each layer (sec)
ρ	Density (g/cm^3)
W	Weight (g)
V	Volume (cm^3)
W_{total}	Weight of the box plus the loose powder (g)
W_{box}	Weight of the box (g)

W_{powder}	Weight of the loose powder (g)
V_{box}	Volume of the box (cm^3)
R_a	Surface roughness (μm)
ρ_A	Average density (g/cm^3)
W	Weight of the block (g)
T	Temperature at which the supersolidus liquid phase sintering is initiated (K)
T_i	Temperature at which maximum density is first obtained (K)
T_o	Optimum sintering temperature (K)
T_d	Compact distortion temperature (K)
T_s	Sintering temperature (K)
T_w	Time of warming (sec)
T_c	Time of cooling (sec)

Abbreviations

3D	Three-dimensional
3DP	Three-Dimensional Printing
BMA	Butylmethacrylate
CAD	Computer Aided Design
CAM	Computer Aided Manufacturing
CMM	Coordinate Measuring Machine
CNC	Computer Numerical Control
DSPC	Direct Shell Production Casting
FDC	Fused Deposition of Ceramic
FDM	Fused Deposition Modelling
HSS	High-Speed Steel
LENS-FORM	Large Scale Tooling for Rapid Manufacture
LCC	Laminated Laser Cut Cavities
LOM	Laminated Object Manufacturing
LPS	Liquid Phase Sintering
MMA	Methylmethacrylate
PM	Powder Metallurgy
PMMA	Polymethylmethacrylate
RM	Rapid Manufacturing
RP	Rapid Prototyping
RT	Rapid Tooling
SEM	Scanning Electron Microscopy
SGC	Solid Ground Curing
SL	Stereolithography
SLS	Selective Laser Sintering
STL	STereoLithography format
TRS	Transverse Rupture Strength

CHAPTER ONE

INTRODUCTION

1.1 Rapid Manufacturing and Tooling

Rapid manufacturing is a term that includes rapid prototyping (RP) and rapid tooling (RT). RP, as will be defined in detail in the next chapter, is a new technology in which physical objects and functional prototypes are fabricated directly from CAD files or from the digitized data of other software sources. RT is a natural extension of RP that concerns the production of tooling using as inserts. RT can be defined as the use of a rapid prototype as a tooling pattern for the purposes of molding production materials, or the direct production of a tool from the rapid prototyping system. The major breakthrough of RP technologies in manufacturing has been their ability to improve product development while at the same time reducing the costs and time required to take the product from conception to market.

There are a number of different RP systems available in the marketplace, including stereolithography (SLA), selective laser sintering (SLS), laminated object manufacturing (LOM), fused deposition modeling (FDM), and three-dimensional printing (3DP) (see section 2-2). In addition, there is a range of other technologies, some of which are not yet commercialised.

RP is now used in many applications such as geometric (form and fit) prototypes, patterns for casting, medical applications, and expendable models or tools which can then be used for manufacturing functional prototypes. Now, RP models are becoming widely used in

several manufacturing applications. Special software tools, build techniques and materials have been developed to satisfy specific requirements of mechanical properties and accuracy for new applications

Rapid manufacturing and tooling techniques utilize various indirect methods (called indirect because they use a RP pattern obtained by an appropriate RP technique as a model for mould and die making) to form a pattern of the component to be molded. Indirect methods for rapid tooling are available for production runs of several hundred parts in the same material as that of the final production part. These methods of tool production require, at least, one intermediate replication process. This might result in the loss of accuracy leading to an increase in the build time. To overcome all or some of the disadvantages of indirect methods, some RP apparatus manufacturers have proposed new rapid tooling methods, called direct RT methods, that allow injection moulding or die-casting inserts to be built directly from 3D CAD models. Only a few such production methods have been commercialised. Direct RT methods enable the production of inserts capable of surviving tens of thousands of cycles and represent good alternatives to traditional mould making techniques. The life or durability of the inserts produced by these methods varies significantly depending on the RT methods and the type of material used.

Some questions must be asked before setting out to get direct tooling. How long does the tool have to last, what kind of finish and quality is essential, what material will be moulded, what properties are required, difficulty of part, cost, and lead-time. Answers to these questions will help recognize which type of tooling can meet the specifications for particular application.

One of the RP processes that is widely used for producing direct tool production is selective laser sintering (SLS). DTM was one of the first companies to commercialise a rapid tooling technology, using SLS, marketing it as the RapidTool™ process [Beaman et al., 1997]. Three types of RapidTool materials were introduced by DTM: RapidSteel 1.0 (announced in 1997), Copper polyamide (announced in 1998), and RapidSteel 2.0 (announced in 1998) [Pham and Dimov, 2001]. LaserForm ST-100 (ST-100) is the latest version of RapidSteel and is a stainless steel 420 material that is sintered and infiltrated in one furnace run [Stucker et al., 2000].

In 1995, EOS introduced their first DirectTool™ rapid tooling process [Khaing et al., 2001]. Ongoing material and process developments have increased the process productivity and the quality of the built parts. The most common application of this process is the production of metal inserts for plastic injection moulding and rubber vulcanisation. In 1999, EOS introduced their second DirectTool™ process. This process is utilized for rapid tooling of complex inserts the surface of which cannot be machined directly.

A range of materials including stainless steel, tungsten, nickel-aluminum-bronze and tungsten carbide can be employed to build metal parts for injection moulding tooling inserts from a CAD by the 3D Printing process [Fuesting et al., 1996; Fukai et al., 2000; and Eric et al., 1999 a].

There are other rapid tooling technologies offered by companies such as Extrudehone, Albright technologies, MCP, Ciba-Geigy, AIM, LENS, Taffa, and Rapid CNC. All of these companies represent potential tooling options [Hilton and Jacobs, 2000; Weaver et al., 1999].

From the above it is concluded that there are several proprietary solutions for direct tool production. A good understanding of the capabilities and limitations of these processes is essential in order to implement the technology successfully.

In order to understand direct tool process and improve the applications the LAST-FORM research program was started in Leeds University. LAST-FORM is an acronym for Large Scale Tooling for Rapid Manufacture. The main aim of LAST-FORM is to develop strategies and to research engineering solutions for the direct rapid creation of tooling for prototype and small batch aerospace and automotive manufacture.

1.2 Aims and Objectives of the Thesis

The pressure to get products to market faster has led to an emergence of numerous rapid tooling processes. Currently, new metal systems that can be used to produce functional metal prototype and tooling parts are in the advanced development stage. Metal powder routes potentially offer more freedom of material choice to be more suitable for more demanding high temperature tooling requirements. Of all Rapid Prototyping technologies, selective laser sintering (direct and indirect) is the one that seems to show the greatest promise for direct production of functional metal prototypes and tools. However, regarding the performance of the tools it is necessary to extend the range of usable raw materials and decrease the building time. This thesis is concerned with the study of the direct and indirect SLS of metal powder to produce direct metal tooling. In the present work, RapidSteel 2.0 has been used for indirect selective laser sintering, and high-speed steel has been used for direct selective laser sintering. The overall aim of this thesis is to characterise the

mechanical properties and microstructure, accuracy, and building time of direct and indirect SLS processes. RapidSteel 2.0 and a DTM Sinterstation 2000 machine will be used for indirect selective laser sintering to provide a commercial benchmark. The high-speed steel material has been chosen for its promising processing characteristics in relation to direct selective laser sintering. A high power Leeds manufactured machine will be used for direct selective laser sintering as this provides the high laser power (240 W) which can not be obtained from the DTM Sinterstation 2000 (50 W).

1.3 Thesis Outline

This thesis consists of eight chapters. Chapter two presents a literature review. Chapter three discusses comparison criteria for direct and indirect SLS. Chapter four describes the experimental methods used in assessing indirect SLS. Chapter five discusses the results from the indirect SLS study. Chapter six describes the experimental methods used in assessing direct SLS. Chapter seven discusses the results of the direct SLS study. A general discussion leading to conclusions and recommendations for future work is presented in chapter eight.

CHAPTER TWO

LITERATURE REVIEW

2.1 Introduction

A prototype is the first or original example of something that has been or will be copied or developed; it is a model or preliminary version. The fabrication of prototypes has been experimented with in many forms such as material removal, casting, and moulding. and with many types of materials such as polymer, wax, ceramic and metal. Prototyping has gone through three phases, first phase: manual prototyping, second phase: soft or virtual prototyping, and third phase: rapid prototyping [Chua and Leong, 1997].

Rapid prototyping of physical parts, also known as solid freeform fabrication, desktop manufacturing or layer manufacturing technology, represents the third phase in the evolution of prototyping. The use of rapid prototyping has enable manufacturers to reduce the early design stage costs associated with the tooling and cutting processes needed to produce prototype models traditionally. In addition, the benefits of making complex parts in a single operation without part specific tools or human intervention are obvious. Objects, which cannot be built with conventional manufacturing methods can be built using layer manufacturing processes [Beaman et al., 1997]. The need for support structures, such as clamping, jigs, or fixtures, also are reduced. A few RP processes, however, do require a support structure. There is no requirement for the design and manufacture of moulds and dies, because RP processes do not use tools. Development time and time-to-market also are drastically reduced; parts are often

completed within a few hours up to a couple of days depending on the size of part, in contrast to conventional processes that may take a few weeks, months, or longer. However, many disadvantages can also be found due to the nature of layer manufacturing technology such as limitation of materials, poor surface quality, and material quality [Beaman et al., 1997].

Material limitations: Most RP processes rely on particular material properties or behaviours for their function. So the range of materials that can be used in each process is usually quite limited. In several cases, materials with good engineering properties are not compatible with the RP process requirements.

Surface quality: In most cases, parts are made-up from a series of layers and this results in a stair-step effect on all inclined part surfaces. Reducing layer thickness reduces the size of the steps but increases the manufacture time. When smooth surfaces are necessary manual finishing is required.

Material quality: Besides the limitations in which types of materials can be used there are material quality issues related with building parts in layers. If there are any bonding defects between layers the properties of the part will be degraded. There may also be anisotropy in properties as a result of combination of inter-layer connection and differences in in-layer processing for different orthogonal directions.

Advancements in rapid prototyping technology over the past ten years have significantly overcome these problems.

Common to all the different rapid prototyping methods is the basic approach, which can be described as following: (i) create a 3D Computer Aided Design (CAD) model of the part to be built, (ii) convert the CAD model to STL format, (iii) slice the STL file into

thin cross-sectional layers, (iv) build the model layer by layer by an additive approach [Chua. and Leong, 1997; and Beaman et al., 1997].

First, the object to be built is modelled using a Computer Aided Design (CAD) software package. The model, which represents the physical part to be built, must be represented as closed surfaces that unambiguously define an enclosed volume. That is, the data must specify the inside, outside and boundary of the model. This is a virtue of using a solid model as it will automatically be an enclosed volume. This requirement ensures that all horizontal cross sections are closed to create the solid object. The second step is to convert the CAD file into a format dubbed the "STL" (**ST**ereo**L**ithography) file format. The STL file format approximates the surfaces of the model by triangles. It is a simple tessellated surface representation as shown in Figure 2.1. Highly curved surfaces must employ many triangles, which means that STL files for curved parts can be very large. In the third step, a computer analyses an STL file that defines the model to be fabricated and "slices" the model into cross sections. The cross sections are systematically recreated as individual layers and then combined to form a 3D model.

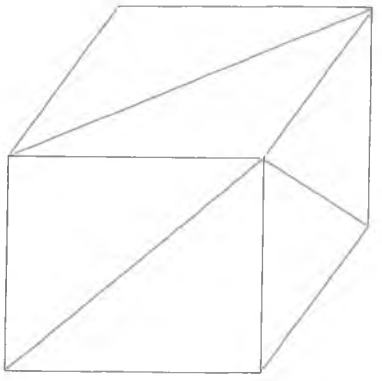

Figure 2-1: STL surface representation of a cube.

2.2 Rapid Prototyping and Tooling

2.2.1 Rapid Prototyping Techniques

The commercially available rapid prototyping processes are Stereolithography (SLA), Fused Deposition Modelling (FDM), Solid Ground Curing (SGC), Laminated Object Manufacturing (LOM), Photosolidification, Desktop Machine Tools, Three Dimensional Printing (3DP), ink-jet, and Selective Laser Sintering (SLS). There are a number of techniques currently under development, such as Ballistic Particle Manufacturing, and selective spray metal deposition [Jacobs, 1992; 1996; Chua and Leong, 1997; Beaman et al., 1997; Comb et al., 1994]. Next sections will describe some of these processes.

2.2.1.1 Stereolithography (SLA)

Stereolithography [Jacobs, 1992; 1996] was the first Rapid Prototyping system to be developed and offered commercially, and it is perhaps the most popular among currently available RP processes. In this system, and all of those mentioned here, 3D CAD data is represented to the system using an STL file. A schematic view of the SLA apparatus is shown in Figure 2.2. SLA is a polymer-based process which uses a laser or ultraviolet light to cure an epoxy or plastic resin [Reeves and Cobb, 1995; Himmer, et al., 1997]. The elevator platform is submerged in a vat of liquid photo-polymeric resin and held near the surface. A low power highly focused ultraviolet laser scans the surface of the liquid to partially cure the first layer. During the solidification of the liquid, the solid bonds to the platform. Next, the elevator drops a user specified distance and a new coating of liquid resin covers the solidified layer and the laser scans a new layer. This process is repeated until the part is complete. Once the part is completed, it is drained

and then removed from the vat and rinsed in a solvent to remove any uncured resin from the part surface. To build overhanging structures SLA uses a weak web of the same polymer material as the part material. This web structure gives enough support to allow the deposition of over-hanging structures and, once the part is completed, the weak support is removed manually. Depending on the type of epoxy resin that is used, the part can be between 65 and 90 percent cured [Colton and Blair, 1999]. In order to complete the cure, the parts are irradiated with ultraviolet light to solidify any uncured resin. The degree of cure will affect part properties, such as strength and hardness. Early stereolithography prototypes were fairly brittle and prone to curing-induced warping and distortion, but recently further research is being conducted into materials and methods to correct these problems.

The advantages of SLA are that it yields a surface finish comparable to that of NC milling, it is a well proven system with over 1000 machines in use world wide and it is reasonably fast and accurate. SLA systems have an accuracy of ± 100 μm and can achieve layers 25 μm thick. Several parts may be built at once.

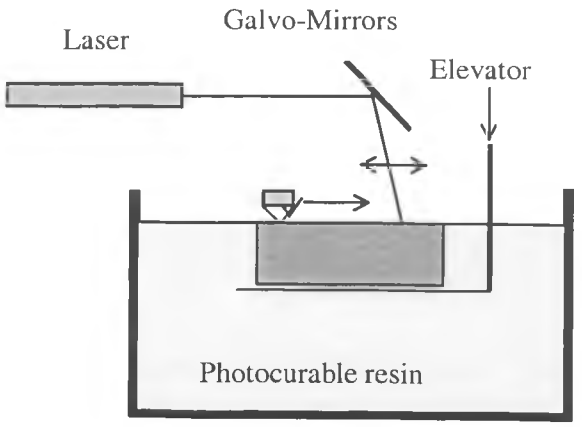

Figure 2.2: Schematic diagram of Stereolithography

The disadvantages of SLA system are that the material is expensive and toxic and must be shielded from light to avoid premature polymerisation and there is also only a limited choice of resins. The parts may be brittle and translucent and they need supports which may adversely affect the surface finish when removed. Changing the resin in the vat is a lengthy and costly procedure.

2.2.1.2 Fused Deposition Modeling (FDM)

Fused deposition modeling [Stratasys, Inc., 1991; Comb et al., 1994] is a process which produces parts by extruding a thermoplastic polymer. This process was developed in 1988 by Crump who founded Stratasys the following year. In this process a spool of thermoplastic polymer feeds into a heated nozzle, which traces an exact outline of each cross-section layer of the part. The polymer melts and flows out of the nozzle onto the part. The nozzle is then scanned over the part leaving solid material where needed. The material solidifies in 0.1s after exiting the nozzle. A computer controls the movement of the nozzle. After one layer is finished, the nozzle moves up a programmed distance in the z direction to build the next layer. The FDM process does not normally need supports, due to the short time of solidification. In some cases, a support may still be required to reduce part distortion. This support can be either a weak structure of thermoplastic that is mechanically removed after the part is completed or a water soluble wax that is removed by soaking in water. A similar process was developed and called Fused Deposition of Ceramic (FDC) in which a mixture of ceramic particles in a polymer binder is extruded out of a heated nozzle. Metal parts have also been produced by mixing metal and polymer powders together and extruding the mixture using the

standard FDM process. After the ceramic or metal part is completed, it is heated in an oven to burn off the polymer binder and to sinter the part [Stratasys; 2000].

The advantages of a FDM system are that the materials used are cheap and commonly available, and the high stability of made parts. The product and process are easy to use. FDM's software can automatically determine if supports are needed and generate them. The FDM modeling process is simple, accurate and fast.

The disadvantage of this process is the poor surface finish of parts.

2.2.1.3 Solid Ground Curing (SGC)

Solid ground curing (SGC) [Chua and Leong, 1997; Pham and Gault, 1998], which is also known as the solider process, is somewhat similar to stereolithography (SLA) in that both use ultraviolet light to produce polymer parts. Instead of scanning a laser over the surface as in SLA, in SGC an ultraviolet light shines through a mask to cure all the part material at the same time. The mask is generated by electrostatically charging a glass plate with a negative image of the layer's cross-section. The mask is then positioned over a uniform layer of liquid photo-polymer and exposed to ultraviolet light such that only the area blocked by the mask is left in liquid form. The liquid polymer is removed and replaced with hot wax. After the wax has cooled, the layer is milled flat to the specific thickness. The mask plate is discharged and the cycle is repeated. After the part is completed, the wax support is removed by melting or by using solvent. This eliminates curling, warping, support structure, and any need for final curing. Cubital Ltd developed SGC systems, and the first SGC system was installed in 1991.

The advantages of SGC system are the short part creation time, the durability of parts over the hatched prototypes created by other processes, that no post-curing is required, and that supports are unnecessary.

The disadvantages of this process are that the machine is large and noisy (wasting a large amount of wax) prone to breakdowns, and the resin models are not suitable for investment casting [Cubital, 2001].

2.2.1.4 Laminated Object Manufacturing (LOM)

Laminated Object Manufacturing (LOM) [Helysis Inc., 2001; Chua and Leong, 1997; Pham and Dimov, 2001] is a process of building prototypes from bonded paper, plastic, metal or composite sheet stock. This process was developed by Helisys Inc. In this technique, thin layers of adhesive-coated sheet material are sequentially bonded together to form a prototype. The original material consists of paper laminated with heat-activated glue and rolled up on spools. As shown in the Figure 2.3, a feeder/collector mechanism advances the sheet over the build platform, where a base has been constructed from paper and double-sided foam tape. Next, a heated roller applies pressure to bond the paper to the base. A focused laser cuts the outline of the first layer into the paper and then cross hatches the excess area. Cross-hatching breaks up the extra material, making it easier to remove during post-processing. After the first layer is cut, the platform lowers out of the way and fresh material is advanced. The platform rises to slightly below the previous height, the roller bonds the second layer to the first, and the laser cuts the second layer. This process is repeated until the part is finished. After the part has been separated, it is recommended that it should be sealed with paint or varnish to prevent moisture absorption and expansion [Helysis Inc, 2001]. This process is now routinely used to create either positive or negative part features from which tooling for sand casting is made.

The advantages of the LOM process are that the parts do not experience warpage, internal residual stresses, or other deformations, and the flexibility to create a master or

a mould. A wide range of relatively cheap materials is available. This process can produce large and bulky parts. This process does not need support generation.

Since post-processing is done manually, waste material removal is time consuming. Another disadvantage of this process is that the waste material can not be reused

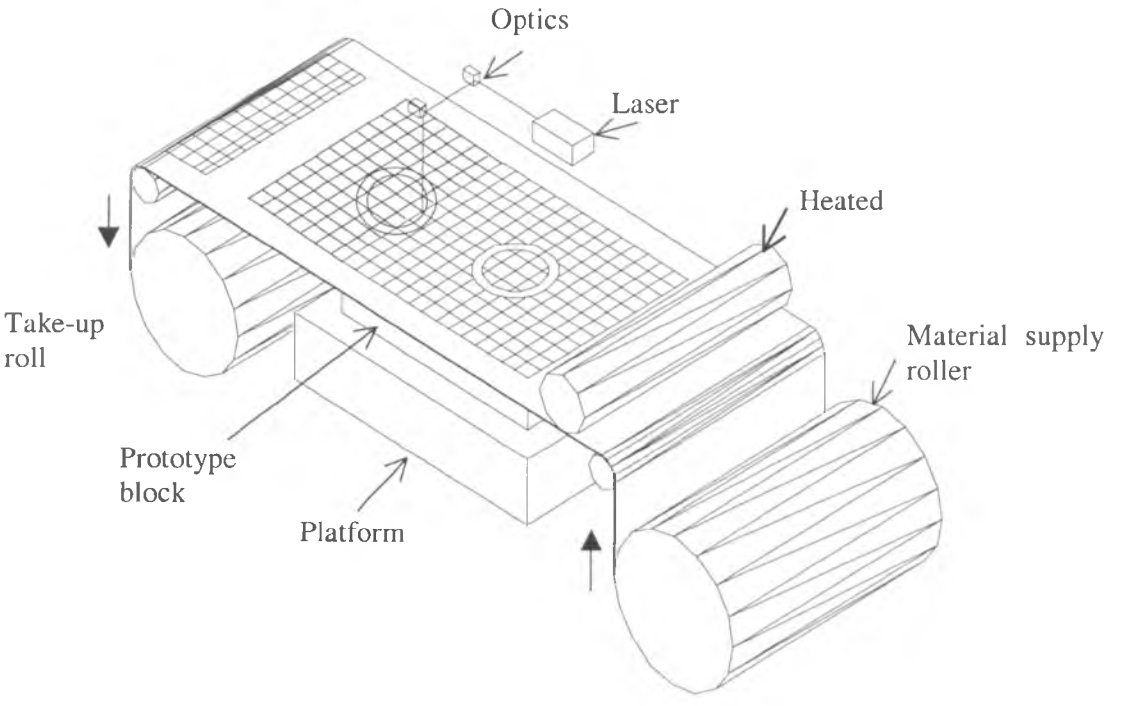

Figure 2.3: Schematic diagram of laminated object manufacturing

2.2.2 Rapid Tooling

Traditional tooling technologies such as electrical discharge machining, milling and drilling, and casting are costly and require too much time to use them to build prototype parts. Testing first designs with conventional tooling methods would lead to long design cycles. An alternative method is required to produce functional prototype tooling. Rapid tooling is the use of solid freeform processes to rapidly build die insert or other forming tools to build real parts in simulated manufacturing rigs, creating a new competitive

edge. Due to the pressure of technological competition, new products must be more rapidly and cheaply developed, manufactured and introduced to the market. The rapid prototype of components, with a view to assessing aesthetics, ergonomics and fitment, have played a positive role in achieving these aims for sometimes. Rapid prototyping (RP) technology allows manufacture not only of prototypes for visualization purposes and models, but also of functional parts. Present RP technologies are neither capable of prototyping in a wide range of commercially available materials nor well suited to producing large numbers of models. This had led to the implementation of multi-step procedures involving various tooling options; these procedures are termed rapid tooling (RT). Thus, RT processes complement the RP options by being capable of producing higher quantities of models in a wider variety of materials. Furthermore, RT extends the benefits of reduced cost and time to the vital area of prototype tooling. The challenge in rapid tooling is related to the fact that the requirements are more rigid than for prototyping.

There are a large number of RT techniques, so there is a tendency to classify them into groups [Rosochowski and Matuszak, 2000; Chua et al., 1999 a and b; McDonald et al., 2001], (see Figure 2.4). The commercial processes are EOS, Metal spray, Laminated laser-cut cavities (LLCC), Keltool, Extrudehone, and DTM rapid tool [Eric, 1999].

2.2.2.1 Direct tooling

Creating tooling directly from RP machines is the main challenge to RT applications. Patterns for casting methods and indirect methods for tool production requires at least one intermediate replication process. Most RP technologies use relatively soft materials as the building medium and therefore are not suitable for direct tooling. However, a lot

of trials have been run, and now there are successful applications in this field. Direct rapid tooling is an industrial concept aimed at the realization of production tooling directly from CAD data files, with the smallest possible process chain. The purpose of direct tooling is the manufacturing of tools that can be used under normal production conditions, in terms of durability, accuracy and surface quality.

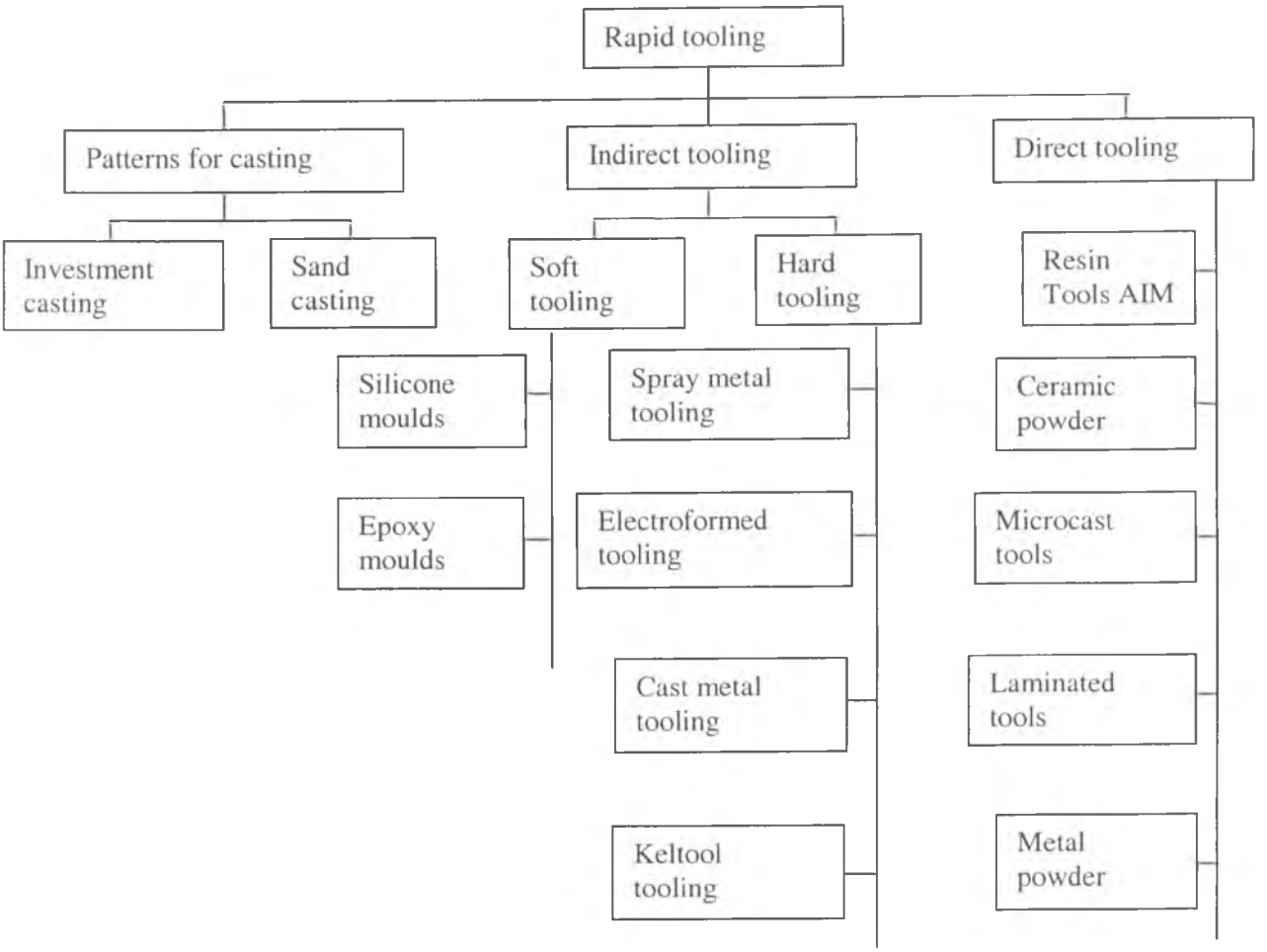

Figure 2.4: Classification of Rapid Tooling [Rosochowski and Matuszak, 2000]

The creation of production tooling is the basic purpose of the direct RT concept. At the moment, true direct RT techniques allow the preparation of pre-production tools applied to the manufacture of moulds for plastic injection. In particular, additive processes

allow cooling channels to be more efficiently placed in thermally strategic areas [Sachs, 1995; Dalgarno and Stewart., 2001], based on thermal field calculation, for example. Cycle time can therefore be reduced, thus improving the profitability of the process. Now direct RT methods enable the production of inserts capable of surviving tens of thousands of cycles.

2.2.2.2 Direct AIM Tooling

The direct AIM tooling process is a process that uses Stereolithography to produce direct tooling. Solid dies of epoxy resin have been used for the injection of wax patterns for investment casting. This technique has taken advantage of the 80°C glass transition temperature of the epoxy resin, which is higher than the melting point of many investment waxes.

Epoxy dies for injection moulding have also been tried with different thermoplastics. Specific rules apply to the production of this type of injection mould, because the temperature resistance of the curable epoxy resins available at present is up to 200°C and the plastics are injected at temperatures as high as 300°C. The number of parts that can be produced from the tools using this process is dependent on the size and shape of the moulded part, but moulding up to 100 parts is typical. Very high levels of accuracy as well as very substantial time saving are claimed for this technique [Chua et al, 1999 a and b]

2.2.2.3 Ceramic powder tools

The 3DP^{TM} process produces ceramic moulds for metal casting directly from CAD design data. This process which is known as Direct Shell Production Casting (DSPC), has been developed at MIT and marketed by Soligen Inc. [Klocke and Wirtz, 1998].

A digital model of the ceramic mould, including a gating system and internal cores for hollow parts, is produced directly in the 3DP machine. After printing the entire mould in ceramic powder, it is fired and the unbound powder is removed. The resulting mould can be used to produce metal castings for a wide range of applications including aerospace, automotive and medical implant.

2.2.2.4 Laminated metal sheets

The idea of this process is using metal sheets for producing laminated metal tools. Experiments to build moulds directly or coated with a thin layer of metal have been reported [Pham and Dimov, 2001]. The sheets are cut in accordance with the computer derived layer information. However, instead of bonding each layer as it is cut, the layers are all assembled after cutting and either bolted or bonded together in some way. The problem of bonding, however, has to be resolved to ensure the structural integrity of the final product. Moulds built by this method can only be used for low melting thermoplastics and are not suitable for injection molding or blow moulding of common thermoplastics. To overcome this problem other materials based on epoxy resins or ceramics capable of withstanding harsh operating conditions have been developed.

2.2.2.5 Accuracy and Surface Finish of Rapid Prototyping Techniques

RT processes are integrated manufacturing processes that include CAD/CAM, control of laser devices, materials, manufacturing parameter set-up, and post processing [Zhou et al., 2000]. The individual processes, (SLA, LOM, FDM, SLS ink-jet, etc.) all introduce geometric errors in producing components. These errors severely reduce RP product accuracy and surface finish and inhibit further applications in rapid tooling and

functional part fabrication. Figures 2.5, a and b summarise the surface quality of unfinished parts for each of the main classes of building process, with the same information for the polished parts respectively. Thin lines show the range from maximum to minimum, thick bars show the average ± standard deviation [Shellabear 1999]. Figures 2.6, a and b summarise the dimensional accuracy of unfinished parts for each of the main classes of building process, and dimensional accuracy of finished parts according to process respectively.

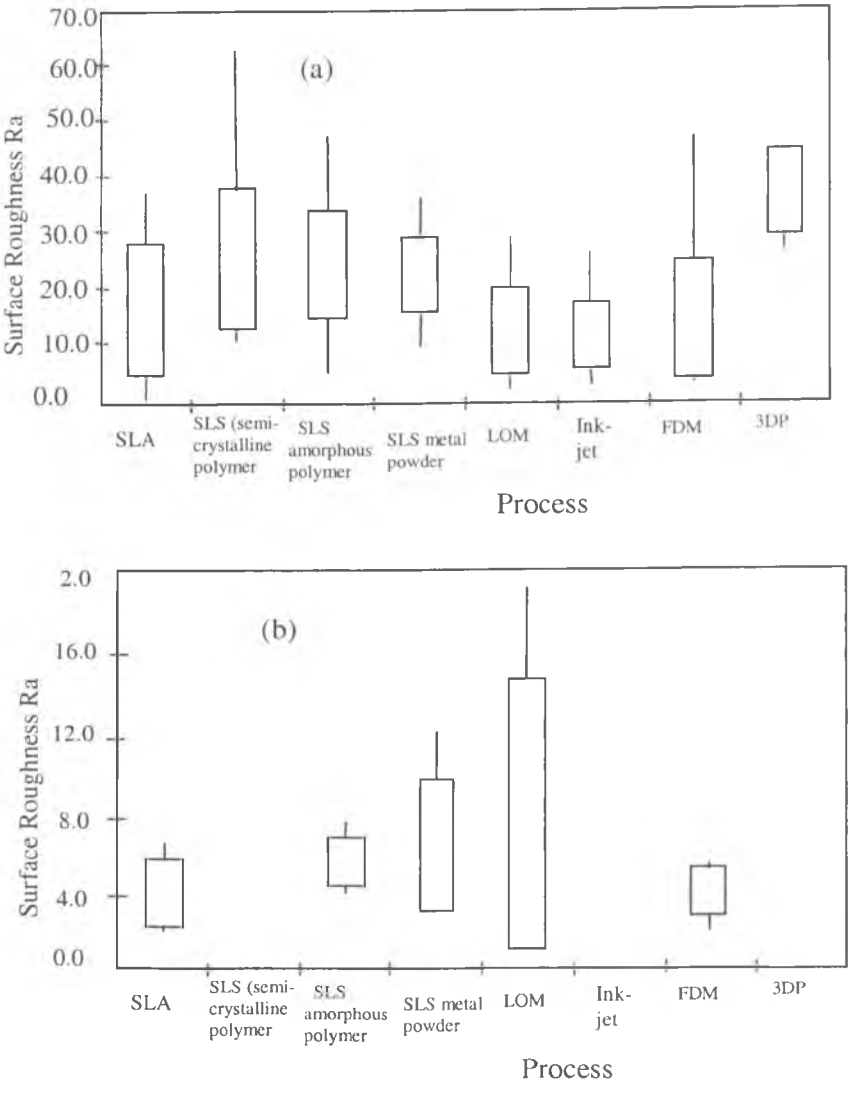

Figure 2.5 (a) Surface finish of unfinished parts according to process, (b) surface finish of polished parts according to process [Shellabear 1999]

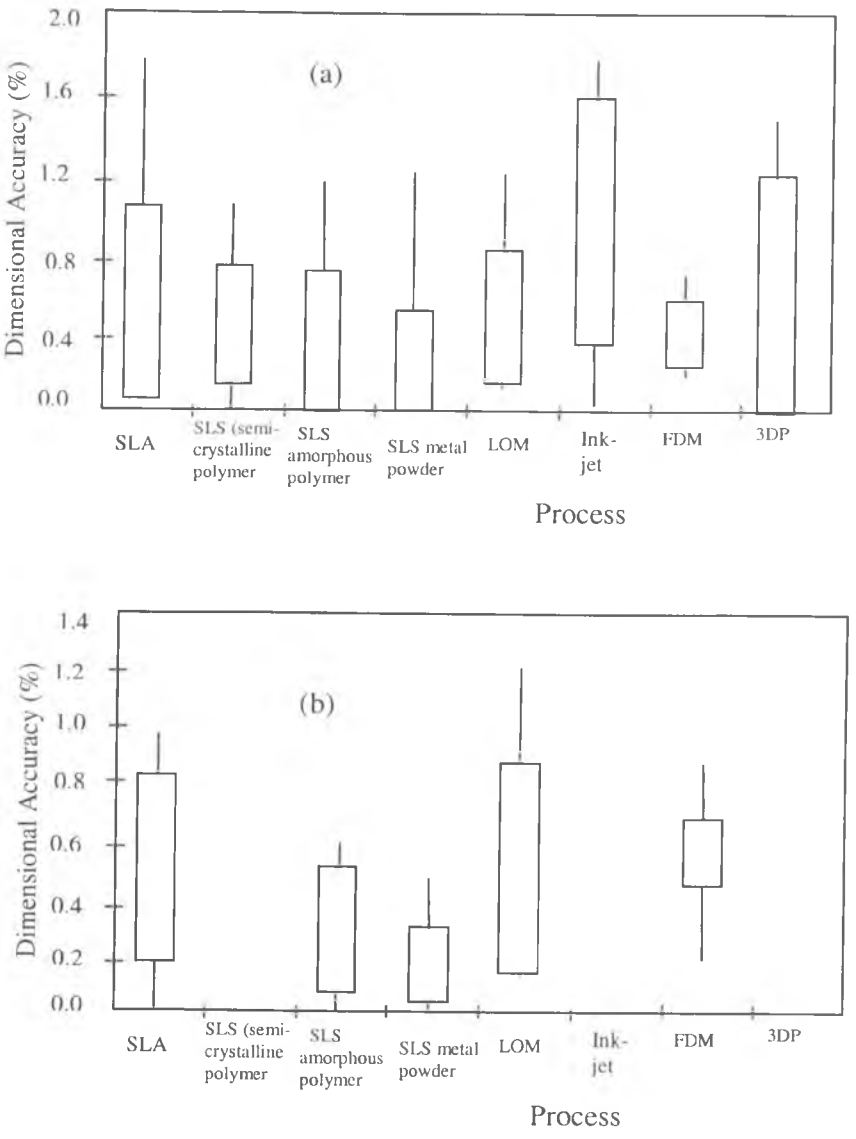

Figure 2.6 (a) Dimensional accuracy of unfinished parts according to process, (b) dimensional accuracy of polished parts according to process [Shellabear 1999]

2.2.2.6 Summary

The industry need to shorten time-to-market has led to the development of Rapid Prototyping techniques, initially and is followed by the rapid manufacture of basic pre-production tools, based on more traditional methods, such as investment casting. If a product is to be brought to market even earlier, more efficient and direct tool making processes are necessary, such as direct RT techniques. At the moment, these allow the manufacturing of pre-production tools directly from the part CAD files of good quality

in short times. However, important developments are required in several fields, including CAD/CAM software, materials, material delivery systems, process control, and part build-up strategy. Therefore, an important effort on physical process modeling is required. This involves the essence of different technological expertise. Hence, direct RT requires strong multidisciplinary research.

2.3 Selective Laser Sintering

Selective Laser Sintering (SLS) is a rapid prototyping process that uses bonded powdered material to form models, prototypes, and patterns [Marcus et al, 1990 a and b; Manthiram et al, 1993]. Within SLS, a compartment contains a laser and the platform upon which the model is built. The compartment walls consist of infrared heat panels, which act to heat the powdered material to just below the material's melting point. The workspace consists of a platform that lowers the model as each successive layer is added. A powder cartridge supplies the powdered material used to produce the part, and a roller is used to distribute the material evenly across the workspace (Figure 2.7).

The SLS process begins with a thin layer of powdered material spread evenly across the workspace. The laser traces the pattern of the slice on the layer of powdered material, heating and fusing the material it comes in contact with. Only the material in the laser's path is sintered; careful modulation of the laser beam intensity assures that the surrounding powdered material remains unaffected. The movable platform lowers the workpiece to allow for the construction of the next layer. After one layer of the component is formed, the area is prepared for the next slice of CAD data as another layer of powdered material is deposited on the workspace and distributed by the roller.

The process repeats itself as the laser sinters and fuses each successive layer to the previous layer until the part is formed. The unsintered powder surrounding the part in formation acts as a support structure for the part. This means there are no support structures to create during the process or to remove afterward. This improves build rates, minimises post-processing labour, and thus creates a distinct advantage over many other rapid prototyping processes. After the part is removed, a jet of air removes excess powder easily. SLS parts may then require some post-processing or secondary finishing, such as heat treatments orsanding, depending upon the application of the prototype built [Beaman et al, 1997; Chua and Leong, 1997].

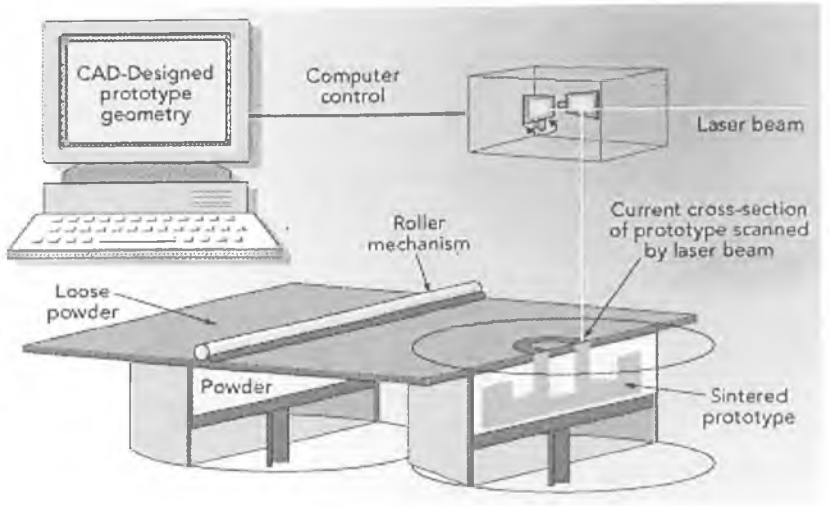

Figure 2.7: Selective laser sintering process

There are two types of lasers currently used in the SLS machine, CO_2 lasers and Nd:YAG lasers. Other different types of lasers can be used if their radiant energy is readily absorbed by the powder. The CO_2 laser operates at a wavelength 10.6 μm and YAG at 1.06 μm, which causes the laser light to be absorbed differently depending on particle size and materials absorptivity. The CO_2 laser is one of the most widely used lasers in industry and the most commonly used in the SLS machine due to its efficiency

for the conversion of electrical to optical energy and lower equipment cost. The main characteristics of CO_2 laser are the well controllable output, long operating life, good beam quality and easy maintenance [Kruth, et al, 1999].

2.3.1 Historical Development

The SLS process was developed and patented at the University of Texas at Austin. DTM Corporation was founded in 1987 to commercialise the SLS technology, and shipped its first commercial machine (Sinterstation 2000) in 1992. The Sinterstation 2000 has a cylindrical build chamber which has a height of 380 mm and a diameter of 300 mm. The SLS process and the Sinterstation 2000 System are not limited to a specific class of materials. The second generation machine was the Sinterstation 2500. The third SLS system is the Sinterstation 2500 Plus with build chamber dimensions 381 mm in width, 330 mm in depth and 457 mm in height. Sinterstation 2000 had a maximum laser scan speed limited to 1500 mm/s by its beam delivery system. In contrast, the beam delivery system on the second generation Sinterstation 2500 and the third generation Sinterstation 2500 plus allows a much faster rate of 5000 mm/s. This modification gives users a significant improvement in build speed. Other improvements on the Sinterstation 2500 plus contain the capability to add powder layers faster than the Sinterstation 2000. Increased laser scans speed and faster powder delivery have resulted in greatly reduced build time. There is about 37% decrease in build time from the Sinterstation 2000 to the 2500 plus system. The last SLS system by DTM is the Vanguard system. The laser power of this machine is 25 or 100 Watt, scan-speed 7500 mm/s, and the size of build chamber is 370 mm in width, 320 mm in depth, and 445 mm in height. The benefits of this machine are high part accuracy, fast build speed, and

unattended operation. This is the key advantage of the process, i.e. providing flexibility in the material used for prototyping and tooling. The main types of materials used in SLS process are safe and non-toxic, easy to use, store and recycle.

The materials, initially commonly used were wax, polymer, nylon, ceramic, and metal [Chua and Leong, 1997; Beaman et al, 1997].

Wax. Conventionally patterns for investment casting are made by injection molding wax. Now, it is possible to build these patterns directly for investment casting by using the SLS process [Chua and Leong, 1997]. This is a standard investment casting wax used by foundries, in powder form. They are typically used to make wax patterns, which are then used in the investment casting process to produce metal prototypes, cast tooling, and limited run parts. Wax patterns are used to define the part shapes that are then melted away. These patterns can also be used to augment investment casting process development.

Polymer. The formation of accurate and strong parts from polymer powder has been studied by a number of authors [Nelson 1993; Dalgarno et al., 1996; Childs et al., 1997].

Nylon. Nylon is one of the most durable rapid prototyping materials available in the industry. This material is suitable for building models and prototypes that can withstand and perform in a demanding environment or parts with working features such as hinges or snap fits [Chua and Leong, 1997]. Initially, four nylon-based materials (standard nylon, fine nylon, fine nylon medical grade, nylon composite) were available commercially. Currently, two new commercial nylon-based materials for SLS process have replaced these four materials. These new materials are Duraform Glass-filled and Duraform Polyamide. The advantages of Duraform prototypes are the relative ease with which they can be finished to a smooth appearance and the low cost when a small

number of parts is required. The disadvantage of nylon materials is that nylon parts need a long cooling cycle in the machine before they can be removed (6-8 hours).

Ceramic. Existing ceramic manufacturing processes have a number of limitations. They are not well suited to the fabrication of complex parts. Ceramics melt at high temperature, this making it difficult to process by SLS [Deckard and Dennis, 1993]. Initial work has indicated that ceramic with polymer coating can be processed by using SLS to make turbine blade cores [Klocke and Wirtz, 1998].

Metal. Because of the high demand for metal tooling the development of rapid metal tooling has a position of central importance in rapid manufacturing research. DTM introduced its first metal materials (RapidSteel 1.0) in 1996. This material was primarily used to create steel/copper mould inserts from which large quantities of plastic parts and prototype quantities of pressure die cast parts can be produced. In 1998, DTM introduced its next generation of this metal material (RapidSteel 2.0), which offers improvements in processing time, finishing time, and accuracy compared to the original material. Laserform ST-100 is the latest version of the DTM RapidTool process. Laserform ST-100 is a stainless steel 420 based powder coated with a plastic binder that is sintered and infiltrated in one furnace cycle.

There are two ways to obtain a metal part by laser sintering, denominated as indirect and direct selective laser sintering. Indirect SLS of metals relies on melting of polymer coating on each metal particle, this "green" part can then be handled with subsequent de-binding, sintering and low melting point infiltration stages which are necessary to produce a full density part [Beaman et al., 1997]. Direct SLS is aimed to melt and consolidate the chosen metal during the SLS process directly to form a desired shape

having full density, eliminating the need for debinding and infiltration. Sections 2.3.2 and 2.3.3 consider these two approaches.

2.3.2 Indirect SLS of Metals

2.3.2.1 Introduction

In the indirect SLS process the raw material is polymer (hybrid thermoplastic/thermoset polymer) coated metal powder, or a mix of polymer and metal powders. The laser is used to melt the polymer and produce a green part in which the particles are bonded together by the solidified polymer. This green part is then processed in a high temperature furnace to remove the polymer and sinter the part, creating metal-metal bonds. The green parts produced by indirect SLS process have a large amount of pore space and so full density consolidation is accompanied by large shrinkages. To overcome this problem, a partially sintered part can be infiltrated with a lower melting point material to produce a fully dense composite structure [Badrinanyan and Barlow, 1992,1994,1995; Tobin et al., 1993].

Two different methods of producing the metal-polymer composite (coating and mixing, Figure 2.8) have been investigated. The strength of green parts made from coated particulate is usually higher than that of parts made using a powder mixture at the same polymer content [Badrinarayan and Barlow, 1995], see Figure 2.9. In addition, coated powder is more homogeneous than mixed powder. Therefore, the problems of segregation that can occur in mixed powders can be overcome.

A large number of different polymers have been investigated for use as a binder; such as copolymers of methylmethacrylate, polymethylmethacrylate, butylmethacrylate, polystyrene and polyethyleneglycol [Klocke et al., 1995; Beaman et al., 1997].

The main advantage of indirect SLS processing is that only the binder material needs to be melted. On the other hand, the indirect SLS processes currently in use still have some restrictions. Models can be made from a limited variety of materials that usually have poor mechanical properties, thermal properties and accuracy. The process to build mould inserts can take a long time.

In addition, the fragile green parts, and especially small features on the green part, can be damaged by handling from the sinterstation to the furnace. Therefore, investigation of new ways to reduce the processing time, improve the properties of products, and increase the accuracy is of great interest.

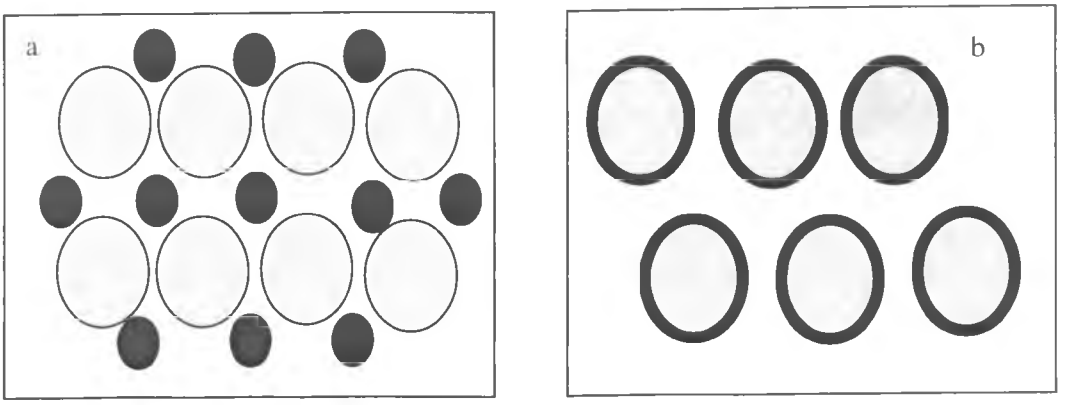

Figure 2.8: Binder/ particle morphologies, (a) the binder is mixed with the particles, (b) binder is coated on the particles.

Boivie [2000] reported an alternative approach to that adopted in the RapidTool process to generate steel components using Fe-Cu-C mixed with 5% of a phenolic binder material and indirect SLS. Of interest in this work was a trial to exploit the fact, that

when Cu dissolves in steel, copper causes the steel to swell to an extent which can compensate to some degree for the shrinkage which can occur during the sintering cycle.

To overcome these problems, the ability to build parts directly from metals without the need for post-processing has been investigated. This process is called direct SLS, as will be described in section 2.3.3.

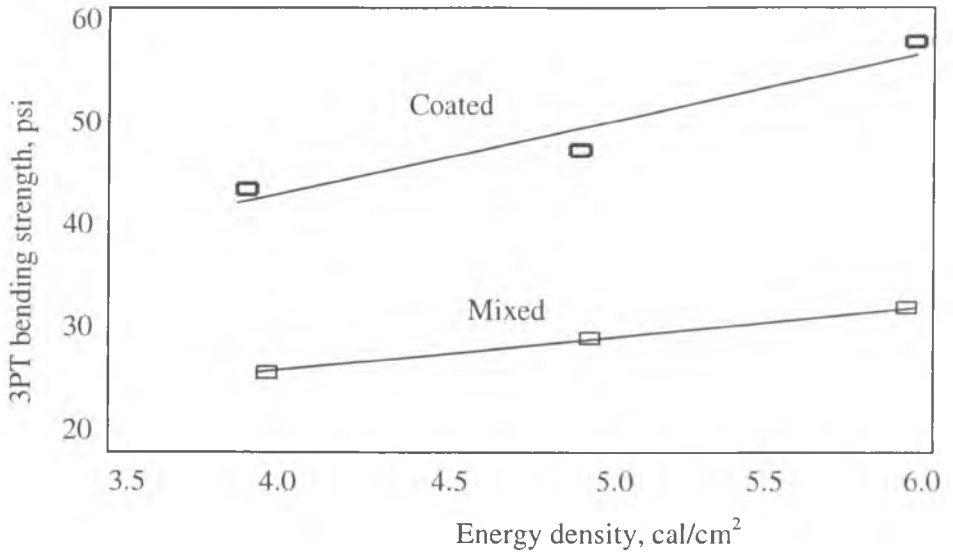

Figure 2.9: Comparison of bending strength of SLS processed green parts made from mixes metal polymer powder and from metal coated powder [Badrinarayan and Barlow, 1995].

2.3.2.2 The DTM RapidTool Process

The DTM RapidTool family of tooling products consists of three materials, RapidSteel 1.0, RapidSteel 2.0 and Laserform ST-100. Each of these materials requires different processing techniques. Each material has different furnace cycles associated with it. The most notable variation being that traditional sintering and infiltration elements have

been carried out in separate cycles, and as part of the same cycle. Currently for the Laserform ST-100 material, there is only one furnace cycle.

A - RapidSteel 1.0

The first product, RapidSteel 1.0 powder, is made up of spherical low-carbon steel (1080 carbon steel) with a mean volume average particle size of 55 μm. This powder is uniformly coated with 0.8 weight % thermoplastic binder. The apparent packing density of the powder is 4.1 g/cm^3, while the tap density and the density of the green parts is 4.3 g/cm^3 which is 55% of the theoretical density of the steel. The strength of green parts depends on the extent of polymer to polymer bonding as reflected in the size of the polymer bonds between steel particles. Green strength increases with an increase in either the binder level in the feed material or the total laser energy delivered to the powder. However, there are practical limitations to both variables. Excessive laser energy causes a reduction in strength due to the thermal degradation of the binder, and as the binder level in the powder increases, shrinkage during furnace processing increases. In addition, the three-point bend test for green parts ranges from 2 MPa to about 2.8 MPa, and this fracture strength is sufficient for parts to be handled and for small features to be built and cleaned [Uday and McAlea, 1996; Beaman et al., 1997]. The processing of RapidSteel 1.0 as described in Figure 2.10 can be broken down mainly into three main stages:

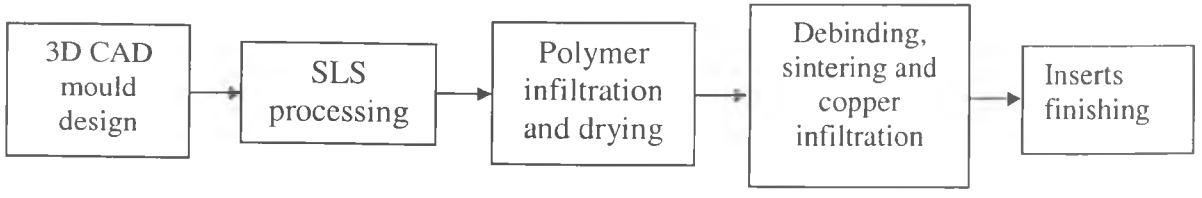

Figure 2.10: Description of the RapidSteel 1.0 process

1- SLS processing: The particles (coated with a polymer binder of low melting point) are processed in SLS sinterstation machine without heating the feed and part bed. Tooling inserts in the green stage are built layer by layer through fusion of the binder. After SLS processing, excess powder next to the parts is brushed away by fine brushed and compressed air.

2- Polymer infiltration and drying: After the green part is manufactured, it is infiltrated with an aqueous acrylic emulsion. Infiltration occurs by capillary action when the parts are placed in the emulsion. Then, the part is dried in an oven to prevent part distortion during the low temperature portion (about 50°C) of the subsequent furnace cycle. The polymer infiltration step is very important to eliminate the shrinkage in the direction of gravity.

3- Furnace processing: After the stage of polymer infiltration and drying, the part is subjected to a thermal cycle. The binder is removed from the part by thermal decomposition during two temperatures hold: one at 350°C for 5 hours and the second at 450°C for 5 hours. Then the temperature is increased to 1000°C for 8 hours to allow the sintering of the steel powder. After the sintering, the furnace temperature is increased to 1120°C with a hold time of 1 hour where copper infiltration occurs driven by capillary action and no external pressure is required. The amount of copper used corresponds to 80% of the green part weight. A mixture of 70% nitrogen and 30% hydrogen is used during furnace cycle to remove the oxides from the steel surface. The total time of this cycle is about 48 hours.

The final infiltrated part of RapidSteel 1.0 powder is 60% weight steel and 40% weight copper which can be finished using any technique.

The advantage of RapidSteel 1.0 material is that there is no restriction on the complexity of the geometry of the part using indirect SLS process. Uday and McAlea [1996] mention that mechanical and thermal properties of RapidSteel 1.0 (the first commercial RapidTool material) are similar to that of aluminium 7075. The strength of DTM RapidSteel 1.0 has been studied by Stewart et al [1999]. They reported that the fully infiltrated RapidSteel material was found to have a yield strength of 500 MPa and an Elastic Modulus of 210 GPa.

B- RapidSteel 2.0

RapidSteel 2.0 is the second version of DTM RapidTool material which was announced in the mid of 1998. This version offers a number of modifications over RapidSteel 1.0 such as; the main metal has been changed from 1080 carbon steel to 316L stainless steel, the thermoplastic binder material has been changed to a thermoset binder, and the infiltrant has been changed from copper to bronze. In addition, the particle size of RapidSteel 2.0 is ranging from 22 to 53 μm, with an average of 34 μm and the amount of polymer mixture is 2.75% by weight [Nelson et al., 1998]. This allows part to be built with smaller layer thickness of .075 mm.

To avoid segregation RapidSteel 2.0 mixture is obtained by putting all the constituents in powder form in a container, which is then heated up and stirred so that the polymers can stick to the metal particles. Realistic surveillance suggests that the polymers only partially stick to the metal particles because of the amount of 'dust' produced when RapidSteel 2.0 is poured from one container to other. This observation also gives evidence about the very small size of polymer particles used, which contributes to the lesser shrinkage experienced by this material during laser sintering, because the fine particles will reside in the interstices between metal particles. RapidSteel 2.0 provides

improvements in processing time, finishing time, strength, and accuracy [Dalgarno et al., 2000], as a result of reduced process shrinkage, compared to the original RapidSteel material.

Because of the modifications of RapidSteel 2.0 over RapidSteel 1.0, the processing of RapidSteel 2.0 differs from that of RapidSteel 1.0 as following:

1. SLS process: The initial temperature of the powder bed is 120°C to prevent part movement at the beginning of the process and after certain height (when Z= 2.54mm) the temperature is dropped to 90°C [DTM, 1999]. The fracture bending strength of green part ranges from 1.4 MPa, (that is the minimum strength to handle and clean without damaging of small feature) to 2.1 MPa.
2. Sintering cycle: The temperature of sintering is 1120°C for 3 hours with a heating rate of 120°C/hour and decreased to room temperature During the heating phase the polymer binder is burned off to leave a steel skeleton.
3. Infiltration cycle: The temperature is raised to 1050°C for three hours and decreased to room temperature at a cooling rate of 180°C/hour.

Figure 2.11 shows the RapidSteel 2.0 processing. The final RapidSteel 2.0 part is made up of 53% stainless steel and 47 % bronze and can also be finished by any conventional technique.

C- Laserform ST-100

Laserform ST-100 is the latest version of the DTM RapidTool process [Stucker, 2000]. Laserform ST-100 is a stainless steel 420 based powder coated with a plastic binder that is sintered and infiltrated in one furnace cycle. The significant difference between Laserform ST-100 and RapidSteel 2.0 is that the Laserform ST-100 has a broader particle size range, with fine particles not being screened out. These fine particles allow

the Laserform ST-100 material to be sintered at a lower temperature than the RapidSteel 2.0 powder, which makes possible the single furnace cycle for sintering and infiltration. The benefits of Laserform ST-100 include that it is a magnetic material and can be fixtured using magnetic chucks, and that the finer particles allow for greater feature definition, sharpness of corners and strength of the parts.

Table 2.1 presents the physical, thermal, and mechanical properties of RapidSteel 2.0 comparison with RapidSteel 1.0 and Laserform ST-100 [Uday and McAlea, 1996; DTM, 1998; DTM 2002].

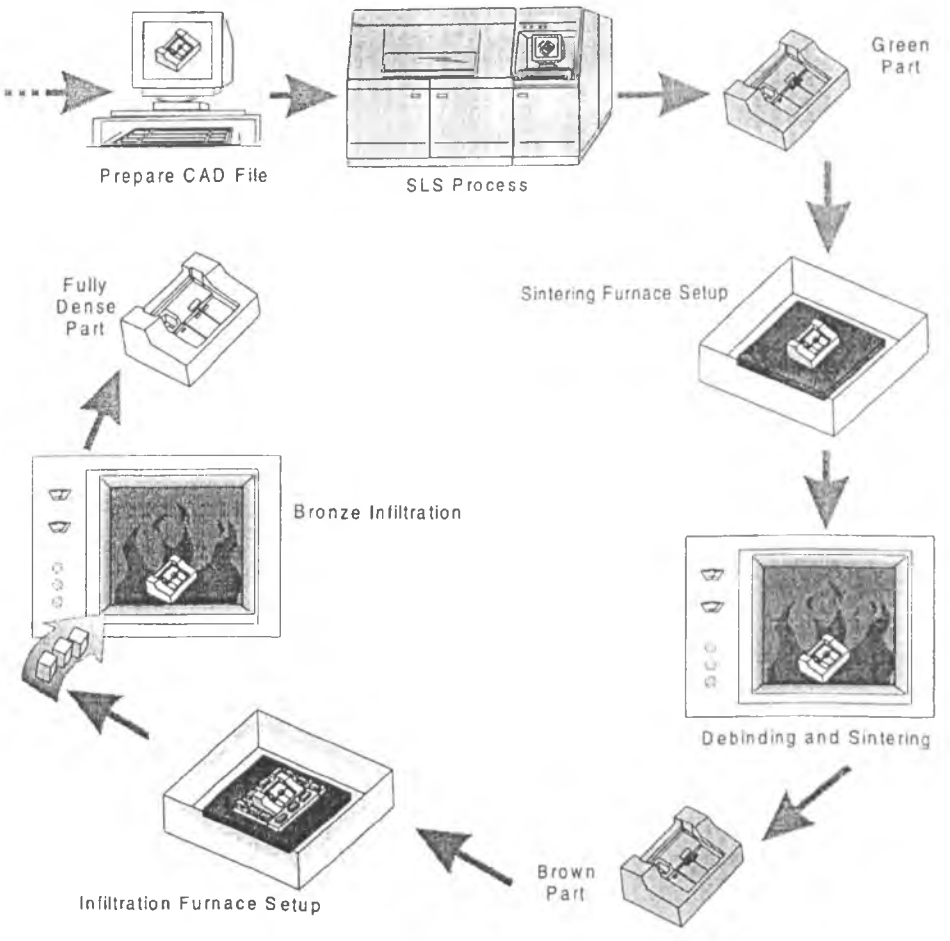

Figure 2.11: The RapidTool process using RapidSteel 2.0 [DTM, 1998]

Table 2.1: Physical, Thermal and Mechanical Properties of Compression RapidSteel 2.0, Laserform ST-100, and RapidSteel 1.0

Properties	RapidSteel 1.0	RapidSteel 2.0	Laserform ST-100
Density g/cm^3	8.23	7.5	7.7
Thermal Conductivity W/m °C @ 100 °C	184	23	49
Thermal Expansion Coefficient 10^{-6} m/m °C	14.4	14.6	12.4
Yield Strength (0.2%) MPa	255	413	326
Tensile Strength MPa	475	580	587
Elongation %	15	0.9	12
Young's Modulus GPa	210	263	153
Hardness - Rockwell	75.3 "B"	22 "C"	87 "B"

2.3.3 Direct SLS of Metals

Direct SLS is a process in which a high energy laser beam directly consolidates a binderless metal powder, to high density, preferably with minimal or no post-processing requirements. Early attempts to use SLS to process single phase metals such as tin or zinc were unsuccessful due to the quick consolidation of molten powder into a sphere diameter approximately equal to the laser beam diameter rather than consolidating into the previous layer, known as balling [Beaman et al., 1997]. To overcome the tendency to form spheres, a two-phase powder approach was developed [Bunnell et al., 1994; Das et al, 2000]. The laser power heats the powder bed inducing melting only of low melting point material. The disadvantage of this processing route was that the components produced exhibited the mechanical properties and characteristics of their weakest composite phase, thus lacking the full mechanical functionality required for heavy-duty

tasks. Klocke et al [1995] and Kruth et al [1996] reported that due to the brief heat interaction time in SLS process, the only means of building parts consisting of high melting point metal is via Liquid Phase Sintering (LPS). The liquid wets the high melting point powder and binds it together. Using this two phase powder approach, it becomes possible to induce melting without balling by adjustment of the volume fraction of the high melting point phase. This approach has been used successfully in SLS processing of metals and ceramics such as Cu-Sn bronze-Ni, Ni-Sn, WC-Co and alumina-boron oxide [Gopalakrishna and Bourell, 1993; Beaman et al., 1997].

There have been other successful attempts to use direct SLS processing for metal and metal-ceramic materials [Deckard et al., 1993]. These material systems include binary and ternary mixtures such as bronze-nickel and tungsten carbide-cobalt-nickel. The nickel is the high temperature component and bronze forms the liquid phase during SLS processing. With this material system densities up to 80% of theoretical density were attained. To increase the density of bronze-nickel parts to 95% of theoretical density, traditional liquid phase sintering at elevated temperatures was used [Agarwala et al., 1993].

Carter et al [1993] sintered iron powder using direct laser sintering, but the density was very low (35% of theoretical density). Carter mentions that due to the greater thermal contraction on the upper surface of each layer the sintered powder tends to warp upward. They built an anchor of thin sintered layers onto which the actual structure was constructed to overcome this problem. There are other ways to avoid warping and distortion of layers, such as heating the powder bed [Carter et al, 1993; Klocke et al., 1995], or bonding the part to a rigid sample of the same material during the first stages of the sintering process. Simchi et al [2001] investigated laser sintering of a steel based

powder mix. They note that careful consideration of shape, size and distribution of the particles and the chemical constitution of the powder system can increase the powder bed density for laser processing. They report densities of 90-97% theoretical for the laser sintered material without shrinkage, with 99% of theoretical density after post processing step. Another approach has been used for production of cermet composite turbine sealing components. This cermet composite is composed of two different types of titanium coated ceramic abrasive grit, a nickel alloy matrix, and a lower melting point cobalt based braze material [Fuesting et al, 1996]. They reported that energy densities of 2000 to 4000 J/cm^2 were required to eliminate porosity. Energy densities of 1900 to 2200 J/cm^2 produced a very fine grained equiaxed fully dense superalloy microstructure which may exhibit superplastic properties at elevated temperature, and energy densities in the range of 2500 to 3500 J/cm^2 produced a fully dendritic microstructure. They also reported that mechanical testing results indicated that direct SLS can produce properties equivalent to or better than conventional labour intensive process.

Wilkening [1996] has been successful in sintering a mixture of Ni, Cu, Sn and P using direct laser sintering. The porosity of parts produced by this process is approximately 25%, which requires a secondary process to fill the pores and to improve the mechanical characteristics of the part and also to obtain a much smoother surface. This process is commercialised by EOS GmbH with the name of EOSINT M. The EOSINT M builds tools for plastic injection molding and metal die-casting. The system offers a high performance layer manufacturing technique where even complex shapes can be built with ease, including geometries which are impossible to cut with conventional tools, such as internal cooling channels. This sinterstation machine can build metallic parts up

to 250 × 250 × 185 mm^3 using a CO_2 laser. The laser scan speed can be up to 3000 mm/s.

Although in some studies, as reported above, it is possible to obtain parts with high density using direct metal sintering [Klocke and Wirtz, 1996; Das et al., 1997] the materials are limited, and the accuracy and surface finishing are poor. More research is needed to able to improve the properties and accuracy of parts that are produced by this process.

2.3.4 Accuracy of SLS parts

The accuracy of SLS process is difficult to predict as it is a function of many different parameters, some of which can be mutually dependent [Nelson et al, 1995]. Pham and Dimov [2001] reported that the parameters that most influence RP accuracy can be considered in three groups. The first group includes the factors causing errors during the preparation stage of STL file and model slicing (pre-processing errors). The second group consists of the factors influencing the part accuracy during build stage (processing errors). The last group involve the part finishing techniques in use (post-processing errors).

First group: The accuracy of STL files, which approximate the surface of the 3D CAD model by triangles, can be controlled during their generation by modifying the chord height and the angle control factor [Williams et al., 1996]. Chord height specifies the maximum distance between a chord and surface (see figure 2.12). The beam offset is compensated in the SLS process by applying a scale factor to the STL file. A procedure to obtain a general scale factor and beam offset value was developed by Nelson and others [Nelson et al., 1995]. Once the scale factor and beam offset values are

determined, the STL file is edited and is then ready to be used to generate a part that will be closer to the required dimensions. The values of scale factor and offset are specific for each material, SLS machine and set of processing parameters used, therefore, if any parameter changes, new values should be obtained.

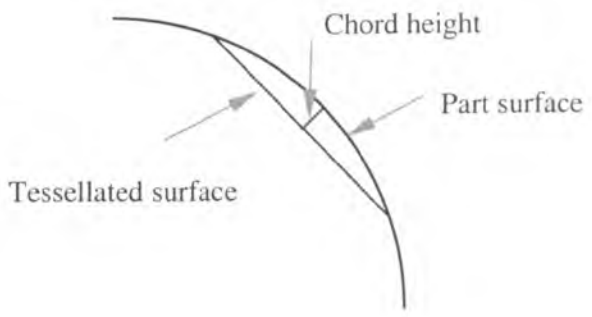

Figure 2.12: Chord height [Pham and Dimov 2001]

The accuracy of the SLS process also depends on the layer thickness. An increase in the layer thickness increases the stair stepping. This problem influences chiefly the roughness of the part and can be alleviated by reducing the thickness of layers. But the layer thickness cannot be decreased too low and a compromise has to be found between thickness and build speed. This source of error is exacerbated by the constant slice thickness. It is possible to overcome this problem partially by using adaptive slicing which generates different slice thickness based on the local slope of the part, see Figure 2.13 [Crawford 1993; Suh and Wozny, 1994]. Karunakaran et al [2000] reported that there are two types of adaptive slicing for a hemispherical die cavity: first adaptive slicing with zeroth order approximation of edges i.e., squared edges; second adaptive slicing with first order approximation of edges. They reported that the first order approximation of edges (second type) would be free from the staircase effect. In addition, there are other types of errors resulting from slicing such as the error due to mismatching in height between slice positions and feature boundaries.

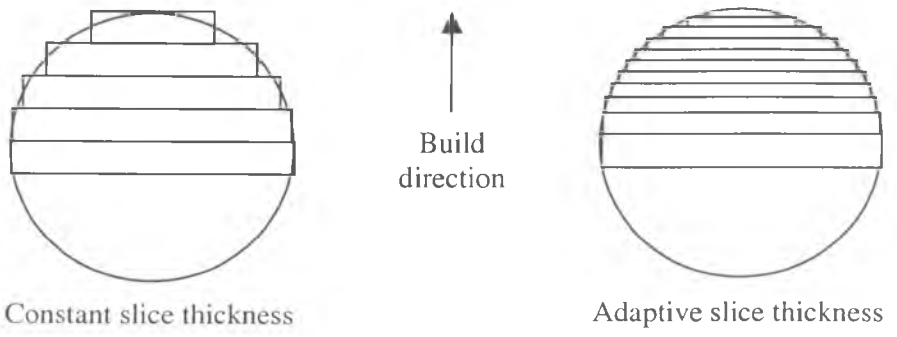

Figure 2.13: The effect of adaptive slice thickness on part accuracy [Crawford, 1993]

Second group: During the build stage process specific errors can occur as a result of material shrinkage and control errors. All materials which can be processed by SLS have different properties that can affect part accuracy. Shrinkage is the main cause of inaccuracy during sintering and does not always occur in a uniform manner. The shrinkage of a next layer can be constrained by support powder trapped within enclosed areas or by the existing part substrate. Beaman et al [1997] reported that the areas at high temperatures tend to shrink more than those at lower temperatures and part geometries such as thick walls or sections can increase the shrinkage. The material shrinkage is compensated in the SLS process by calculation of the material shrinkage coefficient using a test part and applying a scaling factor in each direction to the STL file (see Figure 2.14) in accordance with the following relation:

$$\text{New dimension} = r\,(\text{desired dimension}) + f \qquad (2.1)$$

where r is scaling factor and f is offset value. The values of r and f are calculated from the X and Y axes assuming linear shrinkage for the SLS process.

Beaman [1997] adds that scaling a three-dimensional faceted file uniformly is not a simple duty and the resulting geometry can be a little deformed compared to the

nominal geometry depending on the scaling method used. To overcome problems due to the shrinkage the best method would be to build a trial part, measure its shrinkage and distortion in all directions and rebuild it according to a new design taking into account the dimensions and shape changes that occur during the process. But the disadvantages of this approach are the time consumed and the cost.

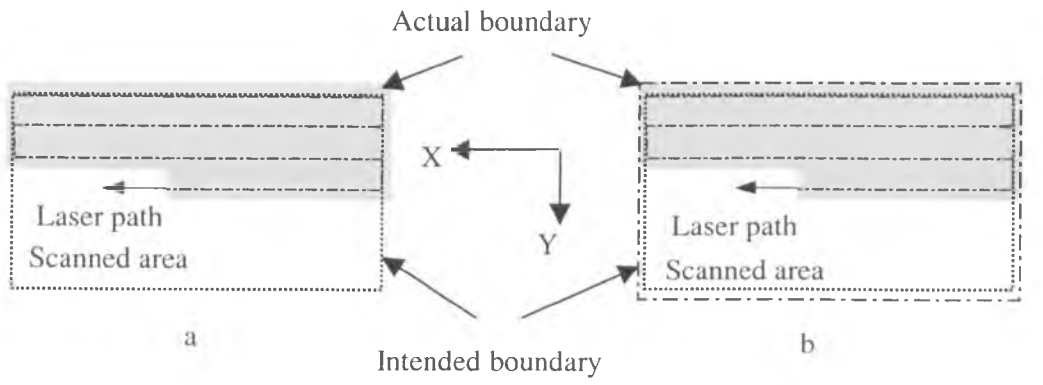

Figure 2.14: Shrinkage, (a) without compensation, (b) with shrinkage and offset compensation [Pham and Dimov 2001]

The other source of the error is laser beam offset. A beam offset is equal to the radius of the laser beam. As the beam scans, more material at the edges of the part will be sintered than necessary. To compensate for this error, twice the beam offset has to subtracted from the size of the part in X and Y directions. An intended size and the excess dimensional in X and Y directions due to the beam offset is shown in Figure 2.15.

In addition, the scanning system is an important subsystem in SLS equipment. The scanning system is responsible for moving the laser beam over the powder bed surface to create the desirable part geometry. The laser beam in the DTM equipment is deflected in an X-Y manner using two mirrors operated by two galvanometers arranged as shown in Figure 2.16.

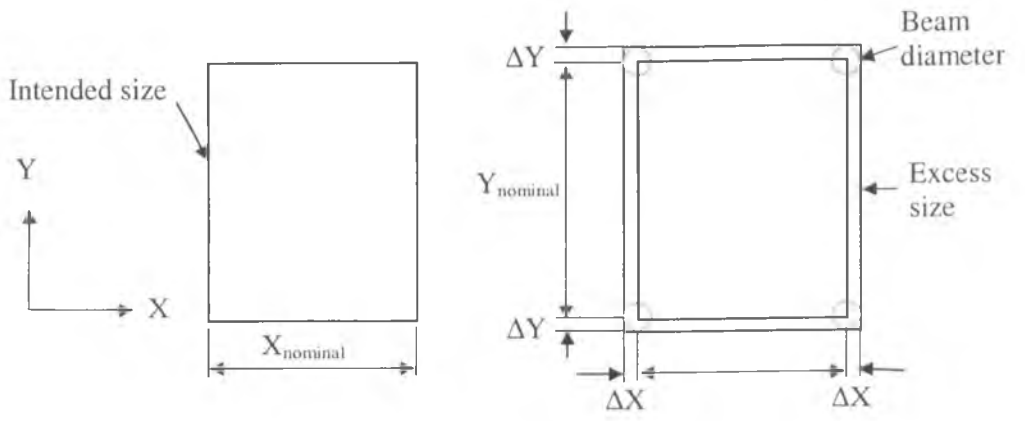

Figure 2.15: Intended size and excess dimensional due to beam offset

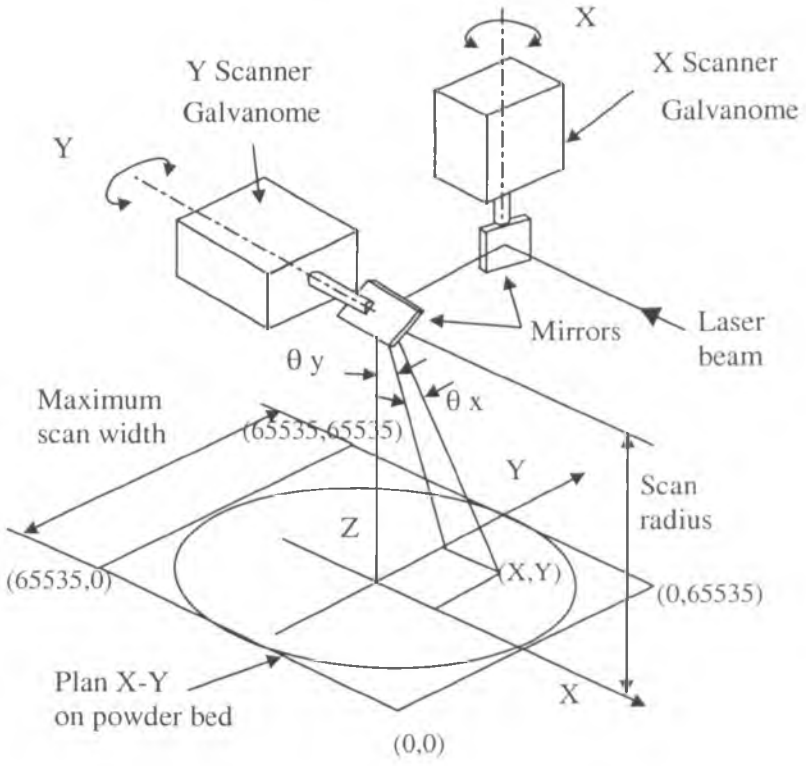

Figure 2.16: Schematic drawing of scanning system for DTM equipment [Volpato 2001]

The range of displacement is ±20° that is divided into 65535 increments, reflecting units of least significant bits [GSI, 1991]. The powder bed is described in a square shape by an X-Y coordinate plane, ranging from 0 to 65536 for each axis.

The length of one scan vector must be subdivided into equal increments or (micro-vectors) and their magnitude is specified by the parameter step size, which will guide the movements of the mirrors

At the beginning of the vector the scanners being to move only after an initial delay caused by the inertia of the mirror and rotors, therefor, to avoid over exposure at the beginning of the line causing blooming, a "laser on delay", which allows turning on the laser just after the scanner has begun accelerating, is required. In addition, at the end of the vector, the scanner still lags the start signal by some amount and requires time to reach the actual endpoint of the drawn vector. So, a "scan delay" is required to allow the beam to catch up with the command signal before the next movement is taking place. In the meantime a "laser off delay" keeps the laser on to allow the scanner to reach the endpoint of the vector. Figure 2.15 shows the effects of the "laser on delay", and 'laser off delay' on scanned vector.

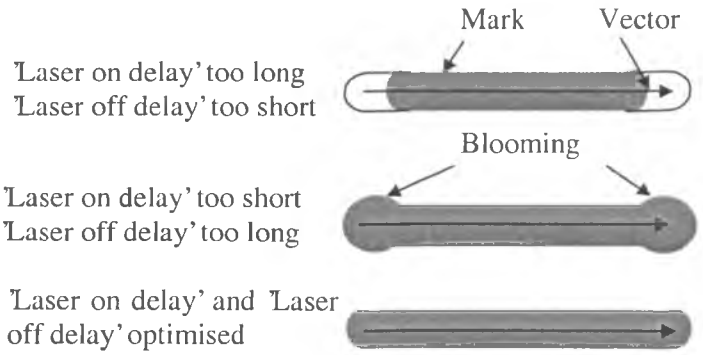

Figure 2.15: The effects of the 'laser on delay', and 'laser off delay' on scanned vector [Volpato 2001]

In order to increase scanning efficiency all parameters mentioned above need to be optimised or tuned. The tuning of these parameters is affected by the beam speed, because of the different response of the galvanometers [Nelson et al., 1995]. Even after

all parameters have been optimised, inherent errors associated with the galvanometers can affect part accuracy [Beaman et al., 1997]. These errors are functions of the mass of the mirrors, the design of the galvanometers, and scan speed.

Third group: To improve the surface appearance of the parts that are produced by some RP applications additional finishing is required. In this stage the stair step effect on important surfaces has to be removed. Pham and Dimov [2001] mention that model accuracy after finishing operations is influenced by two factors, the varying amount of material that has to be removed and the finishing technique adopted.

2.3.5 Process Parameters in SLS

There are many processing parameters which affect how well a SLS object is manufactured. Each parameter has some effect on either the time of sintering during the formation process or the feature definition of the completed SLS object. The process parameters are divided into two groups; building parameters and materials parameters. The next section will outline the process parameters and will discuss briefly how the parameters influence the sintering process.

2.3.5.1 Spot Diameter

The laser beam diameter at the laser material interaction surface is defined as the spot size and can be easily defined in terms of the stand-off distance. A decrease in the spot size will increase the power density, which increases energy absorption, and also will lead to a reduction in exposure area. This reduction in exposure area will allow increased part definition during SLS, and will improve the accuracy, but equally increase the raster time [Steen, 1998; O'Neill et al., 1998]. In addition, a smaller spot

size is used to achieve smaller feature sizes when scanning fine details and to reduce curling.

2.3.5.2 Laser Power and Scan Speed

The main effect of increasing laser power is to decrease the time of melting and increase the depth of heat penetration. Laser power is absorbed by the powder particles and heat is generated instantaneously in the powder layer. The rapid heat generation causes practically complete and very local melting of the powder. The faster the scan speed the less time there is for heating.

The laser power and scanning speed can be used to calculate the linear average energy density, which is a description of the laser energy input per unit area. The energy density is calculated using the Andrew number A_N:

$$A_N = \frac{P}{vs} \quad \text{J/mm}^2 \tag{2.2}$$

where

P is the incident laser power (Watts)

v is the scan speed (mm/sec)

s is the scan spacing (mm)

Equation 2.2 has been used to correlate SLS parameters with sintering behaviour such as sintering depth, strength and density. As shown in Figure 2.18 the dimensions of the sintered region will increase with increasing energy density. The energy received at the powder bed will increase with increasing power and with decreasing scan speed or scan spacing.

Figure 2.19 shows the effect of laser scan speed and power on the density for a bronze-nickel mixture. Density increases with increase energy density, accomplished either by decreasing scan speed or increasing laser power [Agarwala et al., 1993].

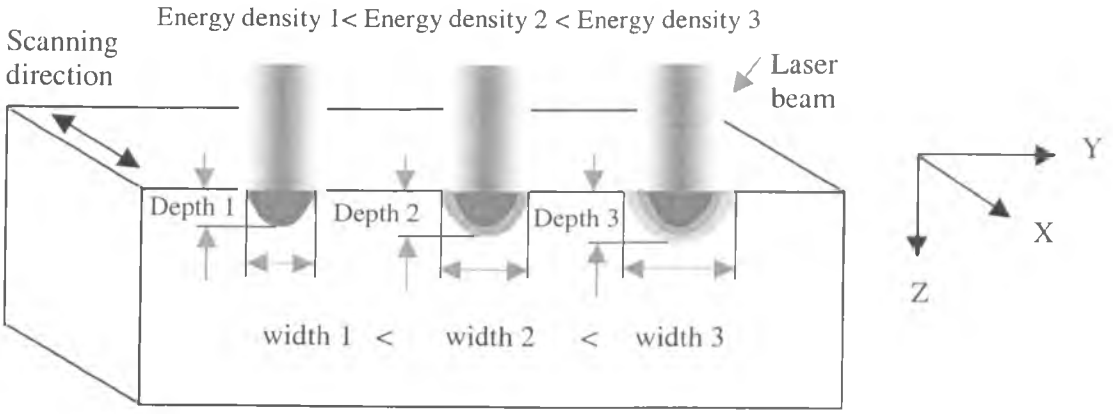

Figure 2.18: Effect of the energy density on track depth and width [Volpato 2001]

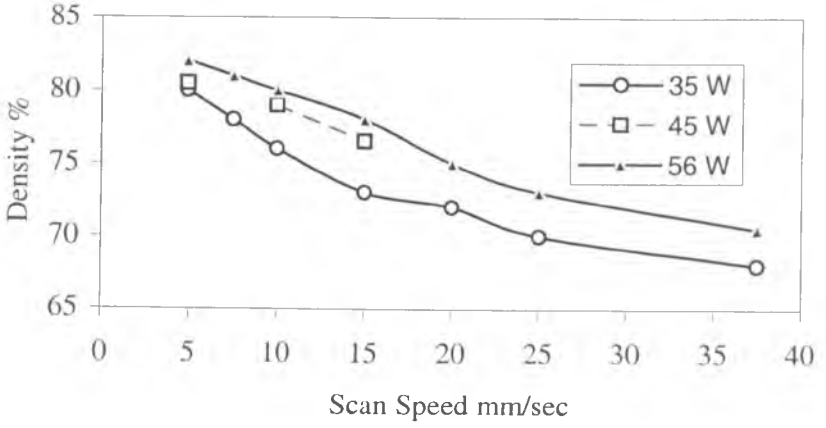

Figure 2.19: Fractional density of selective laser sintered bronze-nickel parts as a function of scan speed and laser power [Agarwala 1993].

The Andrew number can be used to predict physical properties, such as part strength, by including an empirical constant K_1 (see Equation 2.3). But this equation has some limitations because it does not consider the rate of energy which can be imparted to the powder or the influence of energy losses during the laser beam interaction period

[Miller et al., 1997; Beaman et al., 1997; Williams et al., 1998]. Also this assumes only a liner relationship.

$$\text{Strength} = K_I \times A_N \qquad 2.3$$

The change in the width of melt pool has been observed to be almost linear with changes in both laser power and scan speed [Yevko et al, 1998]. Sun [2001] demonstrated that a decrease in specific laser energy leads to a decrease in width and height of clad in laser cladding. Laser cladding is defined as the fusion of a powder layer to a substrate surface, with minimum melting of the substrate, so that surface alloy composition can be controlled more easily, and so is analogous to SLS. However, with decreasing specific laser energy, some defects, such as pores tend to be formed in the clad layer. Yevko [1998] reported that the height of clad was found to increase with decreasing scan speed but the height decreased with increasing laser power level. This phenomenon is due to a large increase in the corresponding cladding width, where the overall volume of the powder available does not change significantly.

Niu and Chang [1999 a] discuss surface tension effects and conclude that surface tension driven fluid flow dictates the melt pool shape. The strong surface tension forces will act to minimise the surface area further by breaking up the liquid bead into a series of balls. This phenomenon was found to be a major concern during early direct metal laser sintering research.

Niu and Chang [1999] further said that the balling problem for M2 high-speed steel could be controlled at scan speeds lower than 20 mm/s. They also demonstrated that at high laser power (80W-150W) and scan speed of 10-20mm/s balling become more widespread and so a balance between power and speed had to be readdressed by decreasing the scan speed further (<10 mm/s). Niu and Chang [1999] attempted to use

Rayleigh stability to explain the phenomena of melt balling, which describes the break up kinetics of a column of liquid, and could be used to help explain metal pool balling during selective laser melting.

2.3.5.3 Scan Spacing

Scan spacing is the distance between two neighbouring parallel scan vectors (Figure 2.20). A variation of scan spacing leads to different effects. For the case when the scan spacing is small compared to the laser diameter, the molten powder particles from the separate larger beads of high density combine, leading to higher overall density of the part, however the surface roughness also increases. For scans spacing larger than the beam diameter, the molten beads of material are not connected to each other, but the gaps are filled with unsintered powder. Dividing the width of layer by scan spacing s gets the number of scans in a 2D section. Usually this division is not accurate, meaning that there could be a gap at the end of the scanned section without sintering which can vary from a very small value to scan spacing millimetres long.

As the scan spacing increases, more energy is absorbed by the powder and transferred to the underneath sintered layers, resulting in a higher density. For small scan spacing, most of the light of the laser beam is reflected or absorbed from the previously drawn, solid line which has a coefficient of absorption significantly less than that of the powder. The amount of energy absorbed by the line melts the material again without adding further to the sintering depth. The amount of energy absorbed by the powder itself is small for a small scan spacing, thus not increasing the sintering depth. Note that this is only true for layers, which are being deposited on a previously scanned layer.

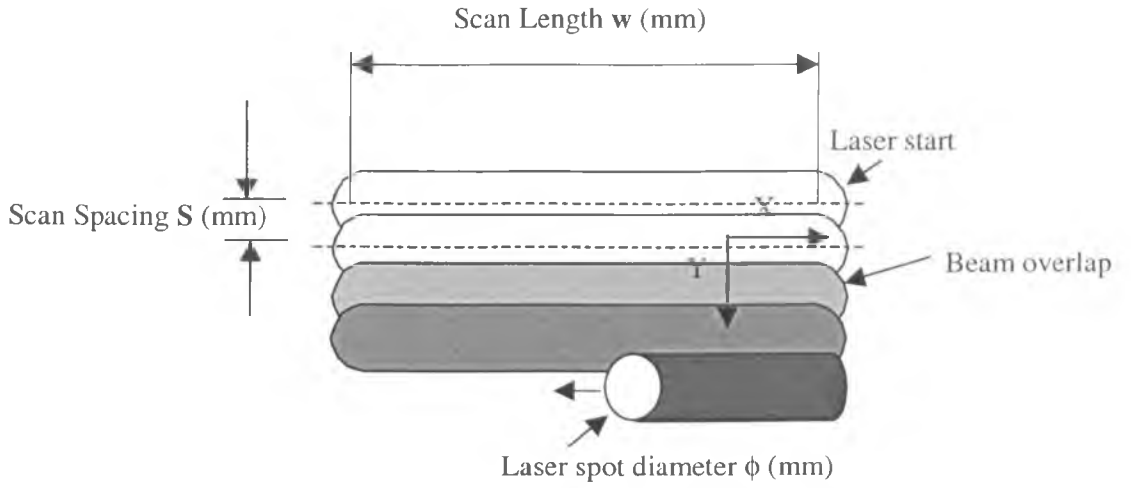

Figure 2.20: Clarification of scanning parameters

2.3.5.4 Layer Thickness

Layer thickness is clearly an important parameter in layer manufacturing technologies. A thick layer of powder is an important requirement during layer manufacturing because the bonding required to fuse consecutive layers is often difficult to achieve [Steen 1996]. Smaller thicknesses will increase the bond strength between layers, resulting in higher density components.

The total energy E (J) induced into a block with a length l, a width w and a height h, built with a layer thickness L_t is calculated using the following formula [Laoui et al., 2000]:

$$E = \frac{P}{v} * \left[l * \left(\text{int}\left(\frac{w}{s}\right) + 1 \right) * \left(\text{int}\left(\frac{h}{L_t}\right) + 1 \right) \right] \qquad (2.4)$$

where P is the laser power (in Watts), v is the scan speed (in mm/s), s is the scan spacing (in mm) and "int" refers to integer.

Laoui [2000] reported that for various combinations of layer thickness and scan spacing the density increased with increasing induced energy. The influence of layer thickness

on density is more pronounced at low amounts of supplied energy. With a smaller layer thickness, more energy is transferred to the underlying sintered layers improving further densification. The layers are barely distinguishable indicating that a high temperature bed and a higher laser power help in improving interlayer bonding.

2.3.6 Atmosphere Control

Many contaminations can be picked up from the surrounding medium through adsorption and chemisorption processes during powder production and sintering processes. Impurities in the sintering atmosphere have a marked effect on the densification of all metals. Oxygen is one of the most damaging impurities during metal powder sintering or melting. During metal powder processing, oxygen can be present in the surrounding atmosphere, contained within the porosity of the powder bed or in the form of a passive layer surface area associated with a powder mass. The presence of oxygen can fuel surface oxide growth, leading to poor wetting conditions and the tendency of the scan track to break up into balls. Decreasing oxygen content in metal powder can cause a substantial decrease in surface tension. This reduces the kinetics of the breaking up of the scan track during SLS process. Hauser et al [1999 a and b] reported that the presence of oxygen within the sintering atmosphere and powder bed allows surface oxides and slags to form as the powder is heated and melted by the scanning laser beam. The existence of surface oxides and slags increase the melt volume, and elimination of the oxygen is required to reduce the melt volume. Reducing the melt volume allows the surface tension force to become less dominant.

In direct SLS atmospheric control is principally driven by the need to prevent or remove oxide. The choice of atmosphere for use in direct SLS still remains diverse with little cohesion. The most common types of atmosphere currently used are:

1- Inert gases

2- Vacuum

3- Forming gas

A nitrogen atmosphere is used for sintering steel powder DirectMetal™ 50-V1 to 95% of theoretical density, resulting in excellent mechanical properties [Frank Petzoldt et al., 1999]. Carter et al [1993] reported that a good single layer of iron powder could be generated in an inert environment of argon. Wohlert et al [1999] demonstrated that single and multi layer components with high densities and good surface finishes were achieved in argon gas.

2.3.7 Material Properties

2.3.7.1 Powder characteristics

The properties of the powder, such as particle size and particle shape, and the collective properties of powder, such as packing density and flowability, can be customised leading to changes in the sintering kinetics, metal pool behaviour and laser absorptivity [Thummler and Oberacher, 1993; German 1994].

Usually powder metallurgy deals with particles that are larger than smoke (0.01-1 μm), but smaller than sand (0.1-3 mm), and most of the common particles have diameter ranging from 25 to 200 μm [German, 1998]. The range <40 μm is sometimes called the sub-sieve range, as with normal dry sieving it is difficult to separate such small particles. Therefore the range > 40 μm is the sieve range [Thummler and Oberacher, 1993]. Usually the powders are produced by gas atomisation techniques which creates a low oxygen content and particles with spherical shape and smooth surfaces [German, 1998]. These characteristics allow for perfect flow properties and reduce surface

contamination, which are possibly the primary concerns when selecting the powders for use in direct SLS. In contrast, powders produced by water atomisation techniques exhibit a high level of oxygen and an irregular morphology. These characteristics cause porous surfaces [Niu and Chang, 1999 b].

Terms like nodular, dendritic, acicular, fibrous, flaky, spheroidal, angular, irregular, and granular are used for a simple qualitative characterisation of powder particle shape. Some of typical examples are given in Figure 2.21. Porous particles differ from irregular ones because of the presence of the porosity, which itself may be very irregular in both size and shape. A large amount of porosity makes any shape characterisation very difficult.

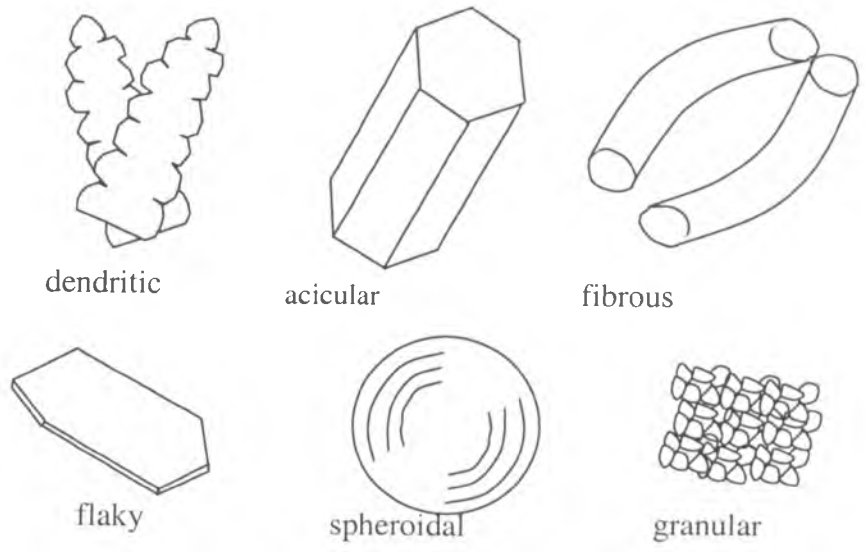

Figure 2. 21: Qualitative characterisation of powder particle shape

Particle size distribution curves as shown in Figure 2.22 relate the particle size to the corresponding fraction of the powder within the size range [Upadhyaya, 1997]. Particle size distribution information is essential for a complete characterisation rather than an average value or even maximum or minimum values of size.

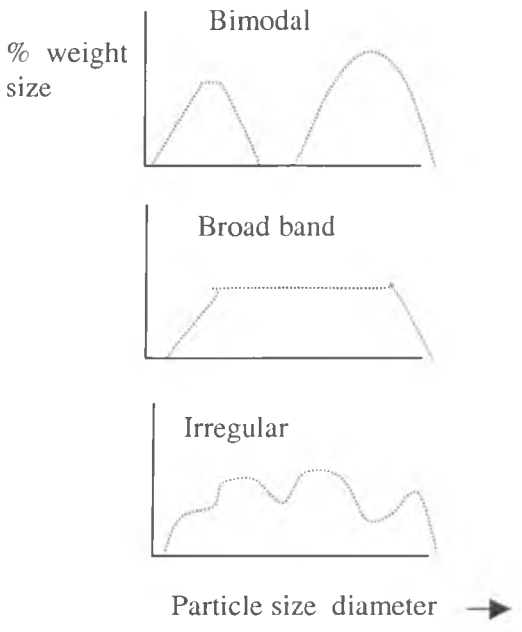

Figure 2.22: Schematic illustration of some realistic particle size distribution [Upadhyaya, 1997]

Niu and Chang [2000] reported that melting of metal powder produced high levels of porosity when the particle size was small (<38 μm) due to a high level of oxygen present in the fine particles. They also said that large particles required higher incident laser energy density to obtain a highly dense surface.

There are other studies which report that particle size often contributes to surface roughness [Das et al., 1999]. Karapatis et al [1998] reported also that the mean surface roughness is a function of particle size due to local heat transfer which will fuse surrounding particles to the molten region. The particle size and the presence of any agglomerated particles will determine the minimum layer thickness that can be deposited during a build process [Agarwala et al., 1995 a and b; and Kapapatis et al, 1998]. A large particle size sets a high value for layer thickness, increasing the stair step effect and also affecting the trueness of features. On the other hand, if the particles are

too fine, powder spreading with a roller becomes increasingly difficult due to static charges [Nelson, 1993; Kapapatis et al., 1998].

Powder packing density is an important parameter in defining the density of the sintered or melted layer following laser exposure. It affects the final part density and shrinkage, and in consequence, part accuracy [Volpato 2001]. Particle size, particle size distribution, and the mixing method all affect the density value. The more irregular the particle shape or the greater the surface roughness, the lower the packing density, as shown in Figure 2.23. The relationship between powder and sintering density for liquid phase sintering is often direct with final consolidated part densities often equating to the initial density of the powder [Lauwers et al., 1998]. Nevertheless, during full melt processing of pre-alloyed powders the effects of particle packing on melt density is reduced.

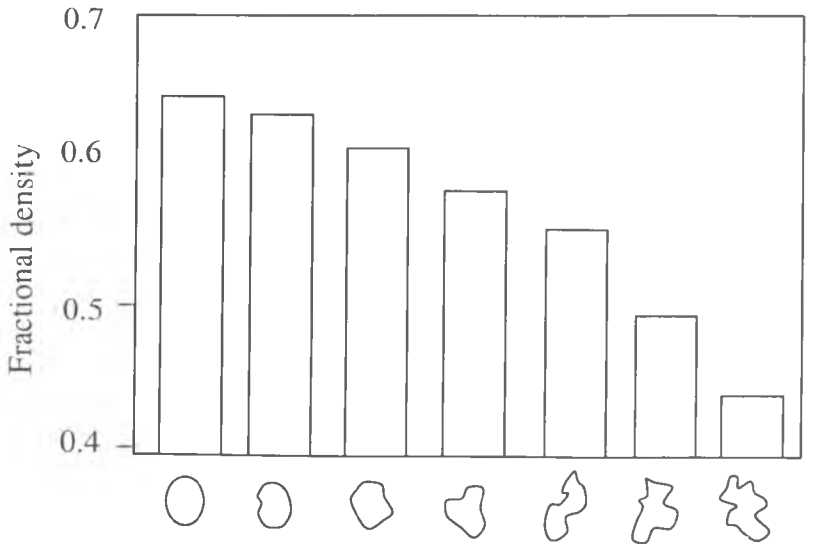

Figure 2.23: Fractional density of monosized powder for varying particle roughness [German, 1994]

Usually powder beds have relative densities ranging from 40 to 60% to the theoretical density, which typically lie between its apparent density and tap density value. The

apparent density of the powder refers to the mass per unit volume of loose powder usually expressed in g/cm^3. Very often a mass of loose powder is mechanically vibrated or tapped without the application of external pressure, this density called tap density [German, 1994; Upadhyaya, 1997]. For the tap density, a graduated cylinder of powder is vibrated for 3000 taps [German, 1998]. The apparent density is one of the most critical characteristics of a powder because it influences the behaviour of the powder during sintering.

The choice of deposition mechanism and the efficiency of powder fluidity play a decisive role in the SLS process. The standard method for powder fluidity determination is by the Hall flowmeter, where the time necessary for 50 g of powder to flow through a prescribed small orifice is measured. Flow times are proportional to the reciprocal of the flow rates. Very fine powders do not flow through a small orifice due to the drastic increase in the specific surface area as the size becomes very small. The higher the apparent density of the powder the lower the flow time [Upadhyaya, 1997]. Particle size and size distribution affect not only flow but also very importantly the behaviour during sintering; fine powders sinter much more readily than coarse powders by reason of the thermodynamic driving force associated with the larger surface area.

2.3.7.2 Thermal properties of the powder bed

Thermal conductivity, powder bed density, and specific heat are important properties of the powder bed for the study of the dynamics of the sintering process. Thermal conductivity is an important property in SLS process as it dictates how the heat flows into the powder bed. The heat transfer through the powder bed is primarily limited by thermal conduction through the gas that fills the voids [Beaman et al., 1997]. According to the type of material and bed density thermal conductivity may change with

temperature. Williams and Deckard [1998] reported that the thermal conductivity increases as the powder bed density increases with density due to the fusion of particles which become connected as the heat flow through conduction is facilitated considerably.

Many models to calculate thermal conductivity of the powder beds have been proposed, considering the contribution of many heat transfer mechanisms to powder conductivity, such as interparticle radiation, conduction through the gas and conduction through the solid [Nelson et al., 1993; Childs et al., 1999].

The absorptivity of a material is defined as the ratio of the absorbed radiation to the incident radiation, and it is dependent upon the material composition, particle size, and temperature of the powder [Nelson, 1993]. A study of powder absorptivity is of interest to SLS because it allows for the formation of more accurate sintering windows [Kruth et al., 1998]. The type of laser used also affects the absorptivity due to the different behaviour of the material according to the wavelength of the laser. The main types of laser are Nd-YAG laser, and CO_2 laser with wavelength 1.06 μm and 10.6 μm respectively. Figure 2.24 gives a first approximation for the magnitude of absorptivity for both Nd:YAG laser and CO_2 laser, and illustrates how the absorptivity changes with chemical composition and wavelength. The incident radiation is not only absorbed by the surface of the particles but also penetrates through the interparticle space into the bed, so powder exhibits a higher absorptivity than solid material [Tolochko et al, 2000]. Table 2.2 shows absorptivity values of some powders and solid materials. Only a fraction of the incident laser power is absorbed by a singular metal particle surface. On the other hand, within a powder, which contains many particles, a high amount of the remaining or reflected energy will go through surrounding porosity where multi

reflection between particles will increase the overall absorptivity, thus allowing the radiation to interact with particles [Tolochko et al, 2000].

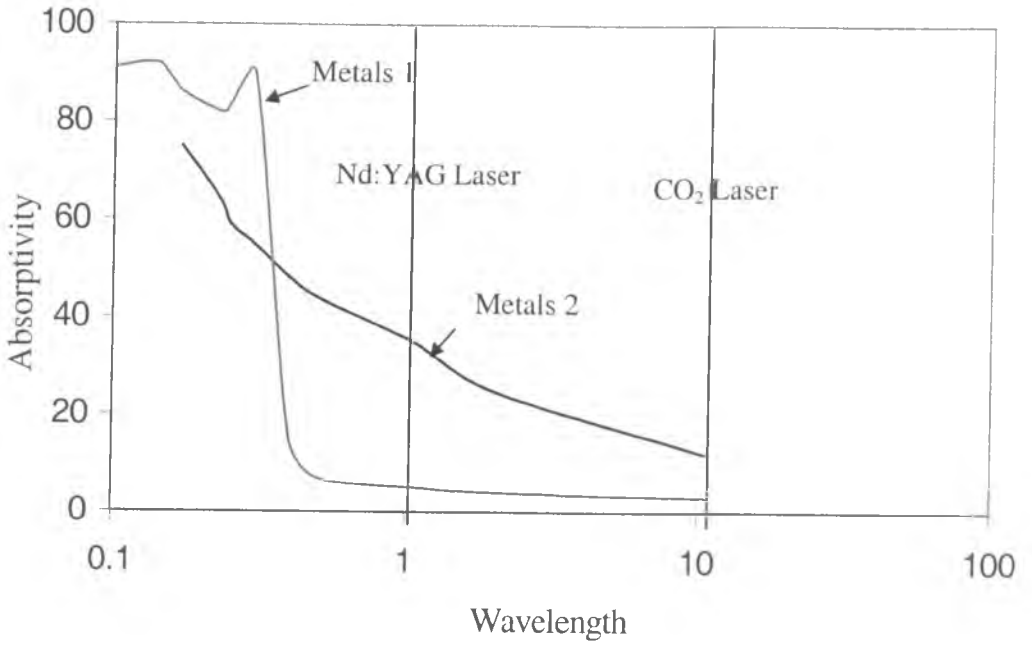

Figure 2.24: Absorptivity as a function of wavelength for a solid, metals 1 (Au, Ag, Cu,) and metals 2 are transition metals (Fe, Ni, Cr, ...) [Hugel and Dausinger, 1996].

Table 2.2: Absorptivity for some powder and solid materials [Tolochko et al., 2000; Nelson, 1993; Sih and Barlow, 1992]

Material	Nd:YAG Laser (λ =1.06 μm)	CO_2 Laser (λ= 10.6 μm)
Iron	0.46 (solid) 0.64 (powder)	0.45 (powder)
Tin	0.47 (solid) 0.66 (powder)	0.23 (powder)
Lead	0.39 (solid) 0.79 (powder)	-----
Polycarbonate	-----	0.95 (powder)
polymethylacrylate	0.06 (powder)	0.75 (powder)
Alumina (15 Micron)	-----	0.90 (powder)

2.4 High Speed Steels

2.4.1 High Speed Steels History

High-speed steels (HSS) have been known in some form for over a century. The original HSS was discovered by Mushent in 1868 and further developed by Maunsel and White in 1898. The first real HSS was T1 (18% tungsten, 4% chromium, 1-% vanadium and about 0.7% carbon) developed by the Crucible Steel Company. This steel remained popular until the 1950 when about one-third of the tungsten in T1 was replaced by about 5% molybdenum, vanadium content raised to 2%, and the carbon to 0.85% to get M2 steel. Now, there are many different varieties of HSS, which can be used to produce tools that are satisfactory in performance and cost.

HSS is basically a type of iron-based alloy, which takes its name from its ability to retain a high level of hardness when cutting materials at high speed. HSS can be hardened to a level of up to 65-70 HRC and the fall off in hardness with temperature does not become rapid until temperatures in the region of 600°C or higher are reached [Hoyle, 1988]. HSS is also characterised by high fracture strength, 1-5 GPa [Hoyle, 1988; Trent, 1991; Westin, 1989]

2.4.1.1 Common High Speed Steel Materials

HSS contains from 20 to 30 wt% alloying additions of the carbide forming elements such as molybdenum, vanadium, tungsten, chromium, and sometimes cobalt. There are other alloying elements that can also be added to HSS such as niobium, tantalum, titanium, silicon, and nickel. There are two major classes of HSS: molybdenum HSS (M grade) based, and tungsten HSS (T grade) based, but not all compositions fall within this classification. Both groups of HSS have equivalent performance; including

hardening ability, but the initial cost of the group M steels is approximately 40 percent lower than the group T steels [Hoyle, 1988].

The term HSS covers a wide range of compositions. The composition of most of the alloys is listed in Table 2.3 [Upadhyaya, 2000]. The characteristics of each HSS grade are due to the alloying elements. Each element contributes in a different way to the final steel properties through the type of carbides produced.

Carbon is the most important constituent element with regard to producing the required amount and type of carbide.

Chromium is present in almost all HSS (3.5 - 5 wt%). The role of chromium is to provide hardenability by slowing down reactions. Chromium increases the fraction of retained austenite and leads to additional hardening, after tempering. It also improves cutting properties and prevents scaling.

Tungsten and molybdenum perform similar functions and are more or less interchangeable on atomic basis [Hoyle, 1988]. The range of compositions is (1.15-21 wt%) for tungsten and (1-11 wt%) for molybdenum. Both the elements promote resistance to tempering, and cutting efficiency is increased as the tungsten content, or its molybdenum equivalent is increased. The austenite in molybdenum HSS is reported to be less stable than that of tungsten steels, giving some practical advantages during heat treatment.

Table 2.3: Composition limits of principal types of HSS

Designation	Composition								
AISI	C	Mn	Si	Cr	Ni	Mo	W	V	Co
Molybdenum HSS									
M1	0.78-0.88	0.15-0.40	0.20-0.50	3.50-4.00	0.30 max	8.20-9.20	1.40-2.10	1.00-1.35	4.50-5.50
M2	0.78-0.88; 0.95-1.05	0.15-0.40	0.20-0.45	3.75-4.50	0.30 max	4.50-5.50	5.50-6.75	1.75-2.20	-
M3/1	1.00-1.10	0.15-0.40	0.20-0.45	3.75-4.50	0.30 max	4.75-6.50	5.00-6.75	2.25-2.75	-
M3/2	1.15-1.25	0.15-0.40	0.20-0.50	3.75-4.50	0.30 max	4.75-6.50	5.00-6.75	2.75-2.75	-
M4	1.25-1.40	0.15-0.40	0.20-0.45	3.75-4.75	0.30 max	4.25-5.50	5.25-6.50	3.75-4.50	-
M7	0.97-1.05	0.15-0.40	0.20-0.45	3.50-4.00	0.30 max	8.20-9.20	1.40-2.10	1.75-2.25	-
M10	0.84-0.94; .95-1.05	0.15-0.40	0.20-0.45	3.75-4.50	0.30 max	7.75-8.50	-	1.8-2.20	-
M30	0.75-0.85	0.15-0.40	0.20-0.50	3.50-4.25	0.30 max	7.75-9.00	1.30-2.30	1.00-1.40	4.50-5.50
M33	0.85-0.92	0.15-0.40	0.15-0.50	3.50-4.00	0.30 max	9.00-10.00	1.30-2.30	1.00-140	4.50-5.50
M34	0.85-0.92	0.15-0.40	0.20-0.45	3.50-4.00	0.30 max	7.75-9.20	1.40-2.10	1.90-2.30	7.75-8.75
M35	0.82-0.88	0.15-0.40	0.20-0.45	3.75-4.50	0.30 max	4.50-5.50	5.50-6.75	1.75-2.25	4.50-5.50
M36	0.80-0.90	0.15-0.40	0.20-0.45	3.75-4.50	0.30 max	4.50-5.50	5.50-6.50	1.75-2.25	7.75-8.75
M41	1.05-1.15	0.20-0.60	0.15-0.50	3.75-4.50	0.30 max	3.25-4.25	6.25-7.00	1.75-2.25	4.75-5.75
M42	1.05-1.15	0.15-0.40	0.15-0.65	3.50-5.25	0.30 max	9.00-10.00	1.15-1.85	0.95-1.35	7.75-8.75
M43	1.15-1.25	0.20-0.40	0.50-0.65	3.50-4.25	0.30 max	7.50-8.50	2.25-3.00	1.50-1.75	7.75-8.75
M44	1.10-1.20	0.20-0.40	0.30-0.55	4.00-4.75	0.30 max	6.00-7.00	5.00-5.75	1.85-2.20	11.00-12.25
M46	1.22-1.30	0.20-0.40	0.40-0.65	3.70-4.20	0.30 max	8.00-8.50	1.90-2.20	3.00-3.30	7.80-8.80
M47	1.05-1.15	0.15-0.40	0.20-0.45	3.05-4.00	0.30 max	9.25-10.00	1.30-1.80	1.15-1.35	4.75-5.25
M48	1.42-1.52	0.15-0.40	0.15-0.40	3.50-4.00	0.30 max	4.75-5.50	9.50-10.50	2.75-3.25	8.00-10.00
M62	1.25-1.35	0.15-0.40	0.15-0.40	3.50-4.00	0.30 max	10.00-11.00	5.75-6.50	1.80-2.10	-
Tungsten HSS									
T1	0.65-0.80	0.10-0.40	0.20-0.40	3.75-4.50	0.30 max	-	17.25-18.75	0.90-1.30	-
T2	0.80-0.90	0.20-0.40	0.20-0.40	3.75-4.50	0.30 max	1.0 max	17.50-19.00	1.80-2.40	-
T4	0.70-0.80	0.10-0.40	0.20-0.40	3.75-4.50	0.30 max	0.40-1.00	17.50-19.00	0.80-1.20	4.25-5.75
T5	0.75-0.85	0.20-0.40	0.20-0.40	3.75-5.00	0.30 max	0.50-1.25	17.50-19.00	1.80-2.40	7.00-9.50
T6	0.75-0.85	0.20-0.40	0.20-0.40	4.00-4.75	0.30 max	0.40-1.00	18.50-21.00	1.50-2.10	11.00-13.00
T8	0.75-0.85	0.20-0.40	0.20-0.40	3.75-4.50	0.30 max	0.40-1.00	13.25-14.75	1.80-2.40	4.25-5.75
T15	1.50-1.60	0.15-0.40	0.15-0.40	3.75-5.00	0.30 max	1.00 max	11.75-13.00	4.50-5.25	4.75-5.25
Intermediate HSS									
M50	0.78-0.88	0.15-0.45	0.20-0.60	3.75-4.50	0.30 max	3.90-4.75	-	0.80-1.25	-
M52	0.85-0.95	0.15-0.45	0.20-0.60	3.50-4.30	0.30 max	4.00-4.90	0.75-1.50	1.65-2.25	-

2.4.2 Powder Metallurgy of High Speed Steel

Powder Metallurgy (PM) is concerned with the processing of metal and non-metal powders, including the fabrication, characterisation and conversion of these powders into useful engineering components. Powder metallurgy processing routes for the manufacture of HSS were developed in the 1960's and 1970's in an attempt to overcome the problems of cast and wrought HSS material waste, expensive labour costs and energy consumption, and anisotopic properties [Hoyle, 1988].

PM components have many advantages that cannot be achieved using other metal working processes [German, 1994; Upadhyaya, 2000]; 1) precise control: the production of near-net-shape components to meet the design specification of the finished product, eliminating both machining and finishing costs; 2) unusual physical properties: density can be varied from very low to fully dense parts; 3) reproducibility: many identical parts can be produced with deviation from tolerances only taking place as the die wears; 4) custom-made compositions: immiscible materials can be combined to produce specific products, such as non-metallic ceramics with metals.

Although the PM technique has the above advantages, there are also a number of limitations [German, 1994; Upadhyaya, 2000]; 1) powders that are pre-alloyed tend to be expensive and incompressible; 2) expensive techniques are often required to produce fully dense compacts in a one operation processes; 3) the properties of PM components may not be uniform because the compressive forces are unaxial, resulting in anisotropy; and 4) the part size is limited by the press capacity, so typical PM components over a maximum depth of 80 mm.

2.4.3 Powder Atomisation

The first step in manufacturing of HSS is powder production. Powders are prepared by disintegration of a pre-alloyed melt by atomisation method. There are several ways to atomise metal powders, mainly: gas, water, centrifugal and plasma rotating electrode process. In each of these processes, the molten metal is poured into the atomiser tundish, which controls the metal flow through a nozzle providing a constant melt stream. The nozzle dimensions constrict both liquid metal flow shape and dimension. Hence, decreasing the nozzle length/diameter ratio, the liquid metal flow changes from turbulent to laminar [German, 1996; Yule and Dunkley, 1994; Dowson, 1990].

2.4.3.1 Gas Atomisation

Gas atomisation consists of pulverisation of liquid metal steam by means of a high-pressure gas. The pressure is normally in the range 2-5 MPa. The gas atomisation concept is sketched in Figure 2.25. The expanding gas around the molten metal stream causes a dramatic disruption of the melt stream. The resulting droplets are accelerated to high velocities and solidify before reaching the walls of the chamber. This means a large chamber is normally required. The resulting droplets contract due to surface tension, spheroidising and solidifying. Gas atomisers can be either vertical or horizontal. Vertical atomisers are used for metals and alloys, because of their high melting point. The final particle size is determined by several factors, with higher gas pressures and gas flow rates being necessary to produce smaller and more spherical particles. Most powders are in the 15-300 μm range [German, 1996].

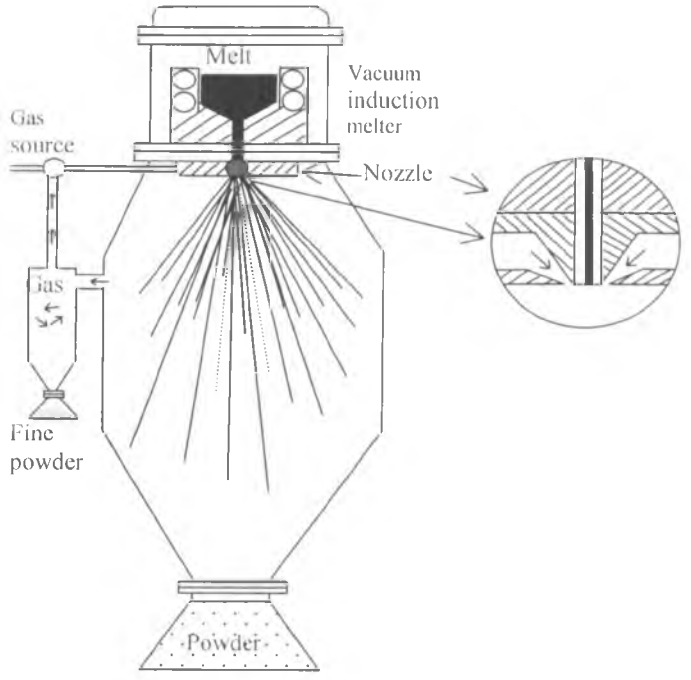

Figure 2.25: Schematic of gas atomisation technique [German, 1996]

2.4.3.2 Water Atomisation

Water atomisation is the most common technique for producing elemental and alloy powders. The mechanism of water atomisation is basically similar to that of gas atomisation, with the obvious exception that water jets are used in place of gas. The water atomisation concept is sketched in Figure 2.26. As contrasted with gas atomisation, powder produced by water atomisation is not spherical. In this process high pressure water jets are sprayed towards the liquid metal stream, forcing its disintegration and rapid cooling. As a consequence of rapid cooling, water atomised powders have very little chemical segregation within each powder particle, which results in a higher chemical homogeneity of the powder. The water can be directed to

melt stream by a single jet, multiple jets, or an annular ring. Like gas atomisation, pressure is the main process control variable in water atomisation.

The typical flow-rate ratios, during atomisation are about 5:1 (5 kg/min of water per kilogram of steel powder). Higher water pressure results in higher water velocities and a smaller particle size. Particles in the 5 μm size range can be produced by pressures up to 150 MPa. This process is most useful for forming low cost powders used to make filters and small metal injection-moulded objects [German, 1994; Yule and Dunkley, 1994].

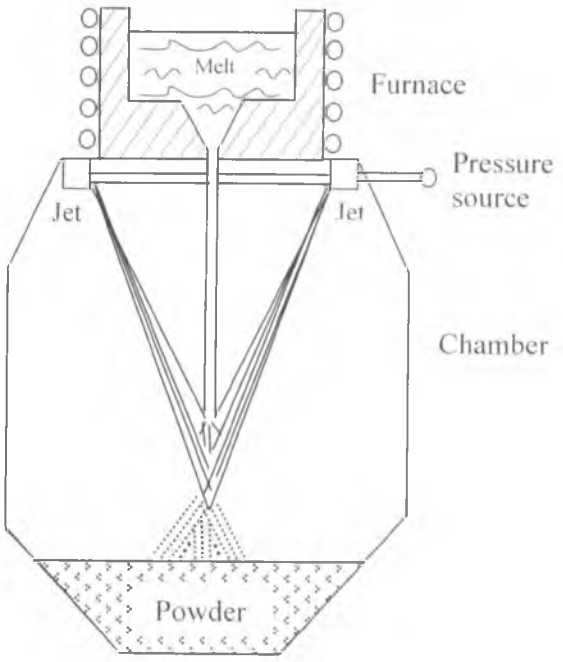

Figure 2.26: Schematic of water atomisation [Yule and Dunkley, 1994]

2.4.4 Sintering Mechanisms

Sintering is a thermally activated process (with or without external pressure application), whereby the powder particles are made to bond together, changing physical and mechanical properties, and developing toward a state of maximum density, i.e. zero porosity, by occurrence of atomic transport [Metals Handbook-Powder Metallurgy, 1984; German, 1994]. A number of different mechanisms have been

identified for different materials, such as solid state sintering and enhanced sintering. The latter incorporates activated, liquid phase and supersolidus sintering, of which the last is associated with the sintering behaviour of high-speed steel.

2.4.4.1 Solid State Sintering

Solid state sintering is a thermal process which occurs when the metal particles bond together by atomic transport events at temperatures T_{solid}: $0.5T_m<T_{solid}<T_m$ where T_m, is the melting point of the powder material. Several different patterns of atomic transport can contribute to the effect including evaporation and condensation, volume diffusion, grain boundary and surface diffusion, and plastic flow [German, 1994; Upadhyaya, 2000] (see Figure 2.27).

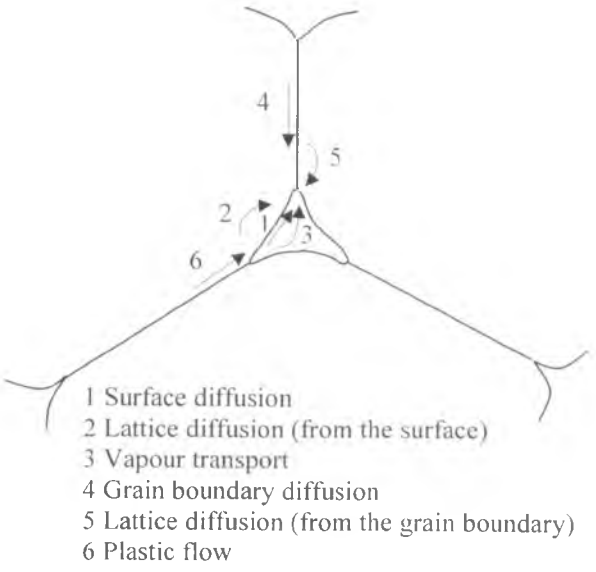

Figure 2. 27: Various sintering mechanisms, [Upadhyaya, 2000]

There are two kinds of transport events to be considered: surface transport and bulk transport. The surface transport involves neck growth without a change in interparticle spacing, resulting in mass flow from the particle surface either by diffusion or by

evaporation and condensation. Bulk transport mechanisms involve the mass originated from the particle interior, which is deposited at the neck region, and include volume diffusion, grain boundary diffusion and plastic flow. The bulk transport methods tend to be dominant in the latter stages of the sintering process contributing significantly to compact densification. The solid state sintering process involves mass transport and consists of an initial stage, an intermediate stage, and a final stage [German, 1994; Jenkins and Wood 1991] (see Figure 2.28)

1- In the initial stage, the pore structure is open and thoroughly interconnected, and the pores sharply defined. This stage is sometimes referred to as neck growth, and it is accompanied by interparticle shrinkage. In this stage a large amount of energy is available which facilitates the movement of particles within the matrix. During this stage of sintering, single-crystal particles in contact cannot undergo grain growth because the solid-vapour surface diverges at an acute angle from the particle-particle contact area [German, 1994; 1996; Upadhyaya, 2000].

2- In the intermediate stage, the porosity becomes smooth but remains continuous until final stage. During this stage of sintering, the cylindrical pores simply shrink, neck growth continues, but the neck shape is lost, as the pores become smooth. The sintering rate is controlled by the geometry of the grain boundaries and the pores. Surface transport events may allow pore migration to the grain boundaries.

3- In the final stage, the pores spheroidize into a closed structure, and grain growth tends to be evident. Bulk diffusion in this stage is the dominant mechanism since the exposed surface area is negligible. The changes in microstructure observed in the final stage influences strength, fracture toughness, and ductility. The densification in

this stage is slower than in the earlier ones, due to the rigid solid skeleton that is formed which also inhibits the final pore removal.

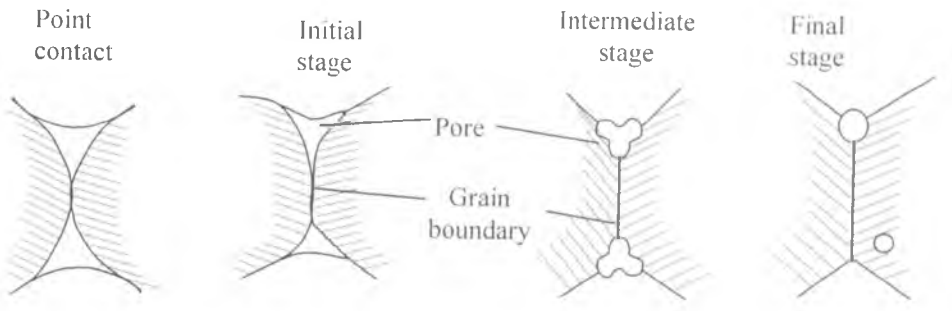

Figure 2.28: Development of the interparticle bond during sintering [Upadhyaya, 2000]

The sintering kinetics are diffusion controlled and therefore is affected by the furnace temperature and the amount of available free surface energy (known as the driving force). This driving force varies according to the amount of surface curvature present in the part. As grain boundaries grow, so the surface energy is converted to grain boundary energy and the amount of available free energy decreases. The reduction in the kinetics of sintering is primarily due to the reduction of diffusion coefficient from a surface diffusion to a bulk diffusion mechanism. Hence the net driving force is low and sintering progresses slowly. The initial surface energy per unit volume varies inversely with particle size, so that a finer particle size increases the driving force.

2.4.4.2 Liquid Phase Sintering

Liquid Phase Sintering (LPS) is defines as sintering involving a coexisting liquid and particulate solid during some part of the thermal cycle [German 1985]. There are two ways to create the liquid phase. The first way is to use mixtures of two or more powders, one of which has a lower melting temperature than the other, enabling a liquid

phase to form during heating. The liquid formed during the sintering cycle may be transient or permanent depending on the solubility relationship. The second way is to use prealloyed powders, which are then heated, to a temperature between the liquidus and solidus temperatures. The resulting mixture of liquid and solid phases leads to supersolidus sintering. This process is useful for systems having large melting ranges and makes high densification possible even with large particle sizes. One of the typical applications of this process is in sintering of high-speed steel. The LPS technique was primarily developed in the early 1900's to produce cemented carbide tools, generating dense, pore-free carbides with mechanical properties far superior to any other known cutting material at that time. Now LPS technology is widely used in sintering steels, cemented carbides, heavy alloys, bronzes and silicon nitride systems.

The main advantage of using LPS is that the rapid atomic motion makes it possible to use short sintering cycle as compared to solid phase sintering.

During LPS three stages of densification are encountered after the liquid forms: rearrangement, solution-reprecipitation, and a final stage sintering, as indicated in Figure 2.29. The logarithmic time scale is only approximate but gives a sense of the densification events.

Liquid forms at the particle boundaries, effectively wetting the solid phases and penetrating along prior grain boundaries by capillary action. This film acts as a lubricant breaking up the particles and allowing them to move over one other subsequently changing the packing arrangement. With continued heating, the alloying elements begin to dissolve and two outcomes are possible depending on the limit of solubility and amount of liquid present. Solution-reprecipitation occurs when the solid phase has limited solubility in the liquid phase, then the amount of liquid grows until saturated

with the solid phase, redistributing the solid particles around the matrix to other sites where they reprecipitate on larger particles. The final stage of this process occurs when the component is held at the sintering temperature. In this stage small changes occur, e.g. increases in density, and complete densification is often reached during the first two stages [German, 1985; 1994].

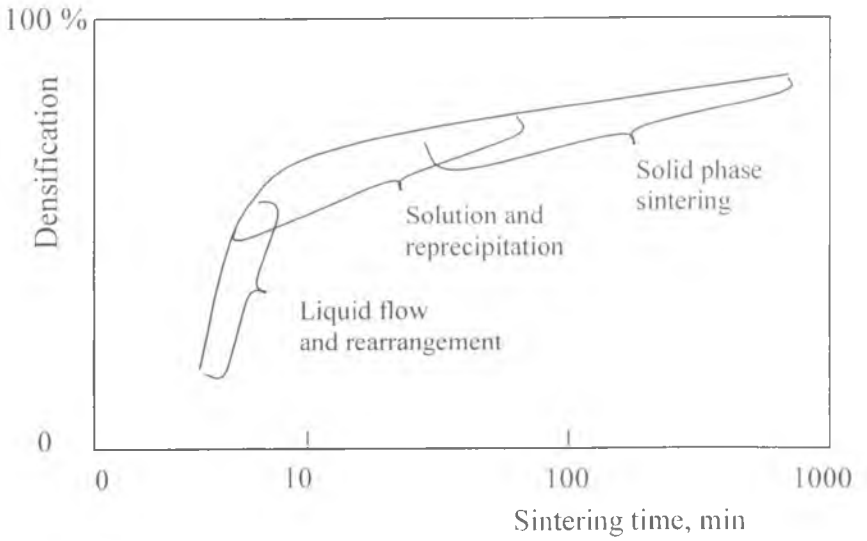

Figure 2.29: Schematic of three stages of liquid phase sintering [German, 1996]

2.4.4.3 Supersolidus Liquid Phase Sintering

Supersolidus Liquid Phase Sintering (SLPS) involves heating prealloyed powders to a temperature intermediate between the liquidus and solidus, promoting partial melting and densification through the operation of particle rearrangement and solution-reprecipitation mechanisms [German 1985, 1994]. The liquid forms within the particles causing each particle to fragment into individual grains. Subsequent repacking of the fragment under the capillary force from the wetting liquid results in rapid densification. The fundamental difference between LPS and SLPS is the sequence of leading to densification. A schematic of the stages in SLPS is shown in Figure 2.30. At

temperatures below the solidus a small amount of solid state sintering produces inter-particle bonding creating a skeletal structure. In the first stage, a liquid form as prealloyed powder is heated above its solidus temperature. The commonly observed sites for liquid melting are the grain boundaries within a polycrystalline particle, the neck region between particles, and the intragranular isolated pores. These sites depend on particle size, heating rate, powder microstructure, and alloy chemistry. As the liquid volume increases, at a critical temperature above the solidus a threshold amount of liquid exists along the grain boundaries. Above this threshold, the grains have enough mobility to rearrange, leading to

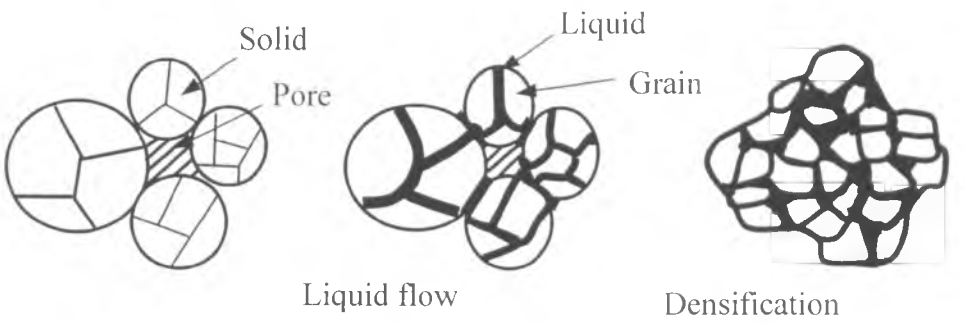

Figure 2.30: Supersolidus liquid phase sintering process [German 1985]

particle fragmentation and capillary induced rearrangement. So, the densification during SLPS is similar to viscous flow sintering, because the semi-solid particles turn mushy and flow once the liquid spreads along the grain boundaries. Subsequently, continued densification occurs by solution reprecipitation, grain shape accommodation, and pore removal, as in LPS.

2.4.4.4 Infiltration

Infiltration is a process that wicks a molten phase into the open pores of previously sintered porous structure by cycling to a temperature between the melting points of the

infiltrant and the skeleton [German, 1996]. In the other words infiltration is an alternative approach to producing substantially pore-free materials. In this process, a porous metallic body having interconnected porosity is infiltrated with other metal of lower melting point by means of a suitably designed heat treatment. The metallic body is known as a matrix and the metal with lower melting point is known as the infiltrant. Molten infiltrant is drawn into the interconnected open pores of the matrix by capillary action, and a highly or fully dense composite structure is produced upon its solidification as shown in Figure 2.31. Capillary pressure (ΔP) varies with the inverse of pore diameter (D) as follows:

$$\Delta P = 2\gamma \cos \theta / D \qquad (2.5)$$

where, γ is the surface energy of the infiltrating liquid and θ is the contact angle between infiltration liquid and solid matrix.

With increased wetting, where the contact angle θ is small, or smaller diameter pores exist the filling will be more complete. Infiltration can be either combined with sintering step (one step), or can be carried out separately (two steps), where sintering of the matrix is carried out separately prior infiltration.

The infiltration technique requires that the pore structure is open and interconnected, and the molten infiltrant must have a low viscosity. The wetting behaviour of molten infiltrant is a function of its fluidity, and this is enhanced by good reducing conditions and by proper selection of infiltration temperature and infiltrant composition. High fluidity in the liquid state is desirable because it aids the driving force of the surface tension.

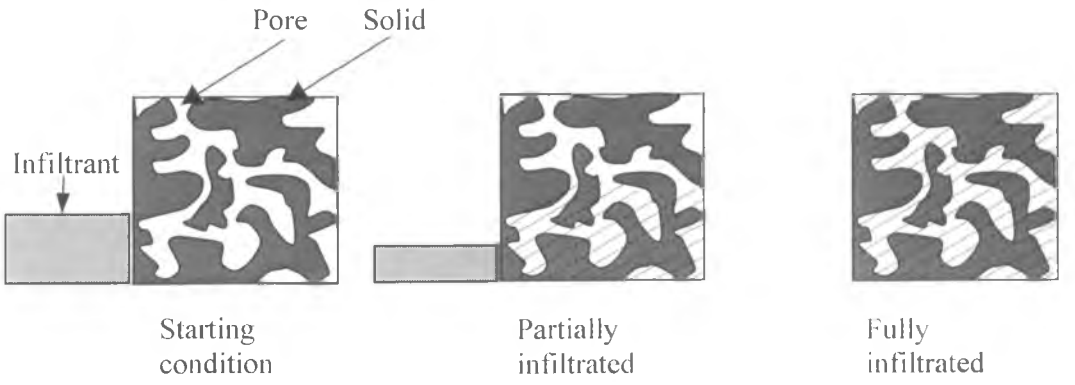

Figure 2.31: Schematic of infiltration process [German 1996]

Generally, infiltration can be used to attain the following advantage: a) precise and complex shapes, using conventional powder metallurgy operations, b) layered powder metallurgy products of different composition, c) improved machinability, d) good mechanical properties, e) increased strength through subsequent effective heat treatment, f) reasonable control of phase distribution that may result in a uniform or a purposely graded microstructure, and g) the main attraction is the elimination of porosity with minimal dimensional change. For these purposes infiltration of pores in a sintered steel with copper and bronze are used to form intermediate performance alloys (mechanical properties are intermediate). This is because copper and bronze are weak metals. Table 2.4 lists the properties of common infiltrated steels. There are other several applications of infiltration technology include Cr-Cu, Co-Cu, TiC-Ni, W-Cu, W-Ag, CdO-Ag, WC-Ag, WC-Cu, and Mo-Ag compositions. There are common problems with infiltration [German, 1985]. The process is sensitive to surface contamination, requiring clean surfaces for wetting. Craters are often seen on surfaces exposed to the infiltration liquid due to erosion. Swelling is common, depending on the

solid skeleton porosity, where low initial properties favor swelling since grains separate due to a penetrating liquid [German, 1994].

Table 2.4: Example mechanical properties of copper-infiltrated steels [German 1998]

Property	Fe-11Cu-0.5C	Fe-20Cu-0.%C
Yield strength, MPa	340	410
Ultimate strength, MPa	530	520
Elongation %	4	2
Elastic Modulus, GPa	160	145
Poisson's ratio	0.28	0.24
Impact energy, J	18	11
Transverse rupture strength, MPa	1090	1020

2.4.5 Mechanical Properties of Sintered High Speed Steel

Mechanical properties standards exist to assess the fitness for purpose of a material and the reproducibility of the property being measured. Most metals standards were first developed for fully dense materials (wrought or cast materials). Application of the same approach to sintered porous metals is necessary for design and quality control.

2.4.5.1 Hardness

Hardness is the property that is mainly used for quality assurance purposes as it is a adequate indication of the material condition and because of the ease of examination and minimum required specimen preparation [German, 1998]. In HSS the hardness mainly depends on the composition and heat treatment. The hardness of several microstructure components can be evaluated by microhardness where low loads are

used for testing. Figure 2.32 shows typical microhardness values of carbide particles found in high-speed steel [Hoyle, 1988].

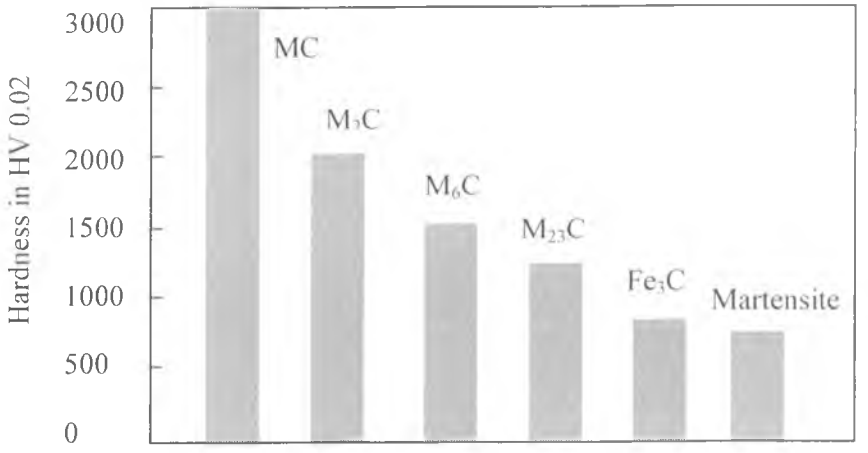

Figure 2.32: Relative hardness of carbide particles found in high-speed steel [Hoyle, 1988]

2.4.5.2 Bending strength

In regard to strength, the bend test is widely accepted as to be the most reliable informative. Machining of tensile test specimens in the hard condition is rather difficult, due to the relatively hardness and high carbide content of high-speed steel, while hardening of the tensile specimen might cause cracking or distortion. However, as it is unusual to test brittle specimens in simple tension, the strength of high-speed steels is commonly evaluated by a bending test. Bending tests may be under three or four point loading [Hoyle, 1988]. Figure 2.33 shows the bending moment of the two test geometries, where for four point mode there is a central span between the two inner supports, in which the calculated stresses are constant, unlike the peak concentration at the central support of the three point method [ASM 1984]. ASTM standard B 528-76 / ISO 3325 [Standard Test Methods, 1991], where linear elastic deformation is used to

calculate the transverse rupture strength (TRS) for three point bending for a rectangular cross section specimen by the following equation:

$$\text{TRS} = \frac{3}{2}\frac{FL}{b.d^2} \tag{2.6}$$

Where F is the maximum load applied to the specimen, L is the span of the testing geometry; b and d are width and depth of the specimen respectively. It is valid only for linear elastic material behaviour such ceramics. Fortunately most metallic materials process macroscopic plasticity, which renders the elastic formulae unsuitable.

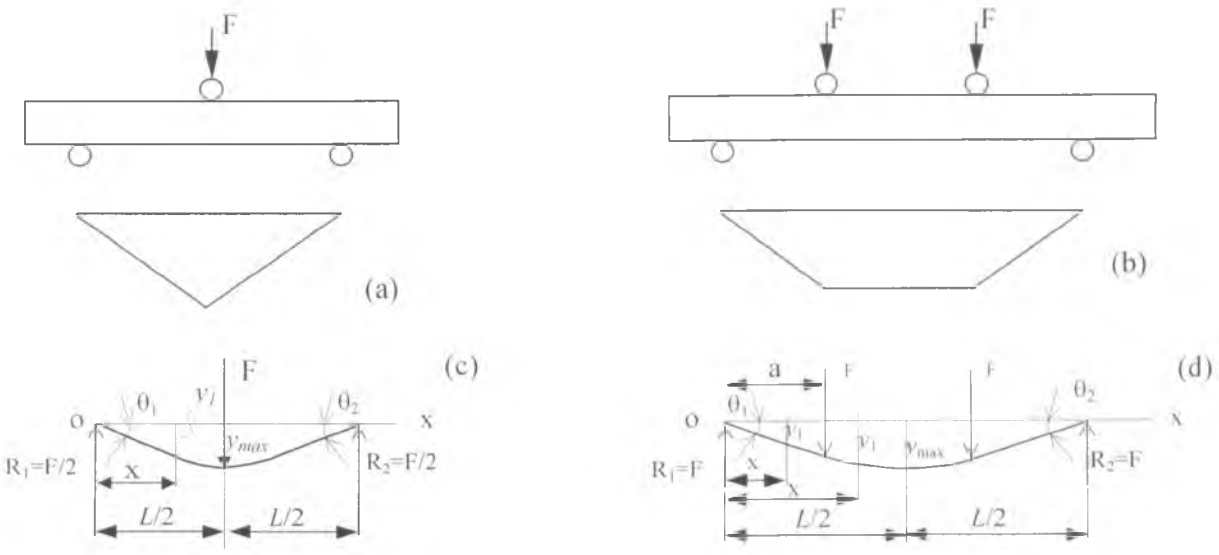

Figure 2.33: Bending moment diagram and deflections for (a) three-point bending test, (b) four-point bending test [Spotts, 1985].

It is deduced from the expression that gives the maximum stress in bending specimen:

$$\sigma = \frac{M.c}{I} \tag{2.6}$$

where M is the bending momentum, c is the half specimen height, and I is the inertia momentum of the main central axis which is perpendicular to the bending momentum plan.

Figure 2.30, c, and d shows also the deflection for three and four point bend test. The maximum deflection for three and four point bend test can be calculated from the following equation [Spotts, 1985]:

For a three point bend test

$$y_{max} = \frac{Fl^3}{48EI} \tag{2.7}$$

or

$$E = \frac{Fl^3}{4bd^3 y_{max}} \tag{2.8}$$

For $0<x< l/2$

$$y_1 = \frac{F}{48EI}\left(3l^2x - 4x^3\right) \tag{2.9}$$

For a four point bend test

$$y_{max} = \frac{Fa}{24EI}\left(3l^2 - 4a^2\right) \tag{2.10}$$

$$y_1 = \frac{Fx}{6EI}\left(3a(l-a) - x^2\right) \tag{2.11}$$

where y_{max} is the deflection increment at midspan as measured from preload at the applied load, y_1 is the deflection at any point of span, x is the distance from the support to the point at which the deflection is to be calculated when the specimen is straight, a (for four point loading) the distance from the support to the load applicator when the specimen is straight, l is span length between supports, I is the inertia momentum of the main central axis which is perpendicular to the bending momentum plan, and E is the modulus of elasticity in bending.

2.5 Summary

This chapter has outlined the different Rapid Prototyping and tooling techniques including advantages and disadvantages of each process. Also this chapter has presented an overview of selective laser sintering and high speed steel. Both direct and indirect selective laser sintering have potential as tool making technologies for polymer processing, however both techniques require further investigation before they can be considered as appropriate tool manufacturing techniques.

CHAPTER THREE

COMPARISON CRITERIA FOR INDIRECT AND DIRECT SLS OF METALS

3.1 Introduction

There are two different approaches to selective laser sintering, indirect SLS, and direct SLS (see section 2.3). Both of these processes can be used to produce tooling. Direct SLS of metals is very desirable as it avoids the time consuming step of binder removal and powder consolidation associated with the indirect fabrication of metal parts. This could make potentially the production of prototype patterns, moulds and dies for injection moulding and casting faster and more economic than indirect SLS.

The overall aim of the work reported in this thesis was a comparison of direct and indirect laser sintering approaches with the intended application being mould tooling. The following sections discuss the criteria used in the comparison.

3.2 Identification of Key Parameters

3.2.1 Mechanical Properties and Microstructure

Clearly any tool making process must result in a tool which is mechanically strong enough to function. An important problem associated with layer manufacturing is determining material properties. In most layer technologies, the properties are different in the X, Y and Z directions. The properties of the materials depend on the type of equipment and the

process parameters. In direct SLS the possibility of using different parameters in predetermined three-dimensional sections of the body makes it even more difficult to characterize the properties in a conventional way.

Because direct SLS is a net-shape sintering process, it inevitably produces porous material, which is naturally not as strong as fully dense material. Mechanical properties can be enhanced by infiltration. Metal infiltration is normally applied to increase the density of sintered inserts [Olli Nyrhilä et al, 1998]. This technique can only be used when dealing with materials that have higher melting point than infiltrant. The mechanical properties gained after metal infiltration are comparable with those of the infiltrant metal itself. The purpose of surface infiltration is to enhance surface properties, not to fill all pores of the insert.

3.2.2 Accuracy and Surface Finishing

A primary concern for most RT users is part accuracy. A particular problem with all prototype models is their relatively poor surface finish, which results from the layered structure inherent in the building method. Most indirect RT techniques accurately reproduce the surface details of the pattern. Part accuracy can be described in a number of ways: bulk accuracy and surface finish, and the accuracy and manufacturability of features [Dalgarno et al, 2000]. RP systems also vary in terms of the level of detail achievable, resulting in a minimum feature size. It can take as long, if not longer, to finish a part as it did to build it in the machine. This is mainly so if the part is to be used for an engineering request such as toolmaking. Such finishing not only uses up expensive skilled labour but also it may be stifling the development of this technology. As indirect SLS and direct SLS

systems have become better understood, so part accuracy has improved and is expected to continue to improve.

If the tools have a good accuracy and good surface finish, where minimal finishing or no finishing is needed, the costs will be decreased. So, accuracy is an important parameter when we want to compare between two potential processes tooling.

3.2.3 Lead Time, Productivity and Cost

Dalgarno et al [2001] reported that the lead-time for a finished tool, with DTM RapidSteel tools for injection moulding, is not significantly affected by the use of layer techniques. Generally this is an effect of the amount of finishing the layer manufactured tools require, and so would be improved by superior accuracy and surface finishing on the near net shape tool.

Productivity mainly depends on the type of machine and the process parameters. In addition, the cost of tools is related to the material cost, machine time, and finishing costs. So the lead-time, productivity and cost are important criteria to compare between indirect SLS and direct SLS.

There are three stages in the SLS process for all materials, a warm-up stage, a build stage and a cool-down stage (Figure 3.1). The aim of warm up stage is to raise the temperature of the part bed and powder feed cartridges. In the cool down stage, the temperature of the part bed is allowed to drop. The time spent in warm up and cool down are mainly dependent on the material and, therefore, on the powder bed temperature required. The warm-up stage is fixed but the cool-down may vary according to the height of the build, i.e. the volume of material to cool down.

Pham and Wang [2000] reported that the warm up stage (T_w) and cool stage (T_c) for RapidSteel 2.0, take only about 36 minutes, so the building stage is the main part of the total time that needs to be predicted.

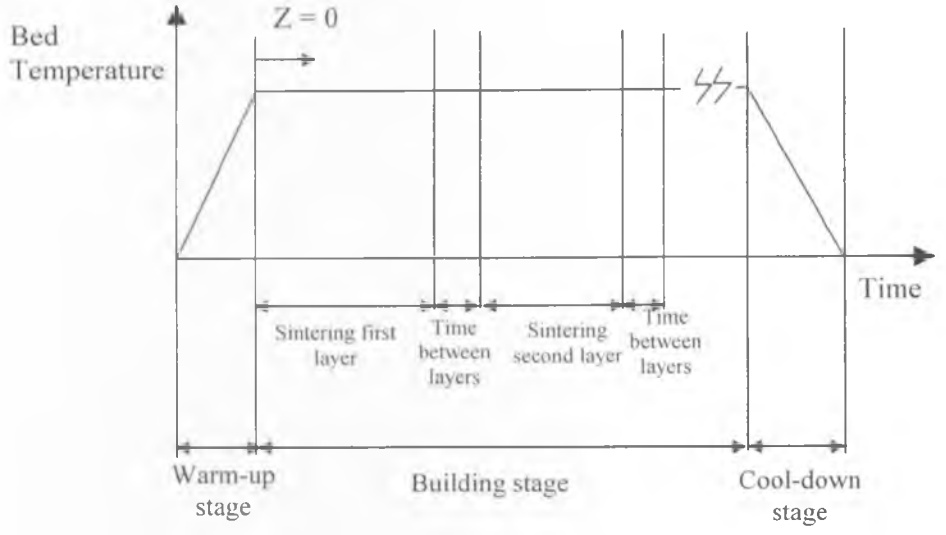

Figure 3.1: Stages of SLS process [Volpato 2001]

The building time for the part consists of the total sintering time plus the total time between layers. The sintering time (T_s) is the time required to scan a 2D section of a part in one layer. The time between layers (T_d) is the time interval between the end of the scanning of one layer and the beginning of scanning of the next one. In a more detailed analysis, T_d can be subdivided into powder addition time, and the idle time before sintering. The powder addition time is fixed and can be easily derived from the roller speed and travelled distance or even measured experimentally. The temperature of the material in the powder cartridges is lower than that of the powder bed. Hence, when a new layer is spread the temperature in the powder bed drops by several degrees and requires time to be raised back to the set point (the idle time before sintering). This time is difficult to calculate, but according to Pham and Wang [2000], it is short and was considered to be

zero in their time predictor. The time for slicing and loading the scanner varies considerably with geometry complexity and the number of parts to be sliced in one layer. Before starting the actual scanning, the controller groups and loads the scanner information for all parts sliced in a layer that have the same process conditions [DTM, 1996]. The slicing and loading operations overlap in part with the powder spreading and temperature raising but usually take longer than these two tasks. Pham and Wang [2000] reported that the Sinterstation 2500plus uses two computers to perform slicing and scanner loading. This time was then reduced to almost zero because these operations can be done in parallel with powder spreading, raising the bed temperature and sintering. On the other hand, for Sinterstation 2000, this time is considerable and is very difficult to calculate.

The difficulties pointed out above make it impractical to develop a program to calculate the total building time for an older machine. However, if the direct SLS process and the indirect SLS process are assumed to have the same total time between layers, the time difference between the two processes will be due only to the sintering time. In this way, a program able to calculate only the total sintering time can be used to assess the time with both processes.

The sintering time (T_s) depends mainly on a series of process parameters such as: scan spacing (s), beam speed (v), layer thickness L_t, scanning delays for each line, set-up time for each layer, and the volume to be scanned (Length (l), height (h), and Width (w)). It is important to realise that not only the area to be scanned needs to be considered but also the geometry of the section. This is because of the delays involved in each scan vector and also the laser jumping to move from the end point of one vector to the start point of the next one.

The time to scan a vector with laser on can be calculated by summing the time taken to travel its length plus the total scanning delay time (T_D=*JD*+*LO*+*SD*). A Jump Delay (*JD*) is needed after a fast positioning of the mirrors at the start of a vector to allow the scanner to settle before starting to draw a vector. Because the scanners begin to move only after an initial delay caused by the inertia of the galvanometers a Laser On Delay (*LO*) is required at the beginning of a vector. At the end of the vector, a Scan Delay (*SD*) is needed to allow the beam to catch up with the command signal before the next movement is started. Set-up time refers to the time that the sinterstation machine takes to spread a thin and even layer of powder to be sintered for the next slice, i.e., material deposition time, time required to heat the material, time required for the work-bed to move down, and time required for the work-bed to rise up.

To use this approach, the length of all vectors should be obtained for each section. Hence, it is necessary to perform an operation similar to that performed by the SLS machine control, i.e. to slice and generate all scan vectors. If we assume that the total scanning delay time is constant for indirect and direct SLS processes. Then, the only variable is scanning time (T_s).

$$T_s = T_o \times N_n \tag{3.1}$$

where T_o is the total time of one layer, and N_n is the total number of the layers

$$T_o = \frac{N_l l}{v} + (T_D \times N_l), \tag{3.2}$$

$$N_l = \frac{w}{s}, \text{ and} \tag{3.3}$$

$$N_n = \frac{h}{L_t} \tag{3.4}$$

Where N_l is the number of lines, T_d is the delay time for each scan vector, s is the scan spacing, v is the scan speed, l is the length, w is the width, h is the height, and L_t is the layer thickness.

The total time (T_t) can be calculated from the following equation:

$$T_t = T_s + (T_d \times N_n) \tag{3.5}$$

where T_d is the set-up time for each layer and this value is constant.

It is clear from the above equations that the building rate depends mainly on the scan speed, scan spacing and layer thickness.

It is important to make rapid tools as cheaply as possible, within accuracy and time constraints. The following costing formula relates mainly to the part build time and material custom:

$$\text{Total cost} = \text{Labour cost} + \text{Software cost} + \text{Laser cost} + \text{Maintenance cost} + \text{Furnace cost} + \text{Finishing cost} + \text{overheads} \tag{3.6}$$

where:

labour cost = (pre-processing period + post-processing period) × labour cost rate, software cost = pre-processing time × software cost rate, laser cost = build time × laser cost rate, maintenance cost = (pre-processing time + build time) × maintenance rate, finishing cost = finishing time × finishing cost rate, and overheads = (labour cost + software cost + laser cost + maintenance cost + furnace cost + finishing cost) × overhead rate.

The effectiveness of this costing formula is difficult to gauge, because rapid tool costs will also depend on other factors such as the number of parts in the build. On the other hand, it is useful to be able to estimate the approximate cost when deciding on the orientation of the model.

3.3 Summary

This chapter has identified the main criteria, which will be used to characterise direct and indirect selective laser sintering. These are the mechanical properties, accuracy and building rate.

CHAPTER FOUR

INDIRECT SELECTIVE LASER SINTERING - EXPERIMENTAL PROCEDURES

4.1 Introduction

In order to achieve the objectives set out in this research several experiments and tests have been carried out to develop and test the feasibility of using indirect SLS to produce mould tooling. The approach to indirect SLS used the DTM RapidSteel 2.0 process and sinterstation 2000. The experiments have addressed accuracy, strength, hardness, young's modulus, surface finish, and microstructure. Initially a density study was carried out to measure the density of loose powder and green material. The influence of the type of the furnace and the position of the bronze on the strength and the density of the parts has also been investigated. The accuracy parts has been studied using geometries designed specifically for this purpose, including the accuracy of small features and channels.

The nominal properties of the RapidSteel 2.0 material according to DTM Corporation are shown in Table 2.1 in Chapter 2 (see section 2.3.2.2). The following sections will describe these experiments.

The final results for all experiments and tests described in this Chapter are presented in Chapter 5.

4.2 Powder

The powder under investigation was supplied by DTM. This powder was a spherical metal powder called RapidSteel 2.0, which is basically a 316 stainless steel coated with a hybrid thermoplastic/thermoset polymer binder. DTM does not reveal the two materials used as the binder. The range of particle size is from 22-53μm, with average of 34μm. The amount of polymer mixture was 2.75% by weight. The process by which the polymer coating is applied to the steel powder is not in the public domain. Further details of the powder preparation have been reported in Chapter two (see section 2.3.2).

4.2.1 Storage

The powder was supplied in 25.0-kg capacity shipping containers to avoid contamination, spilling, or mixing different types of powders. If RapidSteel 2.0 powder becomes contaminated, its processing characteristics may change, and this can produce undesirable part quality. To minimize contamination and keep the powder at optimum conditions, it was stored at a temperature less than 38°C as recommended by DTM. Fresh powder and recycled powder were stored in separate containers. The recycled powder can be sieved to remove debris and re-used.

4.2.2 Powder Apparent Density

Apparent density is the density when the powder is in the loose state, without agitation and tap density is the highest density that can be achieved by vibration of a powder without the application of external pressure. Loose powder was carefully loaded through a funnel into the center of a cup. When the powder completely filled and overflowed the periphery of the

density cup, the top surface of the cup was carefully levelled using a ruler. An electronic balance with 0.001g resolution was used to measure the mass of cup plus powder. The mass of the empty cup was then subtracted from this value to give the mass of powder, which was divided by the internal volume of the cup to give the apparent density. This process was repeated 15 times to give an average apparent density.

The average value of apparent density was determined using the following question:

$$\rho = \frac{1}{n}\sum \frac{w_i}{V_i} \qquad 4.1$$

where ρ is the average density, w is the mass (g) and V is the volume (cm^3) and index i is the number of the test, 1 to n. The volume of the cup is constant at 6 cm^3.

4.3 Manufacture of Test Pieces

4.3.1 Sinterstation Processing

The manufacture of test pieces for experimentation was carried out using Sinterstation 2000, from DTM Corporation, shown in Figure 4.1. A schematic diagram of the machine is shown in Figure 2.5 (see Chapter 2 section 2.3). Also explanation on how the equipment works can be found in chapter 2 section 2.3.1.

This machine uses a CO_2 laser of 50Watts, with a beam diameter of 0.4mm. The Sinterstation 2000 system is capable of producing objects measuring 305 mm in diameter and 380 mm in height. Summarized specifications of the Sinterstation 2000 system are found in Table 4.1. The maximum beam speed scanning of this machine is around

1500mm/s. This machine works mainly with a raster scanning strategy, with an option to combine rastering with the use of an outline to scan the outer contour of 2D sections.

Figure 4.1: Selective laser sintering machine Sinterstation 2000 (DTM Corporation)

The default or recommended parameters for processing RapidSteel 2.0 are presented in Table 4.2. The Sinterstation 2000 is set to heat the powder up to 120°C initially and ramps down to 90°C over a span of one inch of powder depth. This to ensure that the first few layers of powder lie down flat. This temperature is also just below the melting point of thermoset polymer coating the RapidSteel 2.0 material. All of the RapidSteel 2.0 components manufactured for test were built using these main parameters.

Table 4.1: Summary specifications of DTM Corporation's Sinterstation 2000 system

Model	**Sinterstation 2000 system**
Process	Selective Laser sintering
Laser type	CO_2
Laser power (W)	50
Spot diameter (mm)	0.4
XY scan speed (mm/s)	1500
Work volume, ϕ and Z (mm × mm)	305×380
Maximum layer thickness (mm)	0.51
Minimum layer thickness (mm)	0.076
Size of unit, XYZ (mm × mm × mm)	3020 × 1530 ×1930
Layering time per layer (s)	Less than 30
Data control unit	Pentium-based; Unix System
Power supply	208 or 240 V_{AC}, single phase, 40 A

Table 4.2: SLS processing parameters recommended by DTM – RapidSteel 2.0

Parameters	Sinterstation 2000
Laser Power (Watts)	20
Scan Spacing (mm)	0.076
Beam Speed (mm/s)	1524
Layer Thickness (mm)	0.076
Powder Bed Temperature (°C)	90

4.3.2 Furnace Cycle Procedures

Two different types of furnace were used to complete sintering cycle and infiltration cycle. The first furnace used to post-process the RapidSteel 2.0 material is presented in Figure 4.2. It is a Carbolite furnace from Carbolite Furnaces Ltd, which is a bottom loading hearth

furnace, with sand seal (zirconia). The furnace control allows a temperature-time cycle to be run via a program, such that the conditions required by the RapidTool process can be followed. The second furnace is a Lindberg furnace at DTM Germany. Two furnace cycles are used to process RapidSteel 2.0 parts [DTM, 1998]:

Figure 4.2: Carbolite Furnace for RapidSteel 2.0 post-processing

A - Debinding and Sintering Furnace Cycle

Debinding, which is defined as the process of burning the polymer out of green part, occurs during a ramp in temperature to 1120°C. The parts are put on a flat alumina plate inside a graphite crucible and covered with coarse alumina powder. The alumina powder distributes the heat across the part providing an equalised thermal environment with less temperature gradient and help to support the parts during debinding. The atmosphere in the furnace

must be inert gas and it is recommended that a mix of 30% hydrogen and 70% nitrogen be used. The nitrogen helps maintain carbon levels in the steel and the hydrogen reduces oxides on the steel surface. Oxygen is not desirable in the furnace and must be avoided since it can severely affect sintering and subsequent metal infiltration. The polymer burns out of the green part between 450°C and 650°C (recommended by DTM). The polymer decomposes and the degradation products are removed from the furnace by the gas mixture. The porous nature of the parts help in the easy removal of the binder. Above 750°C the steel particles start to sinter, with the formation of microscopic solid-state welds at particle contacts which grow as sintering progresses, developing a porous skeleton.

The sintering occurs at 1120°C for three hours. After sintering of the parts, the cooling rate to room temperature is 180°C/h. This cooling rate is recommended by DTM to avoid cracking the alumina plate. The sintering furnace cycle results in a brown part with an approximately 60% dense structure of stainless steel. It's recommended that some finishing be done at this point, to remove stair stepping. The time to achieve this cycle is about 20 hours, but it can be extended to 24 hours depending on the part size. Figure 4.3 (a) shows the temperatures during the sintering cycle.

B - Infiltration Furnace Cycle

In this stage, the porous brown part produced in the sintering furnace cycle is infiltrated with bronze to produce a near fully dense part. The parts are placed on a flat alumina plate in a crucible surrounded with some rectangular bars called tabs. Bronze cubes with 85% of the mass of the brown parts and they are placed on the tabs along all side edges. To avoid

part erosion the bronze should not touch the parts. The furnace temperature is raised up to 1050°C during infiltration, and the part is exposed to this temperature for approximately two hours. During this time the bronze melts and infiltrates the tabs and then flows into the parts by capillary action. The cooling rate is 180°C/h. The infiltration cycle results in a near fully dense part. The infiltration cycle also requires a 70/30 nitrogen/hydrogen atmosphere. Figure 4.3 (b) shows the temperatures during the infiltration cycle.

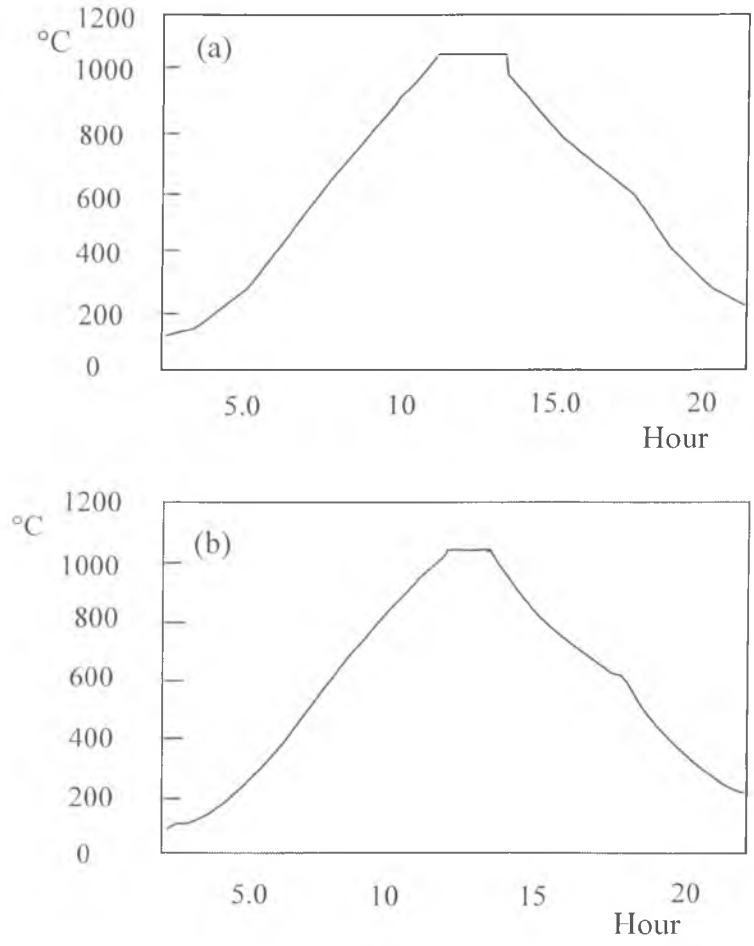

Figure 4.3: (a) Graph of sintering furnace cycle, and (b) graph of infiltration furnace cycle

The overall shrinkage of RapidSteel 2.0 is sensitive to the amount of bronze used because the part swells slightly due to infiltration [Stucker et al 2000]. They reported that using the infiltrant amount equal to 95% by weight of brown part gives the lowest variation in the dimensional results. To produce a part with no interconnected porosity infiltration efficiency should be, 95% by weight or higher [Nelson, 1998].

4.4 Mechanical Properties Measurement

Four cubic test blocks 80 millimetres in size were made from RapidSteel 2.0 both at Leeds University and by DTM Germany. The block size was chosen to represent the thickest cross section expected in a tool manufactured from the RapidSteel 2.0 process. The sintering and infiltration processes were completed using a Carbolite furnace at Leeds and a Lindberg furnace at DTM Germany. Each block was cut into sixteen 20 x 20 x 80 mm specimens with the specimens aligned either horizontally or vertically as shown in Figure 4.4 (a), and (b).

In all cases the infiltration of the blocks was carried out from all four sides of the block, with the infiltrant entering the block at the base of each vertical side. The specimens were then machined on a lathe to tensile test specimens, as illustrated in Figure 4.4 (c).

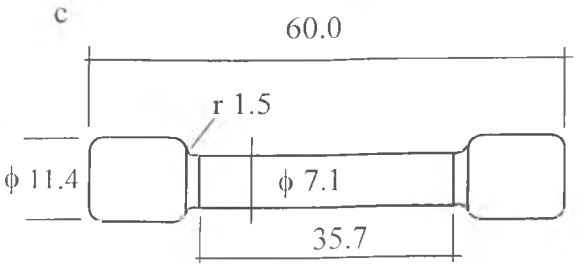

Figure 4.4: (a) 80×80×80mm cubic RapidSteel 2.0 block, (b) 80×80×80 mm cubic RapidSteel 2.0 block cut horizontal sections, and (c) dimensions of RapidSteel tensile specimen

4.4.1 Tensile Test

Strain gages were mounted onto various specimens to obtain an accurate representation of the Young's modulus. Tensile testing of all specimens was conducted using a Dartec Universal Testing Machine (Dartec, Stourbridge, West Midlands, DY98SH, UK) (see Figure 4.5) at a fixed cross-head speed of 0.05 mm/s.

The samples were tested to fracture enabling the ultimate tensile strength, UTS, to be determined. Offset stress, σ_y at 0.2% strain, was determined graphically from the stress-strain curves. After testing, selected test pieces were chosen for fractographic examination using the SEM.

Figure 4.5: The Dartec Universal Testing Machine

4.4.2 Hardness

The hardness tests were performed for brown block samples and infiltrated block samples using Indentec Hardness Machine and load 150 Kg (see Figure 4.6). Samples were mounted in bakelite and polished to a 1000 SiC grit. The HRC values were determined as the mean of at least ten individual measurements.

Figure 4.6 Hardness Machine

4.4.3 Density of Green Parts

The change in density of the green material, i.e. the densification of the powder by laser processing, was studied by varying the laser power applied in the process. Laser powers of 15, 20, 25 and 30Watts were used. Three strips (each 60×25×5 mm) were built for each laser power. The scan speed and scan spacing have not been varied in this experiment. The mass of the strip was measured using a scale with accuracy 0.001 grams. Dimensional measurement of the parts has been carried out using a digital vernier calliper with a resolution of ±0.01mm. Additional care has been taken during measurement in order to not to damage the material due to excessive pressure. Once the volume of the strips has been calculated the density is obtained by Equation (4.1).

4.4.4 Density of sintered parts

The 80 mm cubic blocks were used to measure the density of the green parts, brown parts and infiltrated parts. The mass of the block (green part) was measured using an electronic balance with 0.001 grams accuracy. The volume of the parts was obtained by measuring dimensions in X, Y and Z directions using co-ordinate measuring machine, and the density calculated by dividing weight by volume. This was repeated for each of the four blocks This sequence was repeated after the sintering furnace cycle (brown part), and infiltration furnace cycle (infiltrated part).

4.5 Accuracy and Surface Finish

The studies related to accuracy have considered bulk accuracy and surface finish, and the accuracy and manufacturability of features. The bulk accuracy study has been carried out experimentally using two cubic test blocks 80 mm in size designed not only for this task but also to study the mechanical properties of thick parts. The main objective was to check the dimensional variation in horizontal and vertical planes. Dalgarno et al [2000] reported that the bulk accuracy of RapidSteel 1.0 in the horizontal plane was within ± 0.2 mm, but, as a result of differential shrinkage and vertical consolidation in the resin infiltration/drying phase, was much less accurate with regard to the height of components, which could be millimeters out. A CNC program has been developed to perform the measurement of the blocks in the Coordinate Measuring Machine (CMM), see section 4.5.1.1.

Measurement of all dimensions on each part has been recorded and analyzed. These measurements have been taken after SLS processing (green part) and after each furnace cycle (brown part and infiltrated part). All dimensional measurements after the furnace

processing were compared to the post-SLS state, rather than the .STL file, to eliminate effects of variation from SLS processing.

Many mould tools include small negative and positive features and the degree to which these could be formed with the RapidSteel 2.0 using indirect SLS process was clearly of interest.

The study of small features was divided into two sections, negative and positive. Figure 4.7 (a) and (b) shows the test blocks which were used to characterise the ability of the process to manufacture small negative and positive features. A family of features, made up of a number of bars and cylinders with different dimensions, and shown in Figure 4.8, was defined and applied to a 80 mm cubic block. The dimensions of these features are listed in Table 4.3. The feature set was the same for the positive and negative feature blocks, and an example of each is shown in Figure 4.7 (a), and (b). This design reflects the interest in a detailed accuracy study in the X and Y directions.

The manufactured blocks were then measured to determine what features the process was capable of manufacturing to within the ± 0.2 mm range identified above as the bulk accuracy figure.

processing were compared to the post-SLS state, rather than the .STL file, to eliminate effects of variation from SLS processing.

Many mould tools include small negative and positive features and the degree to which these could be formed with the RapidSteel 2.0 using indirect SLS process was clearly of interest.

The study of small features was divided into two sections, negative and positive. Figure 4.7 (a) and (b) shows the test blocks which were used to characterise the ability of the process to manufacture small negative and positive features. A family of features, made up of a number of bars and cylinders with different dimensions, and shown in Figure 4.8, was defined and applied to a 80 mm cubic block. The dimensions of these features are listed in Table 4.3. The feature set was the same for the positive and negative feature blocks, and an example of each is shown in Figure 4.7 (a), and (b). This design reflects the interest in a detailed accuracy study in the X and Y directions.

The manufactured blocks were then measured to determine what features the process was capable of manufacturing to within the ± 0.2 mm range identified above as the bulk accuracy figure.

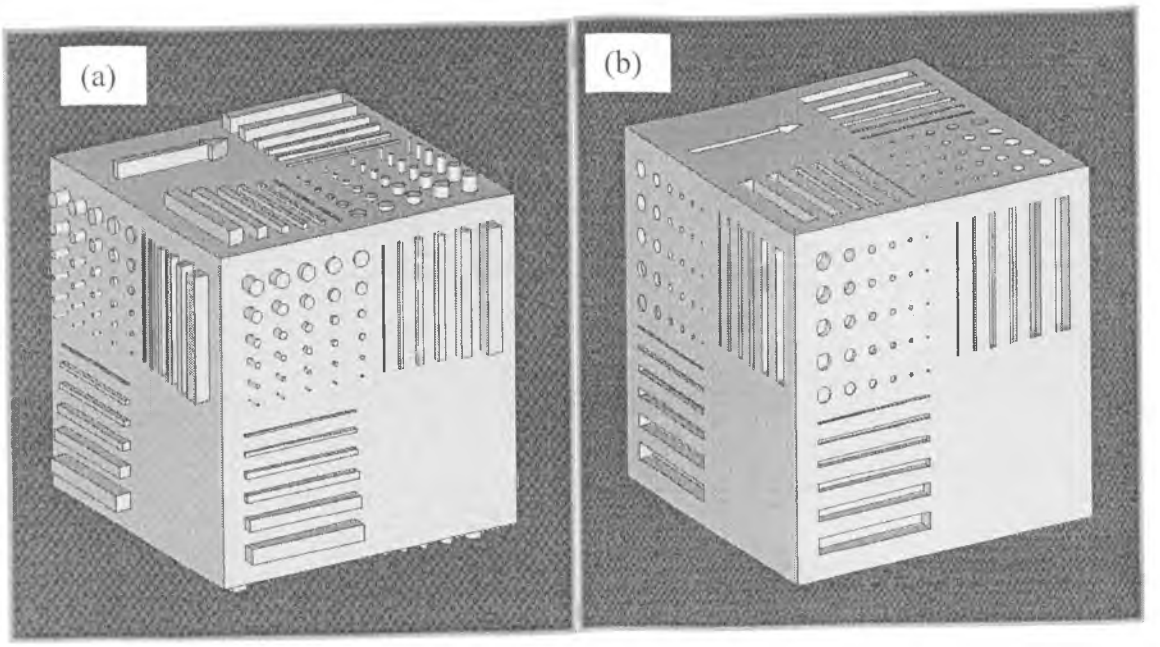

Figure 4.7: Geometry of the test part (a) positive features, and (b) negative features

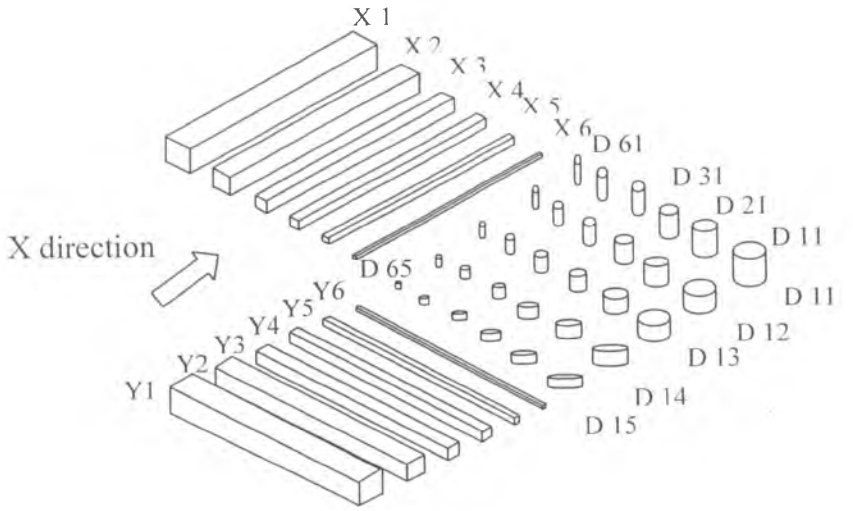

Figure 4.8: Geometry of the small features

Table 4.3: Dimensions of the small features

Feature	Length (mm)	Width (mm)	Height (mm)	Diameter (mm)
X1, and Y1	40	4.0	4	-
X2, and Y2	40	3.0	3.0	-
X3, and Y3	40	2.0	2.0	-
X4, and Y4	40	1.5	1.5	-
X5, and Y5	40	1.0	1.0	-
X6, and Y6	40	0.5	0.5	-
D11, D12, D13, D14 D15	-	-	4.0, 3.0, 2.0, 1.0, and 0.5	4.0
D11, D21, D31, D41, D51 and D61	-	-	4.0	4.0, 3.0, 2.0, 1.5, 1.0, and 0.5

4.5.1 Equipment

4.5.1.1 Coordinate Measuring Machine (CMM)

A Kemco 400 CNC Coordinate Measuring Machine (CMM), (see Figure 4.9), was used to measure most of the parts built in the SLS machine in this work. The accuracy of this machine is ±0.002mm for each axis. Dimension accuracy measurement is carried out in X, Y, and Z directions of the part using a probe with a 2mm ball diameter head. By touching the part to be measured the machine locates the points in 3D space and records their position. The dimensions are then derived by basic arithmetic. This machine can be manually or numerically operated (in which case a CNC program is required).

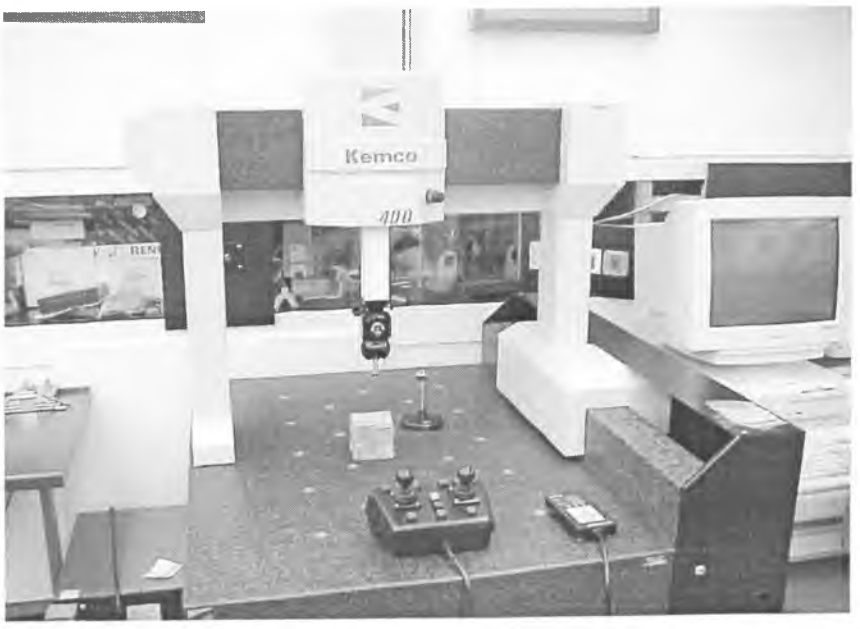

Figure 4.9: Kemco 400 CNC Coordinate Measuring Machine (CMM)

4.5.1.2 Surface Profilometer Form Talysurf 120L

The instrument used to measure surface roughness was a surface profilometer with a stylus that travels along a straight line over the part surface (see Figure 4.10). The profilometer used in this experiment is a Form Talysurf 120L from Taylor Hobson Ltd. A conical diamond stylus with a tip radius of 3mm is used with this profilometer. The cut-off or sample length is one important parameter to set during measurement. It should be long enough to include a statistically consistent amount of roughness, and short enough to eliminate waviness from measurements. The cut-off was set to a standard value of 2.5mm and the results have been checked for any waviness effect. Once the profile is obtained and recorded by the profilometer, the surface roughness R_a (arithmetic average) is calculated automatically using the following Equation.

$$R_a = \frac{1}{L}\int_0^L |y(x)|dx \qquad 4.2$$

where L is the evaluation length, and y(x) = profile deviations from the nominal surface.

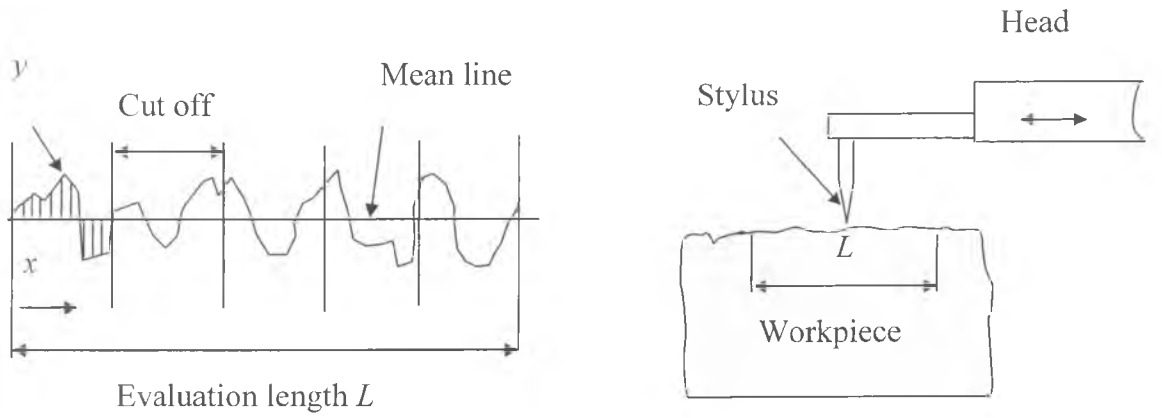

Figure 4.10: Measuring surface roughness with a profilometer

4.5.1.3 Pycnometer

A Micromeritics Accu-Pyc1330 helium pycnometer with accuracy 0.0001g/cm^3 was used to measure the density in order to get a representation of the relative porosity within the samples. Sixteen samples, from fracture tensile test samples, were cut and put in a furnace at temperature 100°C for 48 hours to remove any residual moisture. The first step in operation of the pycnometer is to determine the mass of the specimen. This was completed using a digital microbalance with an accuracy of 0.0001g. The specimen was then placed inside the vacuum chamber of the pycnometer for analysis with the mass of the specimen provided as an input. The pycnometer operates by repeatedly pressurising and evacuating the vacuum chamber containing the specimen with helium gas. The operation is completed

until the volume of Helium evacuated from the chamber reaches an equilibrium. The time for analysis varies according to the amount and size of open porosity in the sample. As the chamber is a fixed volume the device can easily determine the resulting volume of the specimen. By dividing the mass of the specimen which is input at the beginning with the volume of the specimen measured by the pycnometer the density is reported.

4.5.1.4 Metallography

4.5.1.4.1 Sample preparation

Cross sections of the samples from brown part and from fully infiltrated block (B3) were prepared by slicing with a Struers Accoutom-5 cutter (see Figure 4.11 a). All the samples were mounted in a polymeric thermo-plastic resin using (Mataserv) automatic mounting press equipment (see Figure 4.11 b). The samples were ground on water cooled silicon carbide paper with gradually finer grit size (see Figure 4.11 c), and polished using a Buehler automatic polisher (see Figure 4.11 d). The technique for polishing the RapidSteel 2.0 material is detailed in Table 4.3. Manual polishing was carried out using a cloth impregnated with a slurry of alumina (0.5 μm). After polishing, selected samples were etched with 2% nital to reveal grain boundaries. Finally, the samples were graphite coated in order to prevent charging during the use of scanning electronic microscope.

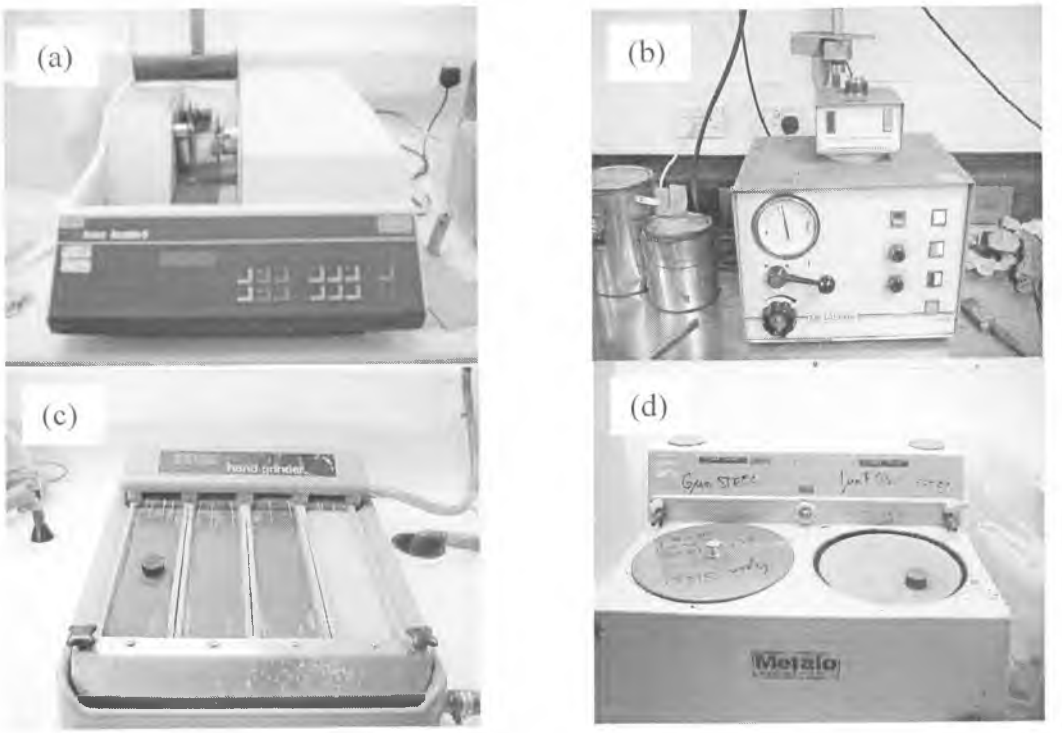

Figure 4.11: Equipments of sample preparation, (a) cutting samples equipment, (b) mounting samples equipment, (c) grinding equipment, and (d) polishing equipment

Table 4.4: Details of individual polishing techniques for RapidSteel 2.0 material after mounting

Material	Surfaces	Particle size	Time (Mins)
RapidSteel 2.0	Paper	80, 140, 180, and 240 SiC grit	Until plane
		6 μm diamond slurry	5
		3 μm diamond slurry	4
		1 μm diamond slurry	4

4.5.1.4.2 Scanning Electron Microscopy

In Scanning Electron Microscopy (SEM) a beam of electrons of 30-40keV is produced from a heated filament cathode and focused and collimated by a magnetic lens system to a

fine spot which is scanned across the sample surface. The electrons from the beam act together with the sample, emitting secondary electron, back-scattered electrons, x-rays and other phenomena. Secondary electrons are low energy electrons emitted mainly from a thin surface layer. Since the intensity of the image is sensitive to the angle of the beam with respect to the surface, secondary electrons images can provide topographical information of the surface. On the other hand, black scattered electrons are emitted from deep in the sample, where the beam electrons have interacted with the atoms of the sample use of BSE image. Scanning electron microscopy was performed using a JEOL JSM 35CF (15 kV) equipped with an EDS spectrometer TRACOR model TN 2000/4000 with a TRACOR Si (Li) detector and a JEOL 6400 device, using a Energy Dispersive Spectrometry (EDS) equipment consisting of a Link Systems LKS detector interfaced to a Kevex Sigma analysis system. Fractography was carried out on sets of fractured specimens (placed side to side), with the fracture surface facing upwards, in order to allow for easier observations of microstructure examination.

4.5.2 Test Piece Geometries

4.5.2.1 Small feature

All features were measured using the CMM described in section 4.5.1.1. A CNC program was used for automatic measurement due to the large number of features to be measured, and also because some of them were very fragile. The position of the probe on the feature being measured is shown in Figure 4.12 a.

Figure 4.12 b shows that there are 16 nodal positions in the X, Y, and Z directions where the probe of the measurement machine has to touch each bar. In addition, the dimensions of the cylinder features are also measured as presented in Figure 4.12 c.

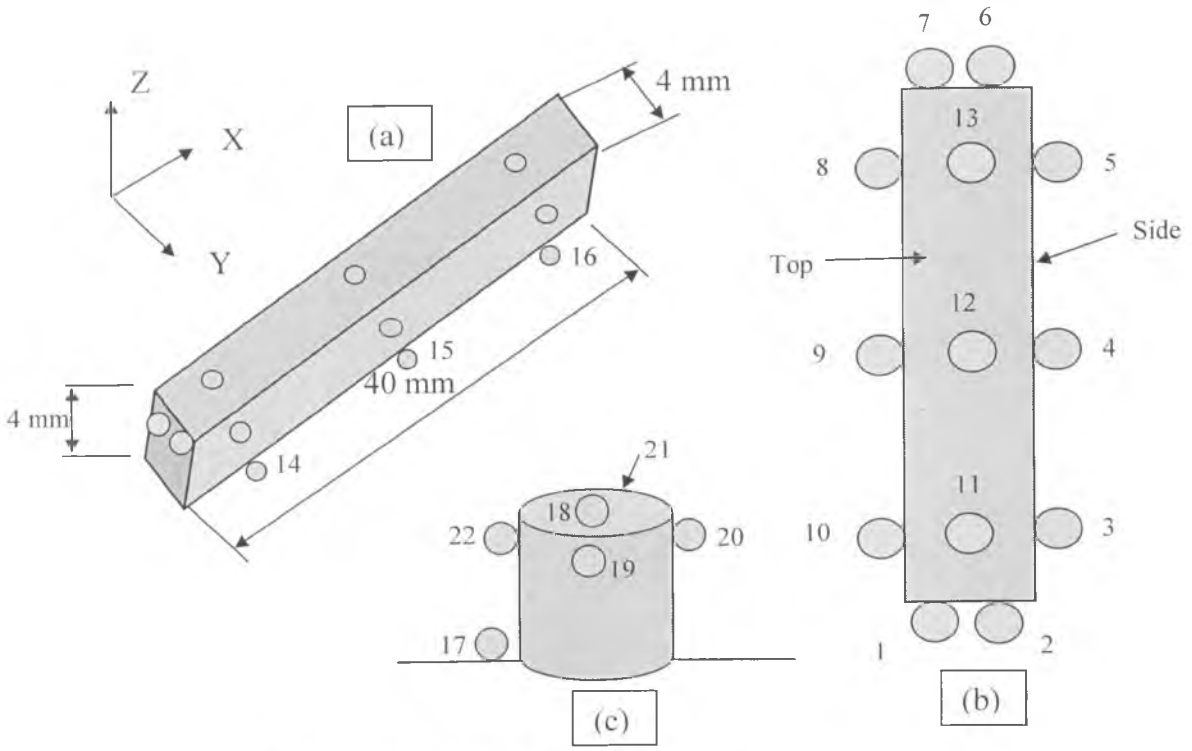

Figure 4.12: Small features measurements

During the measurement the probe touched every node, and recorded and stored its coordinate in the hard disk of the computer. Then, the length, width and height of each bar were calculated as the average of the corresponding nodal positions. The average length, width and height are calculated as following; $X = (X_{1,7} + X_{2,6})/2$, $Y = (Y_{3,10} + Y_{4,9} + Y_{5,8})/3$, and $Z = (Z_{14,11} + Z_{15,12} + Z_{16,13})/3$ respectively. All features, (bars and cylinders, positive and negative) are measured one by one. To identify the dimensional accuracy the results of the

average values were then compared to the nominal values. All measurements were carried out at room temperature.

4.5.2.4 Bulk accuracy.

The accuracy of larger dimensions (bulk accuracy) has been studied using the blocks with dimensions 80×80×80 mm. The averages of five readings in X, Y, and Z direction were obtained after SLS process, sintering cycle, and infiltration cycle, see Figure 4.13. Points 21 to 25 were measured on the base of the CMM.

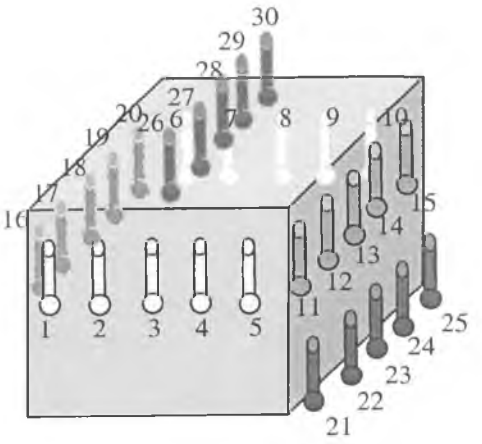

Figure 4.13: Measurement scheme of the large parts

4.5.2.3 Internal channels

The benefits of using a layer manufacture method have been investigated through an assessment of the ease with which channels could be generated within the tools. Studies have shown that conformal channels in mould tools can increase productivity and improve process control [Dalgarno et al., 2000].

To assess the diameter, length, and complexity of channels, which could be manufactured from the RapidSteel 2.0 using indirect SLS process, a number of test parts were made as

shown in Figure 4.14. Figure 4.14 a shows in section an S channel test part with channel diameter 5.0 mm. while Figure 4.14 b shows a whole part with different diameter holes, size 10, 8, 6, 4, 2, and 1 mm.

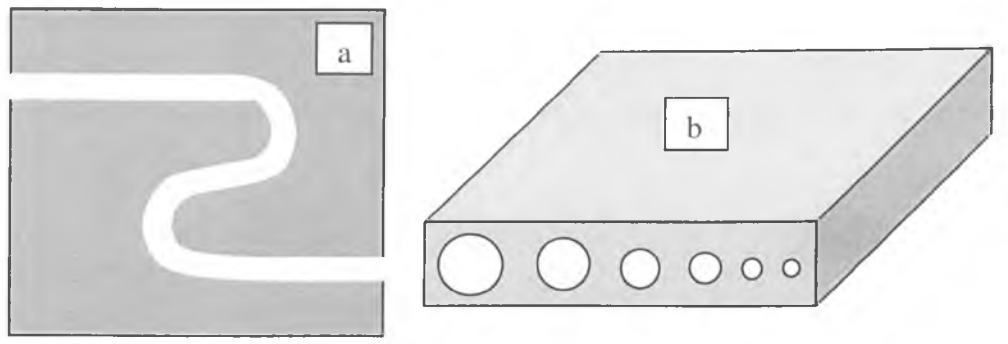

Figure 4.14: (a) Sectioned "S" channel test part, (b) A part with difference diameter size

4.6 Summary

This chapter has outlined the experimental procedures, which will characterise the mechanical properties, density, accuracy and surface finish, and microstructure of indirect SLS process examined using the Sinterstation 2000 machine and the RapidSteel 2.0 material. The results arising from the application of these procedures are presented in the following chapter.

CHAPTER FIVE

RESULTS AND DISCUSSIONS OF INDIRECT SLS

5.1. Introduction

Several experiments and tests required for the development of this work have been described in chapter four. They were directly or indirectly related to the determination the mechanical properties, accuracy, and rate of building time. This chapter presents all the results from these experiments and tests, following the same sequence in which they were described.

5.2 Tensile Strength of RapidSteel 2.0 Material

The influence of type of furnace and the size of parts, on the strength of RapidSteel 2.0 has been studied by the two experiments described in Chapter four in two different types of furnace. Also the influence of infiltration on the strength has been studied. The following sections present the experimental results of the strength of the RS2 material.

5.2.1 Influence of Infiltration on the Strength and Ductility of RapidSteel 2.0

Figure 5.1 shows the strength of RapidSteel 2.0 after sintering cycle (brown part). It is noticed from this figure that the tensile strength of samples is very low and ranging from 30 MPa to 35 MPa. The density of brown parts is about 4.35 g/cm^3.

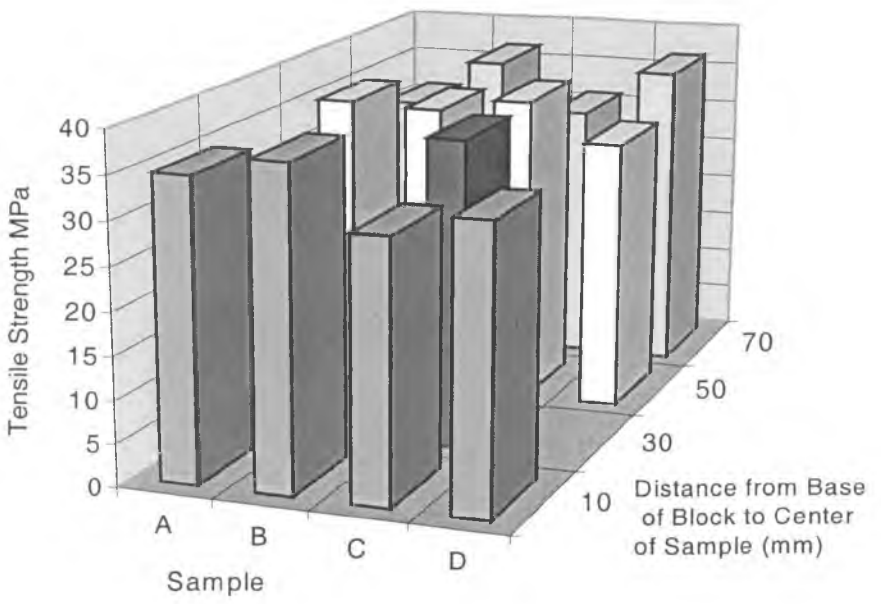

Figure 5.1: Tensile strength of RapidSteel 2.0 using a Carbolite furnace (brown samples)

Figure 5.2 shows the variation in strength for incomplete infiltration of a block cut horizontally. The infiltration was incomplete because the bronze seeped out of the part during the cycle. As recommended by DTM the acceptable efficiency of the infiltrated part should be 95% or more. Incomplete infiltration is caused as a result of the liquid bronze, during the infiltration cycle, not coming into contact with the part. The infiltration efficiency value is not known but was less than 95%. The infiltration efficiency is defined as:

$$\text{Infiltration Efficiency} = \frac{\text{weight of the infiltrated part}}{\text{weight of brown part x 1.85}} \qquad 5.1$$

The tensile strength of the samples which were cut from the base of the block A_1, B_1, C_1, and D_1, were much higher than the samples from the top of the block. The tensile strength values of samples A_1, B_1, C_1, and D_1 are 338.80 MPa, 335.95 MPa, 355.17 MPa, and

361.37 MPa respectively, while the value of tensile strength of A_3, B_3, C_3, and D_3, are 289.54 MPa, 260.78 MPa, 285.37 MPa, and 316.35 MPa. This block had different dimensions because it was built with an insufficient quantity of powder during SLS process. This resulted in the height of the block being reduced in comparison to the other blocks. Generally, the tensile strength of incomplete infiltration samples is higher than the brown samples but lower than the full dense samples due to the residual porosity.

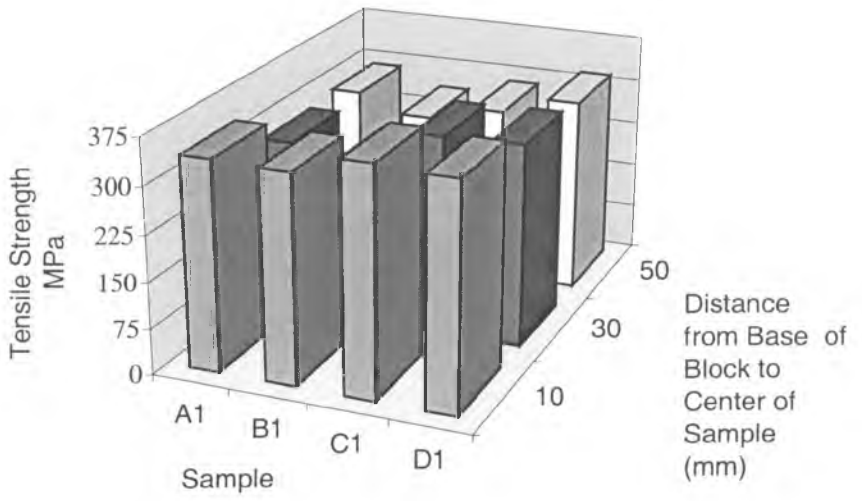

Figure 5.2: The variation in strength for incomplete infiltration block cut horizontally using a Carbolite furnace

Figure 5.3 shows the variation of tensile strength of fully infiltration block cut horizontally. The result shows that the average tensile strength of the RapidSteel 2.0 for full infiltration block cut horizontally is 520 ± 50 MPa. The results suggest that the infiltration cycle is very important to increase the tensile strength of RapidSteel 2.0

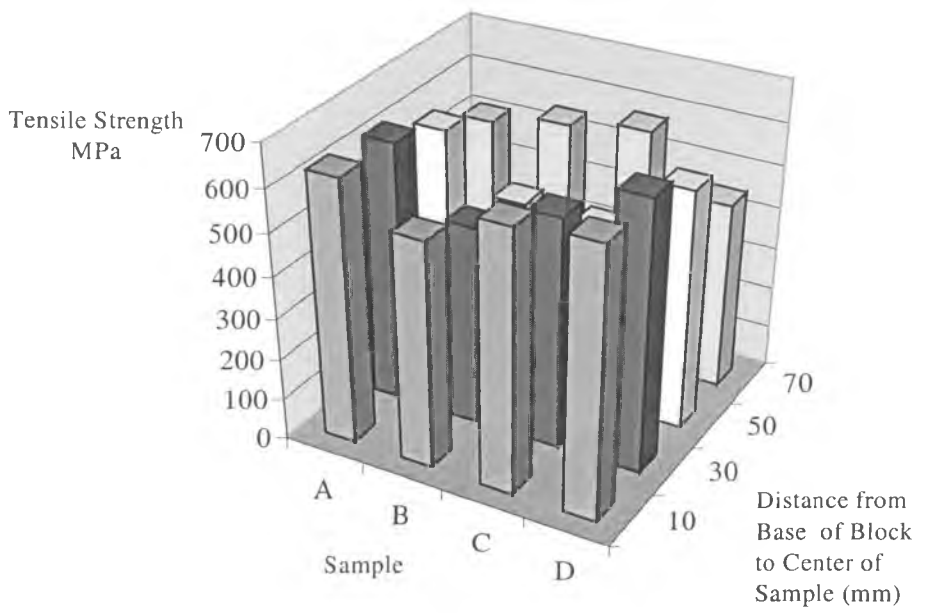

Figure 5.3: Variation in strength of a normally processed RapidSteel 2.0 block infiltrated using Lindberg Furnace

The elongation at break of fully infiltrated block, incompleted infiltration block, and sintered (brown) block are presented in Table 5.1. It can be seen that with increasing infiltration the elongation at break increases.

Table 5.1: (a) Variation in elongation at break of fully infiltrated samples cut horizontally

	A	B	C	D
10	7.85977	6.85042	7.190829	7.365983
30	8.238655	6.12409	6.536695	7.334768
50	6.371429	5.917087	7.157613	6.585434
70	6.017815	8.062185	6.790468	6.556303

Table 5.1: (b) Variation in elongation at break of incompleted block samples cut horizontally

	A	B	C	D
10	3.580	3.960	3.130	3.590
30	2.515	2.563	3.620	3.820
50	3.750	3.097	3.689	3.230

Table 5.1: (c) Variation in elongation at break of sintered block samples (brown part)

	A	B	C	D
10	1.81	1.26	1.38	1.44
30	1.78		1.57	
50	1.88	1.22	1.03	0.94
70	1.37	1.66	1.01	1.07

5.2.2 Influence of Type of Furnace on the Strength of RapidSteel 2.0

Figure 5.3 shows the result of tensile strength tests on a RapidSteel 2.0 block cut horizontally. The sintering cycle and infiltration cycle (using recommended conditions) of this block were completed in a Lindberg furnace at DTM Germany. Figure 5.4 shows also the tensile strength of a block cut horizontally after being processed using a Carbolite furnace at Leeds. The average of tensile strength for this block is about 500 ± 50 MPa. From the Figures 5.3, and Figure 5.4 it can be seen that, there is no significant variation of tensile strength of samples produced using Lindberg furnace and Carbolite furnace. The main variation is the tensile strengths of Lindberg furnace samples are approximately 5%

higher than the samples produced using Carbolite furnace. No reasonable explanation could be found for this variation.

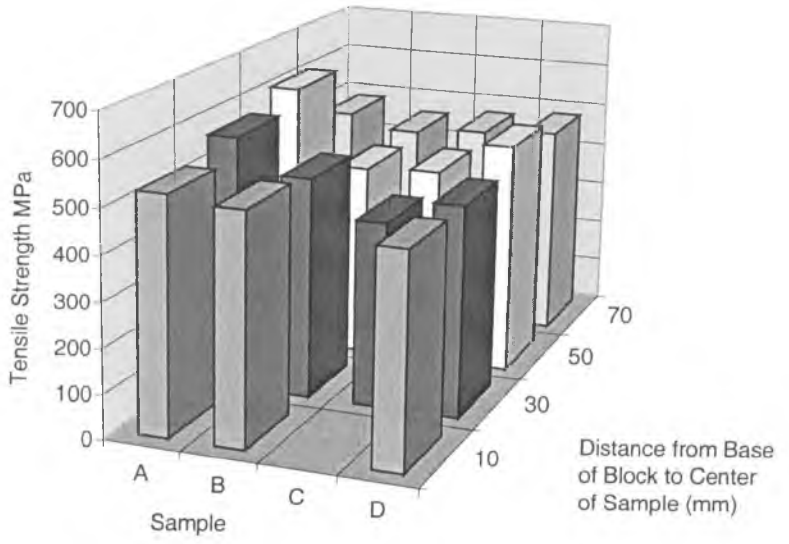

Figure 5.4: Variation in strength of a normally processed RapidSteel 2.0 block infiltrated using Carbolite Furnace

5.2.3 Strength of RapidSteel 2.0 Material

Figure 5.5 shows typical stress-strain variation within a single block manufactured at Leeds using the DTM default furnace cycle. Samples were cut horizontally, A1 is closest to the bronze infiltration place while B3 and C3 are the farthest away. The maximum strength of A1, which is close to the bronze position is 671.3 MPa, where the maximum strengths of B3, and C3, which are farthest away, are 376.25 MPa, and 437.16 MPa respectively.

The resulting variations in the strength for all sixteen samples in the block are plotted in Figures 5.6, 5.7, and 5.8 as a function of the horizontal and vertical distance from the place of bronze infiltration. A pattern of degradation appears to be present with strength

decreasing with distance from the place of bronze infiltration in both the vertical and horizontal directions.

A further visual inspection of the fracture surfaces was also completed. Figure 5.9 shows the side view of the fractured tensile specimens taken from the block previously shown in Figure 5.3 manufactured at DTM Germany using the default furnace cycle. Close examination of the fracture surfaces suggested that the surfaces far from the infiltration point were darker and had more porosity.

The 0.2% yield strength of RapidSteel 2.0 material varied from 250 to 350 MPa, and the ultimate strength ranged between 375 to 693 MPa, with the maximum elastic modulus 256 GPa.

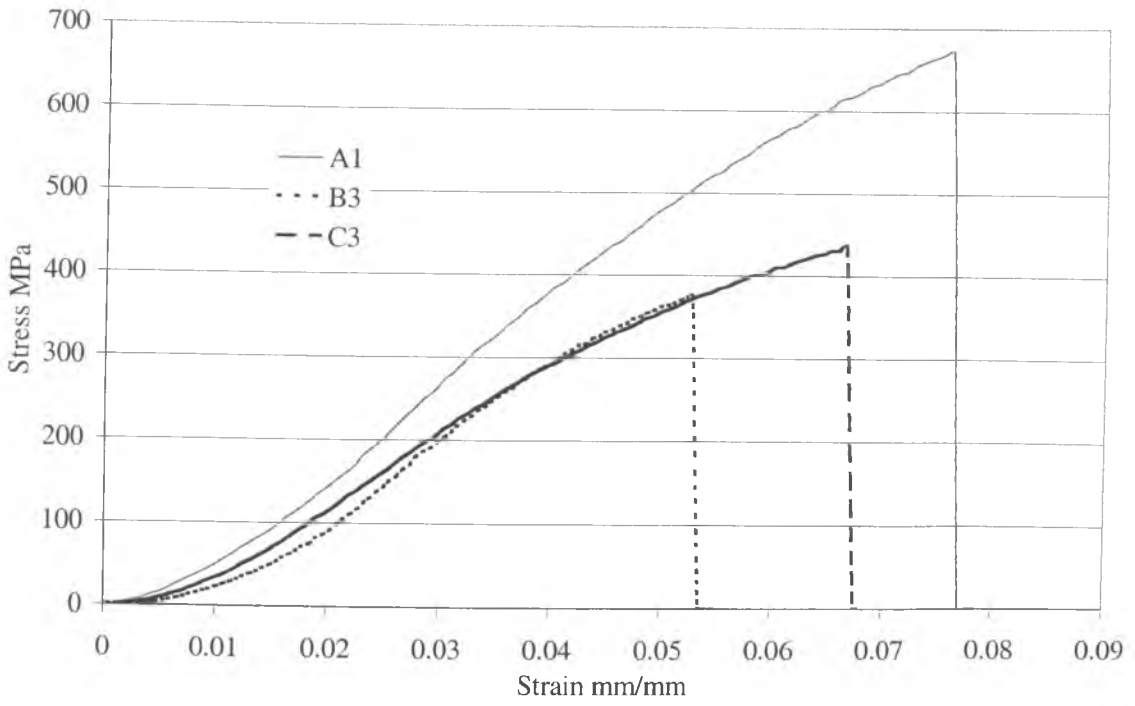

Figure 5.5: Stress - strain curve for three samples of RapidSteel 2.0 material

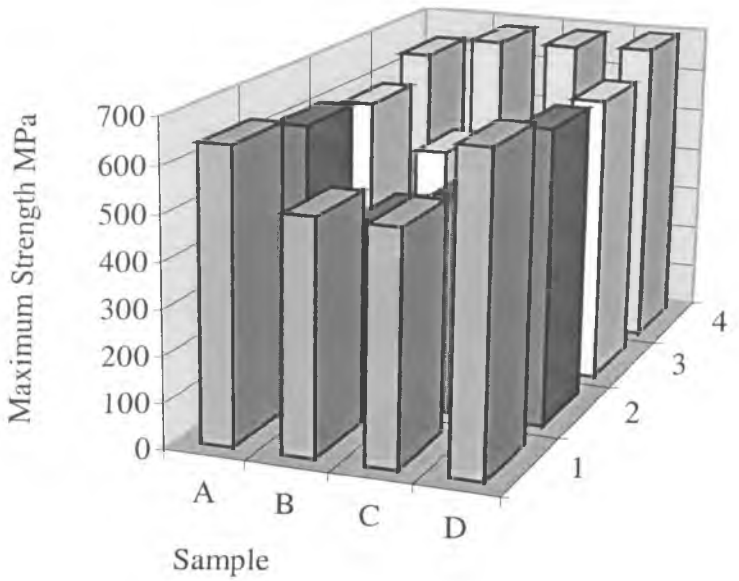

Figure 5.6: Variation in tensile strength of samples cut vertically from 80mm cubic block

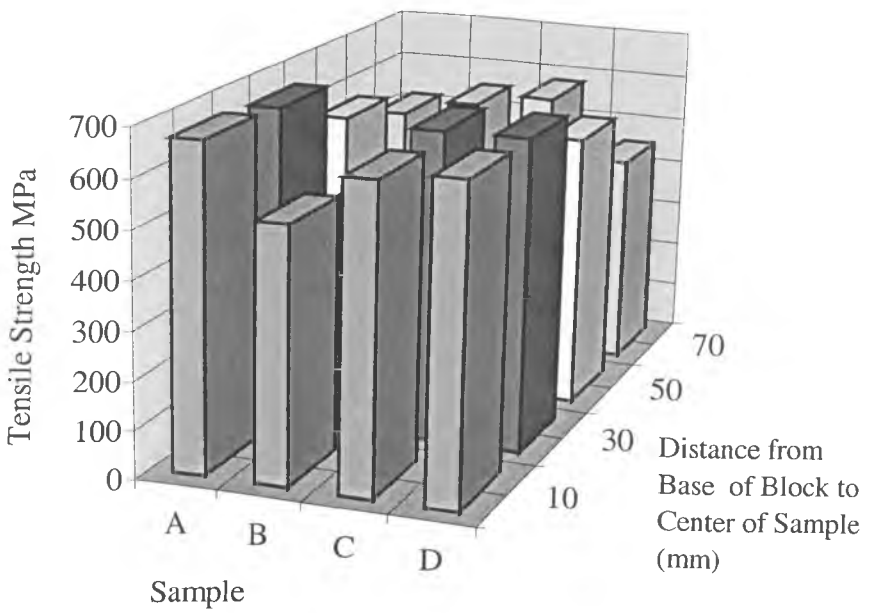

Figure 5.7: Variation in strength of a normally processed RapidSteel 2.0 block

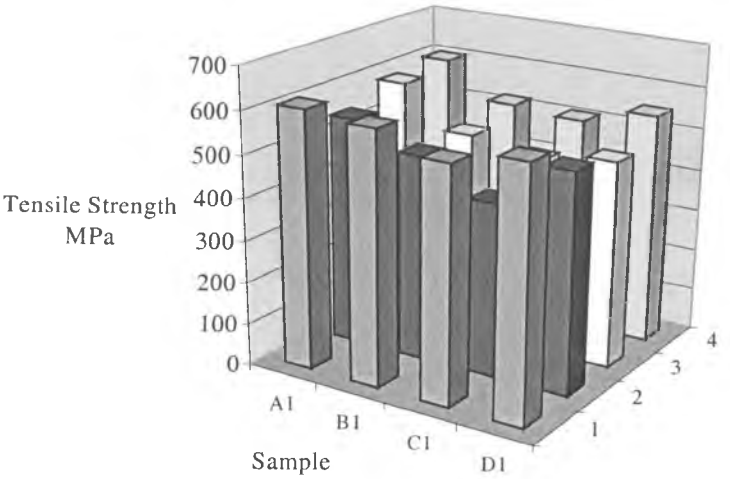

Figure 5.8: Variation of tensile strength of samples cut vertically using Carbolite Furnace

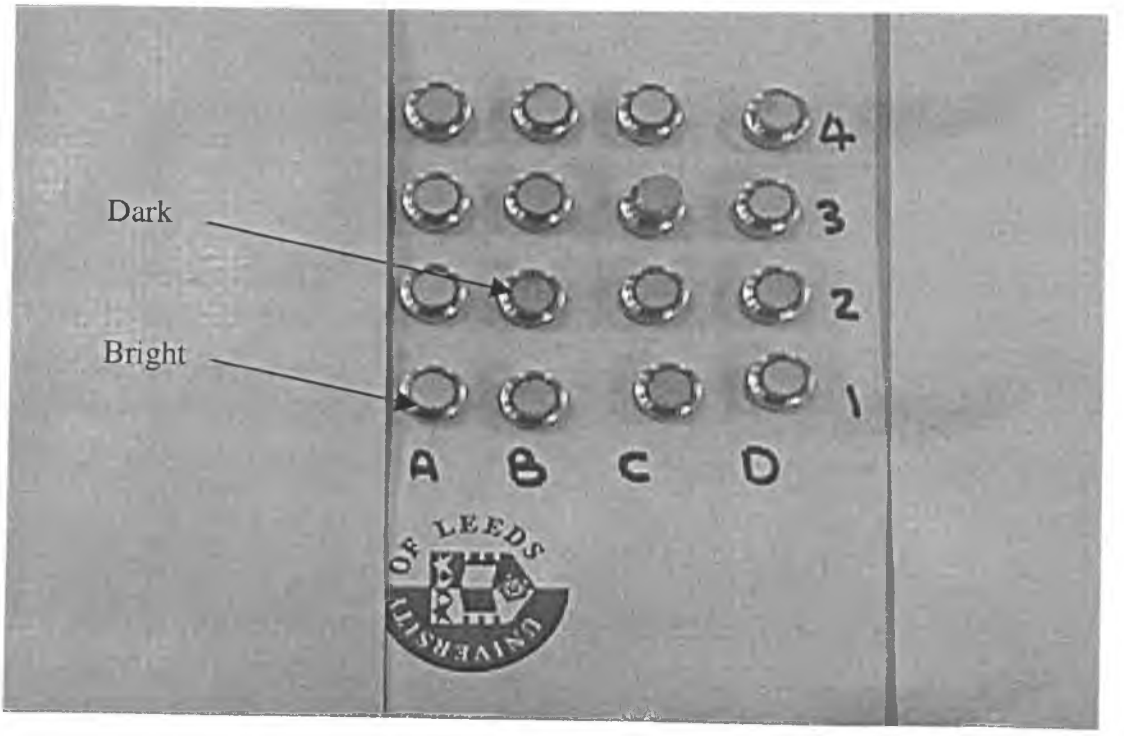

Figure 5.9: Fracture surfaces of horizontally cut samples processed using default furnace cycle in a Lindberg Furnace

5.3 Density Study of RapidSteel 2.0

The results of the three experiments carried out to study density in the SLS processing of RapidSteel 2.0 are presented in the following sections.

5.3.1. Powder Bed Density

Table 5.2 shows the results for the apparent density. In this table, W_{total} is the weight of the box plus the loose powder, W_{box} is the weight of the box, W_{powder} is the weight of the loose powder, and Vol is the volume of the box. The density is represented by ρ. The average apparent density of the powder is $4.2157 \pm 0.026 g/cm^3$.

5.3.2. Density of Green Parts, Brown Parts and Infiltrated Parts

Table 5.3 presents the results of the density tests carried out with the 80×80×80mm blocks, processed at constant laser power, P. In this table, ρ_{Av} means the average density of the 3 blocks with the same processing conditions, W_b is the weight of the block, and Vol is the part volume. The average of green parts, brown parts, and infiltrated parts are 4.2976 g/cm^3, 4.3204 g/cm^3, and 7.9245 g/cm^3 respectively. All dimensions were measured with CMM.

Table 5.2: Apparent density of RapidSteel 2.0 powder

No	Vol (cm^3)	W_{total} (g)	W_{box} (g)	W_{powder} (g)	ρ (g/cm^3)
1	6	60.9876	35.5776	25.4100	4.2350
2	6	60.8876	35.5776	25.3100	4.2183
3	6	61.0076	35.5776	25.4300	4.2383
4	6	60.8576	35.5776	25.2800	4.2133
5	6	60.7536	35.5776	25.1760	4.1950
6	6	61.0086	35.5776	25.4310	4.2385
7	6	61.0276	35.5776	25.4500	4.2417
8	6	60.5856	35.5776	25.1080	4.1847
9	6	60.8845	35.5776	25.3069	4.2178
10	6	60.8574	35.5776	25.2798	4.2133
11	6	60.8176	35.5776	25.2400	4.2067
12	6	60.9084	35.5776	25.3308	4.2218
13	6	60.7531	35.5776	25.1755	4.1959
14	6	60.7248	35.5776	25.1472	4.1912
15	6	60.9176	35.5776	25.3400	4.2233
				Average	4.2157

Table 5.3: Density of RapidSteel 2.0 parts at different stages of the manufacturing processes (all dimensions were measured with CMM)

Condition	Average (mm)			Vol (cm^3)	W_b (g)	ρ (g/cm^3)	ρ_{Av} (g/cm^3)
	X	Y	Z				
Green (1)	80.6066	80.4633	80.7040	523.4365	2250.25	4.2990	4.2976
(2)	80.5823	80.3541	80.6047	521.9250	2244.15	4.2998	
(3)	80.5916	80.4012	80.5091	521.6717	2240.05	4.2940	
Brown (1)	80.5066	80.3466	80.5920	521.3047	2252.00	4.31993	4.3204
(2)	80.5010	80.1302	80.6100	520.0378	2248.07	4.32289	
(3)	80.5102	80.3500	80.5101	520.8194	2249.17	4.31842	
Infiltrated(1)	80.6200	80.4566	80.5020	522.1695	4133.43	7.9159	7.9245
(2)	80.5943	80.3541	80.5598	521.7749	4135.59	7.9260	
(3)	80.6124	80.4125	80.5216	521.9613	4139.95	7.9315	

5.3.3 Density of Green Parts at Different Laser Powers

Table 5.4 presents the results of density tests carried out with 50×25×5mm strips, processed at various laser powers, P. The results shows that the average green density of the RapidSteel 2.0 normally processed (using recommended conditions, laser power=20 W, scan speed=1524 mm/s, scan spacing 0.075 mm, and layer thickness 0.075 mm) is 4.3727 g/cm^3 and that it increases with increasing laser power. The results suggest that there is a maximum density (4.4343 g/cm^3) around 0.2185J/mm^2, with a small drop after that (4.4254 g/cm^3 at 25 W), see Figure 5.10. The drop in density after an energy density 0.2185J/mm^2 is due to the decomposition of the polymer binder at high energy densities.

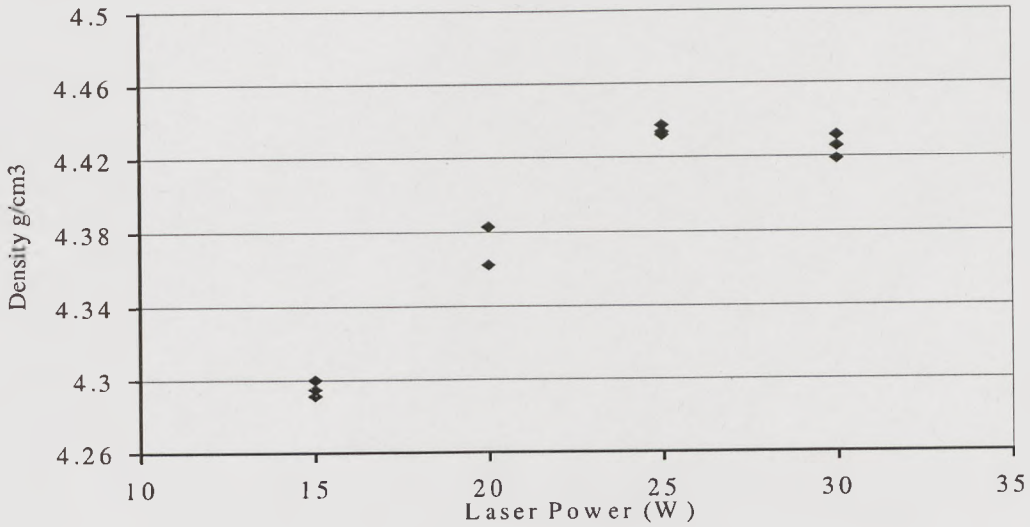

Figure 5.10: Density of green RapidSteel 2.0 parts versus laser power

Table 5.4: Density of strips at various laser powers (scan speed = 1524 mm/s and scan spacing = 0.075 mm)

Power (W)	P/*vs* (J/mm^2)	Average Dimensions (mm)			Vol Cm^3	W g	ρ g/cm^3	ρ_{Av} g/cm^3
		X	Y	Z				
15	0.1295	60.44	25.1	5.01	7.6004	32.6133	4.2910	4.2952
15	0.1295	60.43	25.09	5.00	7.5809	32.5581	4.2947	
15	0.1295	60.42	25.08	5.02	7.6070	32.7101	4.3000	
20	0.1727	60.63	25.22	5.00	7.6454	33.3524	4.3524	4.3727
20	0.1727	60.61	25.21	5.01	7.6552	33.5512	4.3828	
20	0.1727	60.65	25.19	5.02	7.6694	33.6153	4.3830	
25	0.2158	60.72	25.33	4.99	7.6748	34.0154	4.4321	4.4343
25	0.2158	60.71	25.29	5.01	7.6921	34.1321	4.4373	
25	0.2158	60.73	25.34	5.00	7.6945	34.1142	4.4336	
30	0.2590	50.80	25.48	5.01	7.7614	34.3511	4.4259	4.4254
30	0.2590	60.83	25.51	5.02	7.7899	34.5214	4.4316	
30	0.2590	60.84	25.53	5.03	7.8128	34.5230	4.4188	

5.3.3 Density of Infiltrated Parts

Relative density measurements of the fractures samples (fully infiltrated samples) manufactured at DTM Germany using the default furnace cycle has confirmed variable porosity within the structure which appears to be directly proportional to the material strength, as shown in Figure 5.11 (a). Samples closest to the bronze infiltration are only about 3% more dense than samples further away. Appendix A shows density of some samples after infiltration. However, the average density of brown samples are more uniform, about 4.32 g/cm^3, as shown in Figure 5.11 (b).

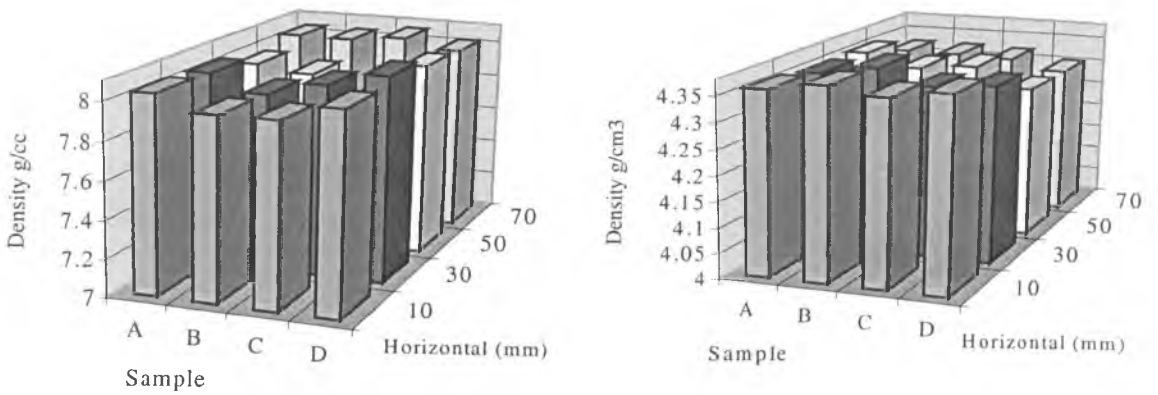

Figure 5.11: (a) Density measurements with the default furnace cycle and horizontally cut samples from DTM Germany, and (b) Density measurements for samples without infiltration (brown block) from Leeds

5.4 Hardness of RapidSteel 2.0

The variation in hardness with infiltrated samples and brown samples is shown in Figure 5.12, and Figure 5.13. For samples far away from the bronze position the density is low or

the porosity is high, as mentioned above, the hardness is decreased (see Figure 5.12). It can be clearly seen from these figures that the average hardness of infiltrated samples, (Figure 5.12) is lower than the average hardness of brown samples, (Figure 5.13). This may be due to the presence of the bronze. The average of hardness of brown samples is about 31±2 HRC.

In summary, infiltration was found to have significant effects on the hardness of RapidSteel 2.0 material. The hardness of infiltrated samples is lower than the hardness of brown samples due to the presence of the bronze. The main reason for this is that the range of hardness of brown samples is narrow (28 to 33 HRC) where the diamond cone always contacts with stainless steel particles. In contrast, in the case of infiltrated samples the range of hardness is wide (15-33). This is because the diamond cone randomly hits hard stainless steel particles or soft bronze particles.

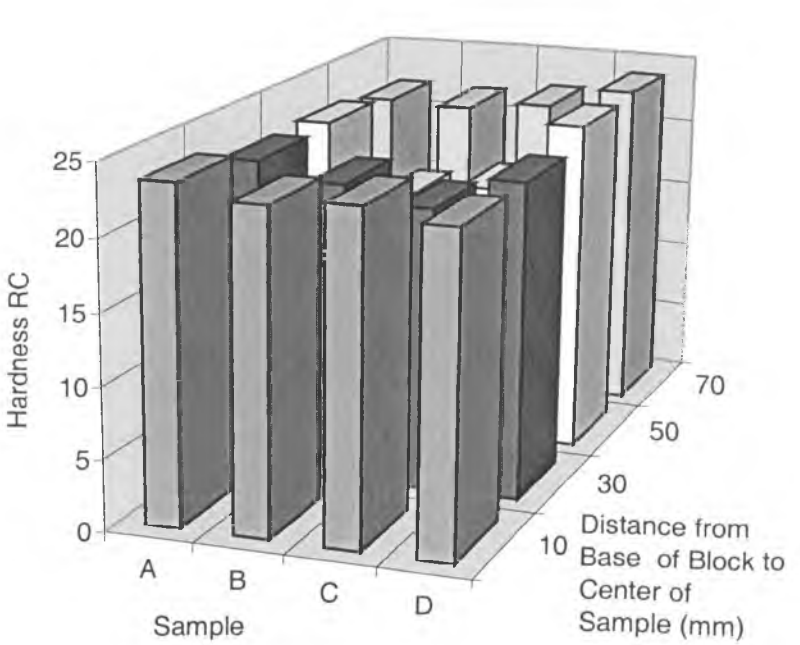

Figure 5.12: Variation in hardness of samples cut horizontally from an infiltrated RapidSteel 2.0 block

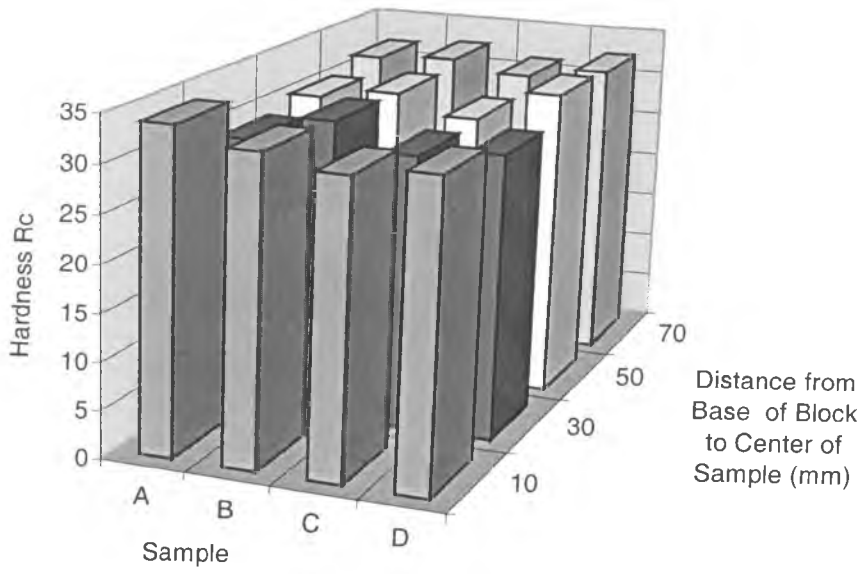

Figure 5.13: Variations in hardness of sintered samples (brown part)

5.5 Accuracy of RapidSteel 2.0 Material

The linear accuracy of the RapidSteel 2.0 process has been studied by the two experiments described in Chapter 4. As was mentioned there, the RapidSteel 2.0 parts were measured after SLS processing (in the green state), after sintering (i.e. in the brown state), and after infiltration (full dense). The results are grouped according to the small features accuracy and bulk accuracy. For the small features, they are separated as positive and negative. In addition, the measurement results for each test are presented separately, firstly the small positive features, then the small negative features, and finally large (bulk) features.

The results of three faces of the blocks, top (X-Y) right (X-Z) and front (Y-Z) faces (as shown in Figure 5.14) are shown for positive and negative features as follows:

Figures from 5.15 to 5.18 show the results of top face with protruding features. Figures 5.15 a and b present the absolute error in the width of rectangular bars 1 and 2 respectively.

Figures 5.15 a and b present the absolute error in height of rectangular bars 1 and 2 respectively. Figure 5.17 shows the absolute error in height of the cylinders. Figure 5.18 shows the absolute error in diameters of the cylinders. Also, the results of right and front face with protruded features are shown in Figures 5.19 to 5.22, and 5.23 to 5.26 respectively.

Figures from 5.27 to 5.30 show the results of top face with depressed features. Figures 5.27 a and b present the absolute error in the width of rectangular bars 1 and 2 respectively. Figures 5.28 a and b show the absolute error in the depth of rectangular bars 1 and 2. Figure 5.29 shows the absolute error in depth of cylinders. Figure 5.30 shows the absolute error in diameters of cylinders. The results of right and front face with depressed features are shown in Figures 5.31 to 5.34, and 5.35 to 5.38 respectively.

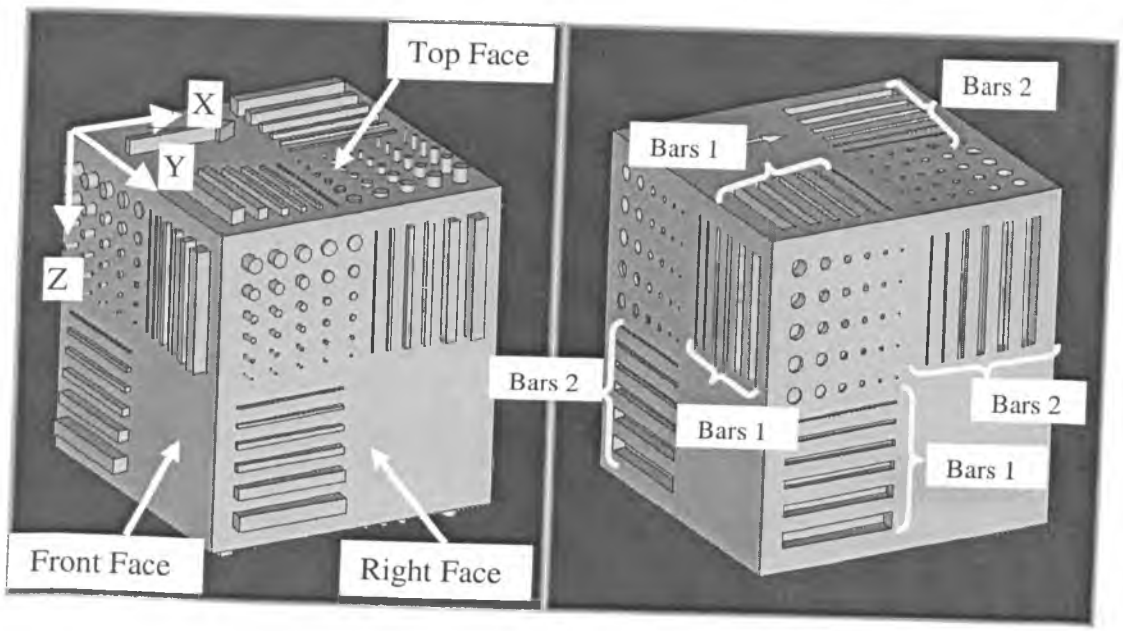

Figure 5.14: Protruded and depressed (positive or negative) blocks with small features.

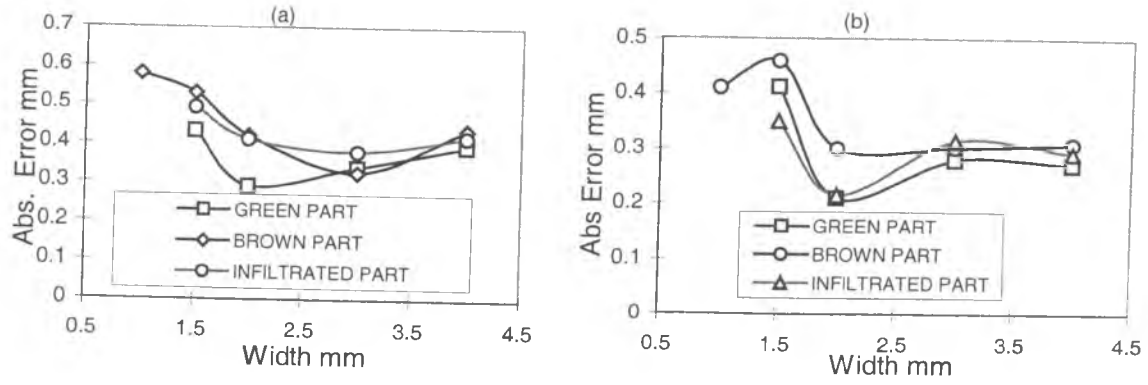

Figure 5.15: (a) Absolute error in width of bars 1 for top face, (b) Absolute error in width of bars 2 for top face (positive features).

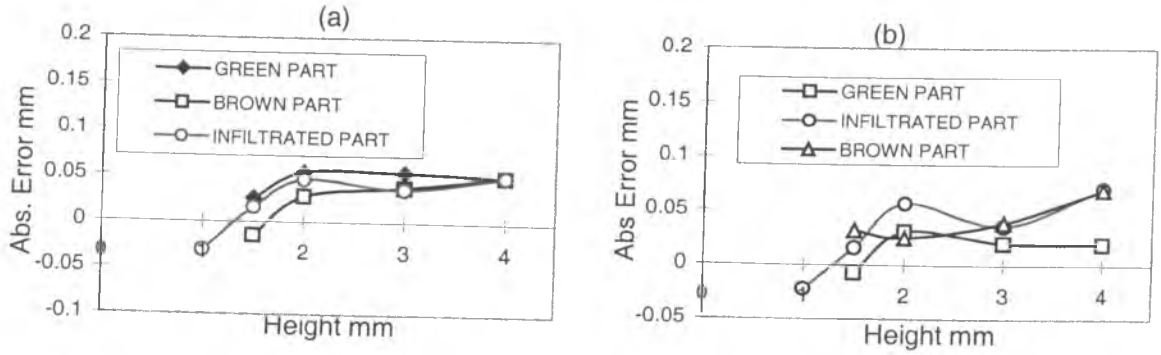

Figure 5.16: (a) Absolute error in height of bars 1 for top face (b) Absolute error in height of bars 2 for top face (positive features).

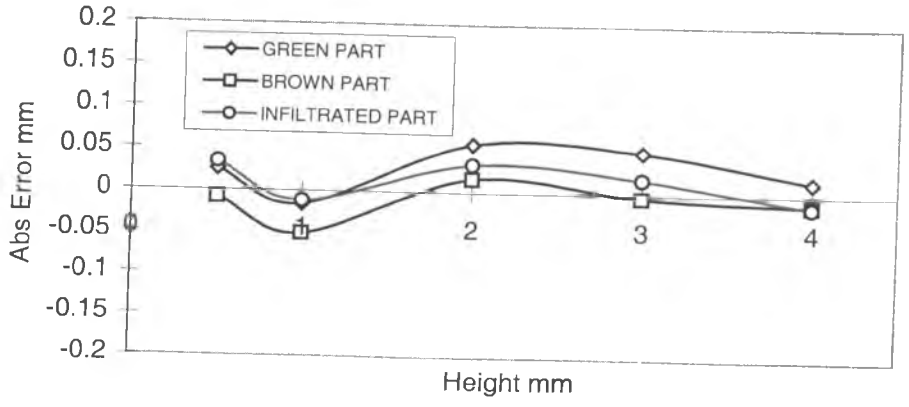

Figure 5.17: Absolute error in height of cylinder for top face (positive features).

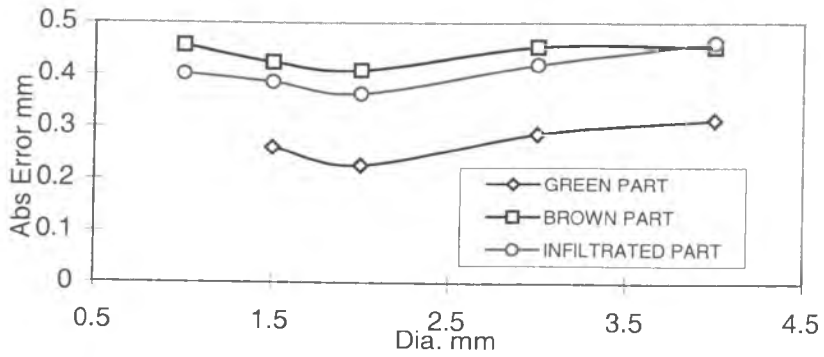

Figure 5.18: Absolute error in diameter of cylinders for top face (positive features).

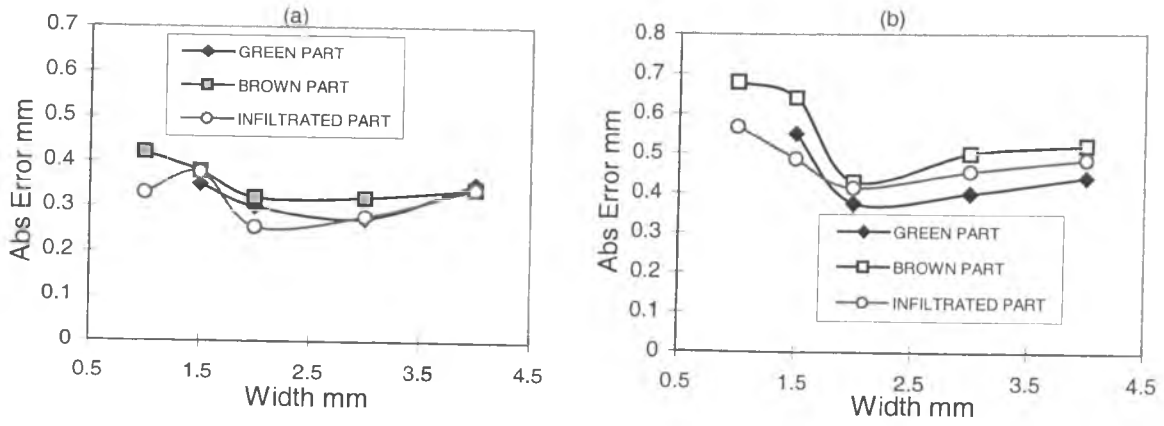

Figure 5.19: (a) Absolute error in width of bars 1 for right face, (b) Absolute error in width of bars 2 for right face (positive features).

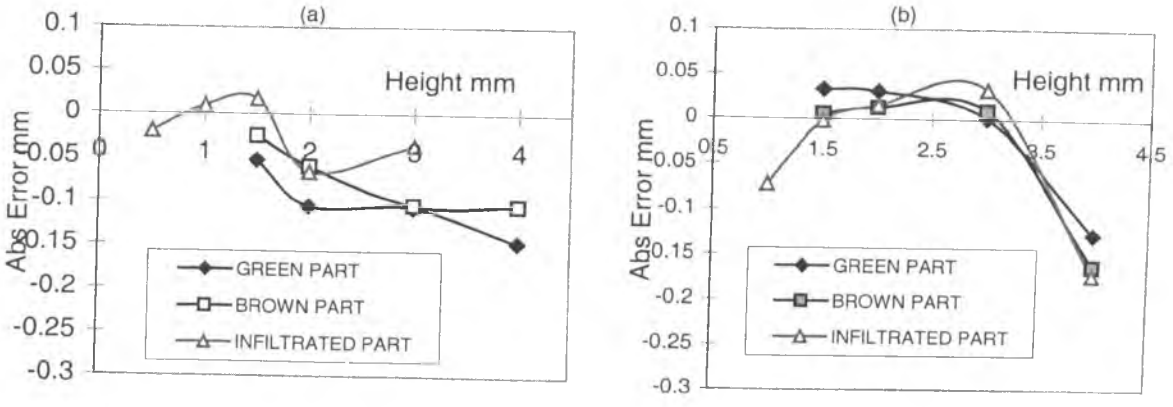

Figure 5.20: (a) Absolute error in height of bars 1 for right face, (b) Absolute error in height of bars 2 for right face (positive features).

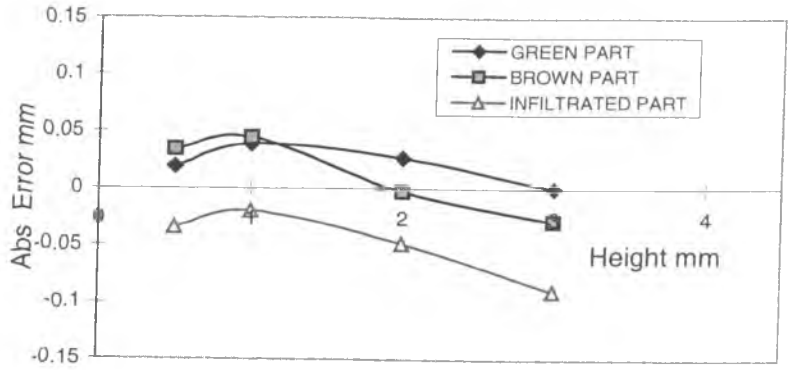

Figure 5.21: Absolute error in height of cylinder for right face (positive features).

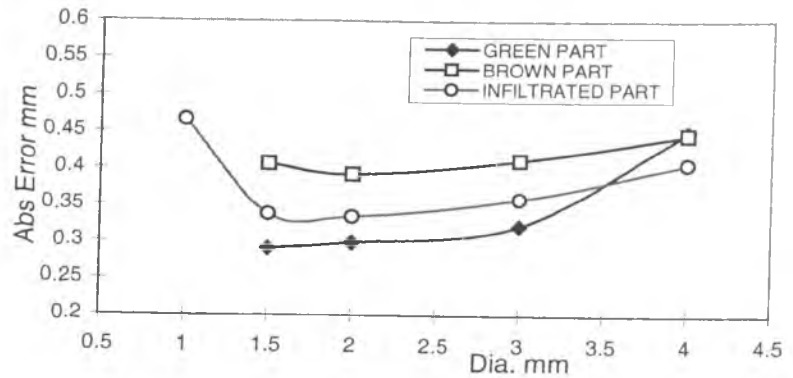

Figure 5.22: Absolute error in diameter of cylinders for right face (positive features).

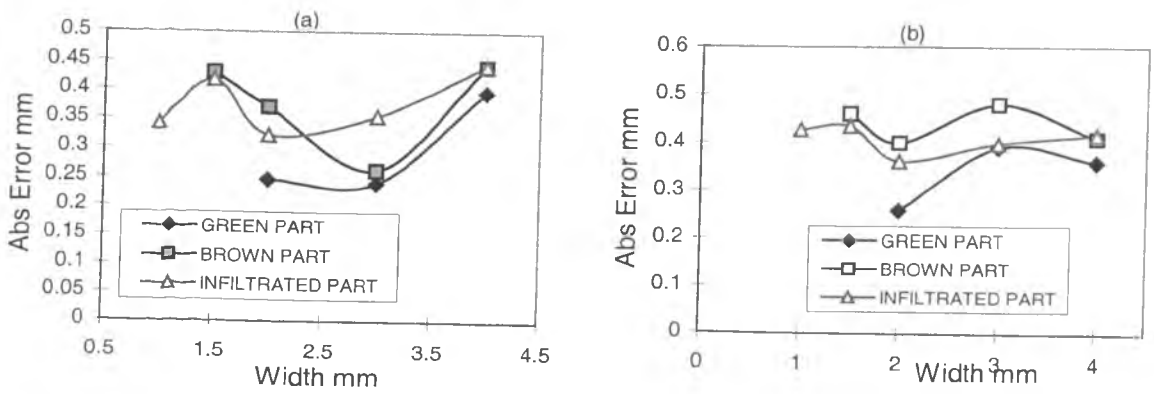

Figure 5.23: (a) Absolute error in width of bars 1 for front face, (b) Absolute error in width of bars 2 for front face (positive features).

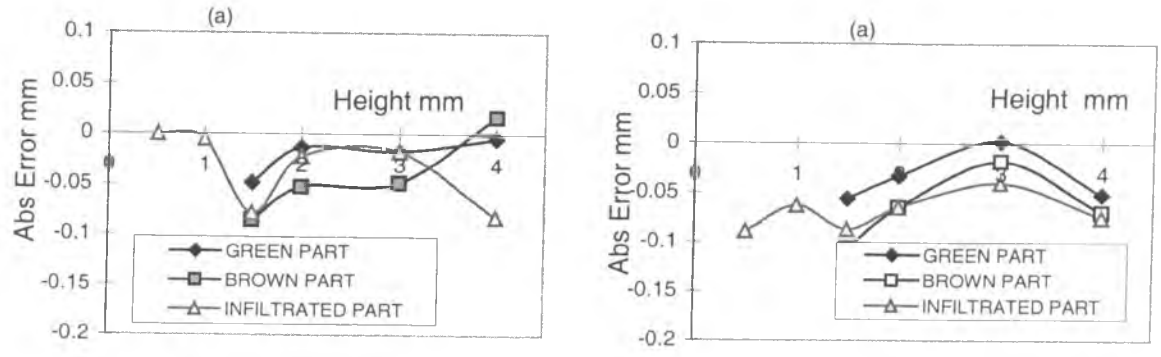

Figure 5.24: (a) Absolute Error in height of bars 1 for front face, (b) Absolute Error in height of bars 2 for front face (positive features).

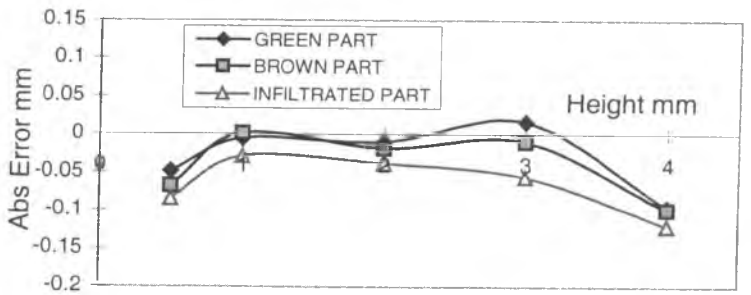

Figure 5.25: Absolute error in height of cylinder for front face (positive features).

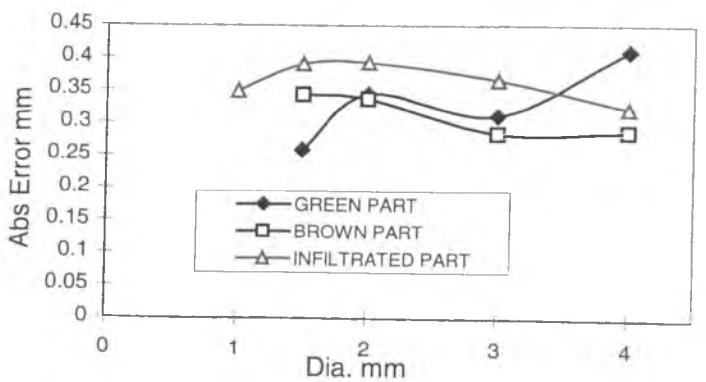

Figure 5.26: Absolute error in diameter of cylinders for front face (positive features).

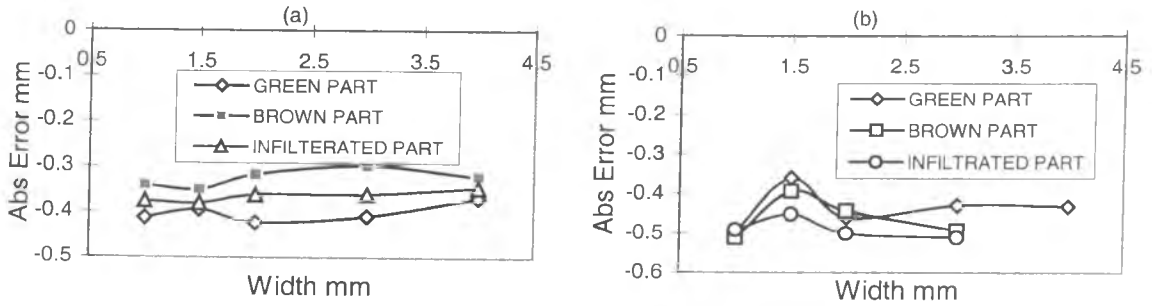

Figure 5.27: (a) Absolute error in width of bars 1 for top face, (b) Absolute error in width of bars 2 for top face (negative features).

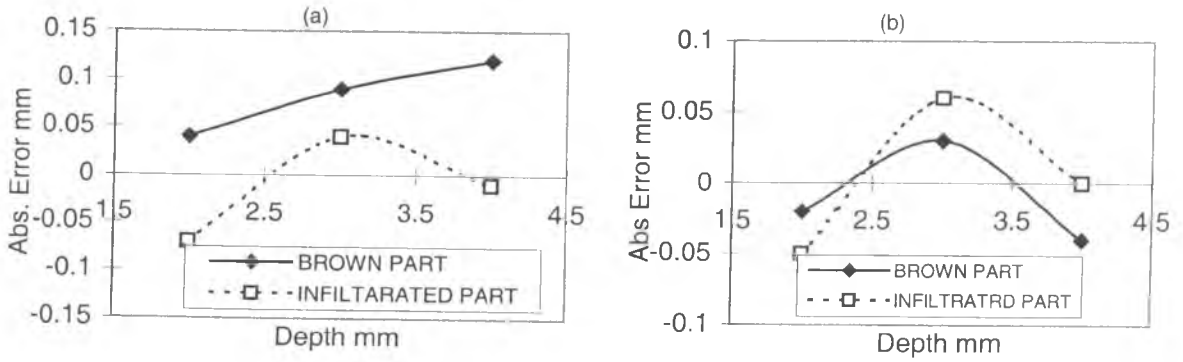

Figure 5.28: (a) Absolute error in depth of bars 1 for top face, (b) Absolute error in depth of bars 2 for top face (negative features).

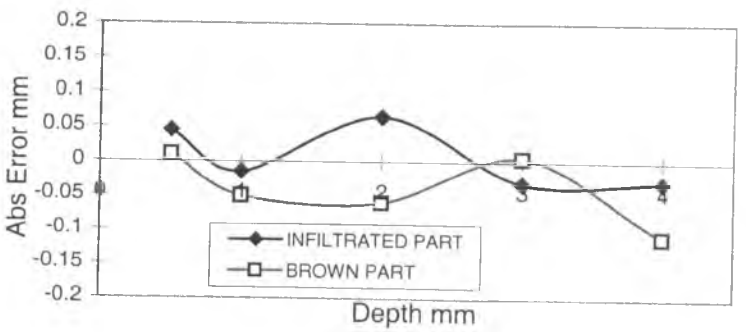

Figure 5.29: Absolute error in depth of cylinder for top face (negative features).

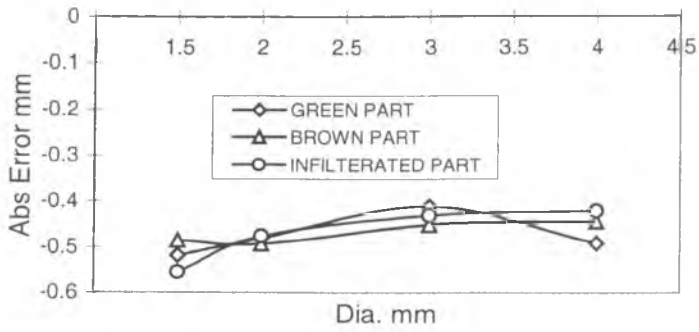

Figure 5.30: Absolute error in diameter of cylinders for top face (negative features).

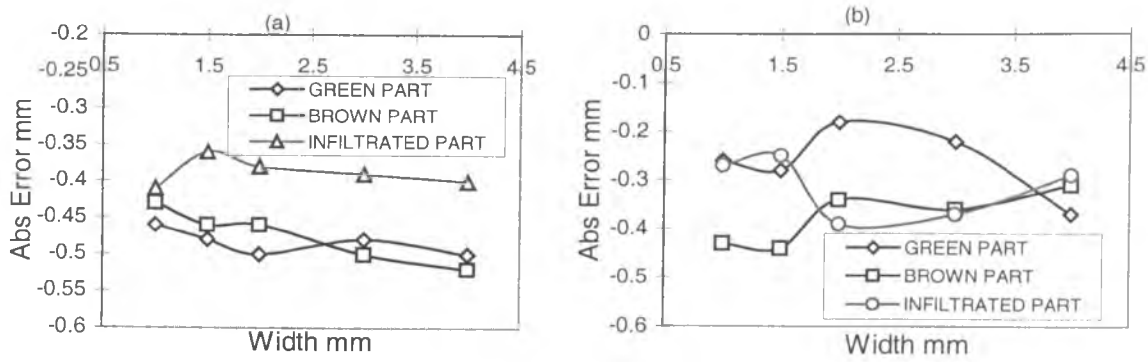

Figure 5.31: (a) Absolute error in width of bars 1 for right face, (b) Absolute error in width of bars 2 for right face (negative features).

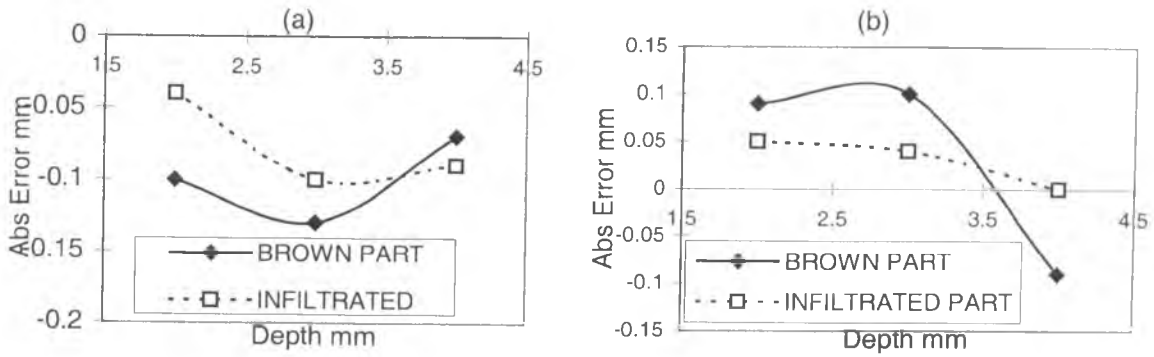

Figure 5.32: (a) Absolute error in depth of bars 1 for right face, (b) Absolute error in depth of bars 2 for right face (negative features).

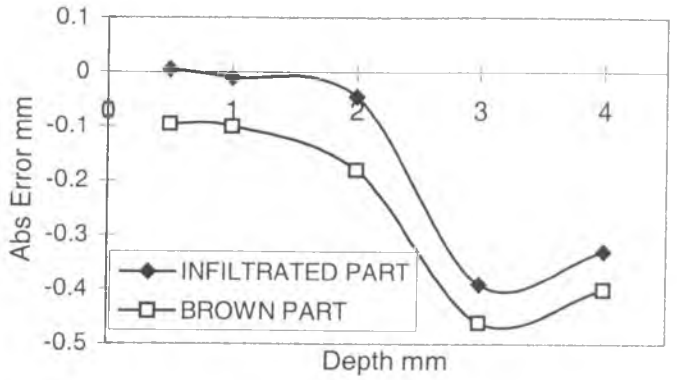

Figure 5.33: Absolute error in depth of cylinder for right face (negative features).

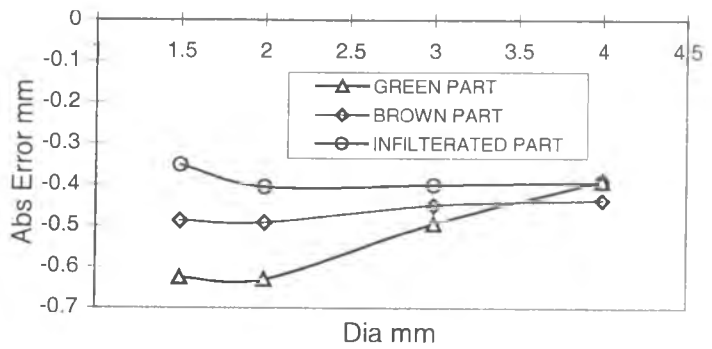

Figure 5.34: Absolute error in diameter of cylinders for right face (negative features).

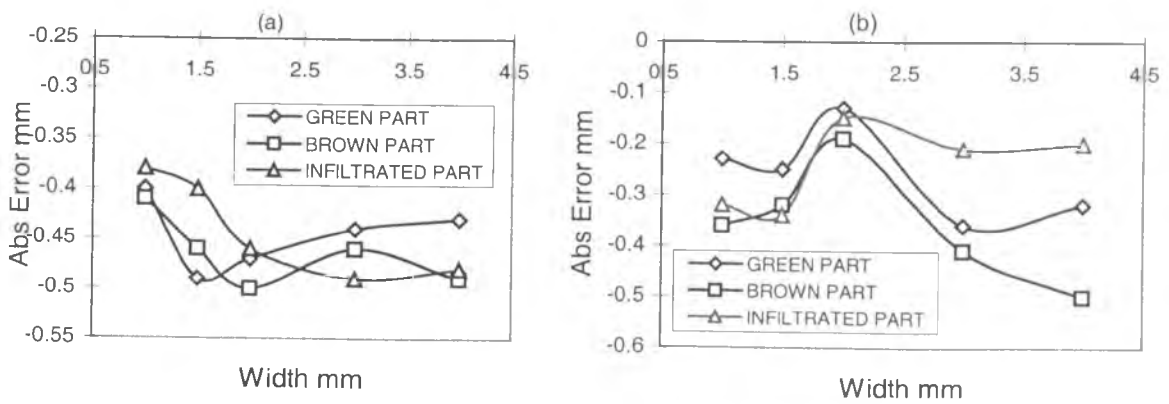

Figure 5.35: (a) Absolute error in width of bars 1 for front face, (b) Absolute error in width of bars 2 for front face (negative features).

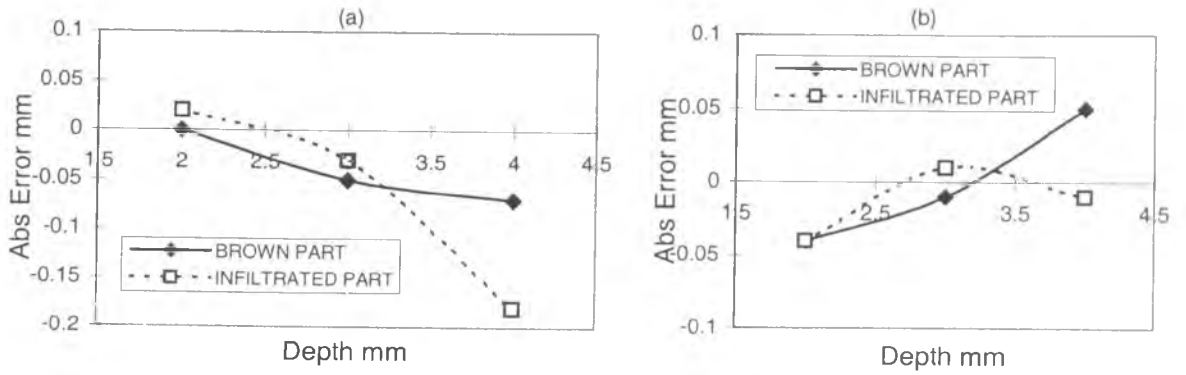

Figure 5.36: (a) Absolute error in depth of bars 1 for front face, (b) Absolute error in depth of bars 2 for front right face (negative features).

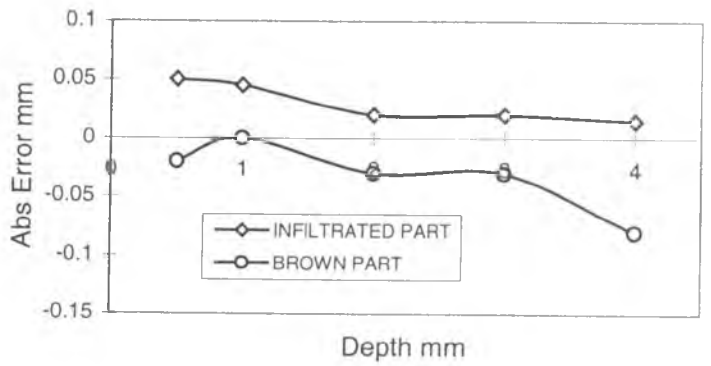

Figure 5.37: Absolute error in depth of cylinder for front face (negative features).

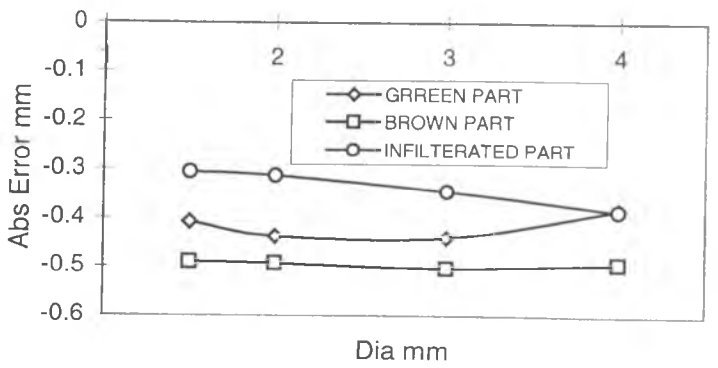

Figure 5.38: Absolute error in diameter of cylinders for front face (negative features).

5.5.1 Small Features Accuracy

Top Face

For positive features the dimension profiles of rectangular bars 1 and 2 are very similar. The absolute errors in width of rectangular bars 1 and 2 are shown in Figure 5.15 (a), and 5.15 (b). Figure 5.15 (a) shows a graph with the oversize results in the X direction for the small features according to the vector length. The oversize in the Y direction is also presented according to the vector length in Figure 5.15 (b). Considering the low shrinkage of RapidSteel 2.0 during SLS processing, the results show that the oversize in the X direction does increase as the feature dimension decreases, at least for widths less than 2.0mm. The oversize increases from 0.33mm at width = 4mm to up to 0.44mm at width = 1.5mm. The shorter the scan vector, the higher the temperature achieved during SLS processing and therefore, the larger the heated volume. The variation is the same for the Y direction.

Figures 5.16 (a) and (b) show the variations of oversize of height of small features. It is clear from this figure that the error profile in height is very similar for bars 1 and 2. The error is approximately constant at about 0.05 mm in both directions. However this error is acceptable because it is under ± 0.2 mm, the quoted accuracy of the SLS machine. In addition, the variation of absolute error among green, sintered, and infiltration dimensions is very small.

In the cylinders, as shown in Figure 5.17, the absolute errors in height varies unevenly as their size changes but the accuracy tolerance is under ± 0.2 mm. In contrast, the absolute errors in diameter for the green part measurements, as shown in Figure 5.18 are

approximately constant at 0.3 mm. Also, as can be seen from this figure the absolute errors of features increased to 0.43 mm after the sintering cycle and decreased to about 0.4 mm after the infiltration cycle. No reasonable explanation could be found for this. The machine was unable to produce the 0.5mm diameter features possibly because the diameter is very close to the diameter of the laser beam (0.4mm). Nevertheless, the features on this face are more accurate overall than those on the other faces.

For negative features the absolute errors in width of bars 1 as shown in Figure 5.27 (a), are approximately constant at 0.4 mm after SLS processing. These errors are decreased to 0.32 mm after the sintering cycle due to shrinkage and increase to 0.35 mm after the infiltration cycle due to the swelling. The absolute errors in width of bars 2 as shown in Figure 5.27 (b) is 0.5 mm for the 1 mm width, reducing to 0.35 mm for the 1.5 mm width and then become constant at 0.45 mm for widths $\geq$ 2 mm. The same trend was observed after the sintering cycle and infiltration cycle with a small variations.

It was not possible to measure the depth of bars and cylinders in the green state. Figures 5.28 and 5.29 show that the absolute errors in the depth of the bars and cylinders after sintering cycle and infiltration cycle are very small and less than 0.1 mm. In the negative cylindrical features, as shown in Figure 5.30 the absolute errors in diameters after SLS processing, sintering cycle and infiltration cycle are very close and ranged between 0.4 and 0.5 mm.

Right Face

In the positive rectangular bars 1 as shown in Figure 5.19 (a), the absolute errors in width varied unevenly as their size changed and ranged between 0.3 to 0.42 mm. In the

rectangular bars 2 (Figure 5.19 b) the absolute errors in width are uneven for the features less than 2.0 mm and then become approximately constant at a value 0.4 mm. This might be due to the shorter the scan vector, the higher the temperature achieved during SLS processing and therefore, the larger the beam offset. The error profile in height of bars 1 and 2 (Figure 5.20 a and b) approximately have the same value 0.15 mm. However, this error is acceptable because it is within machine tolerance.

In the cylinders, the absolute errors in height (Figure 5.21) are quite consistent. The errors in diameter of cylinders (Figure 5.22) are increase as size increase. This might be due to the longer laser scanning time of the bigger features causing extra heat energy to sinter more undesired powder.

For negative features, in rectangular bars 1 (Figure 5.31 a), the absolute errors in width are quite consistent at 0.45 mm after SLS processing and sintering cycle, while these errors are decreased to 0.4 mm. In addition, the errors in bars 2 (Figure 5.31 b), are uneven and range between 0.2 and 0.35 mm.

The absolute errors of heights of the bars 1 and bars 2 after the sintering cycle and infiltration cycle, as shown in Figure 5.32, are approximately the same. However, this error is acceptable because it is within overall tolerances. The parts were not been measured in the green stage.

The absolute errors of heights of the cylinders as shown in Figure 5.33 are constant for small diameters and then increase for diameters of 3mm and 4mm. These errors may be due to the effect of residual powder, arising from the cylinders not being cleaned completely. In the cylinders, the absolute errors in diameters as can be seen from Figure 5.34 are decreased from 0.52mm for the diameter 2mm to about 0.4mm for the diameter 4.0mm for

green stage. After infiltration cycle the absolute errors are approximately constant at 0.4mm.

Front Face

For positive features, the absolute errors in the width of rectangular bars 1 and 2 (Figure 5.23 a and b) increase as the width increases. In rectangular bars 1 and 2 the absolute errors in height (Figure 5.24 a and b) are unevenly distributed, but within the quoted machine accuracy.

Figure 5.25 shows that the absolute errors in the height of cylinders are uneven, but these errors are acceptable. The absolute errors in diameter as shown in Figure 5.26 are constant as height increases.

For negative features, in rectangular bars 1 and 2 (Figure 5.35 a and b) the absolute error in width is unevenly distributed.

The absolute errors of heights of the bars 1 and bars 2 after sintering cycle and infiltration cycle, as shown in Figure 5.36, and the errors of heights of cylinders, as shown in Figure 5.37 are approximately the same. However, this error is acceptable because it is within overall tolerances. In the cylinders, the absolute errors in diameter as shown in Figure 5.38 are constant at 0.4 mm as the diameter increases.

Tables from 5.5 to 5.10 summarize these results and identify whether or not the features have been manufactured to within the quoted machine tolerance of $\pm$ 0.2 mm.

Table 5.5: Errors of green, brown, and infiltrated parts for positive features of top face

Feature Type	Intended Dimension (mm)	Error (mm) (Green)	Error (mm) (Brown)	Error (mm) (Infiltrated)	Within Quoted Accuracy?
Width of Bars 1 Positive (Top)	1	-	0.58	-	-
	1.5	0.452	0.53	0.492	No
	2	0.291	0.42	0.411	No
	3	0.339	0.325	0.379	No
	4	0.393	0.435	0.417	No
Width of Bars 2 Positive (Top)	1	-	0.41	-	No
	1.0	0.432	0.45	0.349	No
	2	0.21	0.4	0.215	No
	3	0.279	0.301	0.314	No
	4	0.271	0.308	0.291	No
Height of Bars 1 Positive (Top)	0.5			0.015	Yes
	1			-0.031	Yes
	1.5	0.025	-0.015	0.015	Yes
	2	0.054	0.028	0.045	Yes
	3	0.054	0.038	0.035	Yes
	4	0.05	0.05	0.05	Yes
Height of Bars 2 Positive (Top)	0.5			0.04	Yes
	1			-0.022	Yes
	1.5	-0.007	0.032	0.015	Yes
	2	0.031	0.025	0.073	Yes
	3	0.02	0.039	0.035	Yes
	4	0.019	0.07	0.071	Yes
Height of Cylinders Positive (Top)	0.5	0.025	-0.0085	0.03375	Yes
	1	-0.0155	-0.052	-0.0125	Yes
	2	0.05733	0.01533	0.033	Yes
	3	0.05	-0.00433	0.01775	Yes
	4	0.01533	-0.012	-0.01433	Yes
Diameter of Cylinders Positive (Top)	1	-	0.45555	0.4025	No
	1.5	0.25155	0.425	0.3855	No
	2	0.22555	0.4095	0.354333	No
	3	0.288	0.4545	0.420557	No
	4	0.31455	0.4545	0.452333	No

Table 5.6: Errors of green, brown, and infiltrated parts for positive features of right face

Feature Type	Intended Dimension (mm)	Error (mm) (Green)	Error (mm) (Brown)	Error (mm) (Infiltrated)	Within Quoted Accuracy?
Width of Bars 1 Positive (Right)	1	-	0.42	0.33	No
	1.5	-	0.38	0.378	No
	2	0.3	0.32	0.154	No
	3	0.274	0.32	0.178	No
	4	0.552	0.5	-	No
Width of Bars 2 Positive (Right)	1		0.58	0.558	No
	1.5		0.54	0.487	No
	2	0.375	0.43	0.414	No
	3	0.4	0.5	0.455	No
	4	0.44	0.52	0.485	No
Height of Bars 1 Positive (Right)	0.5	-	-	-0.02	Yes
	1	-	-	0.01	Yes
	1.5	-0.053	0.005	0.017	Yes
	2	-0.105	0.013	-0.055	Yes
	3	-0.107	0.01	-0.035	Yes
	4	-0.145	-0.152	-	Yes
Height of Bars 2 Positive (Right)	0.5	-	-	-	-
	1	-		-0.072	Yes
	1.5	0.033	-0.025	-0.002	Yes
	2	0.031	-0.05	0.015	Yes
	3	0.001	-0.104	0.033	Yes
	4	-0.127	-0.104	-0.172	Yes
Height of Cylinders Positive (Right)	0.5	0.019	0.034	-0.0342	Yes
	1	0.0385	0.0445	-0.0195	Yes
	2	0.02555	-0.00233	-0.048	Yes
	3	0.00033	-0.02833	-0.0894	Yes
	4	-	-	-	-
Diameter of Cylinders Positive (Right)	1			0.457	No
	1.5	0.29055	0.495557	0.313	No
	2	0.299	0.392333	0.33425	No
	3	0.322	0.411	0.35875	No
	4	0.44955	0.445333	0.4055	No

Table 5.7: Errors of green, brown, and infiltrated parts for positive features of front face

Feature Type	Intended Dimension (mm)	Error (mm) (Green)	Error (mm) (Brown)	Error (mm) (Infiltrated)	Within Quoted Accuracy?
Width of Bars 1 Positive (Front)	1	-	-	0.343	No
	1.5	-	0.43	0.417	No
	2	0.245	0.37	0.322	No
	3	0.24	0.252	0.455	No
	4	0.397	0.541	0.443	No
Width of Bars 2 Positive (Front)	1	-	-	0.427	No
	1.5	-	0.45	0.435	No
	2	0.25	0.4	0.352	No
	3	0.39	0.48	0.399	No
	4	0.35	0.41	0.418	No
Height of Bars 1 Positive (Front	0.5	-	-	0	Yes
	1	-	-	-0.005	Yes
	1.5	-0.048	-0.085	-0.078	Yes
	2	-0.013	-0.052	-0.022	Yes
	3	-0.017	-0.048	-0.017	Yes
	4	-0.004	0.017	-0.082	Yes
Height of Bars 2 Positive (Front)	0.5	-		-0.089	Yes
	1	-		-0.053	Yes
	1.5	-0.055	-0.107	-0.087	Yes
	2	-0.033	-0.055	-0.055	Yes
	3	0.002	-0.018	-0.04	Yes
	4	-0.052	-0.07	-0.075	Yes
Height of Cylinders Positive (Front)	0.5	-0.048	-0.0575	-0.08433	Yes
	1	-0.0055	0.002	-0.0285	Yes
	2	-0.01	-0.01833	-0.03775	Yes
	3	0.0155	-0.01	-0.055	Yes
	4	-0.0955	-0.099	-0.12	Yes
Diameter of Cylinders Positive (Front)	1	-	-	0.349	No
	1.5	0.2585	0.343333	0.390333	No
	2	0.34433	0.3358	0.3925	No
	3	0.311	0.284	0.3555	No
	4	0.41	0.285557	0.32225	No

Table 5.8: Errors of green, brown, and infiltrated parts for negative features of top face

Feature Type	Intended Dimension (mm)	Error (mm) (Green)	Error (mm) (Brown)	Error (mm) (Infiltrated)	Within Quoted Accuracy?
Width of Bars 1 Negative (Top)	1	-0.412	-0.34	-0.375	No
	1.5	-0.394	-0.35	-0.38	No
	2	-0.422	-0.315	-0.352	No
	3	-0.409	-0.297	-0.351	No
	4	-0.359	-0.321	-0.345	No
Width of Bars 2 Negative (Top)	1	-0.495	-0.51	-0.49	No
	1.0	-0.358	-0.393	-0.45	No
	2	-0.459	-0.442	-0.5	No
	3	-0.429	-0.493	-0.51	No
	4	-0.432	-0.74	-0.75	No
Height of Bars 1 Negative (Top)	0.5	-	-	-	-
	1	-	-	-	-
	1.5	-	-	-	-
	2	-	-0.02	-0.07	Yes
	3	-	0.03	0.04	Yes
	4	-	-0.04	-0.01	Yes
Height of Bars 2 Negative (Top)	0.5	-	-	-	-
	1	-	-	-	-
	1.5	-	-	-	-
	2	-	-0.02	-0.05	Yes
	3	-	0.03	0.05	Yes
	4	-	-0.04	0.0	Yes
Height of Cylinders Negative (Top)	0.5	-	0.01	0.045	Yes
	1	-	-0.05	-0.015	Yes
	2	-	-0.05	0.055	Yes
	3	-	0.005	-0.31	Yes
	4	-	-0.41	-0.03	Yes
Diameter of Cylinders Negative (Top)	1	-	-	-	-
	1.5	-0.5175	-0.485	-0.555	No
	2	-0.48	-0.4925	-0.475	No
	3	-0.41	-0.45	-0.43	No
	4	-0.49075	-0.443	-0.42	No

Table 5.9: Errors of green, brown, and infiltrated parts for negative features of right face.

Feature Type	Intended Dimension (mm)	Error (mm) (Green)	Error (mm) (Brown)	Error (mm) (Infiltrated)	Within Quoted Accuracy?
Width of Bars 1 Negative (Right)	1	-0.45	-0.33	-0.41	No
	1.5	-0.48	-0.45	-0.35	No
	2	-0.5	-0.45	-0.38	No
	3	-0.48	-0.54	-0.39	No
	4	-0.52	-0.52	-0.4	No
Width of Bars 2 Negative (Right)	1	-0.25	-0.43	-0.27	No
	1.5	-0.28	-0.44	-0.25	No
	2	-0.18	-0.34	-0.39	No
	3	-0.22	-0.35	-0.37	No
	4	-0.57	-0.31	-0.29	No
Height of Bars 1 Negative (Right)	0.5	-	-	-	-
	1	-	-	-	-
	1.5	-	-	-	-
	2	-	-0.1	-0.04	Yes
	3	-	-0.13	-0.05	Yes
	4	-	-0.07	-0.09	Yes
Height of Bars 2 Negative (Right)	0.5	-	-	-	-
	1	-	-	-	-
	1.5	-	-	-	-
	2	-	0.09	0.05	Yes
	3	-	0.1	0.04	Yes
	4	-	-0.09	0.0	Yes
Height of Cylinders Negative (Right)	0.5	-	-0.095	0.005	Yes
	1	-	-0.10	-0.01	Yes
	2	-	-0.18	-0.045	Yes
	3	-	-0.45	-0.39	No
	4	-	-0.40	-0.33	No
Diameter of Cylinders Negative (Right)	1	-	-	-	-
	1.5	-0.525	-0.48725	-0.3525	No
	2	-0.53	-0.492	-0.405	No
	3	-0.495	-0.4495	0.403	No
	4	-0.39	-0.43775	0.410	No

Table 5.10: Errors of green, brown, and infiltrated parts for negative features of front face

Feature Type	Intended Dimension (mm)	Error (mm) (Green)	Error (mm) (Brown)	Error (mm) (Infiltrated)	Within Quoted Accuracy?
Width of Bars 1 Negative (Front)	1	-0.4	-0.41	-0.38	No
	1.5	-0.49	-0.45	-0.32	No
	2	-0.47	-0.5	-0.45	No
	3	-0.44	-0.45	-0.49	No
	4	-0.43	-0.49	-0.48	No
Width of Bars 2 Negative (Front)	1	-0.23	-0.35	-0.38	No
	1.5	-0.25	-0.32	-0.32	No
	2	-0.13	-0.19	-0.45	No
	3	-0.35	-0.41	-0.49	No
	4	-0.32	-0.5	-0.48	No
Height of Bars 1 Negative (Front	0.5	-	-	-	-
	1	-	-	-	-
	1.5	-	-	-	-
	2	-	0	0.02	Yes
	3	-	-0.05	-0.03	Yes
	4	-	-0.07	-0.18	Yes
Height of Bars 2 Negative (Front)	0.5	-	-	-	-
	1	-	-	-	-
	1.5	-	-	-	-
	2	-	-0.04	0.04	Yes
	3	-	-0.01	0.01	Yes
	4	-	0.05	-0.08	Yes
Height of Cylinders Negative (Front)	0.5	-	-0.02	0.05	Yes
	1	-	0	0.045	Yes
	2	-	-0.03	0.02	Yes
	3	-	-0.03	0.02	Yes
	4	-	-0.08	0.015	Yes
Diameter of Cylinders Negative (Front)	1	-	-	-	-
	1.5	-0.4075	-0.49	-0.305	No
	2	-0.4375	-0.4925	-0.3125	No
	3	-0.44	-0.5025	-0.345	No
	4	-0.3825	-0.4925	-0.385	No

5.5.2 Bulk Accuracy and Surface Roughness

The dimensional results of the large positive and negative features (32 mm in length) in the X, Y, and Z directions are presented in Table 5.11. Figure 5.39 present these results in a graphical way. It can be seen from Figure 5.39 that the absolute errors of the bars in the X direction, which generated in top face and right face, are approximately constant at 0.525±0.01 mm. Also, it can be seen from this figure that there is not a significant variation due to the sintering cycle and infiltration cycle, except that the dimensions were slightly decreased after sintering cycle due to shrinkage and these dimensions were increased after infiltration cycle due to swelling. The same trend was observed for Y direction, and Z direction in top face, right face, and front face, but the values of errors were less than X direction. The absolute error in the Y and Z directions are 0.170 mm, and 0.380 respectively. In general, there is no significant variation in the dimensions of the bars of similar direction in different sides i. e., the dimensional error in the Y direction on the top face and front face is approximately the same, and the dimensional error in the Z direction on the right face and front face is approximately the same.

Concerning the negative features, the absolute errors in the X direction is approximately -0.45 mm in both the top and right faces. In addition, the average of absolute error in the Y direction is about -0.758 mm on the top face and -0.838 mm on the front face. The absolute error in the Z direction is -0. 38 mm in both the right and front faces.

Figure 5.40 presents the average results of dimensional errors of two blocks nominally 80×80×80 mm. The absolute errors of X direction, Y direction, and Z direction after infiltration are about 0.2 mm, 0.1 mm, and 0.25 mm respectively. The absolute errors in all

directions are decreased after sintering by about 0.2 mm due to the shrinkage. In addition, the dimensions are increased after infiltration cycle in X and Y direction due to the swell of bronze. In contrast, the shrinkage of dimensions in Z direction continued after the infiltration cycle. This may be due to the effect of the gravity of the part.

From Figures 5.39, and 5.40 it can be noticed that the absolute error in the X direction was decreased from 0.52 mm for an intended length of 32 mm, to about 0.25 for an intended length 80 mm. In addition, the absolute error in the Y direction was decreased from 0.17 mm for an intended length 32mm to 0.1 mm for an intended length of 80 mm.

In general, the part experiences a considerable difference in shrinkage in the two directions, X and Y, in SLS processing. This difference is likely to be due to scanning accuracy, because it was not possible to find any physical explanation for this effect.

Table 5.11: Measurement results of large features in the X, Y, and Z directions.

Side	Condition Length (32 mm)	Positive			Negative		
		X	Y	Z	X	Y	Z
Top	(Green)	0.517	0.160	-	-0.332	-0.739	-
	(Brown)	0.519	0.153	-	-0.459	-0.776	-
	(Infiltrated)	0.523	0.166	-	-0.466	-0.758	-
Right	(Green)	0.537	-	0.362	-0.464	-	-0.216
	(Brown)	0.522	-	0.353	-0.410	-	-0.360
	(Infiltrated)	0.535	-	0.382	-0.441	-	-0.387
Front	(Green)	-	0.155	0.336	-	-0.742	-0.282
	(Brown)	-	0.140	0.330	-	-0.801	-0.372
	(Infiltrated)	-	0.171	0.381	-	-0.838	-0.380

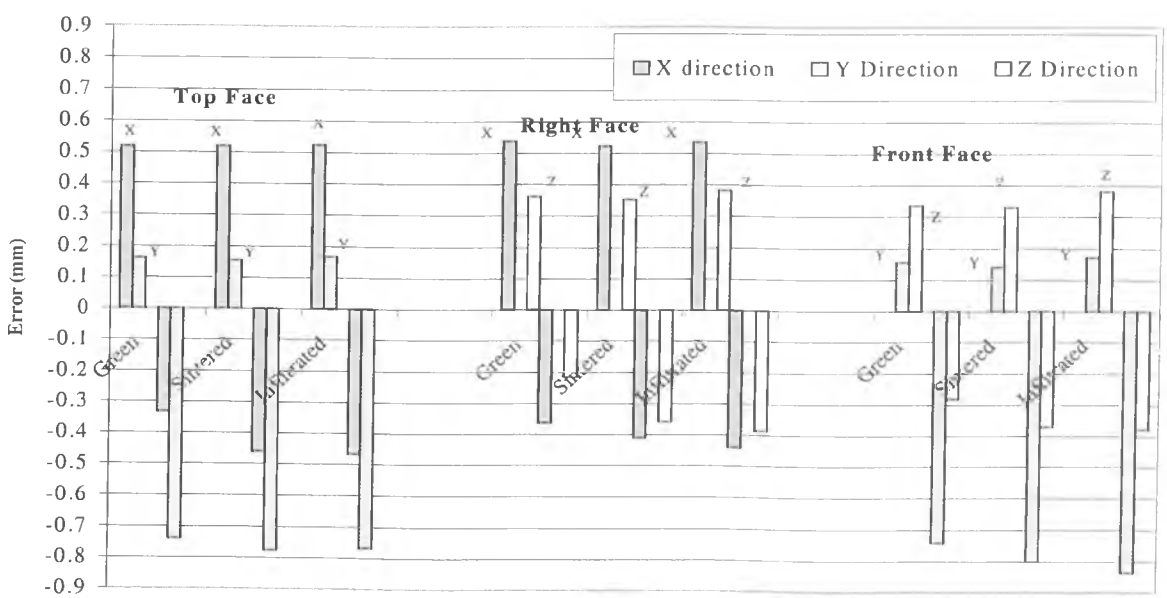

Figure 5.39: Average results of dimensional errors of two blocks 80×80×80 mm

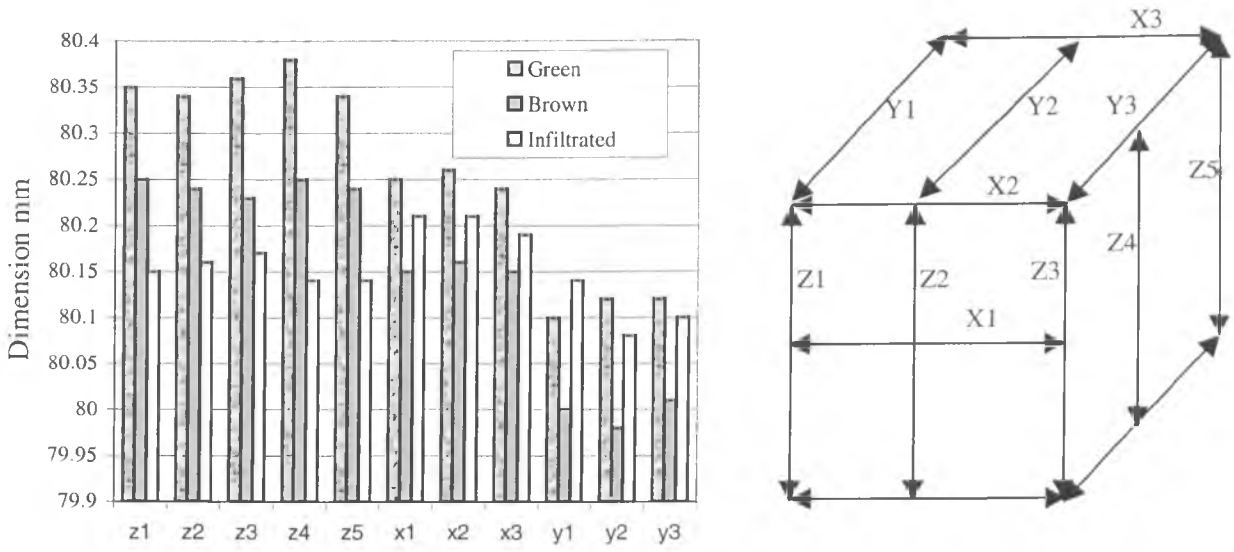

Figure 5.40: Comparison of dimensional accuracy of green, brown, and infiltrated 80×80×80 block

As mentioned in Chapter 2, section 2.2.5.4, effects on accuracy recognized from the analysis of the geometry change are directly related to the variation of the length of the scan vectors. Firstly, the total number of vectors is increased and, as a consequence, so is the number of starts and stops of the laser. This fact increases the influence of the scanning accuracy on the final dimensional results. Secondly, the SLS processing conditions are changed, because the time between laser exposures is reduced. In general, the experimental results showed that these accuracy effects are actually happening during SLS processing. However, because of the interrelation between the processing condition of vector length and the scanning accuracy, it is not an easy task to separate the two effects and quantify the contribution of each one. The following sections present a discussion of the results considering what might be the influence of processing conditions and scanning accuracy on part accuracy.

Numerical studies of SLS processing showed that, as the length decreases, the time between laser exposures is reduced and, therefore, the processing temperature increases [Nelson, 1993; Williams and Deckard, 1998]. Consequently, this may lead to an increase in material density and part oversize. The numerical studies suggested that this is the case for the RapidSteel 2.0 material. From the results of the experimental accuracy tests with small features, it is possible to identify some behaviours that were in accordance with this suggestion.

For small features, it was observed that the oversize increased slightly with the decrease of vector length in all directions. This effect was more pronounced for the X direction, in positive features, (as shown in Figure 5.16 a, and Figure 5.20 a) than it was for the Y direction, (as shown in Figure 5.16 b, and 5.24 a) and Z direction (as shown in Figure 5.20 a, and Figure 5.24 b). In contrast, this effect was more pronounced for the Y direction, in negative features, (as shown in Figure 5.28 b, and Figure 5.36 a) than it was for the X direction, (as shown in Figure 5.28 a, and 5.32 b) and Z direction (as shown in Figure 5.32 a, and Figure 5.36 b).

The results showed a significant shrinkage difference between the X and Y observed directions for RapidSteel 2.0 processed by the Sinterstation 2000. Volpato [2001] reported that a great accuracy improvement in the scanning system of the Sinterstation 2500plus in the X direction when compared to the Sinterstation 2000. Also, he mentioned that the results showed almost no alteration in accuracy in the Y direction for large features between the two machines. This suggests that no improvement in this direction occurred with the current generation of SLS machine. The results for the Sinterstation 2500plus were much closer to the expected behaviour, following a general trend predicted by the

numerical models. This was the case for small and large features.It is, therefore, possible to say that this oversize problem is due to a systematic error in the scanning system of the Sinterstation 2000.

The roughness measurements indicated that the roughness of these as-built parts after infiltration ranges from 6-10 μm R_a.

5.6 Internal channels

Several authors have identified that the use of conformal cooling or heating in polymer mould tools can improve productivity through reduced cycle times, and improve process control [Sachs et al., 1997; Jacobs, 1999; Dalgarno et al., 2000]. Within selective laser sintering an important issue in generating channels is the removal of powder from green parts.

One of the advantages of SLS process over other rapid prototyping processes, as mentioned before, is the ability to make parts with complex internal channels. This is because the part sintered in a powder bed. Therefore, a sintered layer is supported by the powder underneath it, making overhangs and internal channels easy to create. One negative aspect of this is the difficulty in removing the unsintered powder filling these channels after sintering. After a part is sintered, the excess powder must be removed before sintering while the part is in its green state and therefore weak. Excess metal powder left on the part will be detrimental to the final quality of the part.

Figure 5.41 shows one of a number of test parts which were made to assess the diameter and length of channels which could be manufactured using the RapidSteel 2.0 process. The minimum practical size of cooling channel which could be manufactured was of 5mm diameter; the recommended size of cooling channel (for relatively easy powder removal) was 8mm. In addition there is no limit in terms of the complexity which could be manufactured, given an 8mm channel diameter.

Figure 5.41: Brown part with different diameter channels.

5. 7 Build Rate

Time is an important consideration when building a part. The building rate is an important parameter in selective laser sintering because it can gauge the lead-time associated with the process and the cost.

The algorithm to calculate the building time was created using Pascal language. The main steps of the program are presented in Figure 5.42. A copy of this program can be found in

Appendix B. The program starts by asking the user to enter the dimensions of the part (length, width, and height) to be processed, and also the SLS process parameters (scan speed, scan spacing, and layer thickness). The program defines a plane (slicing plane) and intersects it with the part geometry to obtain the 2D section.

The time to scan one track is calculated summing the displacement time (length/scan speed) and adding the delay time for each line. The line is then displaced by scan spacing in y direction and the routine is repeated. This procedure is repeated until the whole 2D section has been scanned. The slicing plane is then displaced by delay time in the +Z direction and the process starts again. This sequence is repeated until the top of the part is reached.

The program can also calculate the building time for a part with changing scan speeds for each layer.

By using the equations from 3.1 to 3.5 in Chapter three (section 3.2.3) it was found that the sintering time of 80×80×80 mm cubic block using DTM default settings is about 17.5 hours. Volpato [2001], reported that the difference of measured time and predicted time is very small (about 1.5%).

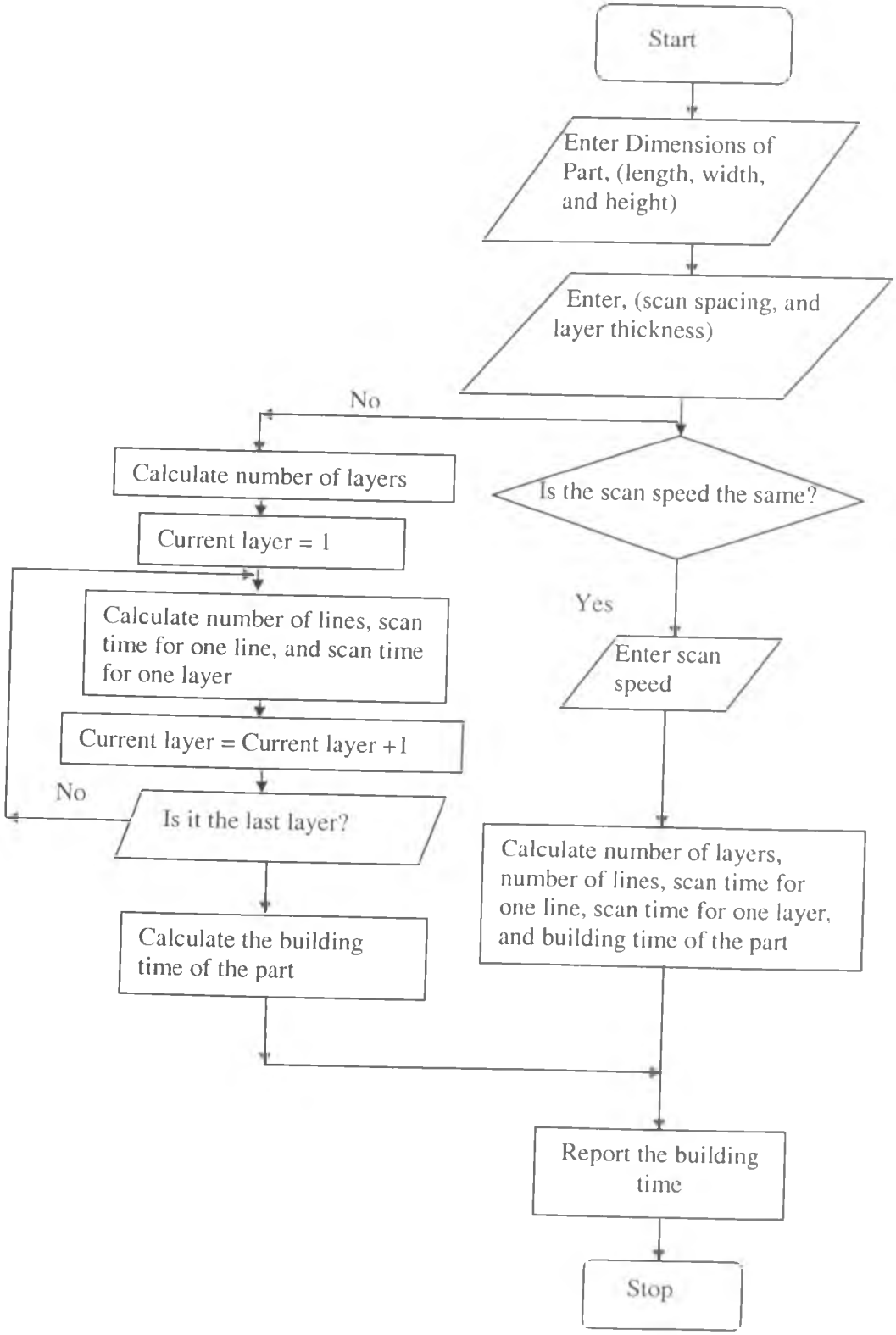

Figure 5.42: Flow chart of the Time Predictor algorithm

5.8 Microstructure of RapidSteel 2.0

The microstructure of sintered RapidSteel 2.0 without infiltration (brown part) is presented in Figure 5.43. This figure shows that the powder particles sinter together to build a skeleton of steel with a large amount of porosity. The sintering cycle was carried out at 1120°C for three hours by constant heating rate of 2°C min^{-1} and constant cool down rate 3°C min^{-1}. Very little dimensional changes of parts are observed between the green part and sintered part. As a result of the sintering cycle, the green body was partially sintered and consisted of an interconnected network of stainless steel particles with a distribution of precipitates as shown in Figure 5.44. Shrinkage during the sintering cycle, as shown in figure 5.40, is very small because the sintering was happened due to solid phase sintering. The porosity leads to low density (about 4.32 g/cm^3 or 57.47% of theoretical density), and poor tensile strength (about 30 MPa). The analysis of the RapidSteel 2.0 material under a microscope reveals spherical metal particles. The obtained sizes, measured along the larger dimension of the grains, were ranging from 20 to 55 μm in diameter. Figures 5.45 and 5.46 represent an image of a sample cut from one of the tensile test blocks, in this case in position B3 of a horizontally cut block. It can be seen from the figures that the sample still has internal porosity within the material because the sample is far from the bronze infiltration position. Also, it can be seen that the RapidSteel 2.0 material under a microscope reveals spherical metal particles located within a bronze matrix. On formation of a liquid phase of bronze, there is a rearrangement of particles to give a more effective packing. The driving force for densification is derived from the capillary pressure of the liquid phase located between the fine solid particles.

Two types of precipitates were found in the sample after sintering cycle and infiltration cycle using $30H_2$-$70N_2$ atmosphere. The precipitates were rich in Cr content, which suggest a rejection of Cr out of the stainless steel particles.

Table 5.12 presents a quantitative analysis of percentage compositions of infiltrated sample. The first type of precipitates was distributed within the stainless steel particles with a small size as shown in Figure 5.46. It had a composition of 71.32 Fe, 12.22 Cr, 11.28 Ni, 2.21 Mo, 1.55 Sn, 1.07 Cu, and 0.35Si (wt-%) as presented in Table 5.12. The second type of precipitate was larger, with a big size as shown in Figure 5.46. These were located near the edge of the stainless steel particles. The composition of the coarse precipitates was 11.47 Fe, 77.99 Cr, 0.64 Ni, 6.64 Mo, 1.53 Sn, 1.56 Cu, and 0.17 Si (wt-%) as presented in Table 5.12.

During the first sintering cycle, the burning out of the binder produces a free carbon source around the particles which reacts with Cr and Mo to form $M_{23}C_6$.

The quantitative analysis of percentage compositions of infiltrated sample revealed that these precipitates were rich in Cr and Mo and contained moderate amount of Fe and Ni. Formation of Cr_2N precipitates occurred as a result of interaction between the stainless steel particles and the N_2 containing atmosphere. If the cooling rate was not fast enough to trap the N_2 in the austenite solid solution, then the excess nitrogen tended to precipitate out as Cr_2N [Uzunsoy et al., 2002].

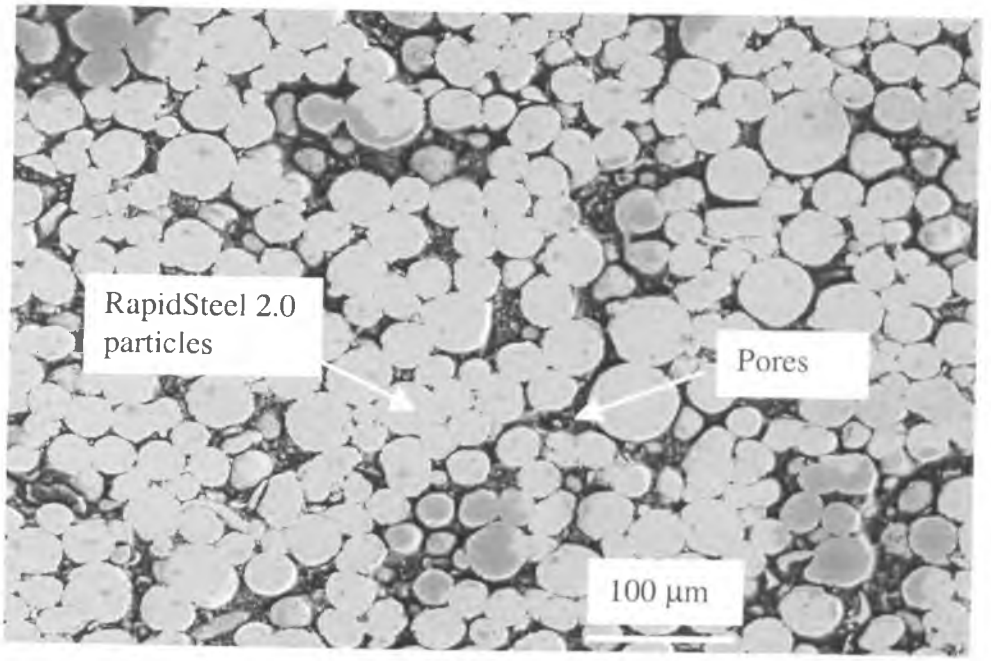

Figure 5.43: SEM micrograph of a sintered part of RapidSteel 2.0 material

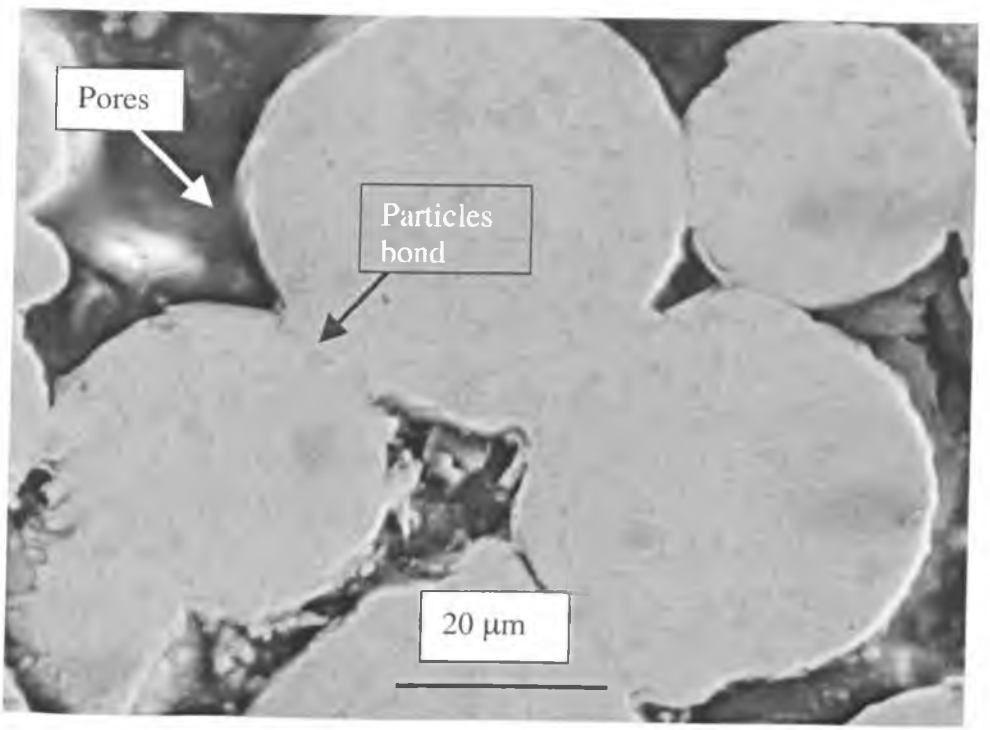

Figure 5.44: SEM of RapidSteel 2.0 material showing the bond between particles.

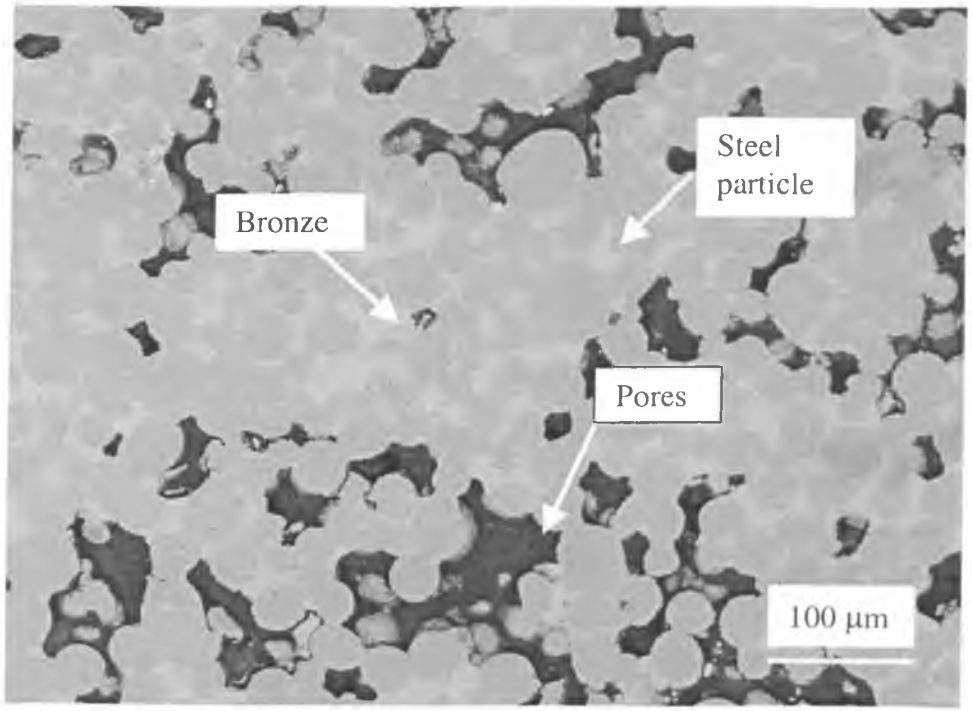

Figure 5.45: SEM of B3 sample cut horizontally

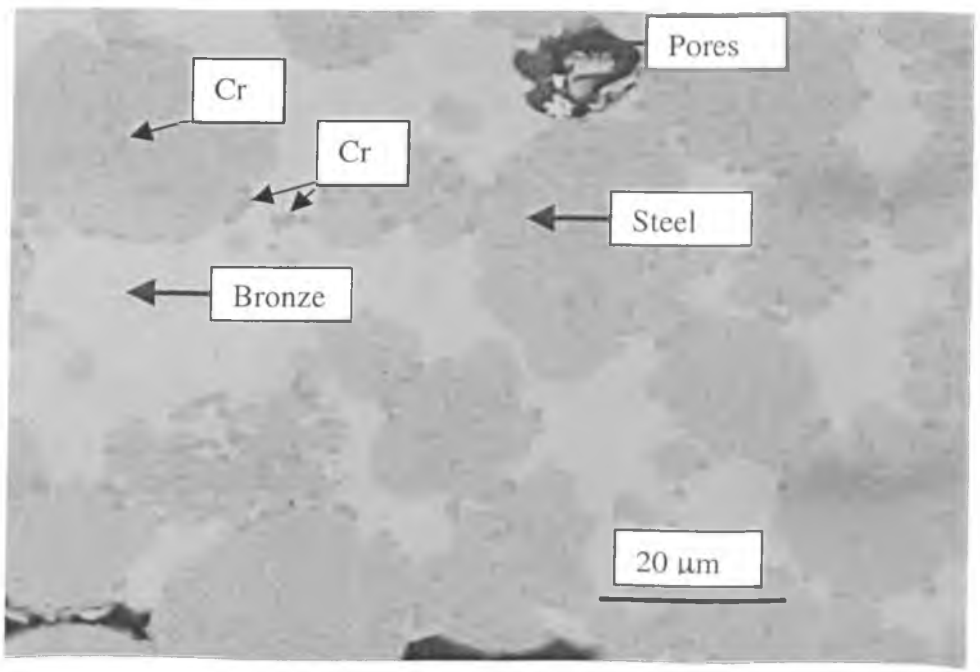

Figure 5.46: SEM of infiltrated sample cut horizontally

Table 5.12: Volumetric EDX analysis of infiltrated sample

Element	Weight %	Atomic %	Error
Si	0.35	0.71	0.011
Cr	12.22	13.27	0.088
Fe	71.32	72.17	0.275
Ni	11.28	10.86	0.140
Cu	1.07	0.95	0.50
Mo	2.21	1.30	0.042
Sn	1.55	0.74	0.039
Total	100.00		

Element	Weight %	Atomic %	Error
Si	0.17	0.34	0.008
Cr	77.99	82.01	0.257
Fe	11.47	11.23	0.124
Ni	0.64	0.59	0.036
Cu	1.56	1.34	0.066
Mo	6.64	3.78	0.077
Sn	1.53	0.70	0.042
Total	100.00		

Element	Weight %	Atomic %	Error
Si	0.09	0.21	0.006
Cr	0.88	1.10	0.024
Mn	1.78	2.11	0.037
Fe	2.27	2.65	0.044
Ni	3.23	3.59	0.068
Cu	83.50	85.70	.413
Mo	0.76	0.51	0.025
Sn	7.49	4.12	0.084
Total	100.00		

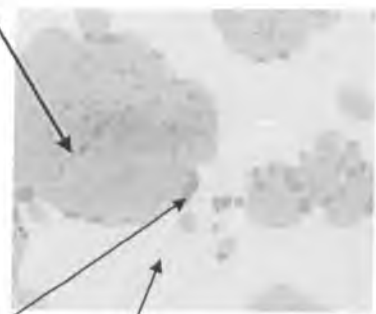

5.9 Summary

This chapter has presented the results of tests designed to characterise the mechanical properties (strength, ductility, and hardness), accuracy of small and large features, of the DTM RapidSteel process using a Sinterstation 2000, and RapidSteel 2.0 material. Also, this

chapter has presented the results of an analysis of building rate of the parts. In addition, the evolution of the microstructure of RapidSteel 2.0 has been described.

CHAPTER SIX

DIRECT SELECTIVE LASER SINTERING - EXPERIMENTAL PROCEDURES

6.1 Introduction

In order to make an assessment of direct laser sintering several different tasks had to be done. The first encompassed a number of SLS machine related tasks; including the development of a software program to perform several duties during machine set-up and scanning, and laser power calibration procedures.

The second task comprised single track melting experiments. Powder was melted by systematically tracing a series of single line scans in an argon atmosphere at different laser powers, scan speeds, and scan lengths. The third task was examining a series of single layer scans at different laser powers, scan speeds and scan spacings. The final task was to build multiple layer parts to measure the accuracy and the mechanical properties of the material.

6.2 Experimental Powder

In traditional sintering high temperatures are necessary to form the appropriate amount of liquid phase needed to attain full density [Wronski et al., 1988]. Several authors have investigated the role of alloying elements on sinterability of high speed steel powders. The processing or sintering window, which is defined as the range of temperatures over which acceptable microstructures and properties can be obtained, is narrow, ranging from 1-6 K

for M2 to at best 10-16 K for other alloys such as T1, T16, and T42 [Wright, et al., 1993]. Wright et al [1989, 1993, and 1999] have shown that the considerably different sintering characteristics of T1, M2, and M3/2 HSS can be correlated with phase diagrams. Particularly they have reported that the sintering window is to be found within the austenite (γ) + carbide (M_6C in T1 and M_6C + MC in M2 and M3/2) + liquid region. The upper and lower temperatures defining this austenite + carbide + liquid phase region for a given composition and how these vary with compositions are the major factors determining sintering behaviour. Knowing how the critical phase field of austenite + carbide + liquid varies with composition would aid greatly the development of new sinterable high-speed steel type alloys. Wright et al [1993] reported that this temperature gap was narrow for M2, 20 K, with a resultant sintering window of less than 6 K. Wright et al [1996] also reported that the optimum sintering temperature of standard T1 (0.8%C) was 1320°C and the sintering window 10 K, and increasing the carbon content to 1.4%C expanded the sintering window to about 40 K, with the optimum sintering temperature reduced to 1260°C. These correlations allow new sinterable tool steel compositions to be identified, provided phase diagrams can be established. Figure 6.1 shows the predicted calculated phase diagram for Fe-C-14Mo-4Cr system. The sintering curve for high-speed steel has the generic form shown in Figure 6.2. Sinterability can be defined in terms of T_{os}, the temperature at which the supersolidus liquid phase sintering is initiated, T_m, the temperature at which maximum density is first obtained, T_{opt}, the optimum sintering temperature, the sintering window (the range of temperatures over which acceptable macrostructures and properties are obtained), and T_d the compact distortion temperature. The absolute values of these temperatures

depend on alloy compositions. Several authors have investigated the role of alloying elements on sinterability of high-speed steels powders [Wright et al., 1989]. The value of T_m is 10-16 K higher than T_{os} and the length of the sintering plateau (T_m-T_d) is 20-30K (see Figure 6.3).

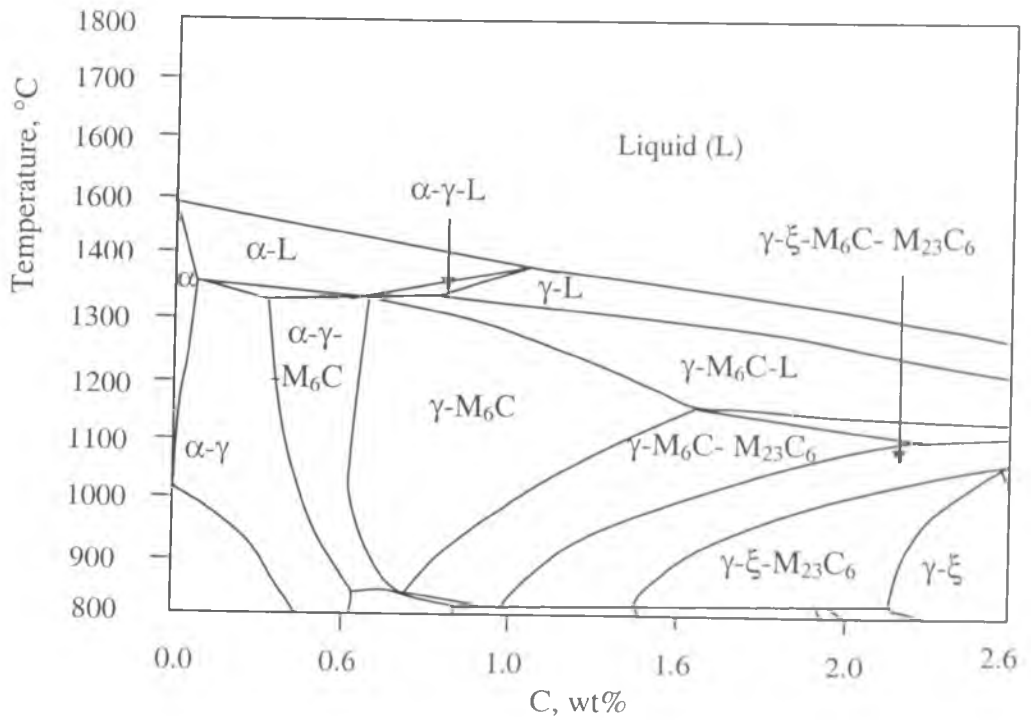

Figure 6.1: The calculated phase diagram for Fe-C-14Mo-4Cr system [Wright et al., 1999]

The powder used in this research was a gas atomised High-Speed Steel (HSS) alloy. The grade of HSS processed was chosen for its high solidus-liquidus range, which was considered to offer the greatest scope for appropriate process control in selective laser sintering. The chemical composition of the powder is given in Table 6.1. The powder was received from the supplier in one batch, with particle size distribution; 20μm < d > 75μm

(see Figure 6.4). This distribution was chosen because it is representative of a suitable particle sizes for direct SLS. The large portion of smaller particles in the powder providing an increased amount of liquid phase during sintering, since smaller particles need less energy to melt than larger particles. A further decrease in grain size of the powder was not possible due to an increased amount of agglomerations. Nui and Chang [2000] reported that powder with large particle sizes (>160 μm), and fine powder particles (<38 μm) was unsuitable for SLS due to the large pores of parts. Gas atomisation was the powder production method of choice because the particles that are formed are generally spherical in shape, have smooth surfaces and generally exhibit low surface oxidation. These characteristics allow for good powder flow properties and reduced levels of contamination prior to handling and processing.

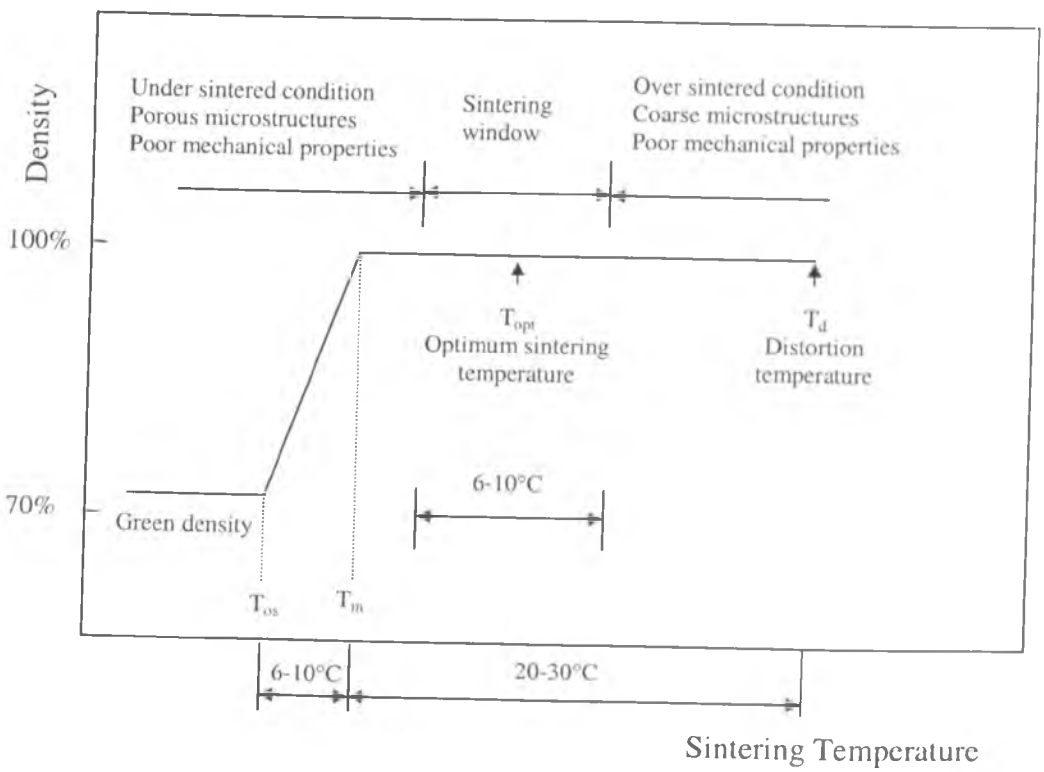

Figure 6.2: Schematic diagram illustrating the sintering window concept.

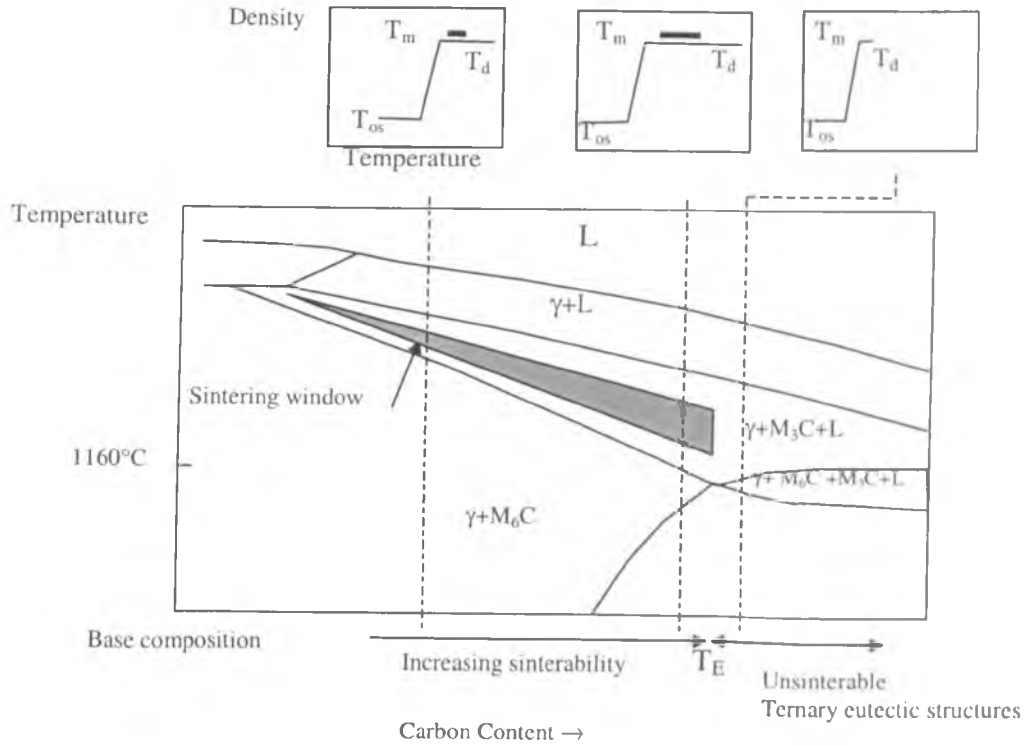

Figure 6.3: Schematic diagram illustrating relationship between alloy composition and sinterability.

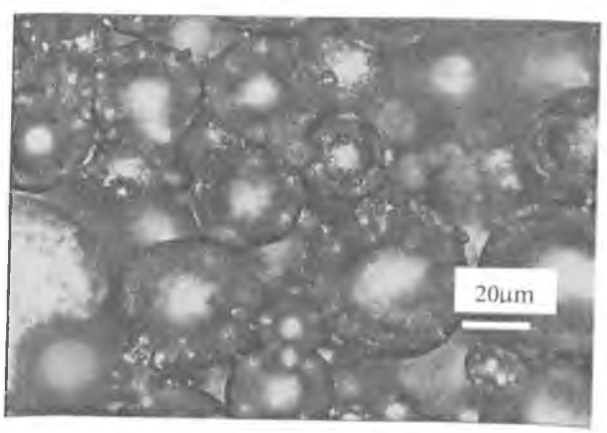

Figure 6.4: SEM of high speed steel powder.

Table 6.1: Composition of the experimental material.

Elements	Fe	Mo	Cr	C
Wt.%	Bal.	14.1	3.6	1.39

6.2.1 Storage and Use of the Powder

The powder was supplied in 5.3kg capacity self-sealing metallic container (see Figure 6.5 a). The batch was divided equally into ten parts, 0.5 kg each, and was stored in plastic containers (see Figure 6.5.b). To avoid contamination the powder was used only once. Used powder was sieved to remove solidified melt debris then stored. Previously used powder was used only for proving trials and machine calibration procedures.

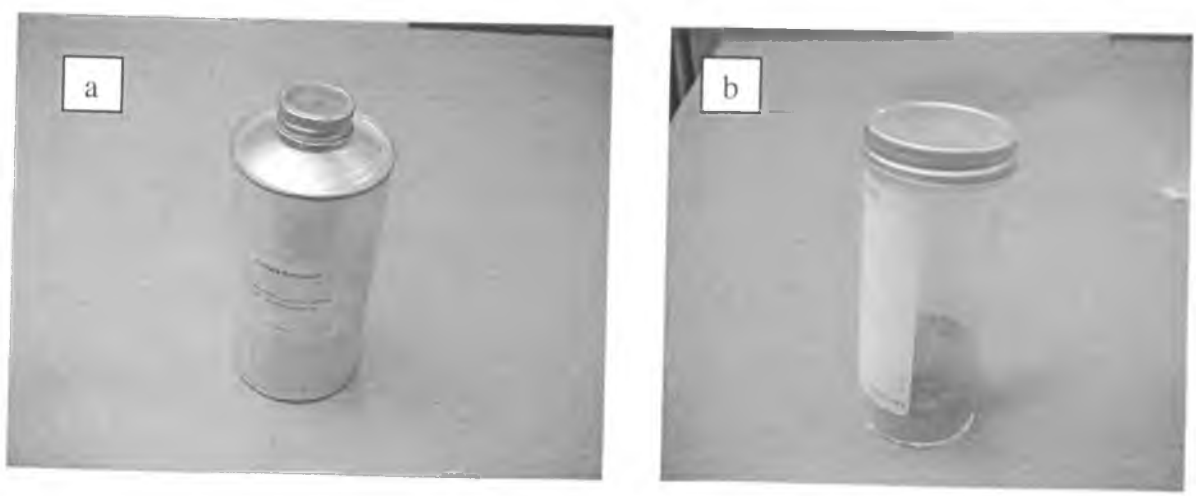

Figure 6.5: Powder containers, a) main container, and b) small container.

6.2.2 Preparation and Handling

The powder was used as received and therefore no attempts were completed to heat treat the powder, condition the powder by inert gas exposure or add fluxes or lubricants to the powder previous to its deposition and spreading in the build tray, and build zone.

Throughout the duration of this work the powder handling was kept to a minimum. There are two reasons for this protected approach. Firstly, to keep the reproducibility of data by preventive particle segregation and exposure during handling. Secondly, to reduce the adsorption of contaminants from the atmosphere. To attain these ends, the caps of storage containers were only opened when powder was required. The pouring height of the powder from the container into the build tray or the hopper was kept to a minimum to minimise exposure to air of the powder.

6.3 Experimental Equipments

6.3.1 Selective Laser Sintering Machine

All experimental work reported in this chapter was carried out using a research SLS machine. This machine was constructed at the University of Leeds. Figure 6.6 shows a schematic diagram of the principle subsystems of the SLS research machine, and Figure 6.7 shows a photograph of the equipment. A preliminary explanation of how an SLS machine works is given in Chapter 2 (see section 2.3).

Mainly the machine consisted of four subsystems; the laser and focusing optics, the X-Y scan head, the build chamber and finally the motion control table [Hauser 2002]. The

control unit was placed around a Pentium PC running X-Y scan head driver and calibration software (PC-Mark MT and Postgrid), motion control software for the positioning table (Talk2bus) and software (L-Scan) written specifically for this research to configure system level commands and to create HPGL (Hewlett Packard Graphics Language) data files based on user requirements. These files were used to direct the movement of the mirrors in the X-Y scan head and to toggle and modulate the laser power output during scanning [Hauser 2002].

6.3.2 Laser and Focussing Optics

The type of laser used in this machine was a SYNRAD 240 Watt "Duo - Lase®" CO_2 Laser emitting an infrared beam. The wavelength of the laser is 10.6μm. The head of the laser and its control software and hardware was supplied by Laser Lines (Banbury, UK). The laser head consisted of two series 125W laser tubes. Each tube is controlled by a water cooled solid state power supply, each delivering 1400W through two cables to the laser head. Both tubes feed an optical beam combiner within the laser head. The beam combiner gives a maximum output power of 250W. The laser was water cooled by a closed loop NESLAB CFT-300 re-circulating chiller unit [Hauser 2002].

At the laser head opening the beam diameter was 4.4mm. A beam expander supplied by V&S Scientific Ltd (London, UK), located at a distance of 350mm from the laser opening, was used to focus the propagating beam onto the powder bed surface. The spot size was 1.1mm at the powder bed surface (a distance of 850mm from the laser output opening

including passage through mirrors) [Hauser 2002]. This parameter was fixed during the period of the experimental work.

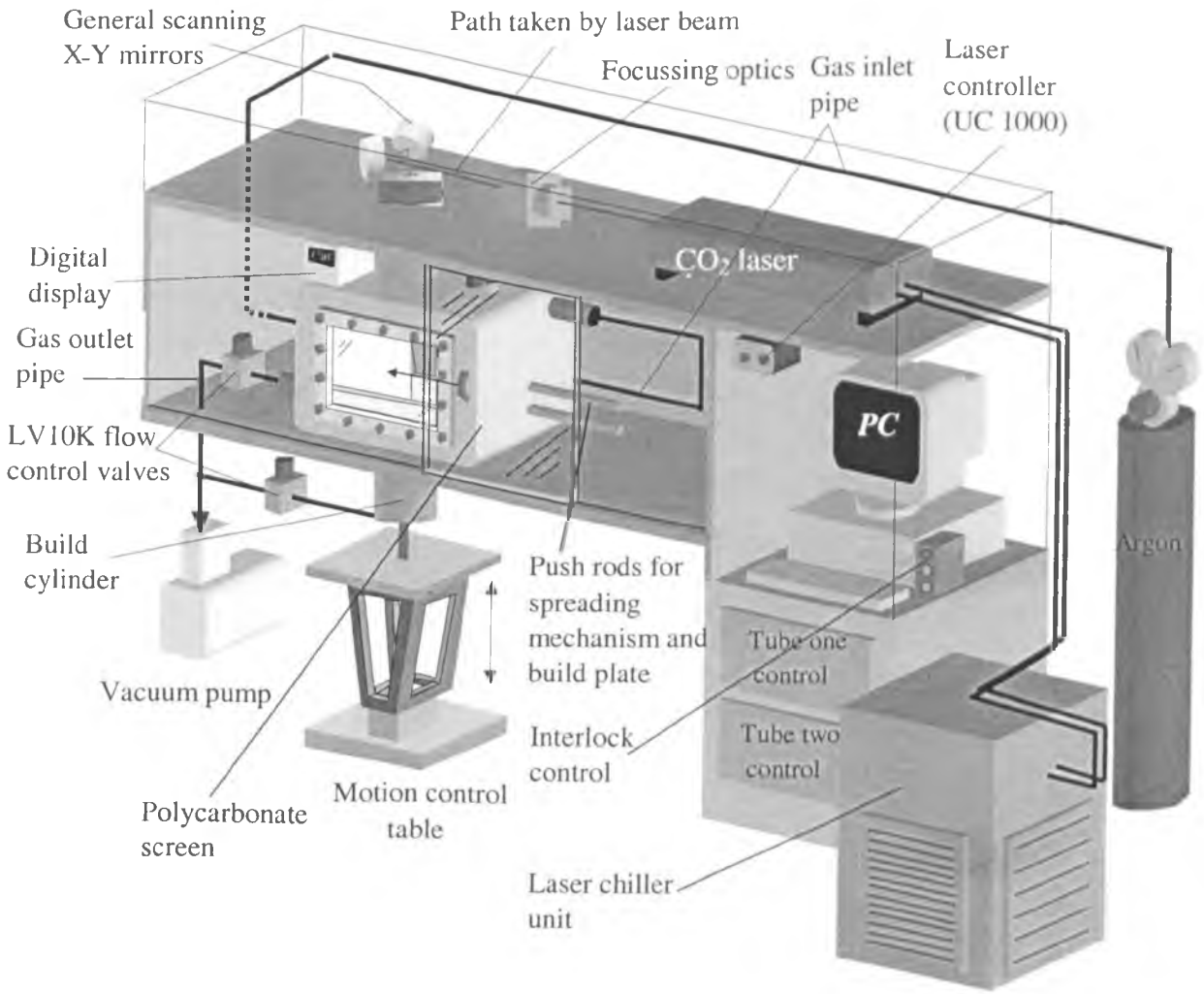

Figure 6.6: Schematic diagram showing the principle subsystems of the SLS research machine [Hauser 2002]

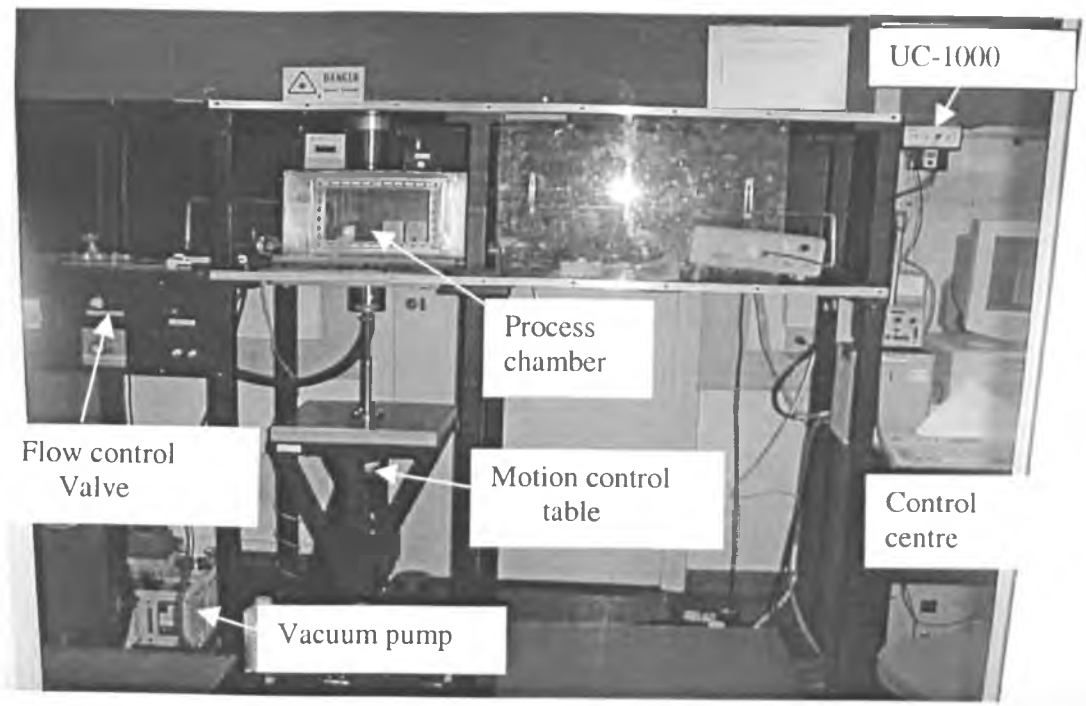

Figure 6.7: Photograph showing the SLS apparatus used to melt powders in this study

The laser power was controlled either by computer or manually. The main advantage of computer control that it allowed for faster processing cycle times, but only eight different laser power settings could be defined for a given scanning routine and only manual control route was used in this work. Manual control was by duty cycle modulation in the 3000 Hz to 20000 Hz range. This was achieved by using a Synrad UC-1000; a universal laser controller which was modified to house a potentiometer with a 1000 division numerical counter. This potentiometer was used to control the laser output power and was more accurate than the supplied potentiometer mounted on the front panel of the UC-1000. Figure 6.8 shows a photograph of UC-1000 laser controller.

Computerisation of the laser power was achieved by supplying the remote voltage control input on the UC-1000 controller with an analogue voltage signal (0 – 10VDC). An external 10VDC power pack and modulator was used to give the signal, via the HC/2 hardware using markers in the HPGL files(s) and the mark parameter settings in the PC-Mark MT software. The mark parameter settings allow for eighteen different laser head and X-Y scan head parameters to be configured. The power setting parameter required a numerical value to be inputted between 0 and 255 bytes [Hauser 2002].

The type of scan head used to direct the laser beam over the powder bed surface is G326DT supplied by General Scanning Inc (Banbury, UK). The mirrors within the scan head are placed orthogonal to each other see Figure 6.9. The lower mirror produces the X scan and the larger upper mirror reflects the X axis in the Y direction, producing the Y axis beam. As the beam passes through the mirrors it translates through 90° and onto the powder bed surface. The movements of both mirrors are controlled by limited rotation closed loop galvanometers which are hard wired to a Digital Scanner Controller (DSC) [Hauser 2002].

Figure 6.8: Photograph showing the UC-1000 laser controller with the additional potentiometer and numerical counter

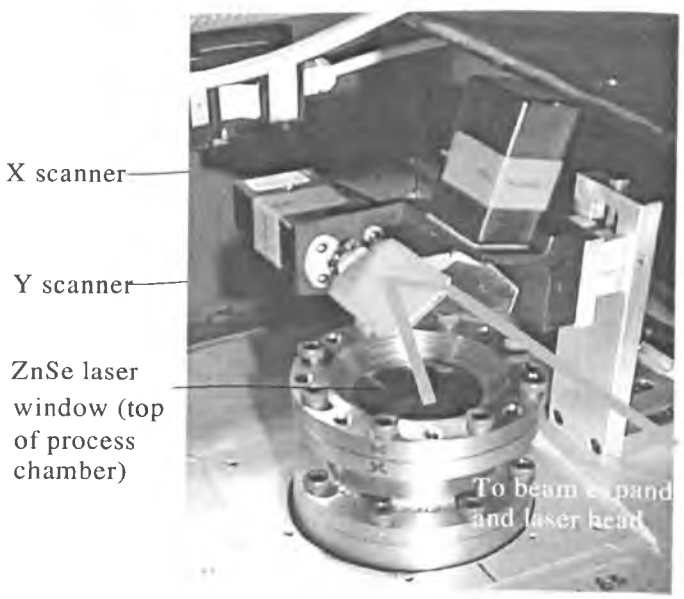

Figure 6.9: Photograph showing the X-Y scan head. The green line shows the path of the laser through the head [Hauser 2002]

6.3.3 Process Chamber and Powder Handling Equipment

The process chamber as shown in Figure 6.10 consisted of four elements; the build chamber, the build cylinder, the powder handling equipment and the build tray [Hauser 2002].

A- Build Chamber

The build chamber is 460mm long, 260mm high and 260mm deep. This cavity housed the powder handling apparatus and two build areas: the build zone and the build tray. A doorway was machined into the front wall of the chamber to give admission to the powder handling equipment and both build areas. The dimensions of the doorway are 260mm long and 160 mm high. During operation an access plate fitted with a polycarbonate viewing window and sealing ring was located over the doorway and secured and sealed to the chamber. To give access to the build cylinder and piston unit a 76mm diameter hole was machined into the base plate of the build chamber. Through an identical hole machined into the roof of the build chamber the laser beam entered the build chamber. A 180mm long stainless steel cylinder with flanged ends, a wall thickness of 6.0mm and an inner diameter of 76mm was located on the outside of the chamber roof and was sealed around the upper hole using twelve M8 cap head bolts. The open end of the assembly was capped and sealed using a flanged collar which housed a Zinc/Selenium laser window. The window was sealed into the collar using rubber o-rings. Inert gas entering the build chamber was regulated using a flow control valve. The exhaust flow was regulated using a vacuum pump and a fine leak control valve, both supplied by Edwards High Vacuum International

(Sussex, UK). An Edwards pressure sensor connected to an Edwards active digital display unit was used to monitor the pressure inside the chamber [Hauser 2002].

B- Build Cylinder

The main functions of build cylinder are to house the piston assembly, and to store the deposited powder and the sintered component during multiple layer construction. The cylinder comprised of a 160mm long stainless steel cylinder with a bore ground to a diameter of 76mm. The wall thickness of the cylinder was 6.0mm. A stainless steel flange was welded to the cylinder at one end. The flange was located and sealed to a machined surface on the underside of the build chamber base plate using eight M8 cap head bolts. The other end of the cylinder was sealed using a threaded end cap and vacuum seal. The end cap was fitted with a gas outlet pipe which was connected via a fine leak control valve to the vacuum pump. The end cap also housed a sealed linear bearing, located axially, which positioned the connecting rod which linked the motion control table to the piston head. The piston head, onto which the powder was deposited, consisted of a conical stainless steel shell. The inert gas can be drawn from the build chamber, through the piston head assembly, and exhausted through the outlet pipe located in the end cap of the build cylinder [Hauser 2002].

C- Build Tray

The tray consisted of a 170mm x 140mm x 10.0mm thick stainless steel plate with a machined pocket of dimensions 140mm x 130mm x 7.0mm deep, into which the powder was deposited and levelled prior to the plates insertion into the build chamber. Four flanged wheels fixed to the plate located the tray onto the upper level of the parallel runners housed

within the build chamber. Once environmental conditions were established inside the chamber the plate could be traversed across the exposure area to maximise the effective powder layer area. The linear movement of the tray was achieved by a push rod which exited through the wall of the build chamber via a vacuum sealed brass fitting [Hauser 2002].

D- Motion Control Table

A single axis positioning system supplied by Naples Coombe Ltd (Chaddleworth, UK) was used to control the depth change of the powder bed within the process. The equipment was centred around an NC2000 series linear translation stage able to index a load of 160Kg over a vertical distance of 260mm while maintaining a guaranteed accuracy of 0.2mm per 100mm of travel. The stage was driven by a gearbox (5:1 reduction) and servo motor while an encoder (accuracy 0.01mm) tracked the position of the stage. Attached to the stage was a 400mm x 400mm mounting platform with an array of M6 inserts onto which was mounted the connecting rod which formed a rigid link between the stage and the piston head. This translation stage was driven by a PC based single axis DMC 1010 motion control card and a Galil DMC 1010 rack mountable enclosure housing a AMC 12A8 brushed servo amplifier. A DOS based software programme, called talk2bus, was used to control the table [Hauser 2002].

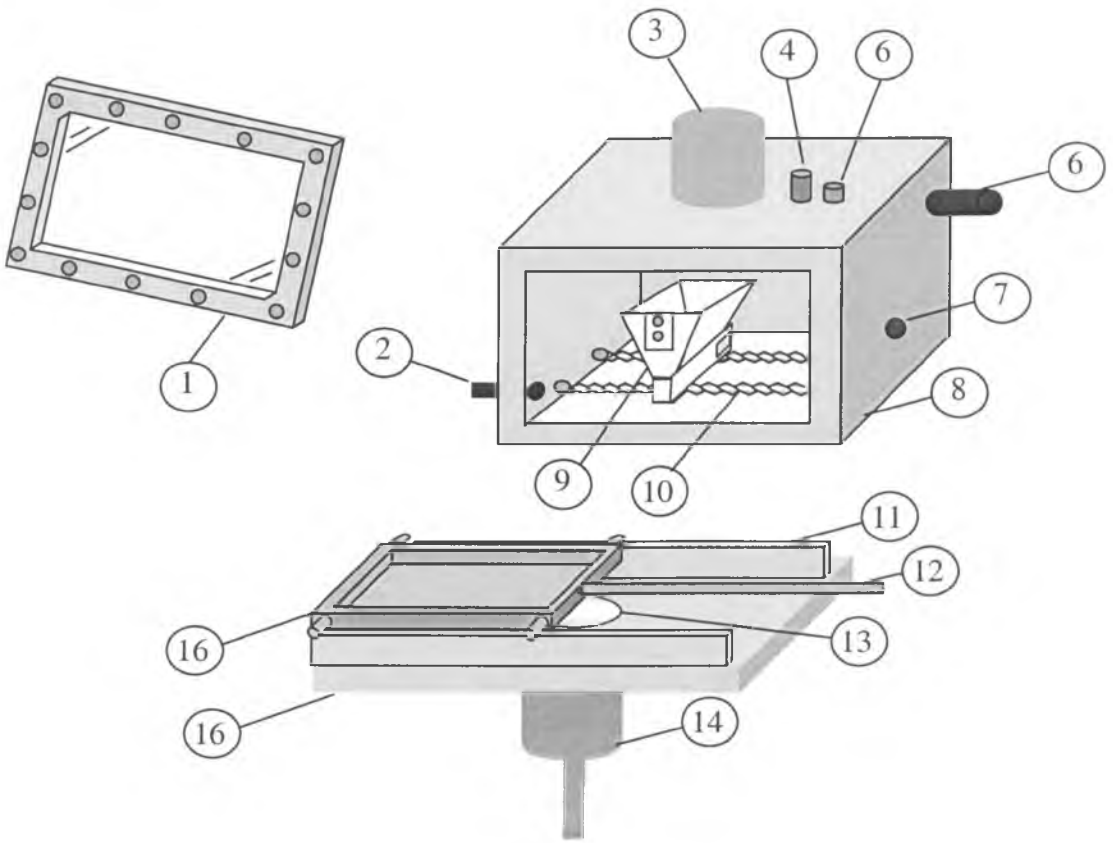

1. Viewing window
2 Gas outlet
3 Laser beam
4 Pressure sensor
6 Powder inlet
6 Gas inlet
7 Push rod hole
8 Build chamber
9. Powder hopper
10 Screw
11 Parallel runners
12 Push rod
13 Build zone
14 Build cylinder
16 Base plate
16 Build plate

Figure 6.10: Schematic diagram of the process chamber

6.4 Software and the Scanning Procedure

Borland Pascal v7.0 was used to write and compile a L-Scan software programme. This programme was designed to aid in the operation of the laser and X-Y scan head. The first task of the programme was to compile and output HPGL graphic files, which describe 2D raster pattern geometries, based on constraints inputted by the user. The second programme requirement was the automatic generation of system parameter files to switch system parameter settings to automate the recalibration of the X-Y scan head when refocusing the laser between the build plate and the build zone.

All raster scanning procedures implemented in the experimental works described in this chapter were created by traversing the laser beam in a forward and back way in the x direction producing a coupon of predefined dimension in the x and y directions. During step over in the y direction and 45° direction, the programming of PC-Mark MT enabled the laser to be automatically switched to limit the build up of heat at the start and end of each scanned vector.

HPGL is a language which can be easily written and read. However, the production of a number of single layer coupons as a series of parameter arrays in one build cycle will enable easy comparison of the effects of the processing conditions, but will result in a very large string of commands within the HPGL file. HPGL was designed for use with HP pen plotters and contains a number of instructions, for example, to move the selected pen to x-y coordinates (PRx,y;), to raise and lower the selected pen (PD; and PU;) and to select up to eight different pen colours (SP1 through 8;). These same commands can be translated by PC-Mark MT to move the mirrors, toggle the output from the laser head and define up to

eight different laser power settings within a single HPGL file respectively [Hauser 2002]. L-Scan proved successful at speeding up both the construction and generation of such HPGL data files.

The offset is equal to the radius of the laser beam. Scan length accuracy was important for scan speed calibration procedures. As the beam scans using its centre as the reference point, excess material at the ends of each scanned line will melt and effect the dimensional accuracy. To compensate for this error, twice the beam offset needs to be subtracted from the scan length. L-Scan automatically configured the HPGL file(s) to compensate for this over sizing effect [Hauser 2002].

The second requirement of L-Scan was the automatic selection then transfer of the correct laser scanning configuration file (default.asc) from holding directories within the PC's hard drive to the PC-Mark MT directory when changing between build areas (zone or plate). Each file contains machine specific information about the dimensions of the build area and the distance between the scan head and the chosen build area (working distance). These file changes were required to maintain dimensional accuracy and mark speed accuracy when moving between build areas. The .asc files were generated using Postgrid [Hauser 2002]

6.4.1 Laser Power Calibration

A calibration was performed for the laser power output using a laser power probe with a ±6% accuracy over 600W. The probe was supplied by L.G. Products Ltd (Slough, UK). The power of the laser was measured by placing the heat sink of the power probe into the path of the laser beam at a position approximately 160mm above the build zone. This position was not critical provided it was at a location sufficiently away from the focal point

of the laser. At the focal point the high heat intensities could damage the surface coating on the heat sink, compromising the accuracy of the probe.

The probe was exposed to the stationary beam for a period of 20 seconds, removed, then left for a further 16 seconds before taking the reading. The reading was then multiplied by a factory set calibration factor of 1.032 to ensure a ± 6% accuracy. Between all measurements, the UC-1000 controller was left in 'standby' mode. This mode supplied a tickle or pulse (every 1μ sec) below the lasing threshold to maintain the plasma in the lasing tubes in an ionised state, allowing positive laser switching; therefore eliminating the need for a warm up period. Figure 6.11 shows the calibration curve for manual laser power modulation.

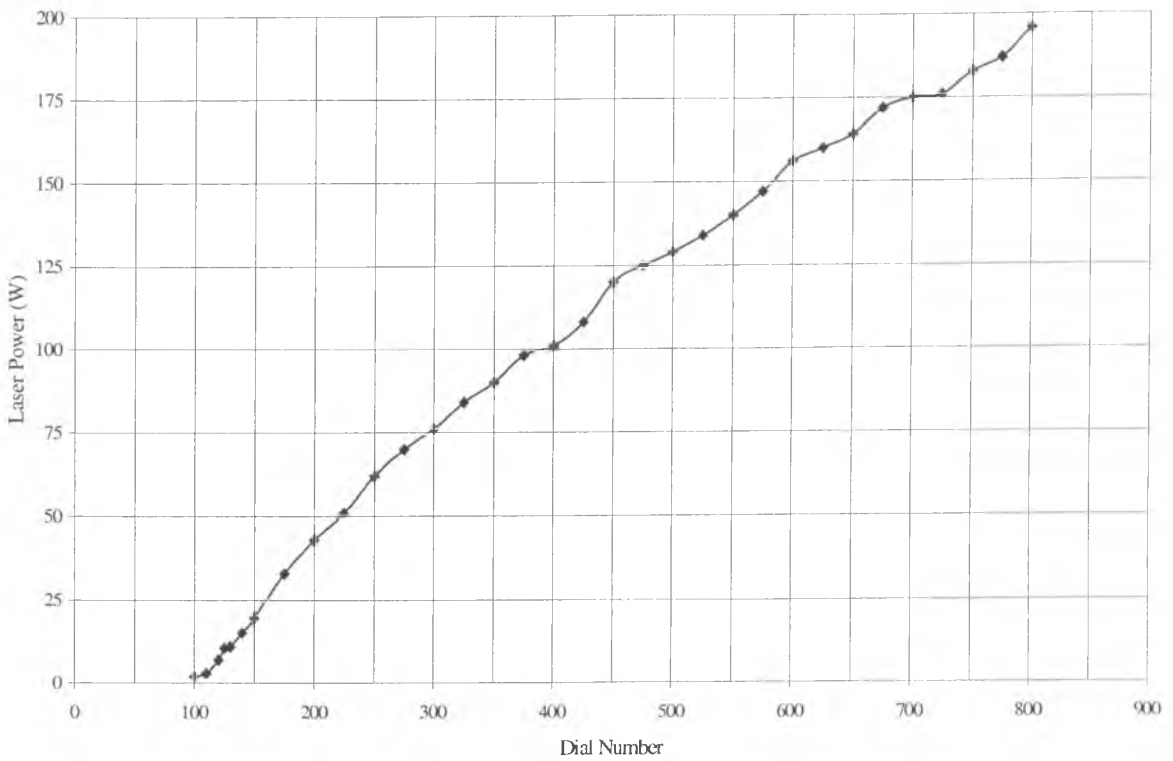

Figure 6.11: Calibration graph for manual laser power modulation

6.5 Experimental Procedure

All tests were carried out using an argon atmosphere, one batch of high speed steel powder (environmental conditions are described in section 6.6.2 and the powder characteristics and composition of the batch is described in section 6.2) and a range of laser scanning conditions.

6.5.1 Scanning Conditions of Single Lines

In order to produce single layers by the direct SLS process, it is first necessary to understand the interactions of the laser and material and to optimise the parameters for the production of single lines. A simple unidirectional traverse was used to mark a series of tracks of 12 mm length in the deposited powder layer (see Figure 6.12). The scan speed was varied from 1mm/s to 60mm/s and the laser power was varied from 10W to 150W. The specific conditions are shown in Figure 6.12.

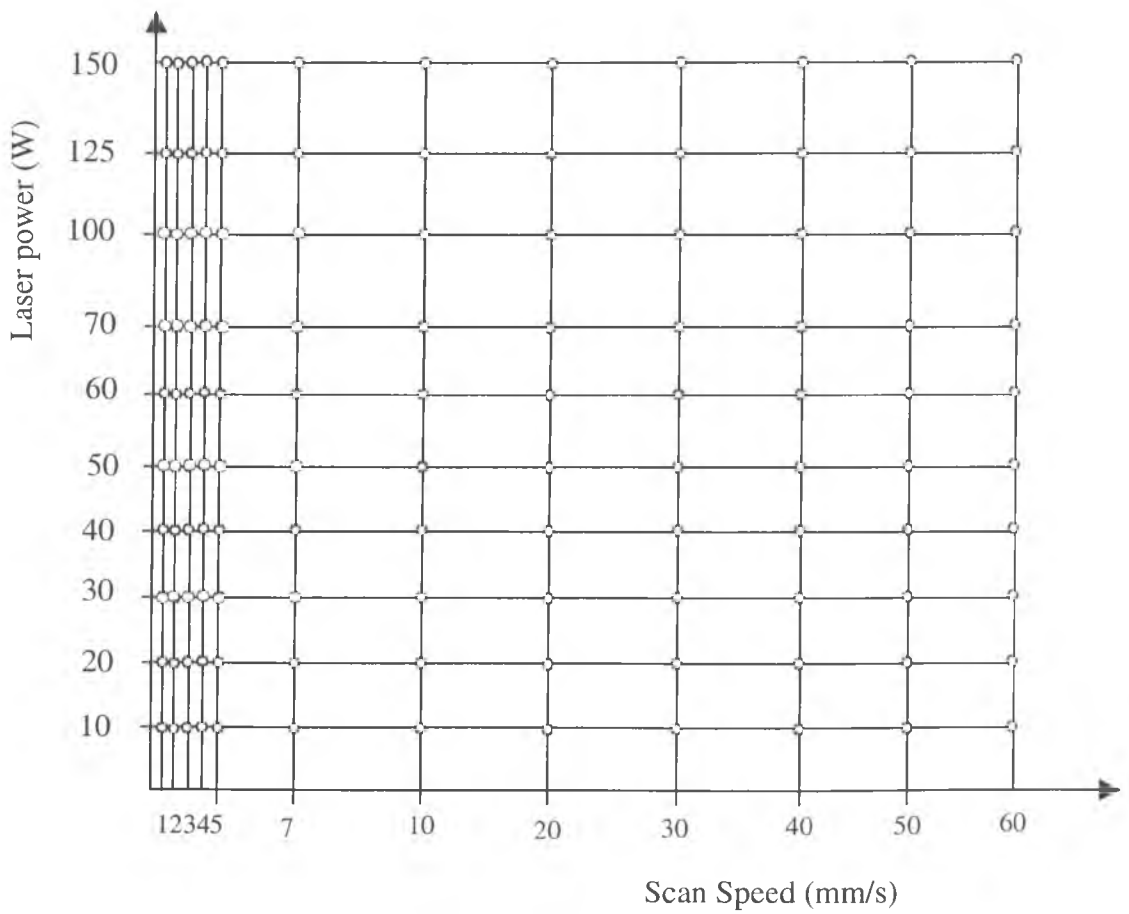

Figure 6.12: Chart showing the scanning conditions used during the experimental works

The length of the tracks were also varied from 5mm to 55 mm in x direction (in steps of 5mm), in order to observe the effects of scan length on melt behaviour. In addition, single lines in the y direction were also made (from 5 mm to 50 mm, in steps of 5mm) using laser power 50W and scan speed 1mm/s The spacing between each track (centre to centre) was assigned a value of 5 mm throughout all testing to ensure no interaction between neighbouring melt tracks. A one minute cooling down period was also enforced between the laser off command at the end of one track to the laser on command at the start of another to minimise the potential effects of changes in powder bed temperature caused by a localised heat affected zone. Finally, a minimum powder layer thickness of 7 mm was also employed during all single layer experiments to ensure that the melt volume was not influenced by or interacted with the top of the piston head or the base plate material of the build tray.

Tracks produced at conditions represented by the nodes were used for dimensional measurement and for testing the repeatability and reproducibility of results.

6.5.2 Scanning Conditions of Single Layer and Multiple Layer Parts

In order to produce multiple layers by the direct SLS process, it is first necessary to understand the interactions of the laser and material and to optimise the parameters for the production of single layers. Trials were performed on a loose powder bed of arbitrary depth, 7mm. The programming of the scanning enabled parameter matrices to be produced by varying laser power, scan speed, and scan spacing variables. A full study of all process variables was undertaken to obtain a complete understanding of the variable interactions.

Monolayers with dimensions 30×25mm were sintered with the laser scanning parallel with the longest axis, and at 45° to the axis as shown in Figure 6.13 a and b. Also monolayer with one direction path was built see Figure 6.13 c. Monolayers with perimeter scanning before and after internal scanning were produced (see Figure 6.13 d). Finally, monolayers with zigzag strategy were also produced as shown in Figure 6.13 (e). The range of parameter values is shown in Table 6.2. Figure 6.14 shows the direction of laser raster for multiple layer samples. A copy of the program to build different shapes can be found in Appendix C.

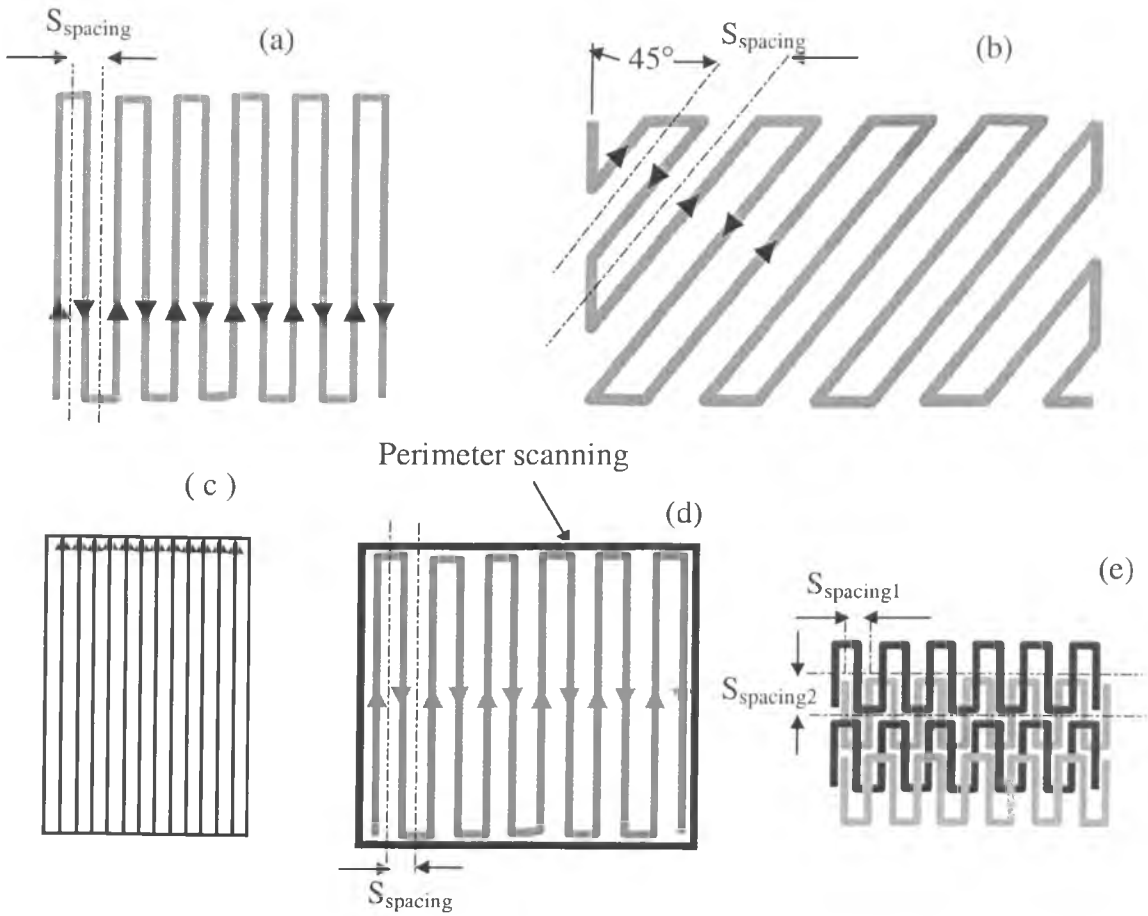

Figure 6.13: Strategy of sample manufacture

Table 6.2 Process parameter ranges for monolayer

Parameter	Minimum	Maximum
Power P (W)	15	100
Scan speed (mm/s)	1	5
Scan spacing (mm)	0.165	0.825
Beam diameter (mm)	1.1	1.1

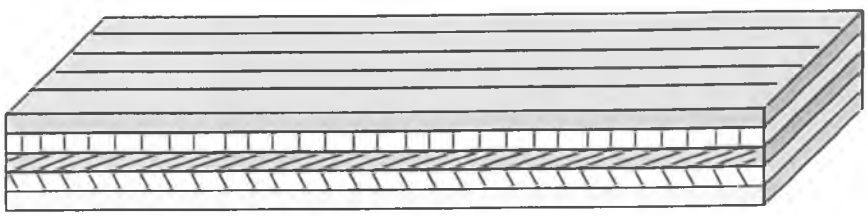

Figure 6.14: The scanning direction of multiple layer sample

6.5.3 Environmental Conditions

The atmosphere used in the experimental work in this chapter was argon. The argon rich atmosphere was achieved by a combination of build chamber evacuation (to approximately 50mbar gauge pressure) followed by an argon gas purge until local atmospheric pressure was re-established. This procedure was repeated twice before balancing the flow rate of argon through the build chamber at a slight overpressure (50mbar). Because no flow gauges were available, to maintain consistency the flow rate was balanced at the maximum pumping speed of the vacuum pump. The inlet flow from the gas bottle was regulated using

the LV10K flow control valve connected to the outlet flow of the build chamber. Flow from the build cylinder remained closed at all times.

Once the flow rate through the build chamber was balanced the build chamber was left for at least a 15 minute settling period before laser exposure. These conditions were maintained throughout the duration of each experimental test and during a 5 minute cooling down period at the end. The total cycle time for build chamber conditioning prior to laser exposure was about 30 minutes. The argon was supplied by BOC and was bottled with a 99.9% purity. Trace elements of other gases, particularly oxygen, are still likely to reside within the build chamber.

6.5.4 Dimensional Measurement

All dimensional measurements were carried out in the x, y and z directions of single tracks, single layer, and multiple layer, produced at different scanning parameter settings. The equipment used for dimensional measurement were a digital vernier calliper with accuracy 0.01 mm and an optical microscope.

Dimensional measurement of melt tracks, monolayers, and multiple layer using electronic calliper was carried out in three steps. The first step was measurement of scan length in the x direction X_1 for single line, and X_1 X_2 X_3 and X_4 for monolayer and multiple layer. Measurement was then continued by measuring the depth in the z direction. Ten measurements from each side were taken, Z_1, Z_2, ... to Z_{10}, and an average value was obtained. The final step was measurement of the track width, monolayer width, and

multiple layer width in the y direction. Ten positions were selected to be measured, at the middle and at the ends. The positions of each are numbered Y_1, Y_2, to Y_{10}. The average width was then obtained and recorded by summing up these values then dividing it by ten. The same procedure was used to measure the single layers and multiple layer samples.

6.5.5 Mass Measurement and Density Calculations

The density proved difficult to calculate accurately due to the complex shape and open porosity of single tracks. As an alternative assessment, the approximate mass per unit length was calculated by dividing the mass of each track by its length.

6.5.6 Post-Processing

6.5.6.1 Vacuum Sintering Infiltration Cycle

A laboratory scale alumina ceramic tube vacuum furnace was used for vacuum sintering. The multiple layer samples were held in the hot zone of the furnace controlled to ±1°C with the aid of Pt/13%Rh-Pt thermocouples. Heating commenced when the vacuum level reached 10^{-5} mbar. Samples were heated at a rate of 10 K min^{-1} to sintering temperature (1250°C), held for one hour, then furnace cooled to room temperature. Controlled cooling was a pre-requisite to prevent cracking of the alumina tube installed in the furnace.

6.5.6.2 Infiltration

The infiltration cycle of some monolayer samples and multiple layer samples was carried out using the Carbolite furnace from Carbolite Furnaces Ltd, which is a bottom loading

hearth furnace, with sand seal (zirconia). The furnace control allows a temperature-time cycle to be run via a program, such that the conditions required by the RapidTool process (Table 6.3) can be followed, as discussed in detail in a previous chapter, see section 4.3.2. The bronze was used as infiltration metal for the following reasons; (1) bronze melting point is lower than the melting point of high speed steel, (2) hardness, heat conductivity, and machinability are good, and (3) wettability to the high speed steel is good.

Table 6.3 Post-processing conditions

Action	Conditions
Heating up rate (^{o}C/hour)	120
Processing temperature (^{o}C)	1060
Holding time (hours)	3
Cooling down rate (^{o}C/hour)	180
Atmosphere	30% hydrogen and 70% nitrogen

6.5.7 Mechanical Testing

6.5.7.1 Bending Test

For the evaluation of the flexural strength and flexural modulus of the sintered specimens (monolayer samples and multiple layer samples) using direct SLS process a four-point bending test was performed using a Dartec Universal Testing machine (Dartec, Stourbridge, West Midlands, DY98SH, UK).

A four point bending test has its own advantages for characterising the mechanical properties of materials in comparison with other commonly used mechanical test methods such as tension and torsion. Firstly, it produces a uniform moment between the two inner loading rollers in the sample which gives rise to uniform tensile stress in the sample surface. Secondly, no special sample gripping is needed for the four point bend test, which makes it possible to test brittle materials in both tension and compression and makes sample preparation relatively simple since a specimen with a uniform rectangular cross-section is usually used in the test.

The load was applied at a rate of 0.05 mm/s. The geometry of the test is shown in Figure 6.15 where h = specimen height, b = specimen width, L = span, a = distance from support to the load, and F = load. The testing specimens had the dimension 30×25×1.1 mm for monolayer samples, and 30×5×3 mm for multiple layer samples. Four point bending tests were also performed for mild steel samples with the same dimensions, 30×25×1.1 mm and 30×5×3 mm. A plot of the load Vs deflection was displayed on the Dartec's connecting computer screen which in turn was printed out.

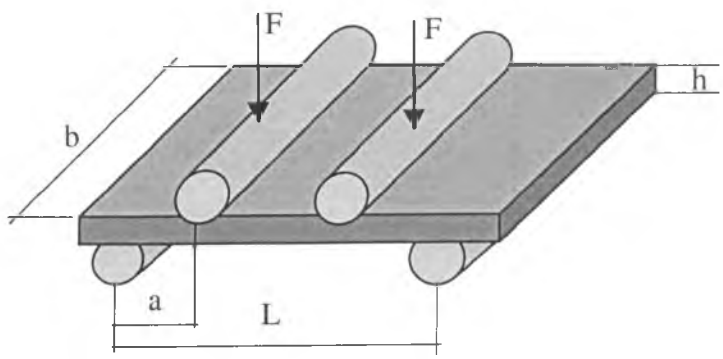

Figure 6.15: Schematic of four-point bend test

The *flexural strength* describes the material's strength:

$$\text{Flexural strength} = \frac{FL}{bh^2} \qquad 6.1$$

The results of the bend test are similar to the stress-strain curves; however, the stress is plotted versus deflection rather than versus strain.

The modulus of elasticity in bending, or the *flexural modulus*, is calculated in the elastic region.

$$\text{Flexural modulus} = \frac{L^3 F}{8bh^3 \delta} \qquad 6.2$$

where δ is the deflection of the beam when a force F is applied.

6.5.7.2 Tensile Test and Hardness

The same procedures used to determine the hardness and the tensile strength of RapidSteel 2.0 were used to determine the hardness and strength of the high speed steel material, see chapter four, sections 4.4.1, and 4.4.2.

6.5.8 Sample Preparation for Microscopy Inspection

6.5.8.1 Single Layer and Multiple Layer Samples

Single layer samples and multiple layer samples were sectioned parallel to the direction of scan. The samples were cut using a Actum 6 (Struers) equipped with a 355CA cutting wheel containing HV 600 grit. The cut specimens were mounted in Bakelite then lapped

with progressively finer grit papers. The specimens were then polished and etched as outlined in section 4.5.1.4.1.

Specimens were etched by placing the specimens face down in Marbles Reagent (10g copper sulphate, 50ml HCL (35%) and 50ml distilled water) for a period of 30 seconds.

6.6 Summary

This chapter has outlined the experimental procedures, which will be used to characterise the mechanical properties, density, accuracy and surface finish, and microstructure of direct SLS process examined using a high power CO_2 laser sinterstation machine and a particular grade of high-speed steel material. The results arising from the application of these procedures are presented in the following chapter.

CHAPTER SEVEN

RESULTS AND DISCUSSION OF DIRECT SLS

7.1. Introduction

This chapter firstly discusses the experimental results for single line melt tests using different scan speed and laser power created by traversing the laser source along a single line within an argon atmosphere. These results fall into separate sections, as following: the effects of scan speed and laser power on heating and melting, warping of single lines and the accuracy of single line at constant scan speed and laser power. The building of monolayers using different scan speeds, scan spacing, and laser powers are presented in the second section followed by the building of multiple layer components using different laser powers, scan speeds, scan spacing and layer thickness. The mechanical properties are discussed in section 7.6 followed by a description of the microstructure of samples. The accuracy of the parts is discussed in section 7.8 followed by an examination of the building rate. Then, the chapter is concluded with a brief summary.

7.2 Single Line Melt Tests Using Different Scan Speed and Laser Power

7.2.1 The Effects of Scan Speed and Laser Power

The results obtained from observing changes in the heating and melting behaviour of the powder during changes in the intensity of the incident energy source as a result of change laser power or scan speed describe in this section. The subject of scan speed and

laser power and their effects on heating and melting will be dealt with in this section. Also, the analysis of melt pool morphologies from good quality melt pools will be discussed in detail. Good quality, in this case, refers to a continuous melt pool.

The results of single lines presented as a series of process map, which is considered to be representative of the changes observed in the powders during the experimental works (see Figure 7.2). The main four areas of the map in agreement with Hauser [2002] are (A) no marking, (B) partial bonding, (C) melting with breakages and (D) melting with bonding.

A- No Marking: At very low laser power and/or very high scan speed on the surface of the powder bed produces no physical changes, with, no melt formation and no bonding between neighbouring particles. It was assumed that a melt phase was required to initiate particle bonding due to the short heating times inherent in direct SLS.

B- Partial Bonding: At a low laser power and/or high scan speed on the surface of the powder bed produces colorations on the surfaces of irradiated particles. Particles with the smallest size fraction may be melting during exposure. However, this liquid achievement is unlikely to wet, and therefore not form bonds, between larger unmelted particles due to a limited liquid volume which is governed by surface tension forces. The other possibility of partial bonding may be the SLS process occurs in solid phase sintering This creates tempered tracks within the powder layer which disintegrate when gently touched.

C- melting with breakages: At a high laser power and high scan speed on the surface of the powder bed produces colorations on the surfaces of irradiated particles. As laser power increases, liquid phase sintering begin to play an important role in the SLS process of the high-speed steel powder. A greater number of smaller particles are melted

during exposure, causing liquid to wick into surrounding porosity. This liquid action forms bonds between adjacent particles in spite of the fact that these particles are being subjected to surface oxidation.

D- Melting with Bonding: Moving the beam on the surface of the powder bed produces full particle melting with bonding.

The above four heating and melting processes will be referred to later as they are related to the rest of the results in this section.

Three different types of melt pool growth in agreement with Hauser [2002] are observed (see Figure 7.1), as the laser spot actions over the surface of the powder bed, melting with balling, melting with breakages, and continuous melting:

Melting with balling: As the surface tension is a function of temperature, the presence of a temperature gradient causes a corresponding variation of the surface tension between the edge and centre of the melt pool. The surface tension gradient will induce a Marangoni flow from a region of low surface tension to a region of high surface tension. This fluid flow will produce an extra force exerted on the molten track of SLS and influence the balling phenomenon.

Melting with breakages: Scan speed had a significant effect on the breaking up of the liquid track. Increasing the scan speed resulted in a decrease of the track width and the break-up of the track. Surface tension also is an important factor to control the kinetics of the scan track break up.

Continuous melting: At a low scan speed the scan track was continuous and smooth. The result is a continuous melt pool with surrounding powder.

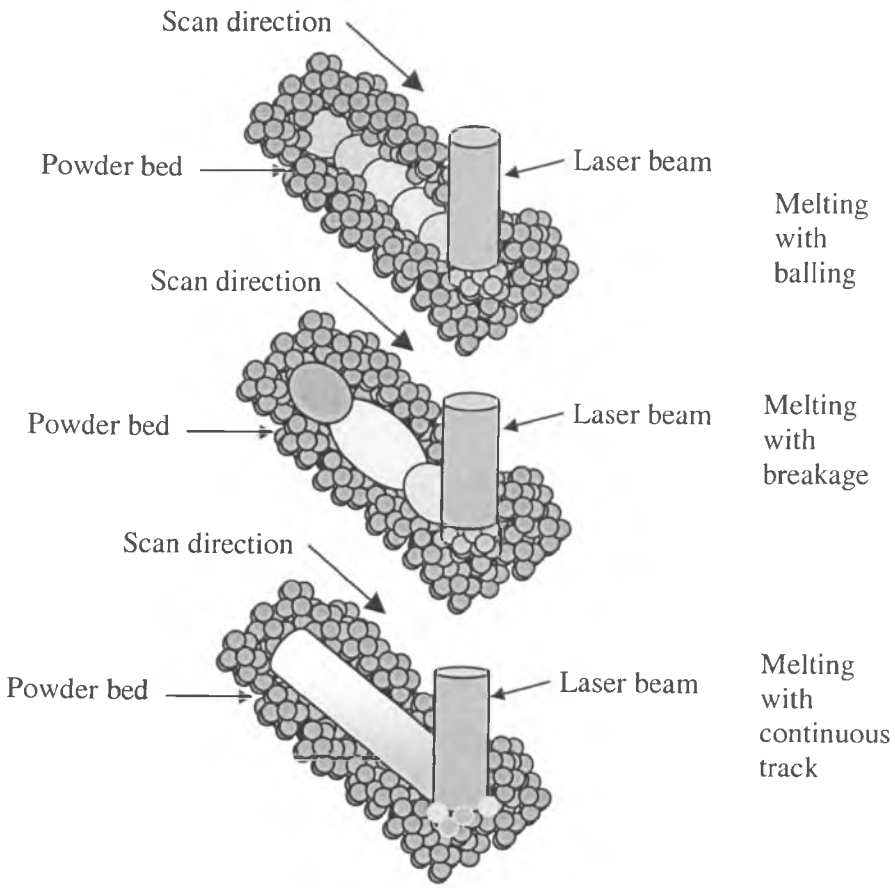

Figure 7.1: Schematic diagram showing the types of solidification

Figure 7.2 mapped out the effects of scan speed and laser power on the heating and melting of the HSS powder. It is clear from Figure 7.2 that at very low laser powers (<10W) over the whole speed range investigated no temperature changes or bonding of the powder took place.

Through the increase in energy density achieved by increasing the laser power or decreasing the scanning speed, more of the powder particles cause the formation of dense agglomerates. Some of the lines break at high scan speed due to surface tension.

However, at laser powers above 30W with a low scanning speed (<5 mm/s), continuous lines with high quality, uniformity, and repeatability can be achieved.

In summary, it can be concluded in agreement with Niu and Chang [1999] that the direct SLS of high-speed steel results in liquid phase sintering (LPS) and supersolidus liquid phase sintering (SLPS). During LPS the laser melts the powders and melting alloy penetrates into and wets the solid particles. The attendance of the liquid phase around the solid particles will cause rapid densification by the rearrangement of the solid particles and subsequent solution-reprecipitation mechanism. However, during SLPS the particles are heated to a temperature at which the austenite + carbide + liquid phases are in equilibrium, and the liquid phase forms along the austenitic grain boundary within the particles. Because direct SLS is carried out line by line, laser scanning causes melting along a row of powder particles, so forming a track of molten region of approximately cylindrical shape. This liquid cylinder can be expected to break up into a row of spheres so as to reduce the surface area, leading to the balling phenomenon. Increasing laser power, or decreasing scan speed makes it difficult for the liquid cylinder to break up into the agglomerates so as to obtain a continuous line. However, it is difficult to obtain the continuous line only by increasing laser power. The balling phenomenon may be caused due to the increasing of melt viscosity caused by the precipitation of solid from the liquid.

Figure 7.3 shows the irradiated tracks created by traversing an unrastered spot size over powder bed taken from the high-speed steel powder.

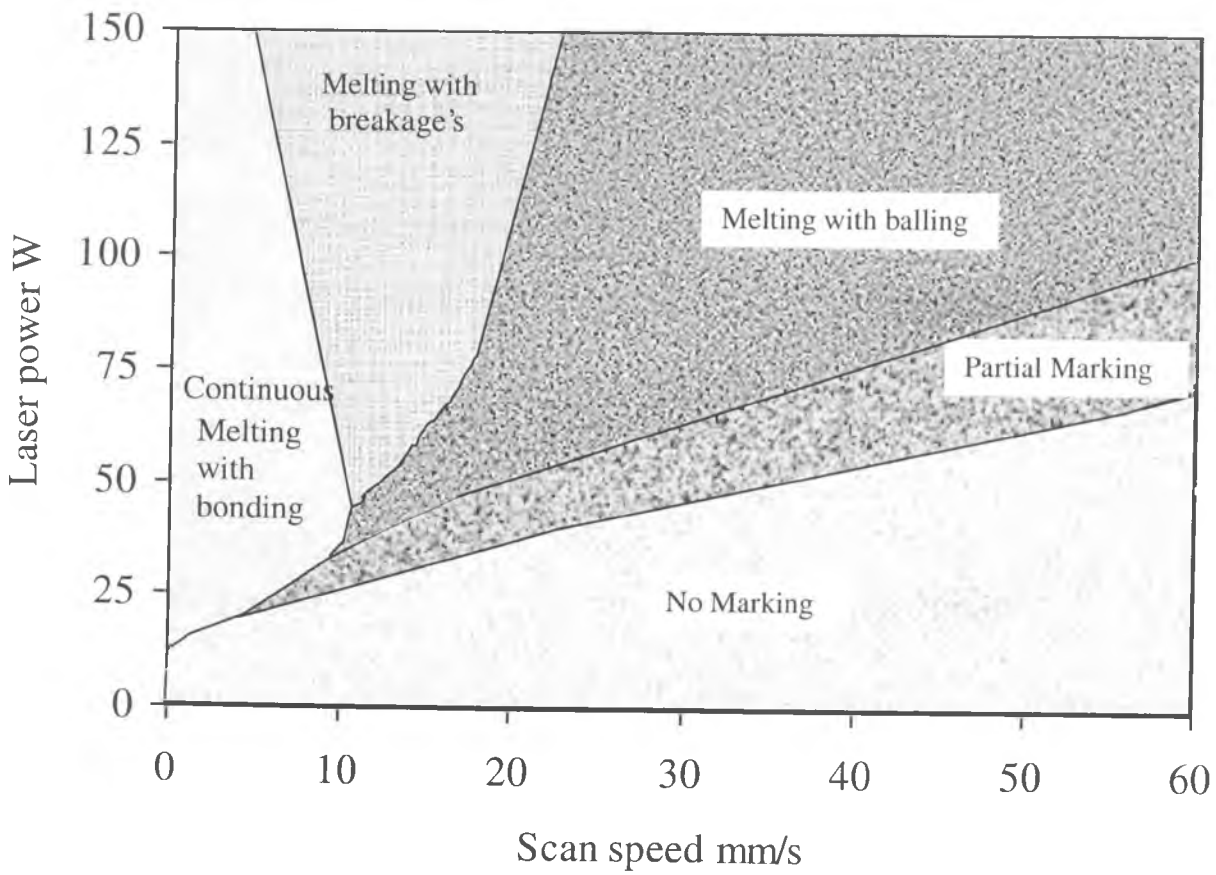

Figure 7.2: Process map of melting regimes for the high-speed steel powder (single line scans).

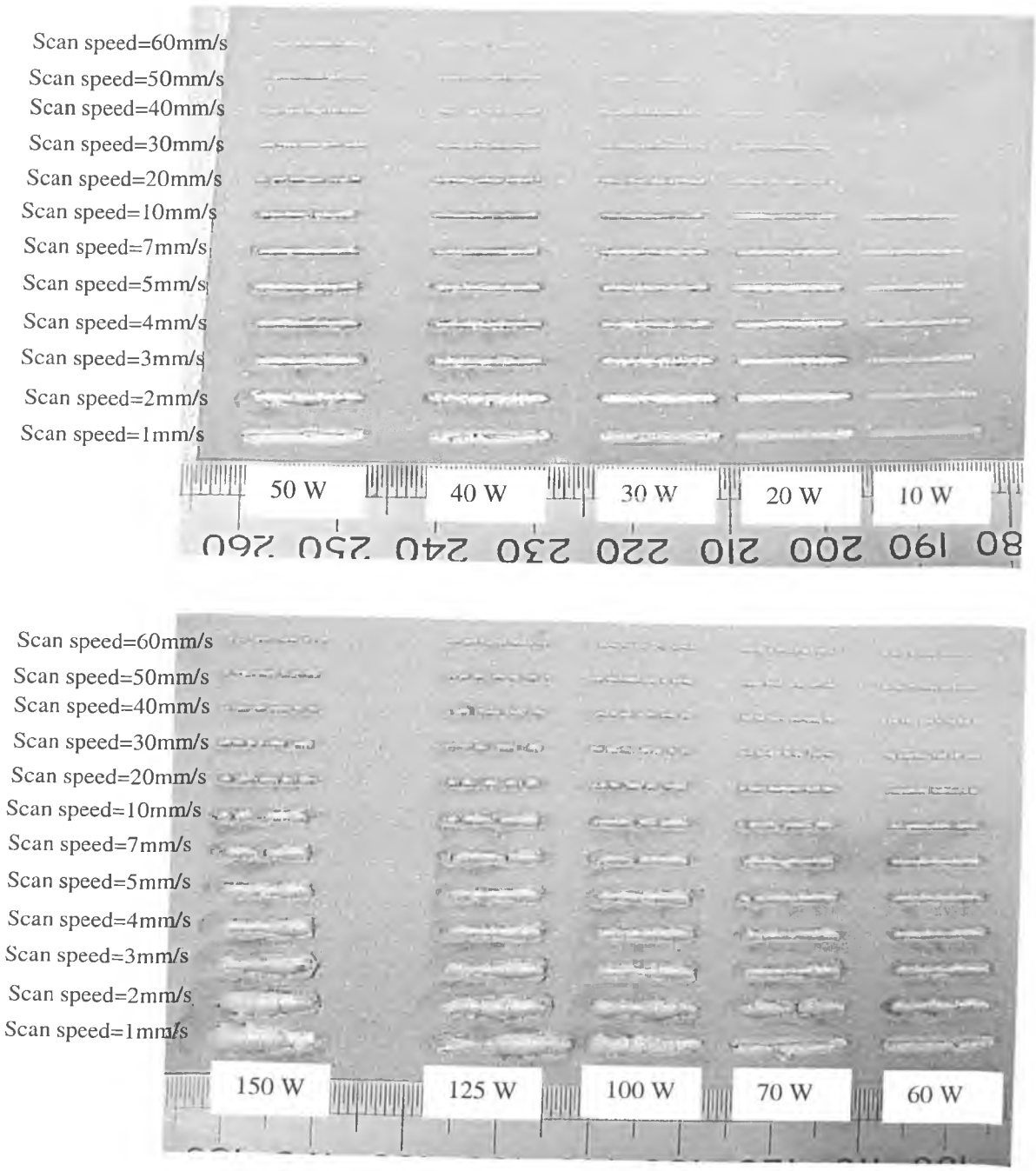

Figure 7.3: Irradiated tracks created by traversing an unrastered spot size over powder bed taken from the high-speed steel powder.

Figures from 7.4 to 7.9 show the effect of scan speed and laser power on the agglomerate width, agglomerate depth, and the depth/width ratio. The effect of scan speed on the line width has been evaluated. The single lines were made on a powder bed of about 7 mm thick as mentioned in chapter 6 (section 6.5.2). The average widths and heights were calculated using over 10 measurements per line.

It can be seen from Figure 7.4 that the width of the agglomerates decreased with increasing scan speed until a width of 1.1 mm is reached because the energy density decreases with the scanning speed. This corresponds to the zone in the laser spot where enough energy exists to the melt the powder.

As shown in Figure 7.5 the width of the agglomerates increased linearly with increasing laser power, since more energy is delivered into the powder.

Figure 7.6 shows the experimentally determined relationship between the depth of the single line and the scan speed at different laser powers. It can be seen from this figure that the depths of the lines decreased gradually with increasing scan speed.

Figure 7.7 shows the experimentally determined relationship between the depth of the single line and the laser power at different scan speeds. It can be seen from this figure that the depths of the lines increased gradually with decreasing laser power.

Figures 7.8 and 7.9 show relationship between the depth/width ratio of the single line with the scan speed and laser power respectively. It can be seen from these figures that the depth/width ratio increased gradually with increasing scan speed and decreased slightly with increasing laser power due to increasing of width.

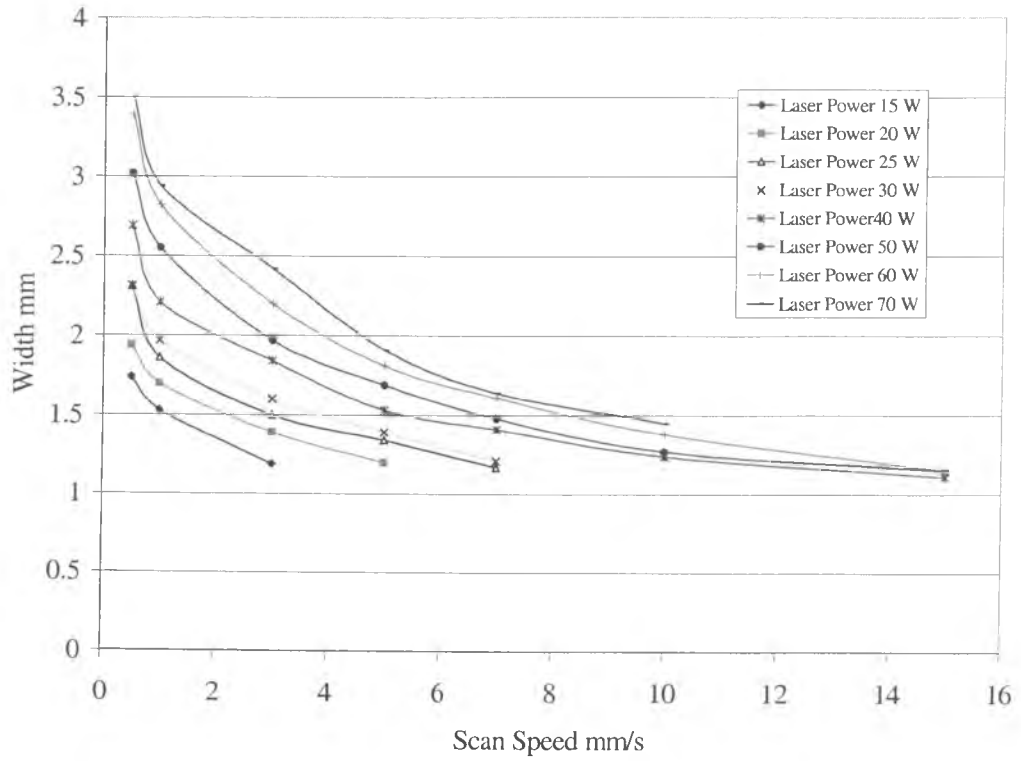

Figure 7.4: Change in width of single lines with changes in scan speed

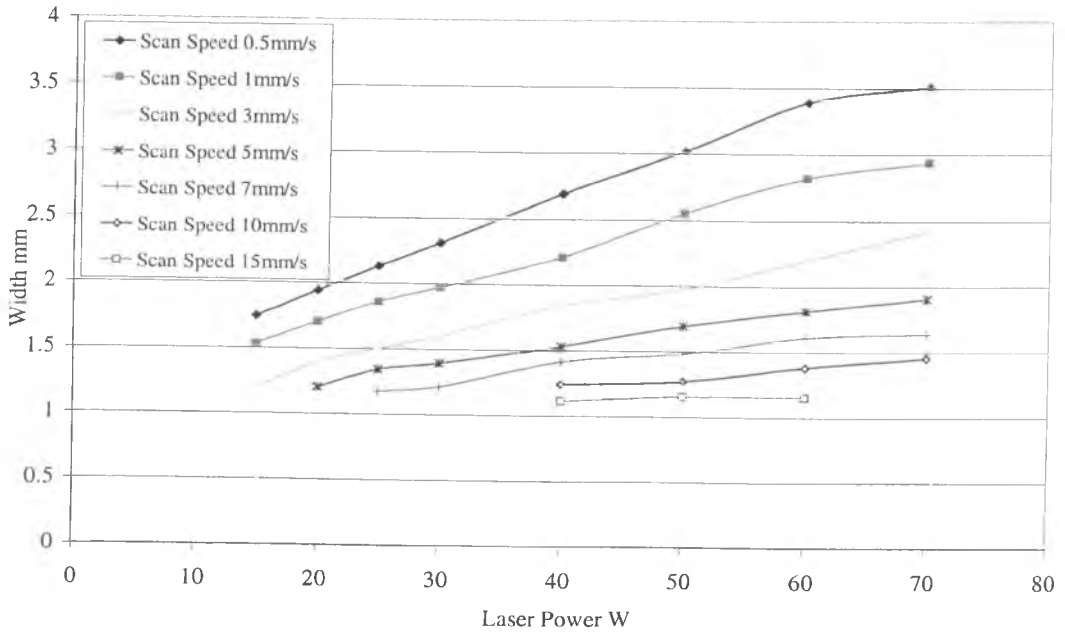

Figure 7.5: Change in width of single lines with changes in laser power

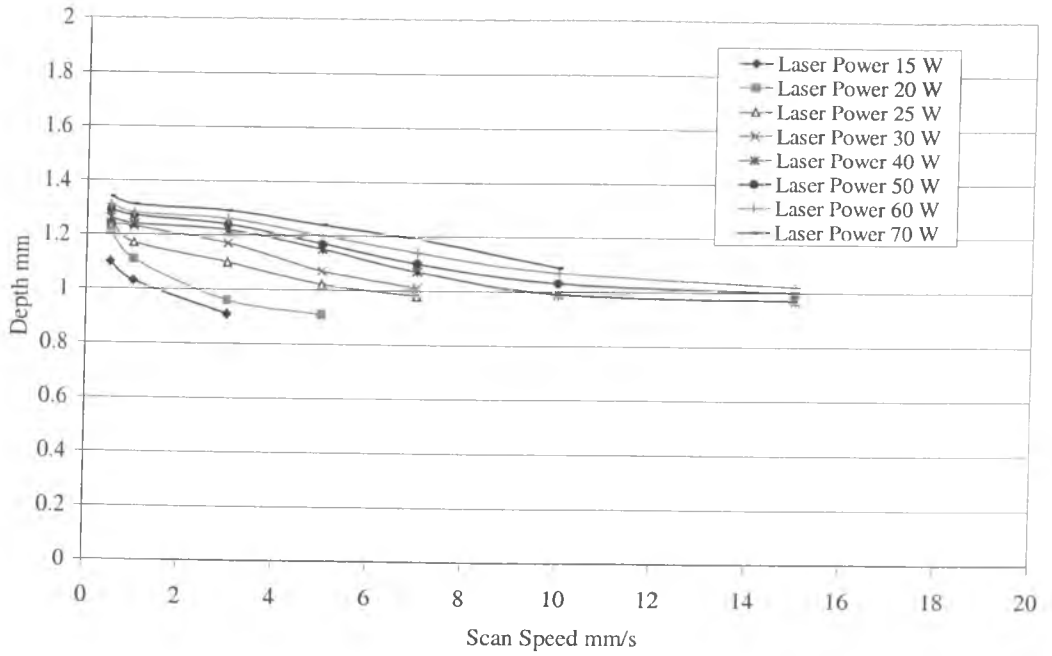

Figure 7.6: Change in depth of single lines with changes in scan speed

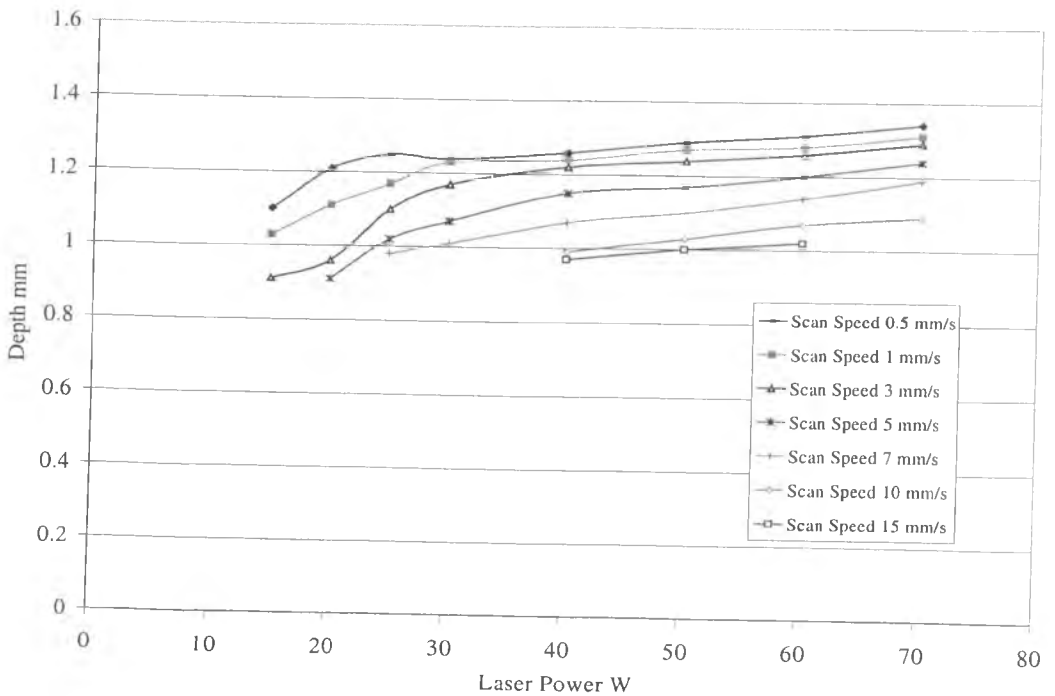

Figure 7.7: Change in depth of single lines with changes in laser power

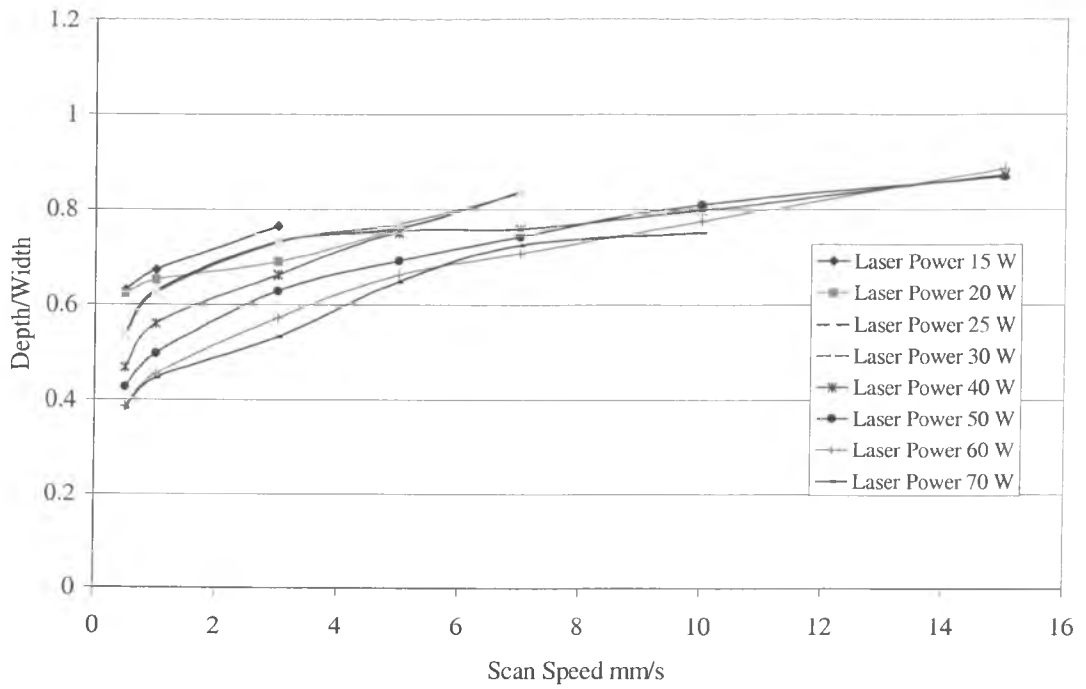

Figure 7.8: Change in depth/width ratio of single lines with changes in scan speed

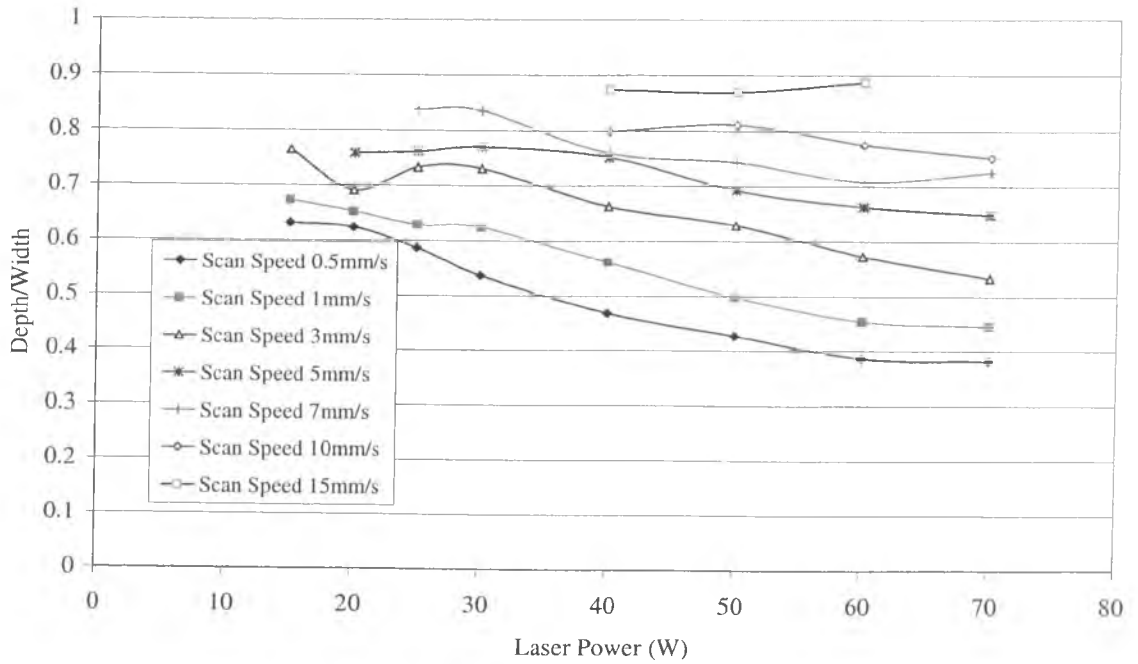

Figure 7.9: Change in depth/width ratio of single lines with changes in laser power

7.2.2 Warping of single lines

Figure 7.10 shows a photograph of single lines with different lengths at constant scan speed (1 mm/s) and constant laser power (50 W). It can be observed from this figure that the warping of the single lines decreased with decreasing length of the line. As mentioned in chapter 6 direct SLS was carried out without preheating of the powder bed. The warping occurred because the heat is applied at the top surface; the top densifies to a greater extent than does the bottom surface of each line. In addition, the upper surface cools from a higher temperature than material below, causing more thermal contraction on the upper surface. So each line of sintered powder tends to warp upward.

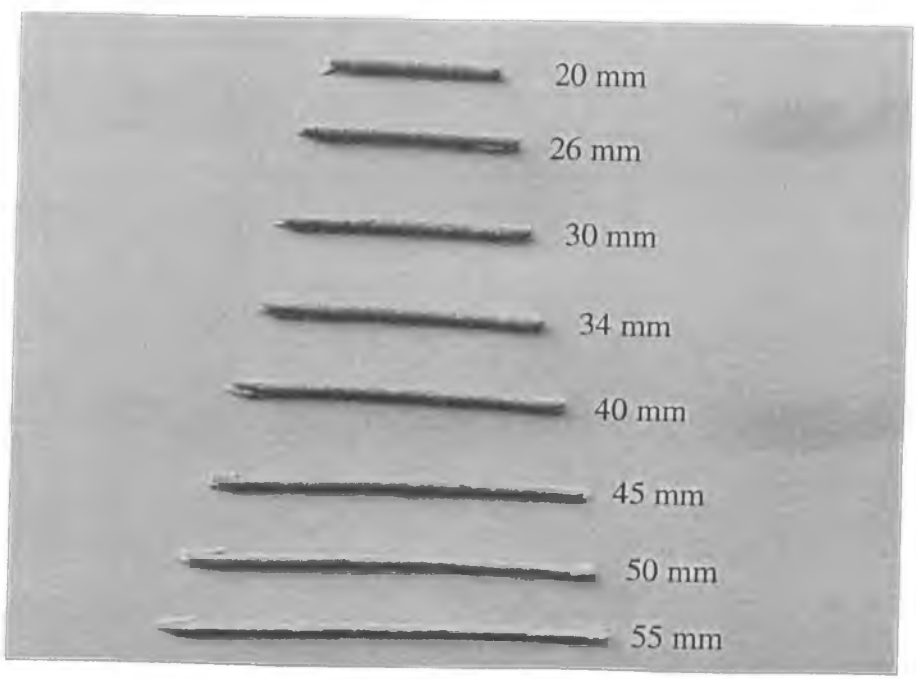

Figure 7.10: Photograph shows the warping of single line

Figure 7.11 shows a photograph of a cross-section of the solidified line processed at scan speed (1 mm/s) and laser power (50 W). The cross section has a semicircular shape with a flat top surface with a slight depression.

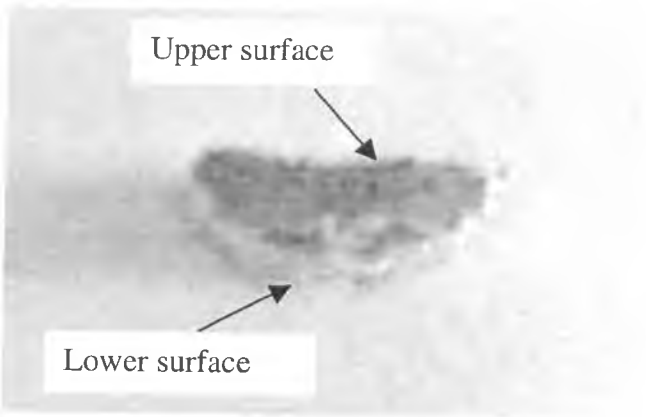

Figure 7.11: Cross-section of single line, laser power 50 W, and scan speed 1mm/s

7.2.3 Accuracy of Single Line at Constant Scan Speed, and Laser Power

Figure 7.12 a, and b shows the variation of the dimensional results of single line in X and Y direction, respectively. The lines were built at constant scan speed (1 mm/s), and constant laser power 50 W.

Figure 7.13 shows the absolute error of single line in both X and Y directions measured from the end to the end. It can be seen from this figure that the absolute error of single line is increased with increasing length in both X and Y directions, but the error in the Y direction is bigger than the error in the X direction for the same length. This effect might have been caused by some systematic error of the scanner in the sinterstation.

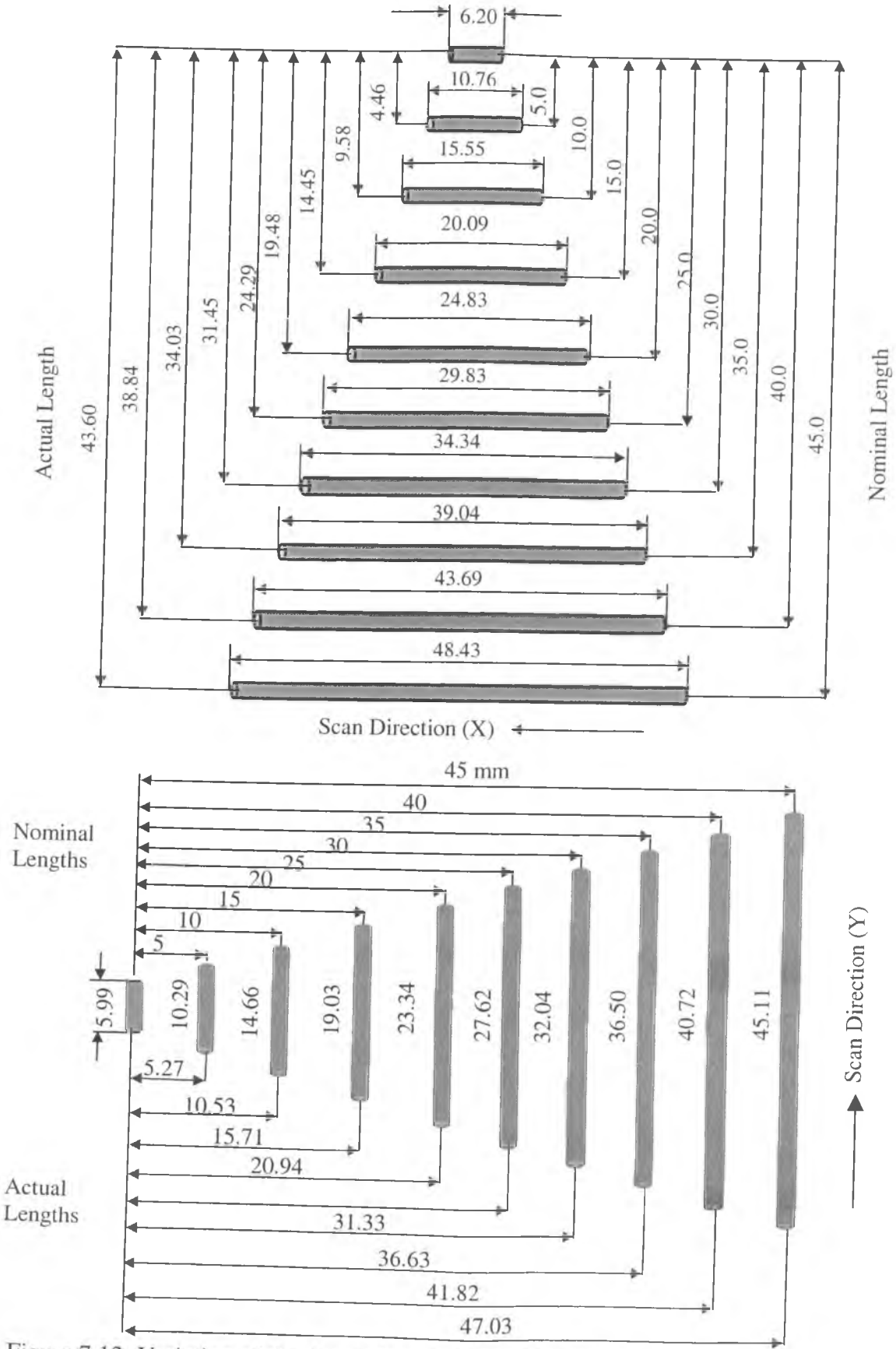

Figure 7.12: Variation of the dimensions in X and Y direction.

It can be also seen from this figure that the error of the 5 mm length is about 1 mm for both X and Y direction. The minimum error (zero error) was found at length 12 mm in Y direction and 23 mm in X direction. In addition, the absolute error of 45 mm length is - 1.31 mm in X direction and -4.28 mm in Y direction. These values suggest that the line experiences a considerable difference in error in the two directions, X and Y.

Figure 7.14 shows the absolute error, measured from the end to the end, for single line, built at constant scan speed (1 mm/s), and constant laser power 50 W, after modification of the CAD program by compensation of the error using the equations 1 and 2 from Figure 7.13 in X and Y directions. It is possible to see in Figure 7.14 that the absolute error in the X and Y directions is less than ± 0.1 mm for any length.

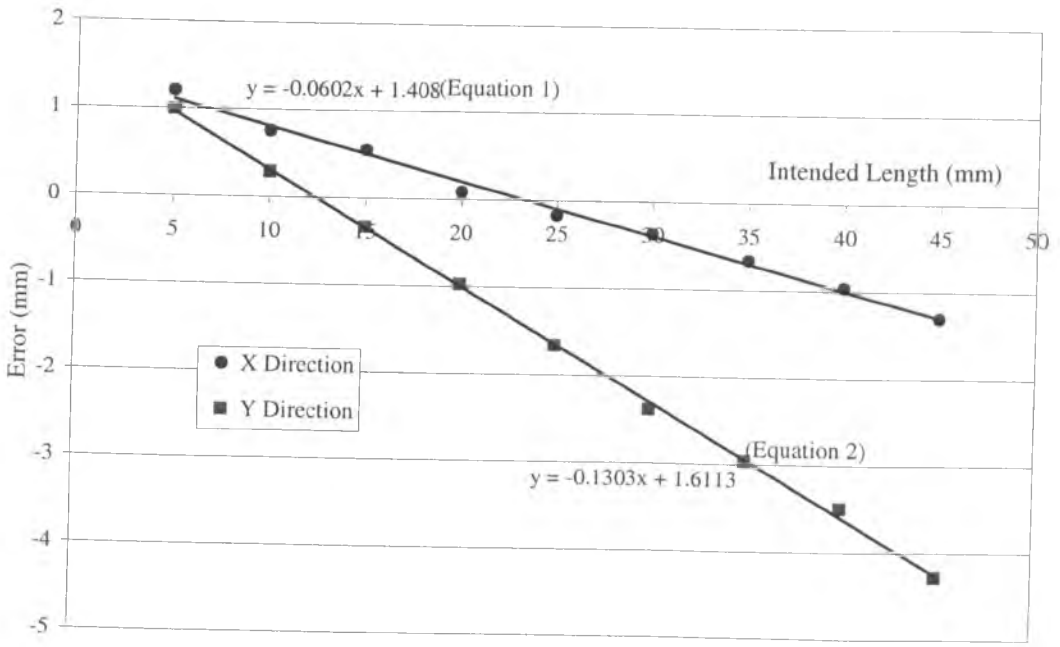

Figure 7.13: Error of single lines in both X and Y directions before the modification of the CAD program built at constant scan speed (1 mm/s), and constant laser power 50 W

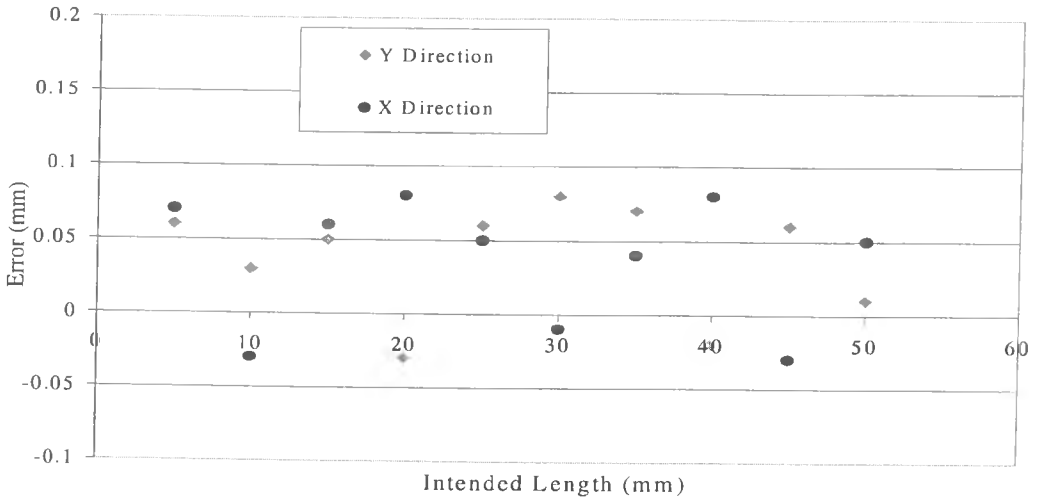

Figure 7.14: Error of single lines in both X and Y directions after the modification of the CAD program

7.3 Building Monolayers Using Different Scan Speed, Scan Spacing, and Laser Power

In order to produce multiple layers, it is first necessary to understand the interactions of the laser and material and to optimise the parameters for the production of single layers. Trials were performed on a loose powder bed of arbitrary depth, 7mm. The programming of the scanning software enabled parameter matrices to be produced by varying laser power, scan speed, and scan spacing, and constant beam diameter (1.1 mm). A full study of all process variables was undertaken to obtain a complete understanding of the variables' interactions.

Single layer scanning was carried out over the range of conditions where single line scanning was successful. However, it was found that single layer scanning could only be achieved at very high energy densities. The processing parameters of the monolayer are mentioned in table 6.2 (see section 6.5.2).

Figures from 7.15 to 7.18 show typical single sintered layers produced using different processing parameters. It can be seen from Figure 7.15 that the effects of warping and distortion of sintered single layers has been noticed. The effect reduces the chance of successful multi layer building with delamination being a major issue.

The cause of warping is due to the thermal time history of each sintered line in a rastered layer causing temperature gradients over the entire laminate. One of the methods to reduce the warping is the heating of the powder bed allowing homogenisation of temperature distributions within each laminate. On the other hand, the pre heat temperatures required to reduce thermal gradients for metal powder processing is approximately half the melting temperature of the material. Such high temperature is very complicated to achieve, so, powder bed pre-heating has been considered an impractical solution.

The length of each scanned line within a raster scan set is a major contributor affecting the degree of warping a single layer exhibits. As the scan length increases the probability of warping also increases, as mentioned in section 7.2.2, resulting in dramatic upwards movements of single layers. It was also noticed that the monolayers built at low laser powers were fragile.

The results at high laser power and small scan speed (see Figure 7.16) indicated that, the surface appears to be good but contains several cracks. The reason for this may be the increased levels of heat created by using a scan spacing of 0.162 mm. This may produce great thermal gradients which led to residual stresses relieved by shape change in the form of cracks of the monolayer. In general, at smaller scan spacing, more scan tracks are required to make the layer. The cumulative compressive stress is increased and therefore several cracks may appear across the samples throughout the scanning.

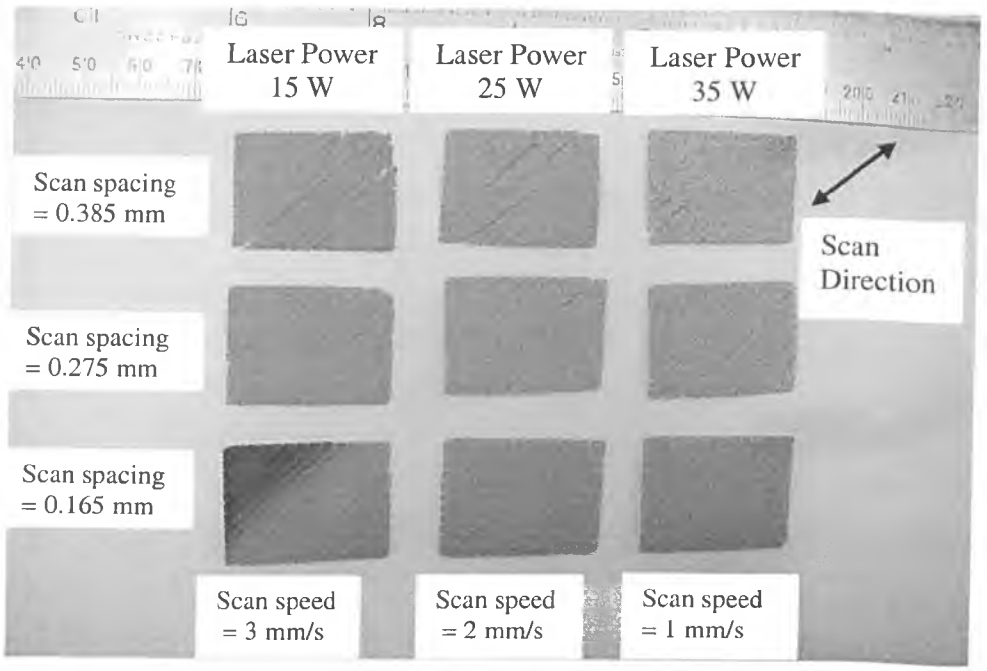

Figure 7.15: Samples with different laser power, scan speed, and scan spacing

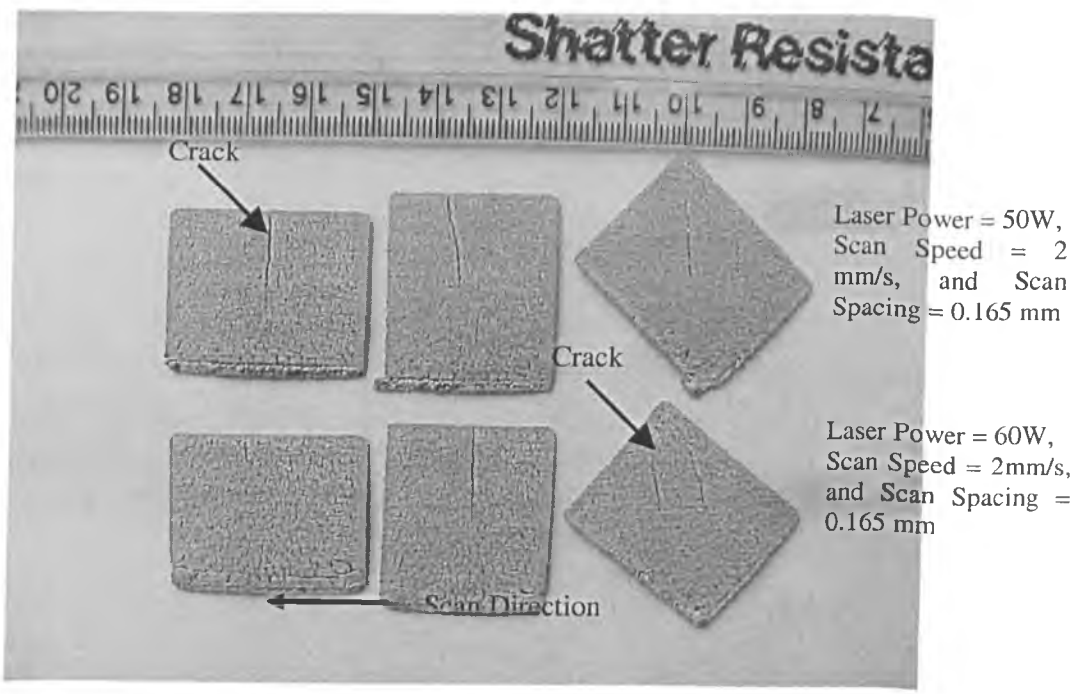

Figure 7.16: Samples with different laser power and constant scan speed, and scan spacing

Figure 7.17 also shows two samples with different laser power and constant scan speed and scan spacing. It can be seen from this Figure that the upper sample, using laser power 50 W, scan speed 1 mm/s, and scan spacing 0.682 mm, have a good surface appearance. It can be also seen from the lower sample that increasing the incident laser energy density lead to an increase of surface roughness since the molten particles tend to form larger spherical structures.

An additional scanning effect is the incidence of the first line scan as shown in Figure 7.17. It is the first line scan of every layer that appears different to every other line in any particular layer. The features of the first line scan is an increased density and thickness compared to that of the other scanned lines in a layer. The first line scan phenomenon occurs may be because all heat absorbed by the powder is used to sinter the first line.

A visual inspection of the surfaces of samples sintered at different processing parameters was completed. Figure 7.18 shows the plane view of two samples sintered at scan speed 3 mm/s, and 5 mm/s and constant laser power (50 W), and scan spacing (0.682 mm). It can be clearly seen by visual inspection alone that the increasing the scan speed increases the surface roughness at the same laser power and scan spacing. The surface roughness increase since the molten particles tend to form large spherical stricture.

Figure 7.19 shows a map of the effects of laser power and scan speed scanning at constant scan spacing (0.682 mm).

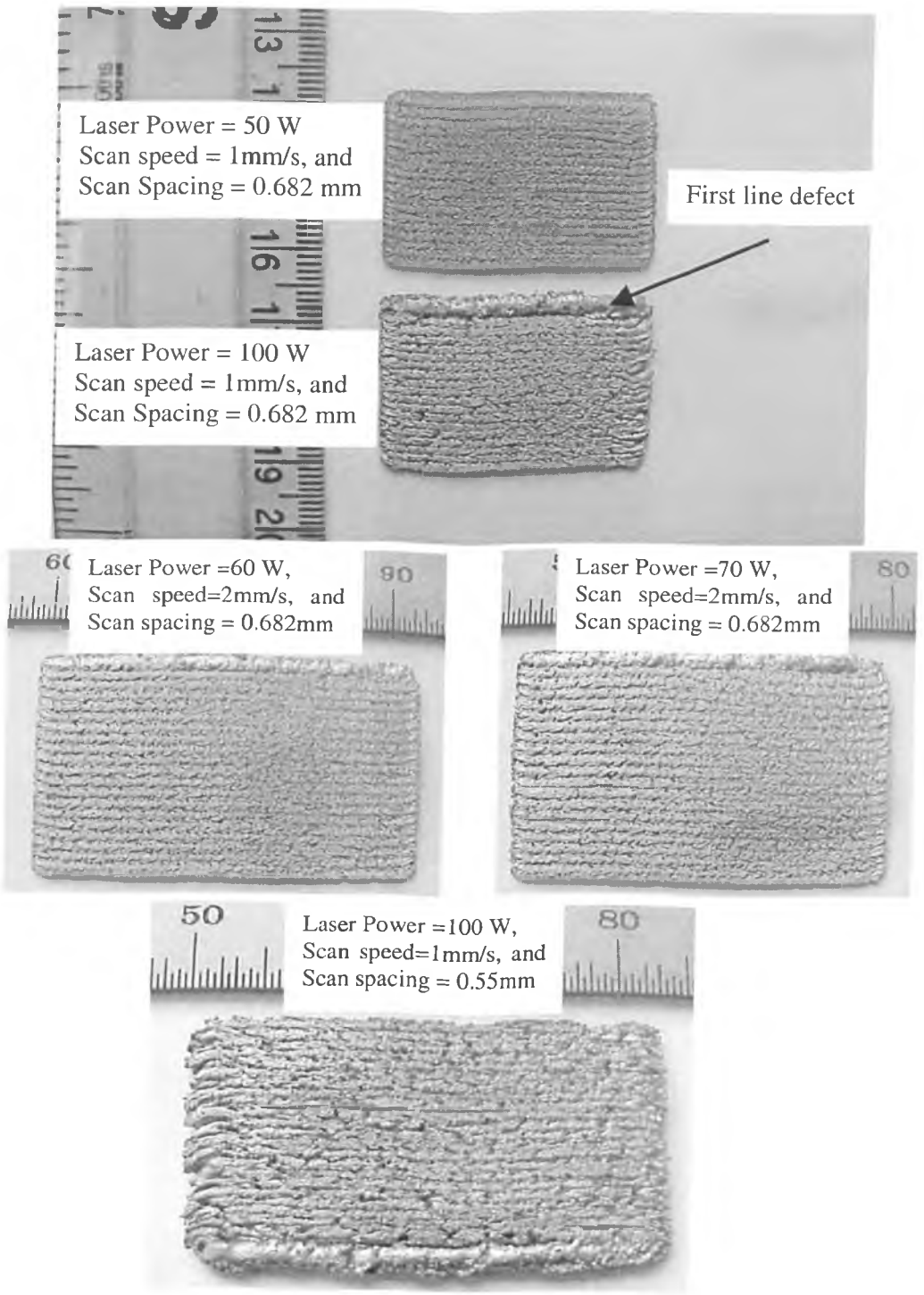

Figure 7.17: Samples with different laser power, scan speed, and scan spacing

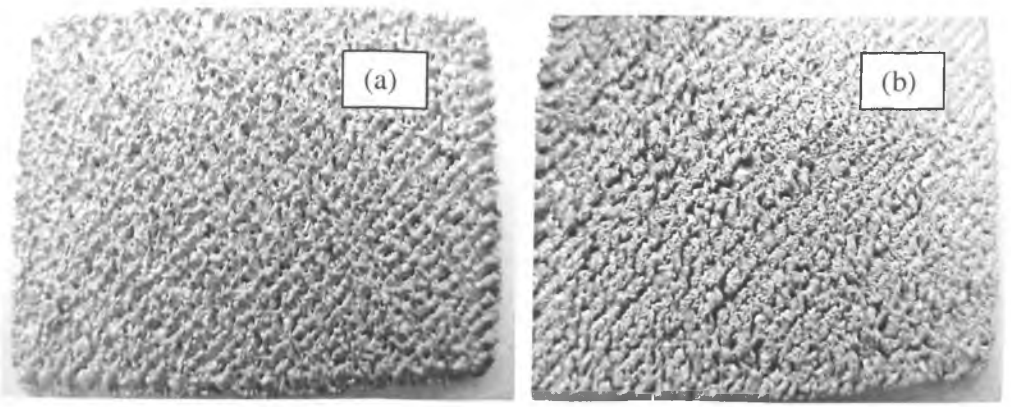

Figure 7.18: (a) Laser power (50 W), scan speed 3mm/s, and scan spacing (0.682), and (b) Laser power (50 W), scan speed 5 mm/s, and scan spacing (0.682)

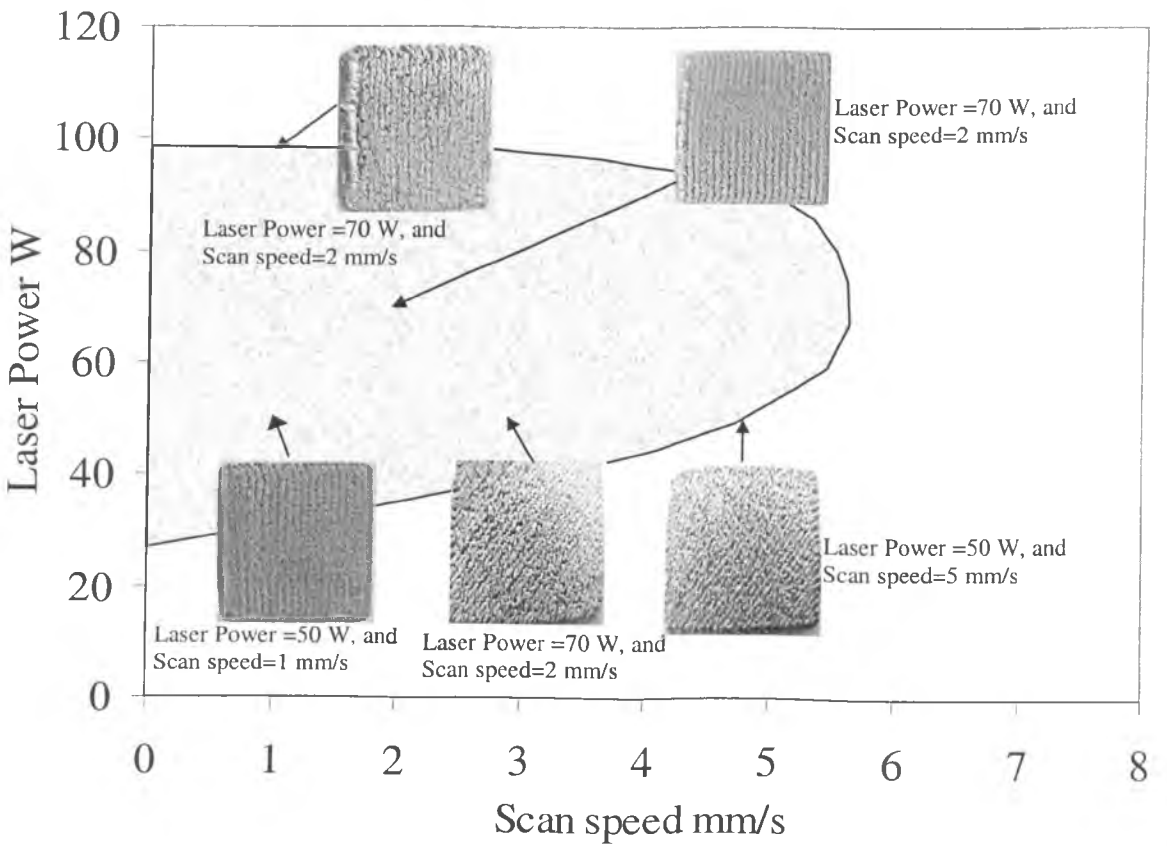

Figure 7.19: Process map of single layer for laser power and scan speed variations at constant scan spacing (0.682 mm)

7.3.1 Defects of Monolayer Samples

The effect of warping of long sintered single layers at low laser power or high scan speed has been noticed during sintering experiments. The other defect of long single layer samples was the thickness of the middle third of the sample is less than the outer two thirds. One possible explanation of this phenomenon is probably due to an increase in heat loss as a result of dissipation in the middle portion of the layer than edges. At the edges the laser beam returns quickly and the previous line is still hot, the time to lose heat is very short compared with the middle portion during the sintering process.

To measure the warping value some samples with different vector lengths and sinter directions were built. Figures 7.20 and 7.71 shows some samples with different dimensions sintered with the laser scanning parallel with the longest axis, and at 45° to the longest axis using laser power 50 W, scan speed 1 mm/s, and scan spacing 0.682 mm. The results of these samples show that the lower the scan length the less the warping.

Figure 7.22 shows the effect of vector length on warping of monolayer samples sintered with the laser scanning parallel with the longest axis, and at 45° to that axis using laser power 50 W, scan speed 1 mm/s, and scan spacing 0.682 mm. The average warping increases with increasing scan length at the same scanning parameters. It can be also seen from this figure that the average warping of parts sintered with the laser scanning parallel with the longest axis parts is greater than parts sintered at 45° to the longest axis.

Figure 7.23 shows a schematic cross-section and cross-sectional area of monolayer sample. It can be seen from this figure that the surfaces of the sample are uneven. This

is because the centre of beam has higher energy density to give higher temperature so more shrinkage occurs due to consolidation.

Figure 7.24 shows schematic of monolayer samples sintered at 45° to the axis, distortion of a sample before modification the CAD program, and a sample after modification the program. It can be seen from this figure that there is distortion of the sample (see Figure 7.24 c). This distortion is due to the variation of error in X direction and Y direction as mention in section 7.2.3. Figure 7.24 (d) shows a sample with less distortion after modification the program.

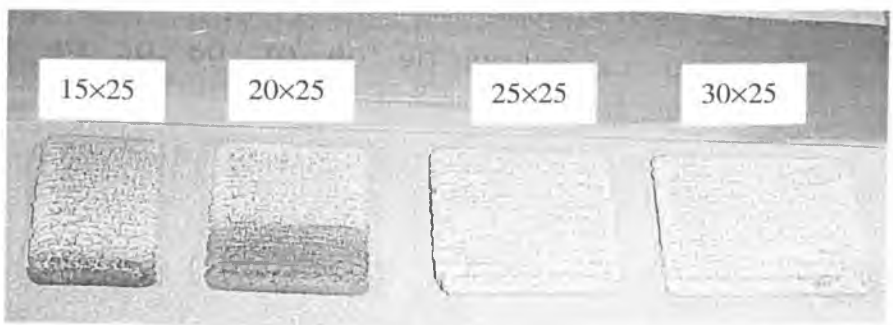

Figure 7.20: Samples with different vector length sintered longitudinally at constant scanning parameter.

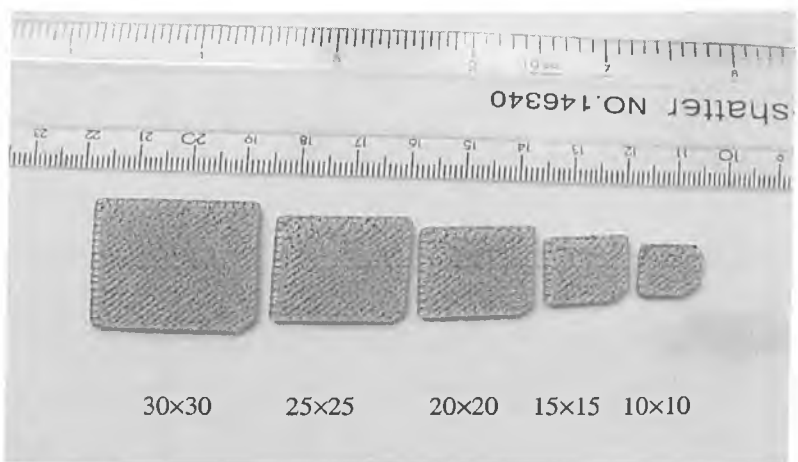

Figure 7.21: Samples with different vector length sintered at 45° to that axis at constant scanning parameter.

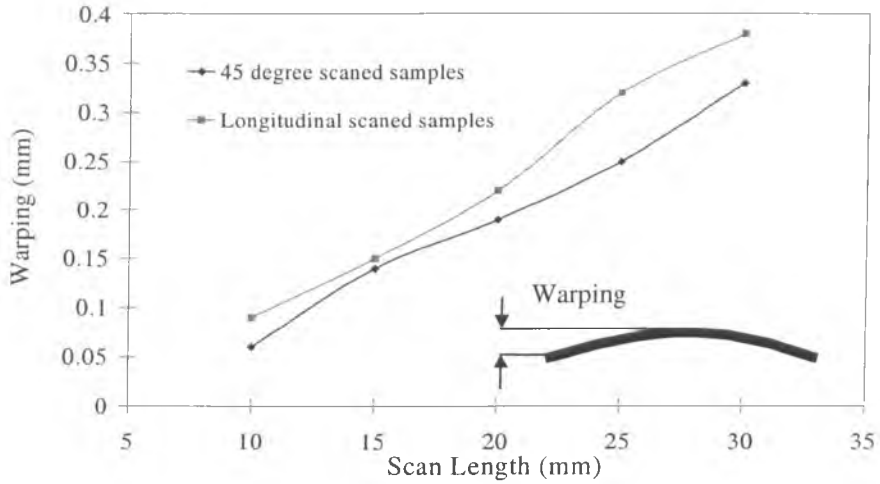

Figure 7.22: Variation of the warping with vector length at constant scanning parameters

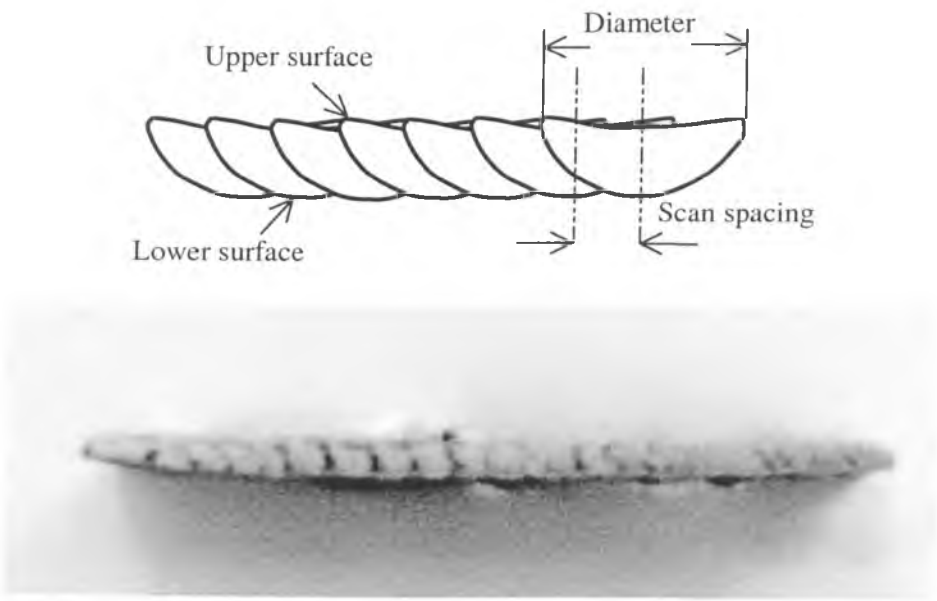

Figure 7.23: (a) Schematic of cross-section for single layer, (b) Cross-section area of single layer (laser power=50 W, scan speed =1mm/s, and scan spacing=0.682 mm)

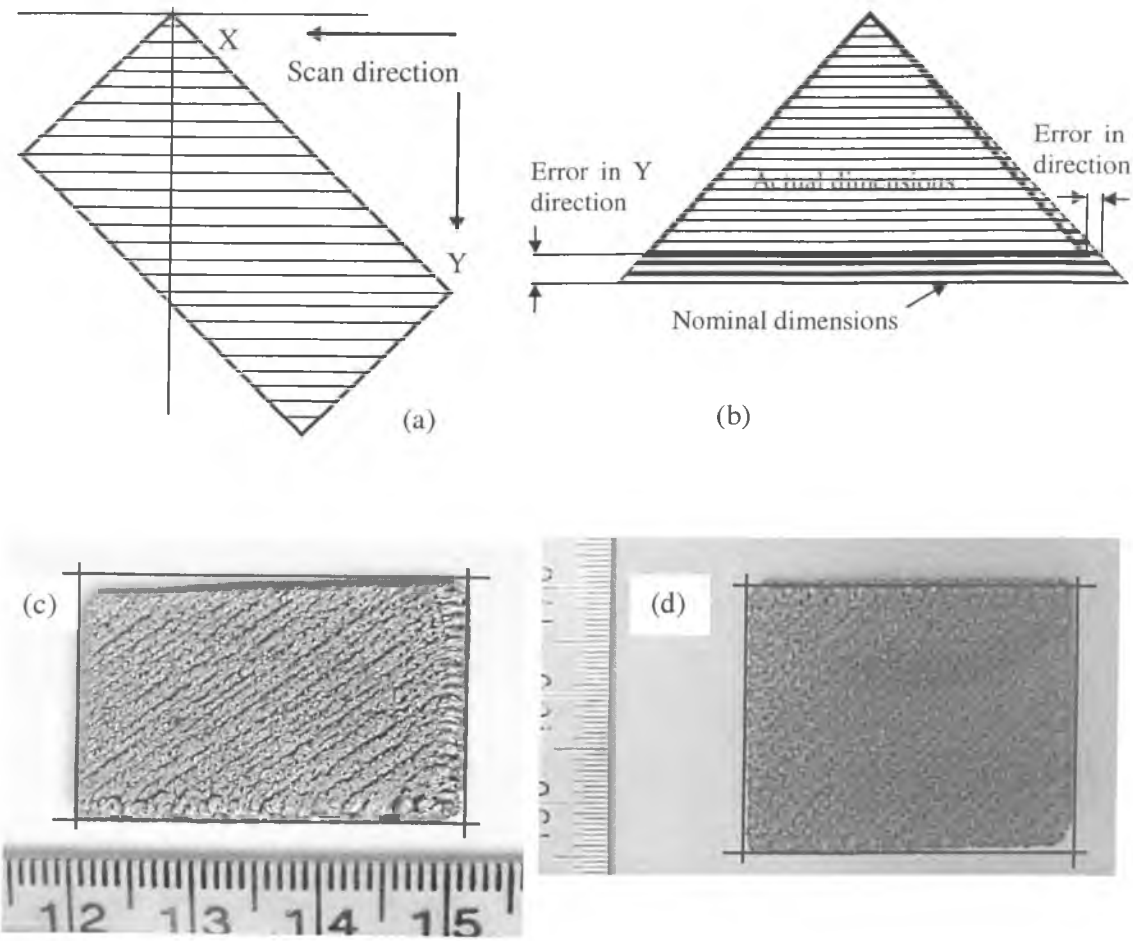

Figure 7.24: (a) Direction of scanning, (b) schematic of distortion (c) distortion of sample before modification the program, and (d) sample after modification

7.3.2 Strategy of Building

7.3.2.1 One layer

An attempt was carried out in order to overcome the phenomenon of variations of layer thickness from section to section, where the thickness of middle section is slightly thinner than the edges. This attempt scanned the layers in one direction. This trial was unsuccessful due to the cracks in the layer as shown in Figure 7.25. These cracks may be due to thermal stresses. When the neighbouring track began to solidify, a large

tensile stress between the solidified tracks appeared at the side end of the solid part which may cause the cracking of the layer.

In an attempt to increase the density of the part some samples with a zigzag scanning routine were built. This attempt was unsuccessful because shrinkage between the coupons appeared (see figure 7.26).

In an attempt to produce an accurate layer, contour scanning prior to internal scanning was utilised. The trial was also unsuccessful because gaps between the perimeter scan and internal scans appeared due to shrinkage (see Figure7.27).

After many trials and series of experiments it was found that the best conditions to build a good monolayer (high quality, uniformity, good density, and repeatability) are; laser power=50 W, scan speed=1mm/s, and scan spacing=0.682 mm. Many monolayer samples with dimensions 30×25 mm using the previous conditions were built to determined the bend strength of the material (see figure 7.28).

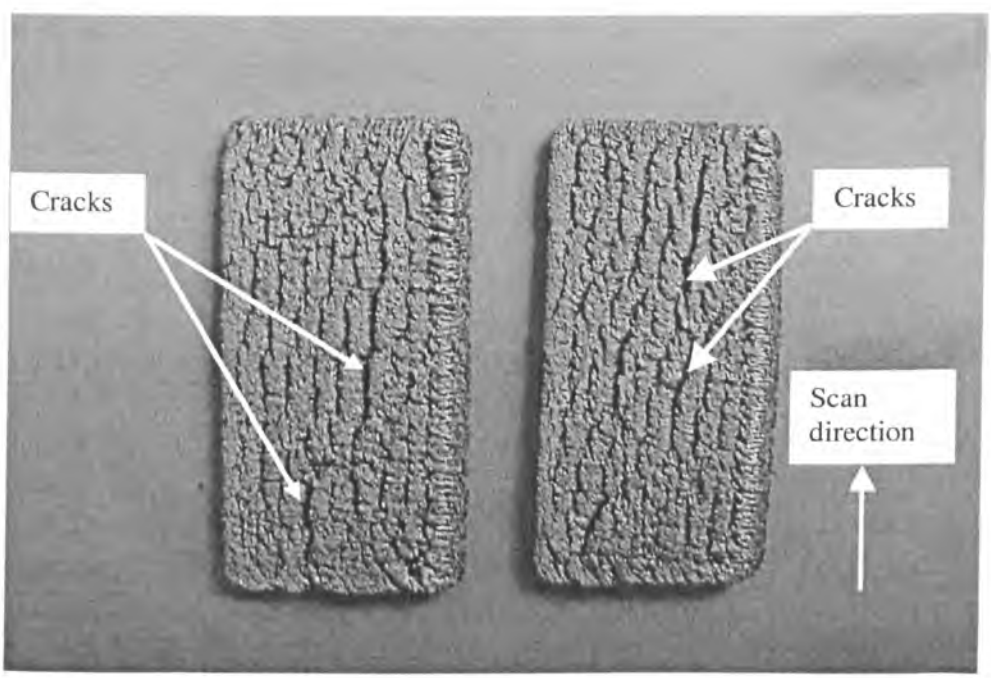

Figure 7.25: Two samples scanned at one direction

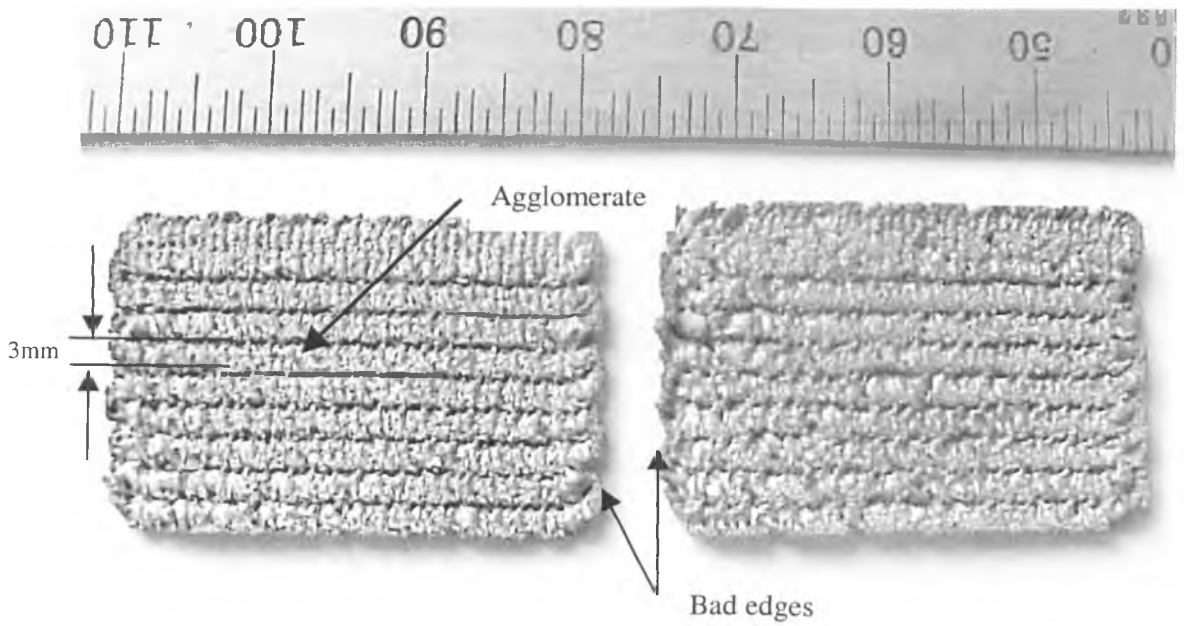

Figure 7.26: Top view of Zigzag (a) left: Scan speed=2mm/s ss=0.682mm, and Laser power=75 W, (b) right Scan speed=1mm/s scan spacing=0.682mm, and laser power=75 W)

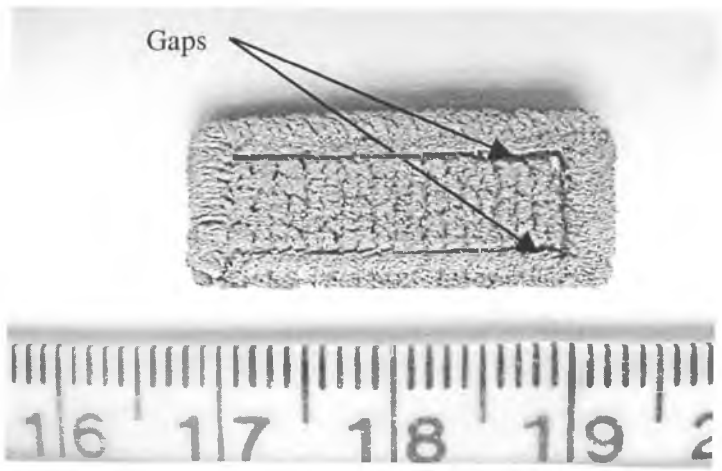

Figure 7.27: Sample with perimeter scans, power=50 W, scan speed=1 mm/s, and scan spacing=0.682 mm

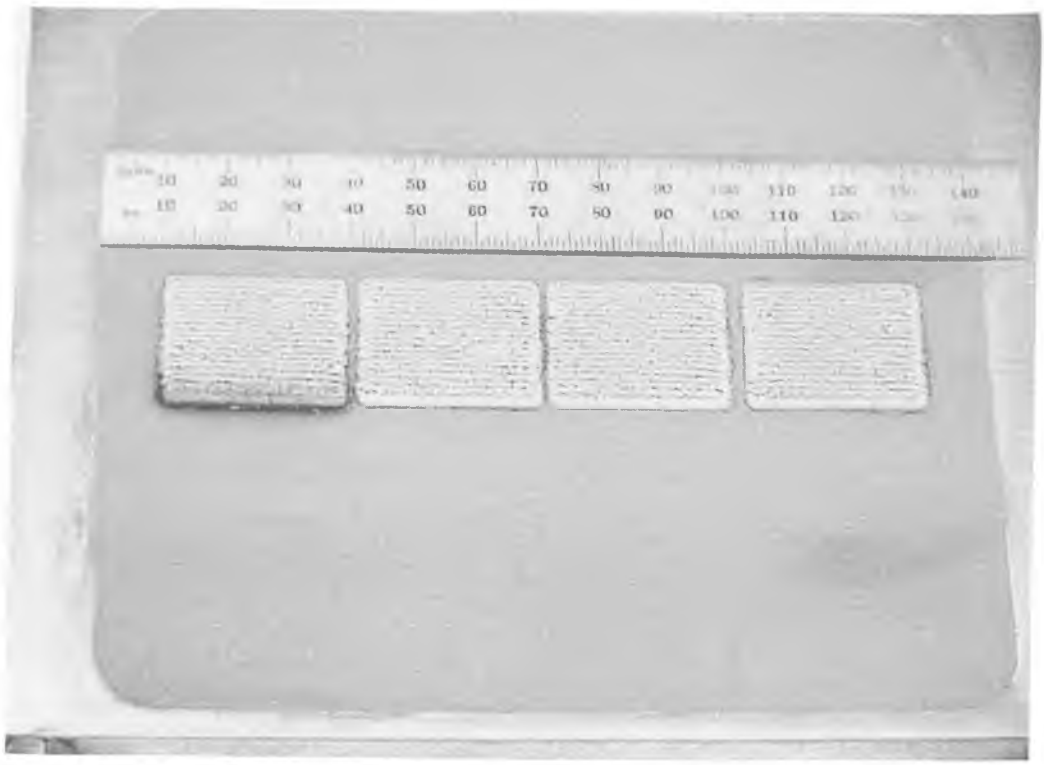

Figure 7.28: Four samples of HSS material sintered at laser power 50 W, scan speed 1 mm/s, and scan spacing 0.682 mm

7.4.3 Post-processing of Monolayers of HSS

An infiltration cycle was carried out for some monolayer samples using the conditions as mentioned in Chapter 4 for the RapidSteel 2.0 material (see section 4.3.2). Some of samples were sintered with the laser scanning parallel with the longest axis, perpendicular on the longest axis, and at 45° to that axis. Figure 7.29 shows a photograph of some monolayer samples after infiltration. The infiltration cycle was carried out to increase the density of the monolayer samples. The average density of the monolayer is increased from 4.6213 g/cm^3 to 6.7276 to g/cm^3. The percentage of the HSS and bronze of the monolayer samples is approximately 52% by weight and 48% by weight respectively.

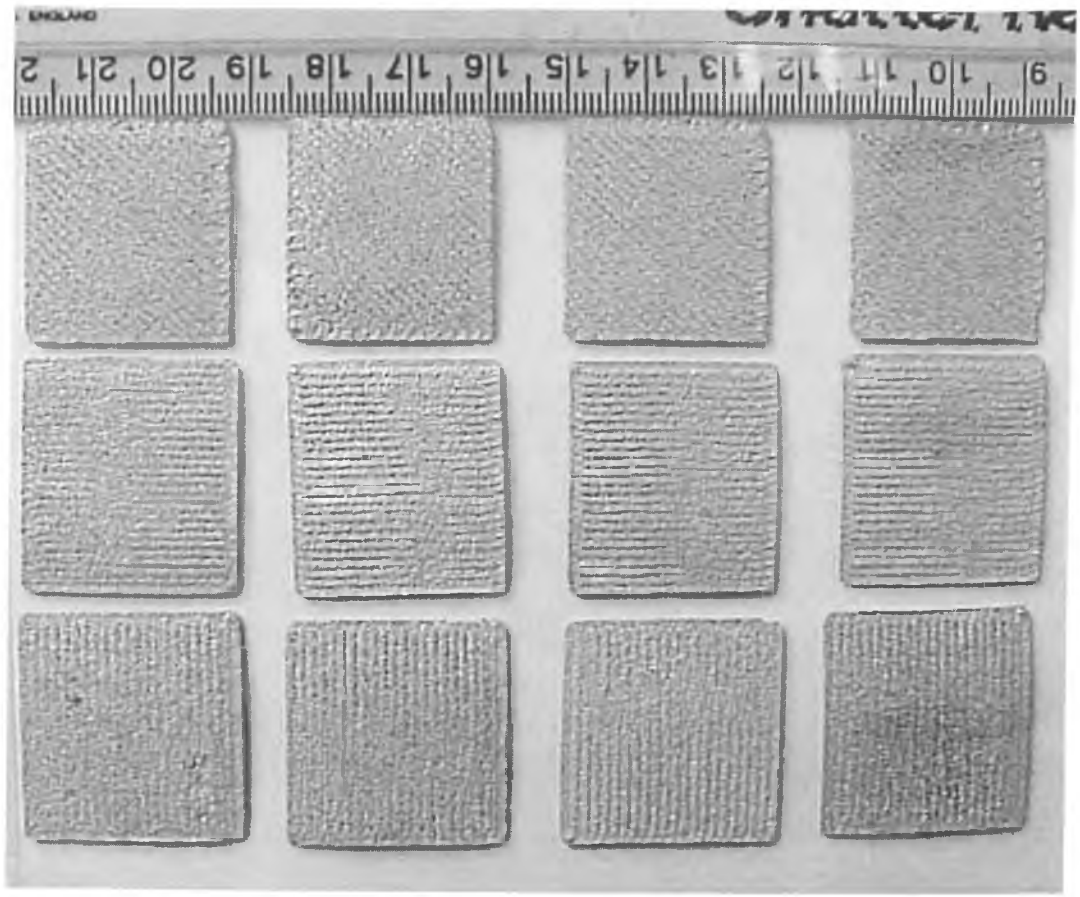

Figure 7.29: Photograph of monolayer samples of HSS.

7.5 Building Multiple Layer Using Different Laser Power, Scan Speed, Scan Spacing, and Layer Thickness

A single layer typically is not enough material to build a part. Several layers have to be fabricated in order to build parts. It was found that the processing parameters of monolayer are unsuitable, particularly the laser power, for the multiple layer samples. It was found that the laser power (50 W) is not enough to create multiple layers with good sintering between the layers. The picture shown in figure 7.30 is a multiple layer sample, with dimensions 30 mm length, 5 mm width, and 8 layers thickness, created

from the HSS material. The processing parameters are; laser power 75 W, scan speed 1 mm/s, scan spacing 0.682 mm, and layer thickness 1.0 mm. The scanning direction was changed from one layer to another. The scanning direction was carried out as following: first layer was sintered with laser scanning perpendicular on the longest axis, second layer was sintered laser scanning parallel with the longest axis, third layer was sintered with at + 45° to the longest axis, and fourth layer was sintered at -45° to longest axis (see figure 7.31). This sequence of scanning direction was repeated twice. The variation of scanning direction was used to improve the mechanical properties of the parts. From this figure it may be observed that there is delamination between layers i.e., the sintering between layers is not good because the layer thickness is big and the energy density is not enough for good bonding between layers.

Figure 7.32 shows a picture of multiple layer (a five layer) sample using laser power 75 W, scan speed 1 mm/s, scan spacing 0.682 mm, and layer thickness 0.8 mm. It can be seen from this figure that the sintering between layers is much better than the sintering between layer when the layer thickness was 1.0 mm. The scanning direction was carried out as described above. It was noticed that the bonding between layers was not strong and the layers could be separated easily. The weak bonding between layers is also due to insufficient energy density.

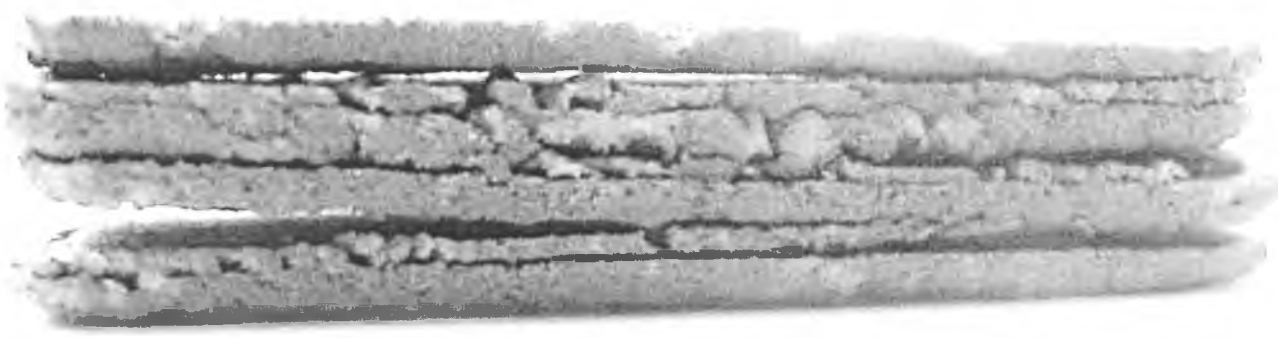

Figure 7.30: Eight Layer with different scan direction using layer thickness 1.0 mm, laser power = 75W, scan speed = 1mm/s, and scan spacing = 0.682mm

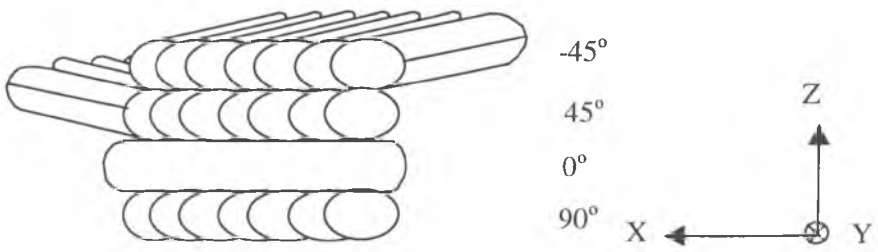

Figure 7.31: Typical scanning direction of multiple layer sample

Figure 7.32: Side view of five layer Sample built using laser power 75 W, scan speed 1 mm/s, scan spacing 0.682 mm, and layer thickness 0.8 mm

Lowering the layer thickness further resulted in difficulty in spreading fresh layers of powders without disturbing previously sintered layers. The minimum layer thickness

that could be achieved successfully was 0.6mm. Below this layer thickness, the hopper mechanism tends to displace the previously sintered layers from their position, thus disturbing the geometry of the part. This problem is particularly serious during the early build up of the part. When sintering a second layer on top of the first layer sintered on a loose powder, curling in a concave shape of both layers was observed for a lot of samples. This curling may be due to the thermal stresses induces during rapid heating and cooling of the sintered powder/layer. This makes the deposition of further layers of powder difficult since the hopper destroys the initial curled sintered layers. A few samples (with three layers) using layer thickness 0.55 mm, 0.50, 0.45 mm, and 0.40 mm were carried out. These samples were used only to calculate the density of the multiple layers to determine the effect of layer thickness on the density. The lower layer thickness resulted in better sintering between layers thus improving the part density as will be discussed.

Figure 7.33 shows a side view of a picture of two samples. It should be noted that the parameters used for this samples were laser power 75 W, scan speed 1 mm/s, scan spacing 0.682 mm, and layer thickness 0.7 mm for (a) sample, and laser power 75 W, scan speed 1 mm/s, scan spacing 0.682 mm, and layer thickness 0.6 mm for (b) sample. It can be seen that the 0.6 mm thick sample has a good appearance and good sintering between layers.

Several samples were built with the same processing parameter laser power 75 W, scan speed 1 mm/s, scan spacing 0.682 mm, and layer thickness 0.6 mm. Some of samples were infiltrated in the same manner as the monolayer samples. Figure 7.34 shows four samples as sintered (without post processing).

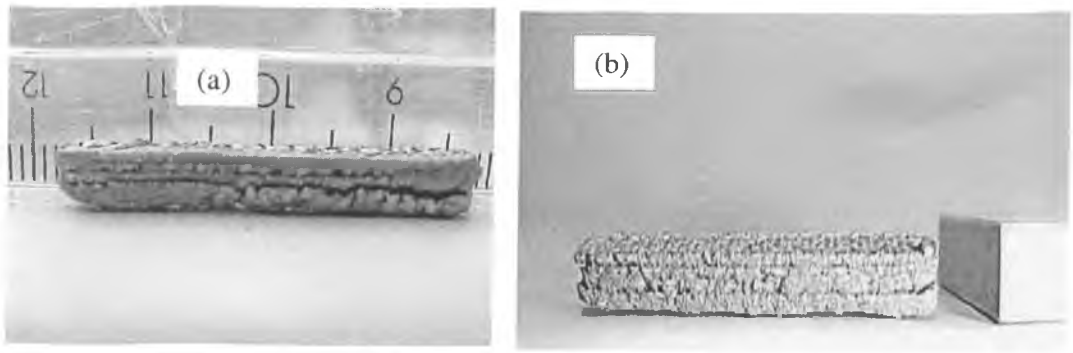

Figure 7.33: (a) Five layers sample with layer thickness 0.7 mm (b) five layer with thickness 0.6 mm

Figure 7.35 shows the effect of increasing scan spacing and scan speed at constant laser power 90 W. It can be seen from this figure that decreasing scan spacing leads to improved surface roughness, and decreased porosity. It was also found that increasing scan speed leads to increase surface roughness, and delamination between layers due to the decreasing the total energy delivered to the powder. Figure 7.36 shows two samples after infiltration.

Figure 7.34: Four samples with layer thickness 0.6 mm each

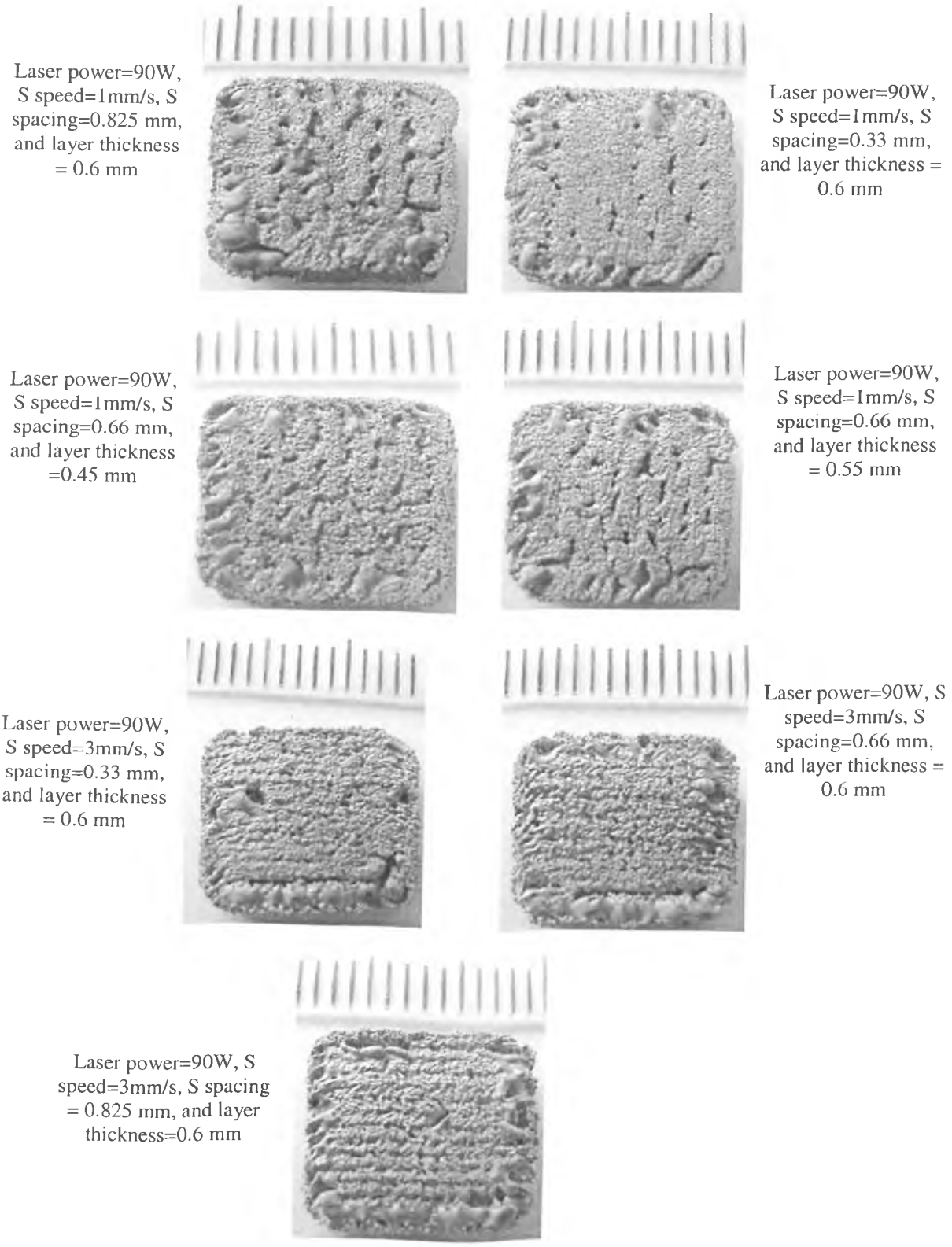

Figure 7.35: Photographs of some samples with different processing conditions

Figure 7.36: Two multiple layer samples after infiltration

7.6 Density Study with HSS

The results of the three experiments carried out to study density in the direct SLS processing of HSS are presented in the following sections.

7.6.3 Powder Bed Density

Table 7.1 shows the results for the apparent density of high-speed steel powder. In this table, W_{total} is the weight of the tray plus the loose powder, W_{tray} is the weight of the box, W_{powder} is the weight of the loose powder, and Vol is the volume of the tray. The density is represented by ρ. The average apparent density of the powder is 4.8969 ± 0.048 g/cm^3.

Table 7.1 Apparent Density of HSS Powder

No	Vol (cm^3)	W_{total} (g)	W_{tray} (g)	W_{powder} (g)	ρ (g/cm^3)
1	93.3229	1577	1119	458	4.907691
2	93.3229	1573	1119	454	4.86483
3	93.3229	1578	1119	459	4.918407
4	93.3229	1576	1119	457	4.896976
5	93.3229	1579	1119	460	4.929122
6	93.3229	1577	1119	458	4.907691
7	93.3229	1575	1119	456	4.88626
8	93.3229	1574	1119	455	4.875545
9	93.3229	1580	1119	461	4.939838
10	93.3229	1571	1119	452	4.843399
			Average Density		4.896976

7.6.4 Density of Monolayer Samples Sintered by Direct SLS Process

7.5.2.1 Density of Monolayer Samples Sintered by Direct SLS Process before Infiltration

Figure 7.37 shows the density of monolayers at different laser power, scan speed, and scan spacing. The laser power was varied from 30 W to 70 W, scan speed was varied from 1 mm/s to 5 mm/s, and scan spacing was varied from 0.22 mm to 0.66 mm. It can be seen from this figure that the density of single layer increases with increasing laser power or decreasing scan speed. A variation of scan speed and laser power has a greater effect on density than a variation of scan spacing, since the melted agglomerates of HSS material are positioned closer together for slower scan speeds and higher laser power. Thus, an increase in scan speed or a decrease in laser power may not be compensated by a decrease in scan spacing.

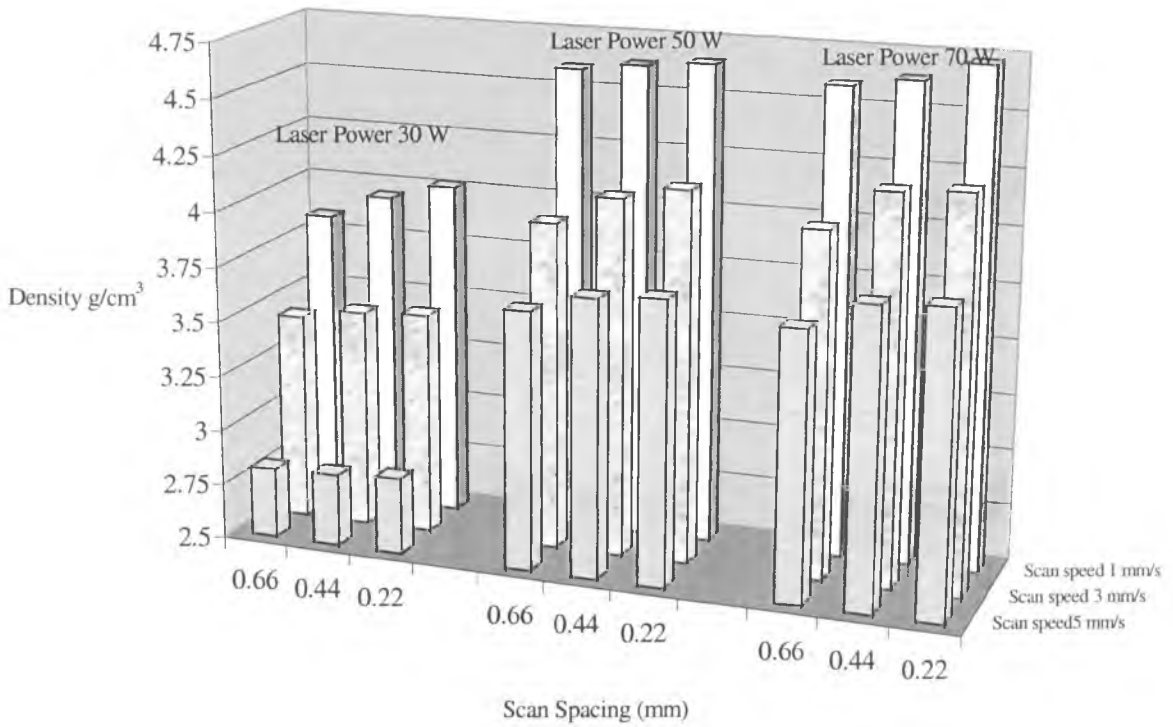

Figure 7.37: Influence of scan speed, laser power, and scan spacing on density of monolayer samples

7.5.2.2 Density of Monolayer Samples Sintered by Direct SLS Process after Infiltration

Table 7.2 presents the density results of monolayer samples before and after infiltration of the test carried out with the samples 30x25mm, processed at constant laser power 50 W, constant scan speed 1 mm/s, and constant scan spacing 0.682 mm/s. In this Table, It can be noticed the average density of the sample before infiltration is 4.6213 g/cm^3, and the average density of the sample after infiltration is 6.7276 g/cm^3.

Table 7.2 Density of monolayer samples before and after infiltration

No	ρ= g/cm^3 Before Infiltration	ρ= g/cm^3 After Infiltration
1	4.591	6.7305
2	4.601	6.7285
3	4.672	6.6247
4	4.675	6.7652
5	4.597	6.684
6	4.598	6.848
7	4.586	6.7354
8	4.598	6.7345
9	4.624	6.6843
10	4.671	6.7412
Average Density	4.6213	6.72763

7.6.5 Density of Multiple Layer Samples Sintered by Direct SLS Process

As shown in Figure 7.38 for a constant laser power (75 W), constant layer thickness 0.6 mm, and constant scan spacing 0.682, the density of multiple layer of HSS samples increased as the scan speed decreased. Also, the density was found to increase with increasing laser power, at a constant scan speed. Higher density is achieved with slower scan speed and higher laser power due to an increased amount of energy input to the powder surface. A higher amount of energy to the powder bed increases the temperature locally to result in a large amount of liquid phase formation.

As shown in Figure 7.39 the density of multiple layer samples of the direct SLS HSS increased as the layer thickness decreased. After the formation of a liquid phase inside the powder structure, the liquid phase wets the remaining solid particles. In addition, the melting causes a rearrangement the orientation and position of particles remaining solid. The increasing of density is due to the thermocapillary and gravitational forces as the melt flows deeper into the previously sintered structure.

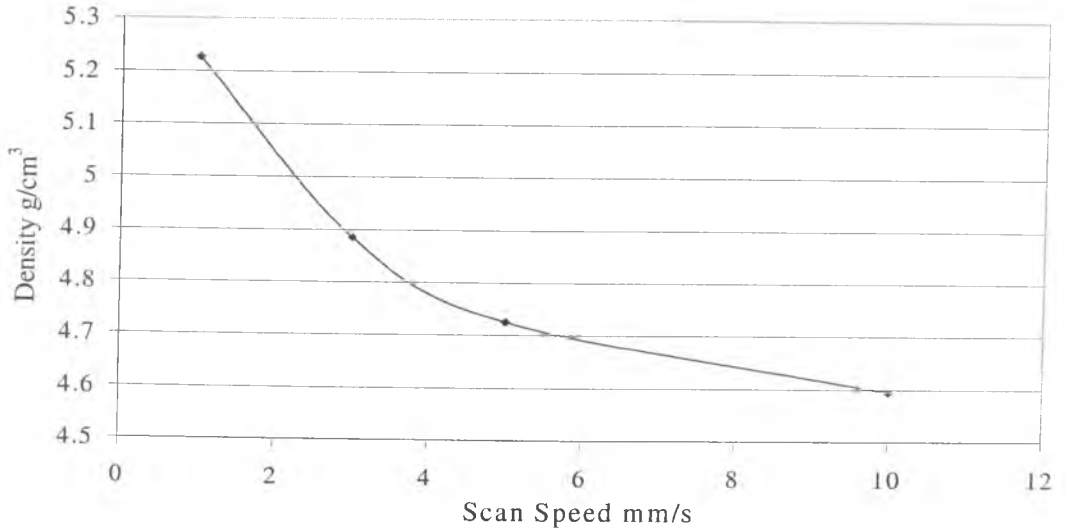

Figure 7.38: Density of direct SLS of HSS parts as a function of scan speed (Scan spacing 0.682 mm/s, laser power 75 W, layer thickness 0.6 mm and scan speed 1mm/s)

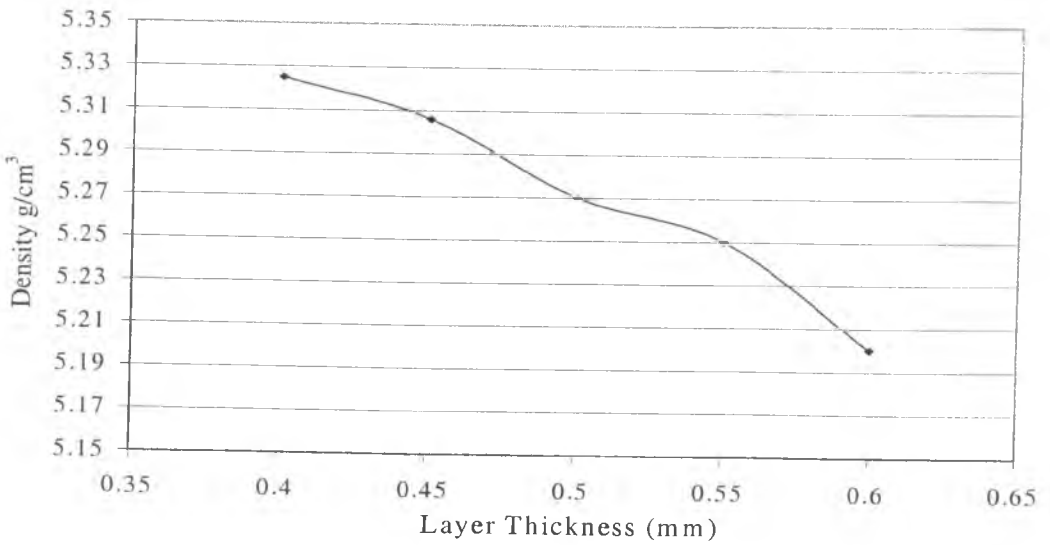

Figure 7.39: Density of direct SLS of HSS parts as a function of scan speed (Scan spacing 0.682 mm/s, laser power 75 W, layer thickness 0.5 mm and scan speed 1mm/s)

Table 7.3 presents the density results of sintered samples before and after infiltration of the test carried out with the samples 30x5x3.3mm, processed at constant laser power 75 W, constant scan speed 1 mm/s, constant scan spacing 0.682 mm/s, and constant layer thickness 0.5 mm. In this Table, It can be noticed the average density of the sample before infiltration is 5.1039 g/cm^3, and the average density of the sample after infiltration is 7.2878 g/cm^3.

Table 7.3 Multiple layer before and after infiltration

Sample No	ρ= g/cm^3 Before Infiltration	ρ= g/cm^3 After Infiltration
1	5.223	7.546
2	5.2176	7.4726
3	5.02	7.30257
4	4.904	7.448
5	5.1719	7.2639
6	5.02234	7.0785
7	5.0974	7.0216
8	4.92726	7.0778
9	5.21568	7.251
10	5.2401	7.4163
Average Density	5.1039	7.2878

7.6 Mechanical Properties of HSS

7.6.1 Mechanical Properties of Monolayer

7.6.1.1 Effect of Scan Spacing on Bending Strength

Figure 7.40 shows the effect of scan spacing on bending strength. The bend strength of the samples was determined when the load direction is parallel to scan direction. Although the density of monolayer samples increases with decrease the scan spacing as shown in figure 7.37 it was found that the bending strengths of monolayer samples are decreased with decreasing scan spacing. The scan spacing of 0.275 mm resulted in a lower bending strength than the scan spacing 0.55 mm and 0.682 mm; it is considered that excessive energy at the scan spacing 0.275 mm caused microscopic cracks.

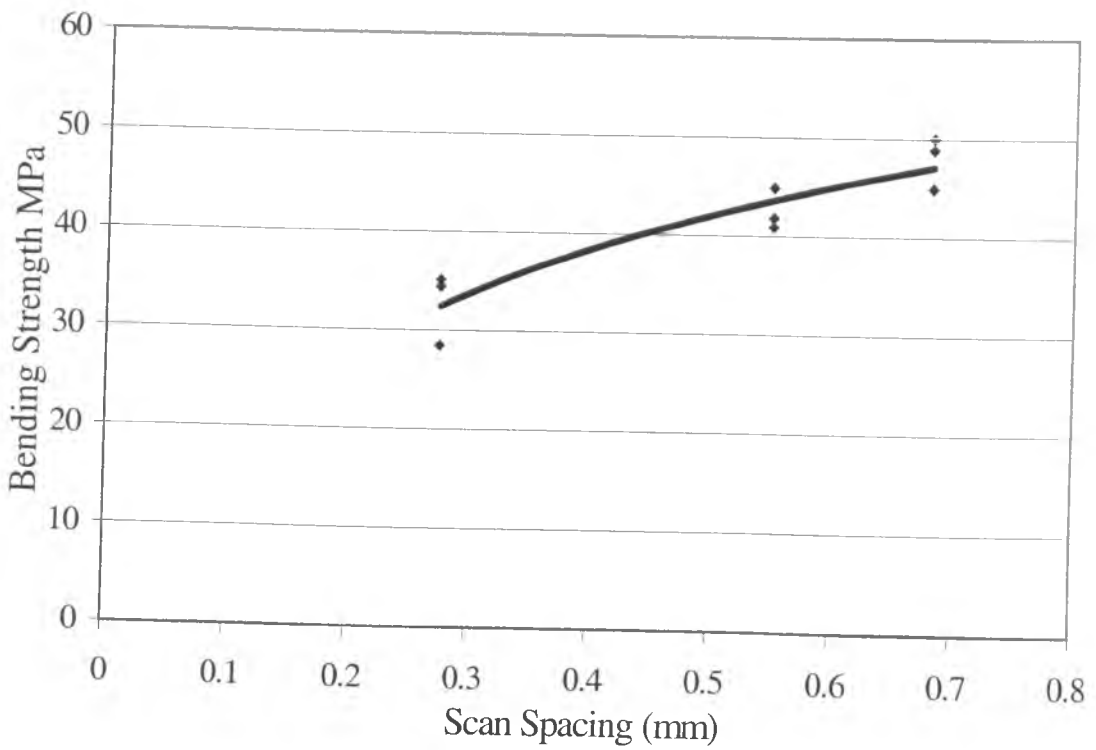

Figure 7.40: Influence of scan spacing on bending strength of HSS

7.6.2.2 Effect of Scan Direction on Bending Strength

Because of the SLS processing is a directional, layer-by-layer sintering process, it is expected that the degree of sintering will vary depending on the laser scanning direction and the build direction. The degree of sintering is higher in the direction of scanning and lower in the direction normal to scan direction in the build plane.

The variation of bend stress versus deflection of sintered samples (without infiltration) is shown in Figure 7.41. The bend strength of the samples when the load direction is perpendicular to scanning direction, parallel to scanning direction, and 45-degree to scanning direction was 255MPa, 47MPa, and 120.6MPa respectively.

The variation of bend stress versus deflection of infiltrated samples is shown in Figure 7.42. The bend strength of the samples when the load direction is perpendicular to scanning direction, parallel to scanning direction, and 45-degree to scanning direction was 631.77 MPa, 381.537 MPa, and 464.33 MPa respectively

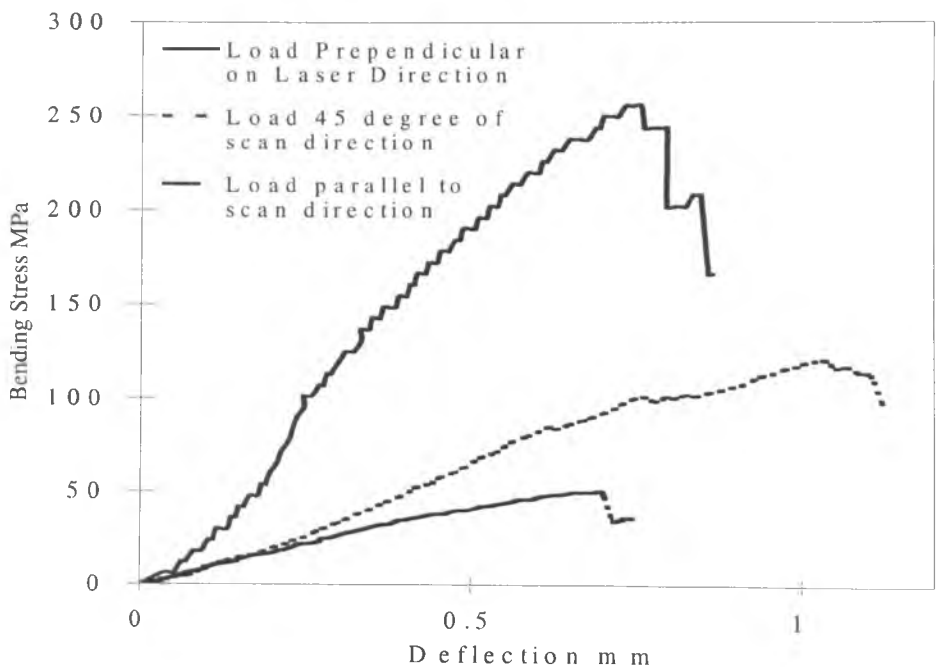

Figure 7.41: Bend stress-deflection curve for HSS obtained from four-point bend test, (apparent density 4.62 g/cm^3)

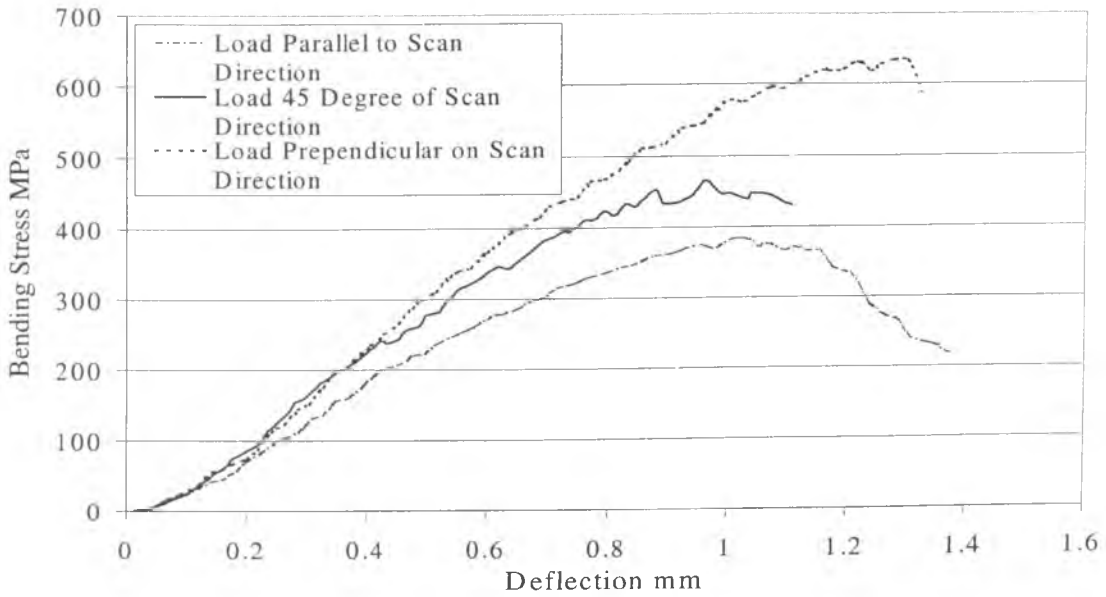

Figure 7.42: Bend stress-deflection curve for infiltrated HSS obtained from four-point bend test, (apparent density 6.7276 g/cm^3)

The average value of modulus of elasticity of mild steel samples cut from a sheet with length 30 mm, width 25 mm, and thickness 1.19 mm was 177.5 GPa. Table 7.4 summarise the variation in modulus of elasticity and bending strength with load direction for sintered HSS samples without infiltration which had a sintered apparent density of 4.62 g/cm^3 and infiltrated samples which had an apparent density of 6.7276 g/cm^3.

The important feature to mention on elastic modulus of sintered samples is the anisotropy. The variation of modulus of elasticity has occurred because the orientation of the agglomerates is parallel to the direction of scanning. The value of elastic modulus when the load was perpendicular on the scan direction is higher than those when the load was parallel to scan direction since pores and weak boundaries contribute

to the reduction of elastic modulus value in the in-plane direction. Inter-agglomerate pores between laser scan lines are shown in Figure 7.43.

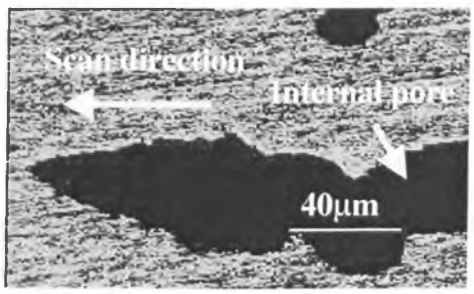

Figure 7.43: SEM images of laser sintered HSS.

Table 7.4: Flexural modulus and flexural strength for HSS material sintered by direct SLS obtained from four-point bend test

	After Infiltration		Before Infiltration	
	Flexural Strength MPa	Flexural Modulus GPa	Flexural Strength MPa	Flexural Modulus GPa
Load Perpendicular on Scan Direction	631.707±60.47	123.75±2.15	250±5	79
Load Parallel to Scan Direction	381.537±13	73.079±6.421	47±3.03	26.75
Load 45 degree of Scan Direction	464.33±33.6	88.275±10.41	120.6±20	34.45

7.6.2 Mechanical Properties of Multiple Layer

The variation of bend stress versus deflection of multiple layer sintered sample (without infiltration and with dimensions 30×5.5×3.2 mm) and multiple layer infiltrated sample with the same dimension as sintered sample is shown in Figure 7.44. It can be seen from

this figure that the bending strength of the sintered sample is about 150 MPa and the bending strength of infiltrated sample is about 460 MPa. The results also show that there are variations in the values of modulus of elasticity and bending strength of monolayer samples and multiple layer samples for the same material (see figures 7.42, and 7.44). This is may be due to the variation of aspect ratio of the samples.

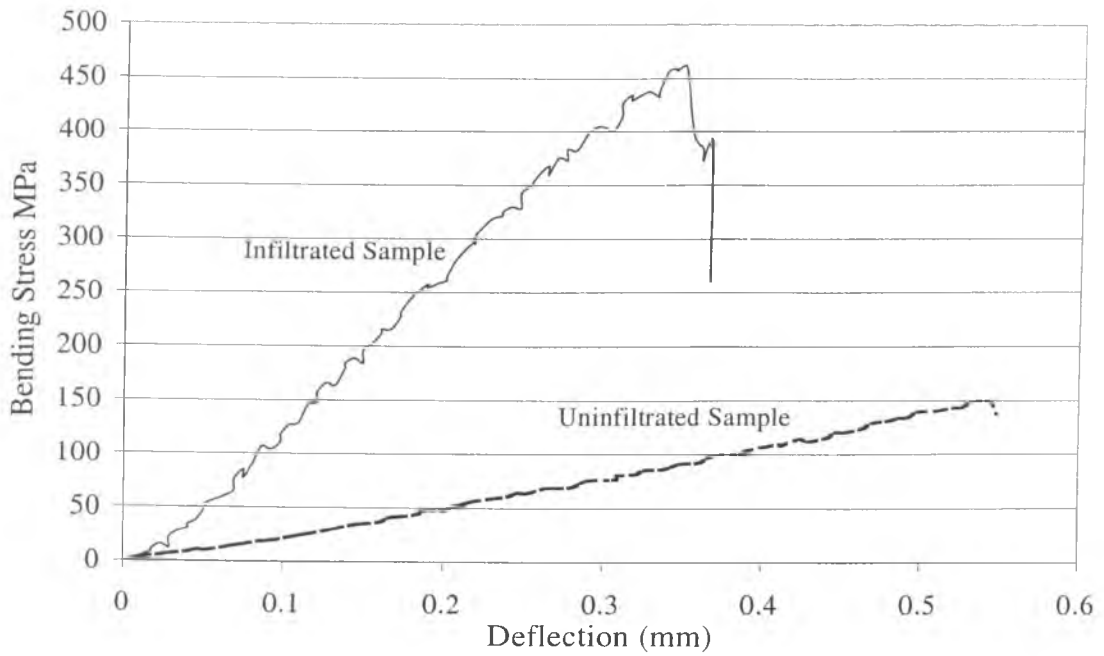

Figure 7.44: Bend stress-deflection curve for HSS obtained from four-point bend test before and after infiltration.

Figure 7.45 shows stress-strain curve for two samples of high-speed steel material of sintered sample and infiltrated sample. The 0.2% yield strength of infiltrated and sintered samples was found to be 200 MPa and 130 MPa respectively. The tensile strength of infiltrated sample was found to be 426.3 MPa, and 208 MPa for sintered sample with low modulus of elasticity 120 GPa.

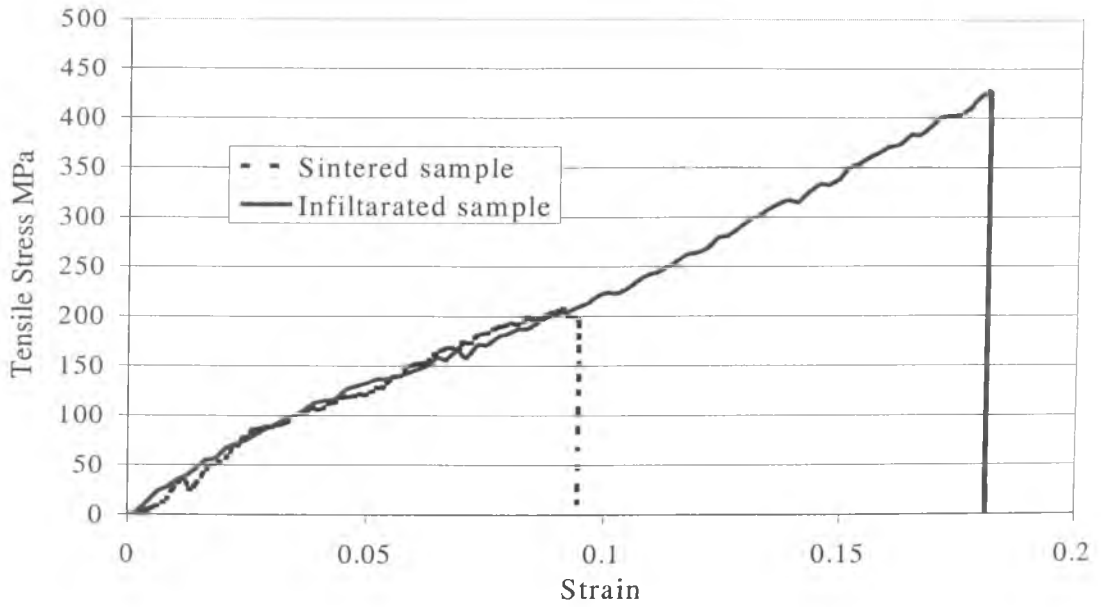

Figure 7.45: Stress-strain curve for HSS obtained from four-point bend test for sintered sample and infiltrated sample.

7.6.3 Hardness of HSS

The average hardness of infiltrated samples of high-speed steel was 36.2 HRC. This value distributes unevenly within the cross section from 30 HRC to 43 HRC.

7.7 Microstructure of Samples

7.7.1 Monolayer

Figure 7.46 shows a SEM of HSS powder sintered at power=50W, scan speed 1mm/s, and scan spacing 0.682mm. It can be seen from this figure that M_6C forms a continuous grain boundary film around austenite matrix with evidence of the early stages of M_6C eutectic formation.

Figure 7.47 shows a SEM of monolayer of HSS powder sintered at power=50W, scan speed 1mm/s, and scan spacing 0.682mm after infiltration cycle. This figure evidences the existence of small angular carbides M_6C dispersed in austenite matrix. The microstructures consist of large angular intergranular M_6C carbides, smaller intergranular M_6C, and grain boundary Fe–Mo rich and Fe–Cr rich phases.

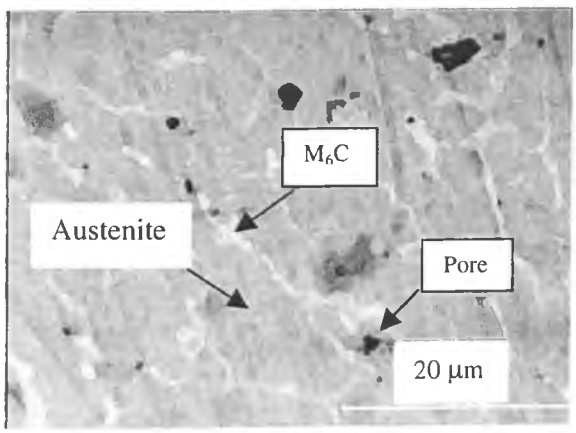

Figure 7:46 SEM of HSS powder sintered at power=50W, scan speed 1mm/s, and scan spacing 0.682mm.

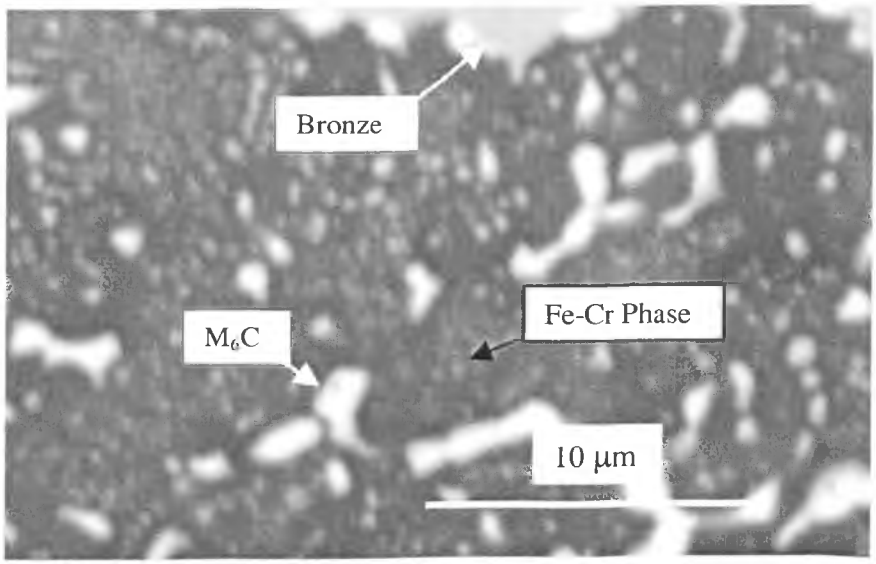

Figure 7:47 SEM of HSS powder sintered at power=50W, scan speed 1mm/s, and scan spacing 0.682mm after infiltration cycle.

7.7.2 **Multiple Layer**

Figure 7.48 shows a microstructure of cross sectional area of multiple layer sample sintered (five layers) using laser power 75 W, scan speed 1 mm/s, scan spacing 0.682 mm, and layer thickness 0.6 mm. It can be seen from this figure that the bonding between layers is not good, and the first layer is thicker than other layers due to bonus z.

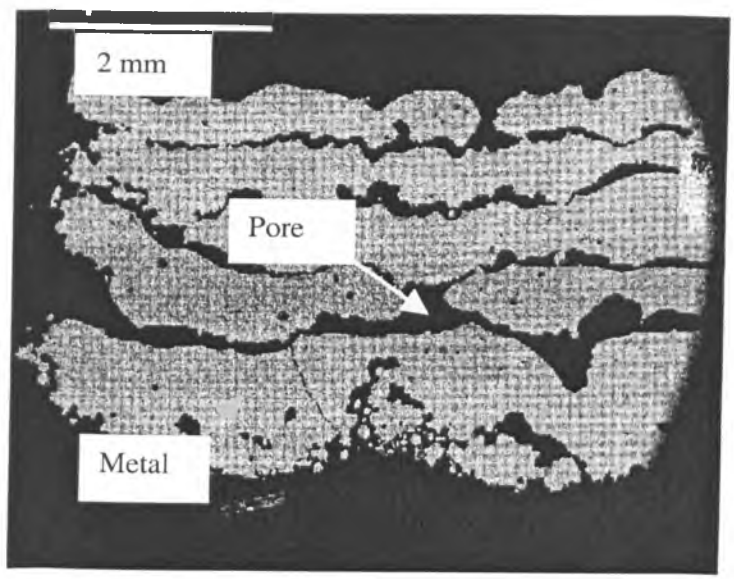

Figure 7.48: SEM of cross sectional area of multiple layer sample sintered using laser power 75 W, scan speed 1 mm/s, scan spacing 0.682 mm, and layer thickness 0.6 mm.

Figure 7.49 shows a SEM of cross sectional area of multiple layer sample (five layers) scanned using laser power 75 W, scan speed 1 mm/s, scan spacing 0.682 mm, and layer thickness 0.5 mm and sintered in a vacuum furnace at temperature 1240 $^{\circ}$C. It can be seen from this figure that the bonding between layers was improved, but still there is a lot of residual porosity. In addition, the average density of the samples was increased from 5.1039 g/cm^3 before sintering to 5.3623 g/cm^3 after sintering cycle.

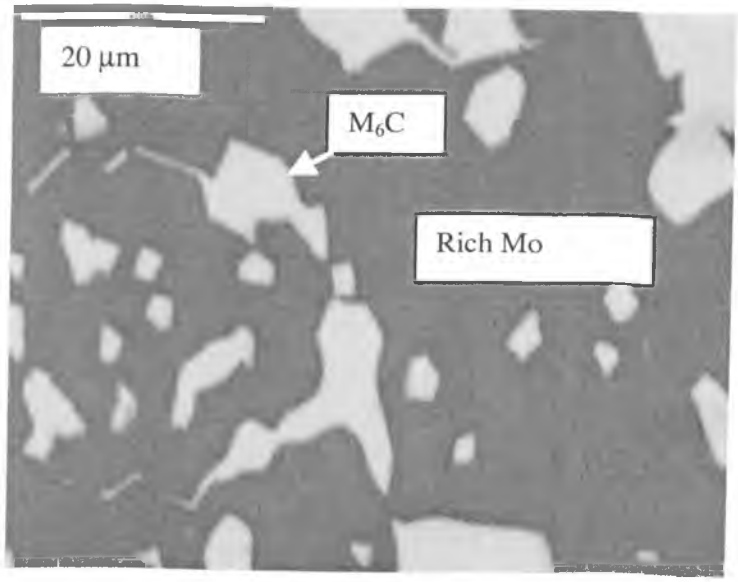

Figure 7.50: SEM of multiple layer sample scanned using laser power 75 W, scan speed 1 mm/s, scan spacing 0.682 mm, and layer thickness 0.5 mm and sintered in vacuum furnace at temperature 1250 °C.

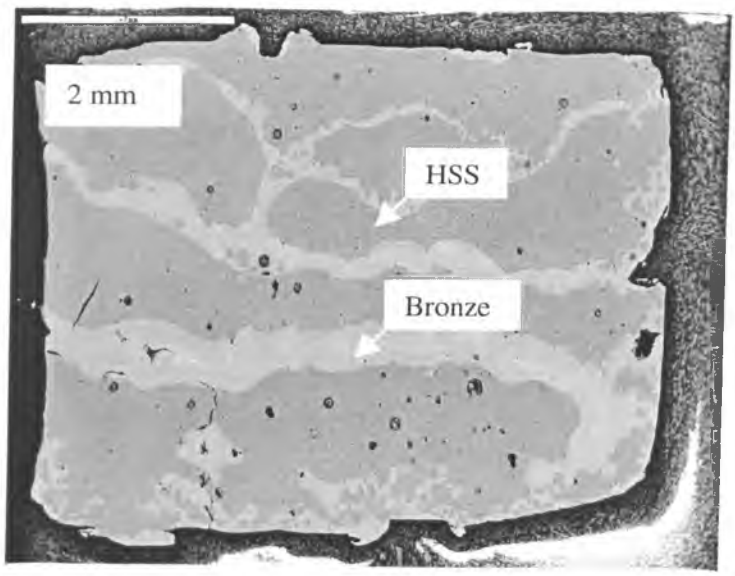

Figure 7.51: SEM of cross sectional area of multiple layer sample scanned using laser power 75 W, scan speed 1 mm/s, scan spacing 0.682 mm, and layer thickness 0.5 mm after infiltration cycle.

Figures 7.52, and 7.53 show a SEM of the bottom of the first layer. It can be seen from this figure that the carbides formed thin layers along the grain boundaries. The general principles of liquid phase sintering apply to the present sample, for which a liquid that wets the boundaries is formed in sufficient quantity during the process. The carbide films consisted of isolated particles and formed a necklace microstructure. As shown in Figure 7.53 the particles contain both of M_6C carbide, and $M_{23}C_6$ carbide which have small size. Due to the liquid phase sintering molybdenum rich M_6C carbides of large size, in an austenitic matrix were obtained.

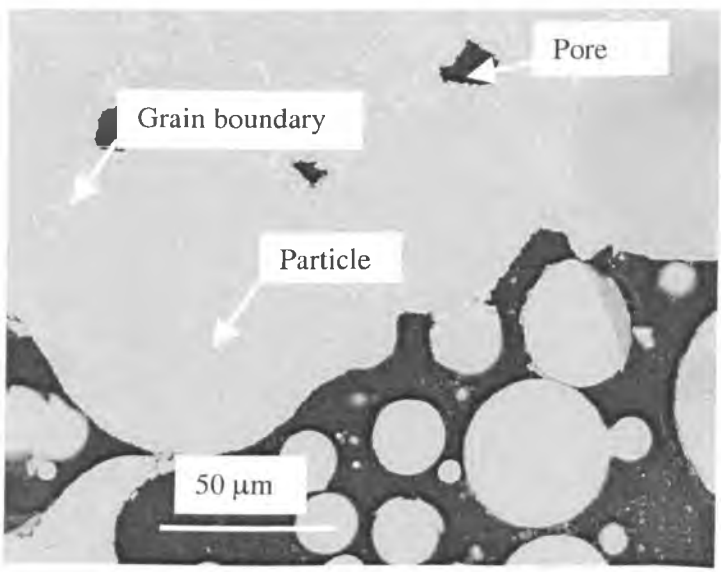

Figure 7.52: SEM of bottom of the first layer of multiple layer sample

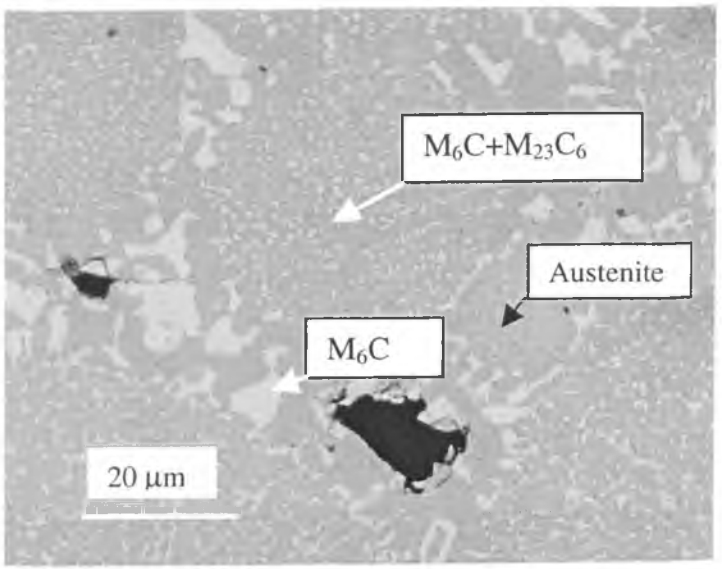

Figure 7.53: SEM of the bottom of the first layer of multiple layer sample

Figures 7.54 and 7.55 show scanning electron micrographs of the last layer of a multiple layer sample sintered at power=75W, scan speed 1mm/s, scan spacing 0.682mm, and layer thickness 0.6 mm without any post-processing. It can be seen from these figures that the significant incipient fusion of the itergranular M_6C carbides, leading to the formation of thick and continuous grain boundary films with evidence of early undesirable M_6C eutectic formation. This is due to the high energy density, which led to temperature value higher than the optimum sintering temperature of the HSS material.

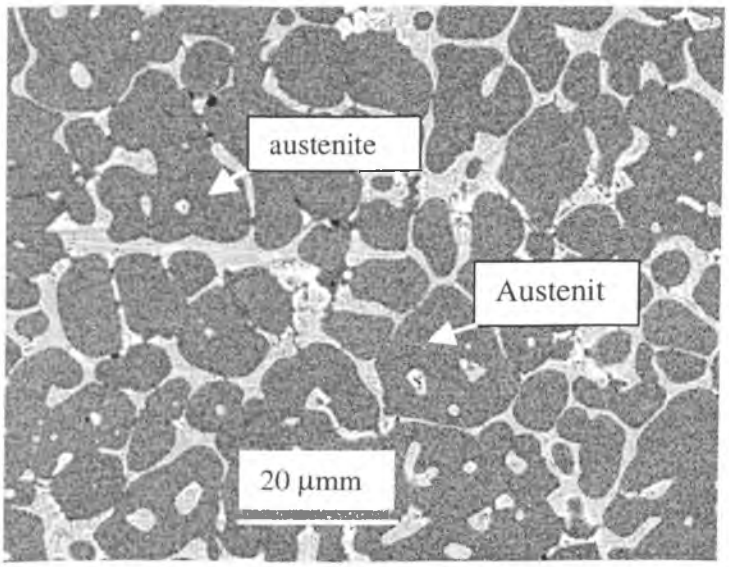

Figure 7.54: SEM of the last layer of multiple layer sample

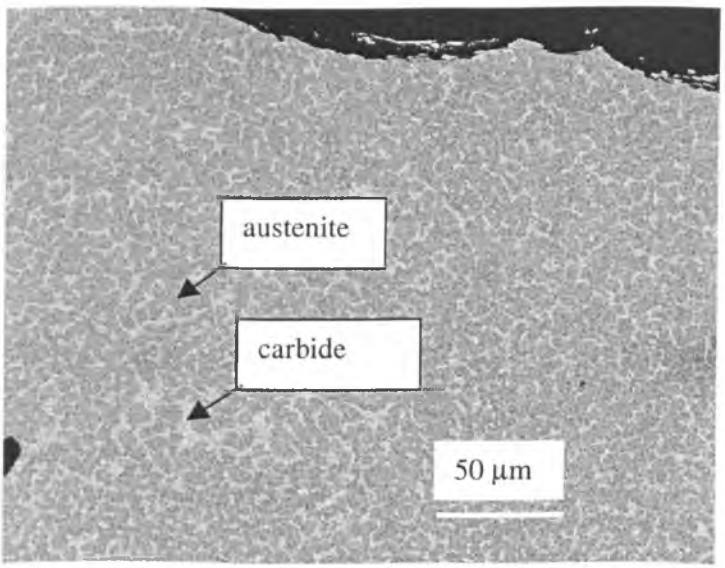

Figure 7.55: SEM of the last layer of multiple layer sample

Sintering at high temperature (due to increasing laser power, and/or decreasing scan speed, scan spacing, and layer thickness) as shown in figures 7.56 and 7.57 resulted in the gradual replacement of angular M_6C carbides with herringbone M_6C eutectic carbides of comparable composition. Melting of M_6C carbides occurred at higher

temperatures and coincided with sample distortion. Hence the sintering is located in the region defined by the solidus temperature and the reaction labelled austenite + M_6C + $M_{23}C_6$+ L phase region as shown in Figure 6.57.

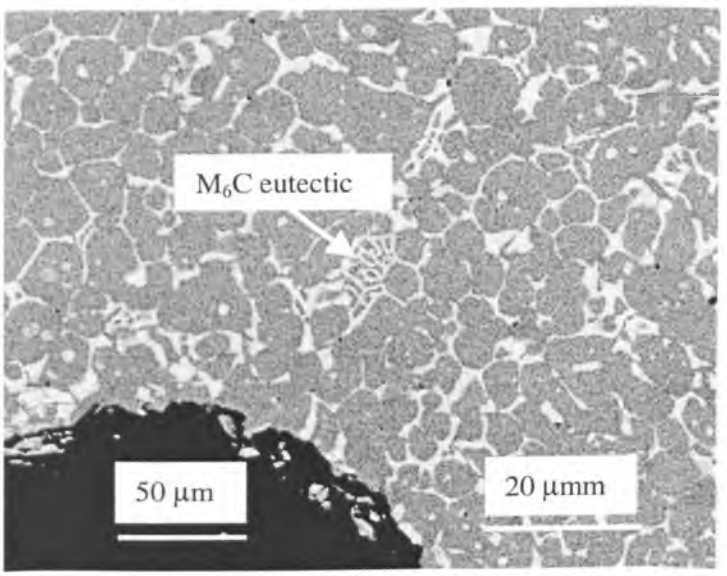

Figure 7.56: SEM of the second layer of multiple layer sample

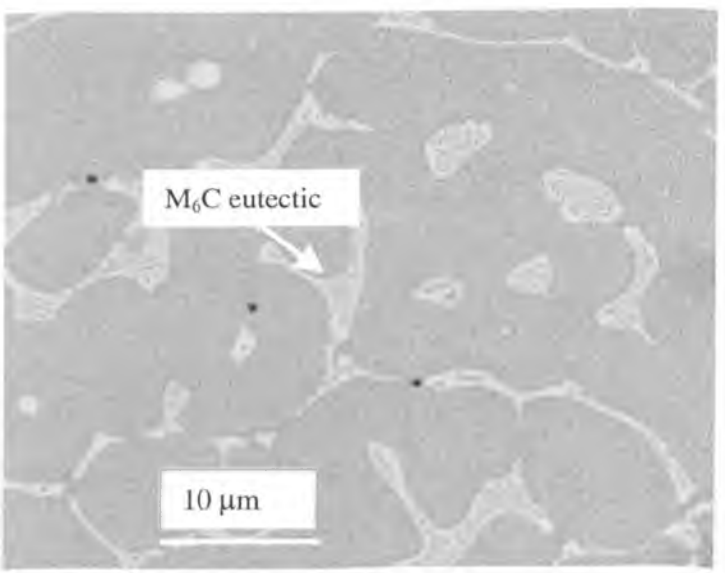

Figure 7.57: SEM of the second layer of multiple layer sample

Energy dispersive X-ray (EDX) analysis was performed to detect the components of the sample and their approximate percentage compositions. The EDX results and corresponding quantitative analysis are shown in Figure 7.58

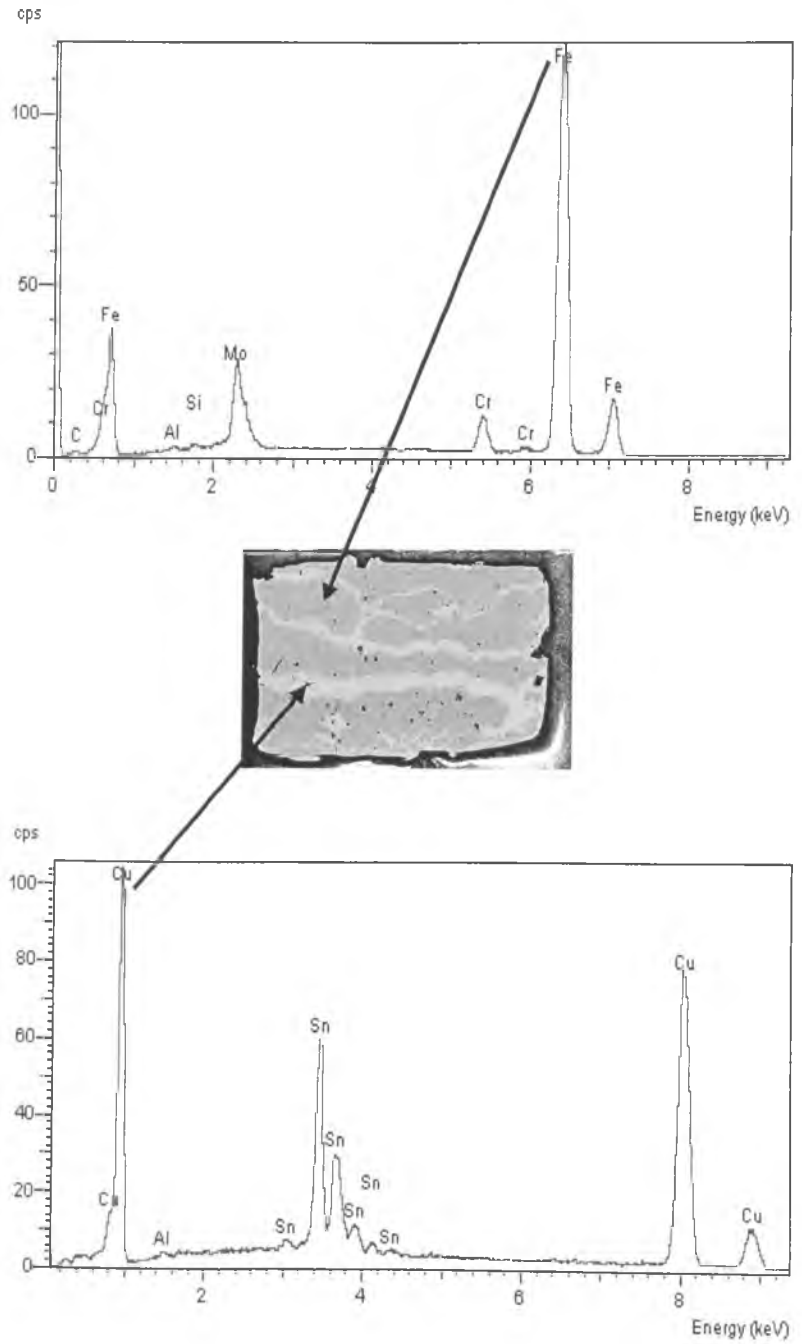

Figure 7.58: Energy dispersive X-ray (EDX) spectrum of infiltrated sample

7.8 Accuracy of Parts Using Direct SLS

As mentioned in section 7.2.1 the width of the single track depends mainly on the scan speed and laser power. So the accuracy of parts was varied in X direction and Y direction with varying the laser power and scan speed. To overcome problems due to shrinkage a trial monolayer (30×25 mm) with the best processing parameters for single layer (laser power 50 W, scan speed 1 mm/s, and scan spacing 0.682 mm) had been built, and measured its shrinkage and distortion in X direction and Y direction. According to the measurements a new design taking into account the dimensions and shape changes that occur during the process was created. The monolayer was then rebuilt with correction for the observed errors. Several measurements for many samples in X direction and Y direction were carried out. The dimensional results of sintered and infiltrated monolayer samples are presented in Table 7.5.

Table 7.5: Measurement results of monolayer samples in X, and Y directions

	Before Infiltration		After Infiltration		Before Infiltration		After Infiltration	
	Length mm	Error (mm)	Length mm	Error (mm)	width mm	Error (mm)	Width (mm)	Error (mm)
Sample 1	30.402	0.402	30.394	0.394	25.386	0.386	25.372	0.372
Sample 2	30.408	0.408	30.388	0.388	25.392	0.392	25.375	0.375
Sample 3	30.398	0.398	30.385	0.385	25.398	0.398	25.378	0.378
Sample 4	30.392	0.392	30.384	0.384	25.394	0.394	25.376	0.376
Sample 5	30.396	0.396	30.386	0.386	25.388	0.388	25.371	0.371

It can be seen from the table 7.5 that the absolute error in both X and Y directions for the samples produced by direct SLS was found to be ± 0.4 mm. The error of direct SLS parts is big compared with the indirect SLS parts, which may be due to the size of beam diameter (1.1 mm). There is no significant variation in dimensions after the infiltration cycle. The accuracy in Z direction was not measured. Because of the large beam diameter no attempt has been made to manufacture small features using direct SLS.

In addition, it was found that the average roughness R_a of the samples sintered using laser power 50 W, scan speed 1mm/s, and scan spacing 0.682 mm in the range 40-50 μm, which reduced to 40-45 μm after infiltration.

7.8 Building Rate

By using the equations from 3.1 to 3.5 in Chapter three (section 3.2.3) and the program which described in chapter 5 section 5.7, it was found that the sintering time of 80×80×80 mm cubic block using scan speed 1 mm/s, scan spacing 0.682 mm, and layer thickness 0.6 mm, is 347hours. Volpato [2001], reported that the difference of measured time and predicted time is very small (about 1.5%). The sintering time of this part using direct SLS process is larger than the sintering time of the same part using indirect SLS process by about 20 times. The delay time was assumed zero.

Other trials to use direct SLS for metals were performed in Birmingham University by Niu and Chang [1998, 1999, and 2000], and Liverpool University by O'Neill and Morgan [1998, 1999, and 2001]. Niu and Chang [2000] reported that the processing parameters to produce a dense surface of M2 high-speed steel materials are; laser power ranges from 40 to 80 W, scan spacing 0.15 mm, and scan speed ranges from 1 to 25

mm/s. From the above conditions it was found that the sintering time of 80×80×80 mm cubic block, by using the prediction program, will be ranged from 63 to 1580 hours, if the layer thickness was assumed constant (0.6 mm). The delay time was assumed zero.

O'Neill, and Morgan [1999, 2001] reported that the processing parameters to produce a dense part of gas atomised 316L stainless steel materials are; laser power ranges from 25 to 75 W, scan spacing 0.025 to 0.05 mm, scan speed ranges from 100 to 200 mm/s, and layer thickness 0.04mm. From the above conditions it was found that the sintering time of 80×80×80 mm cubic block, by using the prediction program, will be ranged from 355to 1422 hours. The delay time was also assumed zero.

Simchi [2001] on direct metal SLS with powder mixes has shown that some direct metal SLS systems can operate at more competitive build rates.

Figure 7.59 shows the predicted time for different scan speeds and layer thickness at constant scan spacing (0.682 mm). It can be seen from this figure that decreasing scan speed or layer thickness leaded to increase sintering time.

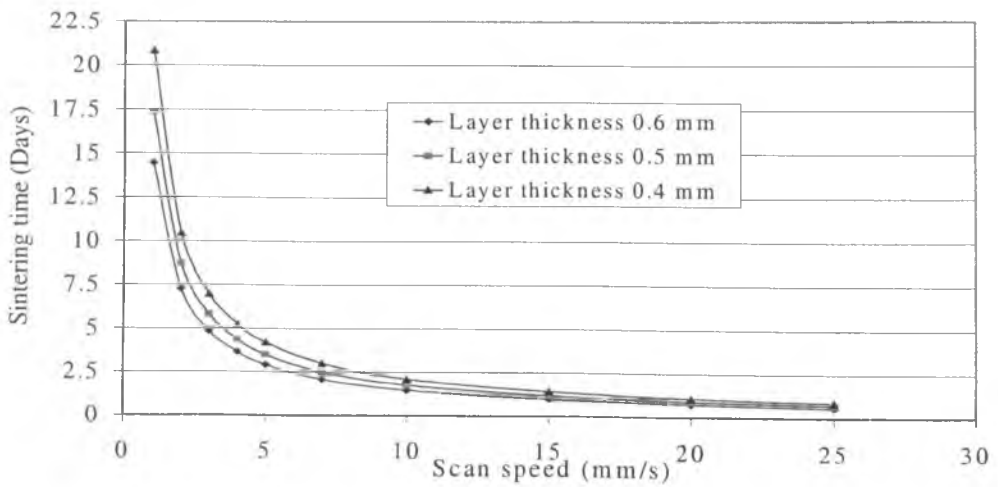

Figure 7.59 Sinter time needed to build a 80×80×80 mm part at constant scan spacing (0.682 mm), and constant layer thickness (0.6 mm)

7.9 Summary

This chapter has described how the processing conditions for a particular grade of high-speed steel were developed, and has introduced the results of tests designed to measure the mechanical properties of high-speed steel produced using direct selective laser sintering process (strength and hardness). The results of density on the powder bed, sintered parts, and infiltrated parts have been presented. In addition, the results of dimensional accuracy were presented and analysed in this chapter. Also the evolution of microstructure of high-speed steel has been described. Finally, the building rate for this material (HSS) using direct selective laser sintering was calculated.

CHAPTER EIGHT

GENERAL DISCUSSIONS AND CONCLUSIONS

8.1 Introduction

The main aim of this work is to characterise between indirect selective laser sintering process and direct selective laser sintering process of metals, to create rapid tooling, has been carried out. Three main areas were addressed during the study: mechanical properties and density of the DTM RapidSteel 2.0 material and the high speed steel material, bulk accuracy and small features accuracy of RapidSteel 2.0 material and the high speed steel material produced using indirect and direct SLS processes respectively, and build rate for parts produced using indirect and direct SLS processes.

A series study was carried out to understand and find the optimum processing conditions of HSS material using direct SLS process. In the SLS stage, the bulk and small features accuracy was investigated experimentally for both indirect and direct SLS processes. The influence of scan length on linear accuracy was studied using two generations of SLS machines (Sinterstation 2000 and research machine, which constructed in Leeds) and also two materials (RapidSteel 2.0 and high-speed steel).

Density and size accuracy of sintered parts using indirect and direct SLS processes have been measured. Measurements of the dimension have been carried out using a Co-ordinate Measuring Machine (CMM) with accuracy 0.001 mm and a vernier calliper with accuracy 0.01mm. Weights of the sintered parts have been measured using an electronic balance with accuracy 0.001 g. A Scanning Electron Microscope (SEM) has

also been used to observe microstructure of the sintered parts and the effect of infiltration cycle on microstructure.

This chapter presents initially some discussions about the results of the investigations carried out in this work. Discussions are focused on three main sections. The first is the experimental results of density and mechanical properties of metals using indirect and direct SLS processes. The second is the experimental accuracy results, and finally the building rate for both processes. The chapter ends with conclusions.

8.2 Experiment Results on Sintered Part Density

8.2.1 Density of RapidSteel 2.0

The average apparent density of the RapidSteel 2.0 was found to be 4.2157±0.026 g/cm^3, and the average density of sintered RapidSteel 2.0 material was found to be 4.3727 g/cm^3. The density measurement results have shown that the density of the RapidSteel 2.0 material after sintering, using the recommended conditions, was increased about 3.7%. This small increase was expected and it is in agreement with other authors related to the SLS processing of similar composites.

Experimental results were also shown that when RapidSteel 2.0 was processed with low energy density, some measured densities of the green material were lower than the average density of the powder bed. Because the density increase after indirect selective laser sintering is small (3.7%), any small error during the dimensional measurement can have a great effect on the results. One possible source of this difference in the results was that the measurement systems used for the density box (caliper) and for the strips (Coordinate Measuring Machine), work with different methods of measurement. The

CMM uses a probe with a spherical head of 2mm in diameter whereas the calliper uses a flat contact area. Due to the softness of the green RapidSteel 2.0, mainly when processed with lower energy density, this can make a difference in the final dimension. It would be preferred to have used the same measurement system for all the experiments.

It was also found that increasing laser power (energy density) leads to increase the density of the green parts until certain value, and then falls off. The drop in density is due to an excess of energy, causing the decomposition or burning of the polymer binder. It was found, as expected, that increasing the density by partial or full infiltration has significant effect on strength of RapidSteel 2.0 material. The density of the brown samples (samples without infiltration) and full dense samples were found to be 4.307 g/cm^3 and 8.03 g/cm^3 respectively. Samples without infiltration (brown part), incompleted infiltration, and full infiltrated were presented average tensile strength 35 MPa, 366.17MPa, and 671.3 MPa respectively.

In addition, samples closest to the bronze infiltration are only 3% more dense than samples further away, however, this small variation in density appears to weaken the internal structure by up to 35%.

8.2.2 Density of High Speed Steel

An increase in laser power leads to an increase in the sintering depth of the layer, and an increase in the density of the part, since more energy is delivered into the powder and large melt pools fill up the porous structures of previous layers. However, surface roughness also increases since the molten particles tend to form large spherical structures.

The direct selective laser sintering at low scan speeds has a tendency to cause the formation of the coarse and dense agglomerates because of the highly localised heat input and greater heat affected zone around the laser beam, thus increasing agglomeration of powder particles outside the laser beam, and increasing the density of the part. However, at high scan speeds, the amount of heat transferred to the powder material per unit time is reduced, resulting in a lower amount of supersolidus liquid phase sintering per unit volume and so giving less agglomeration outside the laser beam, with small agglomerates and pores which leads to low density. In general, increasing scan speed leads to a decrease in the width, depth, and density of the part.

The effect of increasing scan spacing on incident laser energy density is the same as that of decreasing laser power. Small scan spacing results in an increased overlap of the scan lines and an increase of the total energy imparted on the powder layer. When the scan spacing is small the molten powder particles from separate larger beads of high density leading to an overall high density of the part, yet the surface roughness also increases due to increasing interaction between the latter scan and the previous scan. In addition, a very small scan spacing tends to create a lot of tears and cracks due to thermal effects. However, very large scan spacing tends to decrease the bonding between the scan tracks and increase the formation of the lateral pore in the sintered part, resulting also in a rough surface and low density.

The warping phenomenon was noticed during building. The solid layer on the powder bed warped due to heating and cooling while the laser beam travelled on the track. The laser beam moves on the powder bed accompanying the high temperature region within the solid. Since the layer is subjected to thermal expansion and shrinkage, thermal stresses are caused within the solid part. The amount of the distortion of the layer

increases as the length of the layer increases. Therefore, scanning of a long track should be avoided to fabricate a large area on the powder bed. To avoid the warping of large layers, it is desirable to reduce the scan length by dividing the area into small segments. The influence of layer thickness is important for the density. With a smaller layer thickness, more energy is transferred to the underlying sintered layers improving further densification.

Of all the parameter combinations that led to a stable sintering process, the average density of monolayer and multiple layer sintered high speed steel material was 4.6213 g/cm^3 or 57.776% of theoretical density (laser power = 50 W, scan speed = 1 mm/s, and scan spacing = 0.682 mm), and 5.1039 g/cm^3 or 63.80% of theoretical density (laser power = 75 W, scan speed = 1 mm/s, scan spacing = 0.682 mm, and layer thickness = 0.6 mm) respectively. The average apparent density of the high speed steel was found to be 4.8969±0.048 g/cm^3. This indicates that the average density of the sintered part obtained in this work is close to the apparent density of the loose powder.

The densities of the sintered monolayer parts were lower than the average density of the loose powder. One possible source of this difference in the results was that the error of measurements because the surface of the monolayer is not completely flats. The other possible reason of this difference may be the effect of the internal pores of the parts. The density of the monolayer samples and multiple layer samples after infiltration cycle were found to be 6.7276 g/cm^3 and 7.2878 g/cm^3 respectively. These values are less than the full dense by about 15% and 9%. These variations may be also as a result of error of measurements or due to the effect of residual pores.

8.3: Tensile Strength of RapidSteel 2.0 and High Speed Steel Materials

8.3.1 Tensile Strength and Hardness of RapidSteel 2.0 Materials

As mentioned, many studies have been completed on the variation in mechanical properties of materials produced by indirect selective laser sintering, considering the effects of parameters such as laser orientation and energy density. The additional furnace sintering and infiltration required to manufacture RapidSteel 2.0 parts adds a further source of variation. The results presented in chapter 5 show that variations of strength of samples using two types of furnace, which are recommended by DTM for processing the RapidSteel material, are not significant. When comparing the Leeds results to those taken from identical samples with the default furnace cycle manufactured in Germany a similar pattern is observed. In addition, all of samples which were taken vertically generally fractured at the top of the block where the pores more largely than the bottom. This is because the top of the block far away than the bronze (infiltrant) position.

A pattern of degradation appears to be present with strength decreasing with distance from the position on bronze infiltration in the horizontal direction.

The 0.2% yield strength of RapidSteel 2.0 material varied from 250 to 350 MPa, and the ultimate strength ranged between 375 to 693 MPa, with the maximum elastic modulus about 256 GPa.

The maximum hardness of infiltrated was found to be 23.81 HRC and the maximum value of hardness for brown samples was found to be 33 HRC. The hardness of infiltrated samples is lower than the hardness of brown samples due to the attendance of

the bronze. The main reason for this is that the range of hardness of brown samples is narrow (28 to 33 HRC) where the diamond cone always contacts with stainless steel particles. In contrast, in the case of infiltrated samples the range of hardness is wide (15-33). This is because the diamond cone randomly hits hard stainless steel particles or soft bronze particles.

The attendance of the bronze also leads to increase the ductility of the RapidSteel 2.0 material, where the elongation of the brown samples is ranging from 0.94% to 1.88%, and the elongation of the infiltrated samples is ranging from 5.912% to 8.238%.

Table 8.1 summarises the mechanical properties of RapidSteel 2.0 produced by DTM and the mechanical properties produced during this work. It can be seen that there is no significant variation between the two of them.

Table 8.1: RapidSteel 2.0 Properties

Material	0.2% Yield strength (MPa)	Fracture strength (MPa)	Modulus of elasticity (GPa)	Hardness (HRC)
RapidSteel 2.0 (Leeds)	350	693	256	23.81
RapidSteel 2.0 (DTM)	413	580	263	22.0

8.3.2 Mechanical Properties of High Speed Steel

The results of sintered high-speed steel material show that the strength is a function of fractional density (or porosity), which pores reduce the effective load carrying capacity of a material. Also pores act as stress concentrations and as effective crack initiation sites. The strength would decrease as the porosity of the sintered part increases because of the presence of voids in the microstructure. The initial cracks will thus require less

force to break. Therefore, a sample with density less the 100% is expected to have a strength less than that of a fully dense wrought material.

The results show that the bending strength of the samples the bend strength of the samples when the load direction is perpendicular to scanning direction, parallel to scanning direction, and 45-degree to scanning direction was 255 MPa, 47 MPa, and 120.6 MPa respectively, and the modulus of elasticity is 79 GPa, 26.75 GPa, and 34.45 GPa respectively. The variation of bending strength and modulus of elasticity has occurred because the orientation of the agglomerates is parallel to the direction of scanning, and attendance inter-agglomerate pores between laser scan lines. The same trend was observed for infiltrated samples, but the values are higher than for sintered samples. From the above it can be concluded that the infiltration is very important to improve the mechanical properties and density of the sintered high-speed steel material. The 0.2% yield strength of infiltrated and sintered samples of high-speed steel material was found to be 200 MPa, and 130 MPa respectively. The tensile strength of infiltrated sample was found to be 426.3 MPa, and 208 MPa for sintered sample with relatively constant modulus of elasticity 120 GPa. Bronze penetrates into the parent metal, fills the voids and makes the metal denser and stronger. In general, these values are lower than the corresponding values of RapidSteel 2.0.

Although the variation of the modulus of elasticity of the samples for the same material (sintered high-speed steel), the modulus of elasticity is not a variable material properties. The reason for these differences, mainly because the material is not homogeneous, isotropic and linearly elastic.

The hardness of infiltrated samples of high-speed steel material was found 36.2 HRC.

8.4: Accuracy of RapidSteel 2.0 and High Speed Steel Materials

8.4.1 Indirect SLS Accuracy (RapidSteel 2.0 Material)

As discussed in chapter 2, section 2.2.6.4, accuracy can be defined as the deviation of the geometry from the progenitor CAD model to the part. The error of accuracy can be mainly due to pre-process errors, process errors, and post-process errors.

This work was concerned about the processing and the post-processing errors only. From the results of the experimental accuracy tests with bulk and small features it was observed that the absolute error increased with the decrease the scan length. This effect was observed in all directions. The error in width of small features (negative and positive) is ranging from ±0.3 to ±0.5 mm. This error is considered to be big because the time between laser exposures is reduced, therefore, the processing temperature increases. Consequently, this may lead to an increase in absolute error. Apart from this error, the error for all dimensions and in all directions is within ±0.2mm. It was also observed that the sintering and infiltration cycles have no significant effect on the absolute error. The sintering cycle led to some shrinkage, while the infiltration cycle led to swell. In addition, it was observed that the bulk accuracy within ±0.2mm in all directions.

8.4.2 Direct SLS Accuracy (High Speed Steel Material)

The accuracy of single lines and monolayers of high speed steel material using direct selective sintering in the X and Y directions was measured. It was observed that the error were not similar in X and Y directions. The difference between the error in both

directions has no physical explanation. This error was found to be due to some systematic error in the scanning system in sinterstation research machine. An accuracy improvement was observed in large dimensions after modification the scanning program. The error was found to be ±0.4mm in both X and Y directions. The error of direct SLS parts is large compared with the indirect SLS parts, which may be due to the big size of beam diameter (1.1 mm). In addition, there is no significant variation in dimensions after the infiltration cycle. Because of the large beam diameter no attempt has been made to manufacture features and internal channels on a small scale using direct SLS.

An average roughness R_a in the range 40-45 μm was obtained after infiltration cycle.

8.5 Building Rate

Building-time rate can be defined as the time required for building a physical part. Although the SLS machine has an integrated build-time estimator, it is highly inaccurate. This reason, thus, led us to create a build-time estimator for the SLS process. A new algorithm was created to estimate the build time. This algorithm is useful step in developing a build time estimator for any SLS machines. This algorithm also includes the material properties, process parameters like layer thickness, scan spacing, and the machine parameters like work-bed temperature. The estimated build times for 80×80×80 mm cubic part using indirect SLS process and direct SLS process were found to be about 17 hours for indirect SLS process, and ranging from 63.21 to 1580 hours for using direct SLS process. The large build time using the direct SLS process is due to the low scan speed during the SLS process. It was also found that the direct SLS parts still

need post-processing. Table 8.2 presents a comparison between RapidSteel 2.0 material using indirect SLS process, and high-speed steel material using direct SLS process

Table 8.2 Presents a comparison between RapidSteel 2.0 material using indirect SLS process, and high-speed steel material using direct SLS process. Both infiltrated with bronze

Property	RapidSteel 2.0	High speed steel
Hardness	23.81	36.2
Yield Strength (MPa)	350	200
Ultimate Strength (MPa)	693	426
Modulus of elasticity (GPa)	256	110
Surface quality R_a (μm)	6-10	40-45
Building time for 80×80×80 mm part (h)	17.5	348

8.6 Future Work

As mentioned the aim of Rapid Tooling is to reduce the cost and lead times required for the tooling phase in production cycle. For successful tooling using indirect or direct selective laser sintering several considerations must be taken into account. Beside the influence of processing parameters such as scan speed, scan spacing, and layer thickness, the laser type and powder characteristics are also special concern. Kruth et al [1999] reported that the Nd:YAG laser gives better results than the CO_2 laser for direct selective laser sintering of metal powders. This is because the Nd:YAG laser has a better penetration, a large processing window and results in parts with higher density.

These advantages along with the physical property that metals have a better absorption coefficient for laser light with smaller wavelength make the Nd:YAG laser at the moment the best laser for direct selective laser sintering of metal powders. So it would be appropriate to test high-speed steel with the Nd:YAG laser. Additionally, to improve the accuracy of high-speed steel parts small laser beam diameter should be used. Considering the maximum density of high-speed steel was approximately 67%, there is still room for improvement in the density of the parts. This can be achieved by several ways, firstly, changing the chemical composition of high-speed steel to increase the sinterability of the powder, secondly, improving the distribution mechanism to decrease layer thickness, thirdly, using finer powders, and finally changing the strategy of building.

This work has focussed on injection moulding as the application, and has identified mechanical properties, accuracy and surface finishing, and building rate as the key criteria for this application. An extension of this approach would be to develop in detail process requirements and to then map these to specific processing conditions. This would result in a more detailed process model, which could be applied in principle to any application of SLS.

8.7 Conclusion

A brief summary of the differences we have found between the indirect SLS process and the direct SLS process so far are:

Both direct and indirect SLS process can generate components with sufficient mechanical properties to act as mould tools. Neither direct nor indirect SLS is currently capable of making a net shape component at the accuracy (±0.2 mm) and surface

roughness levels (3 to 6 μm) mould tooling applications demand. For the two material systems studied here indirect SLS is capable of building components at a significantly higher rate than direct SLS. Other work [Simchi 2001] on direct metal SLS with powder mixes has shown that some direct metal SLS systems can operate at more competitive build rates (of the order of two days manufacture tool), but further assessment of this is required. The variation in accuracy caused by furnace cycles is very limited for both processes, so good sinterstation process control is essential to ensure accuracy. With regard to using the indirect SLS process to generate full production tooling, it has been found that it is possible to generate near net shape tools which require post-processing (finishing operation) to meet production specification. There are geometric limitations on this process with regard to small features (2mm or less). The RapidSteel 2.0 with indirect SLS gives better opportunity for direct tooling for plastic injection moulding than high-speed steel with direct SLS.

The thermal gradients that exist during direct SLS caused warping when the scan length is long in both single line and single layer. The density of laser sintered HSS increases with decreasing scan spacing, scan speed and/or increasing the laser power, but the surface roughness increases. The samples obtained are hard solid structures but with porosity which can be removed by infiltration or sintering in furnace. The flexural modulus as a function of the density of the samples when the load is perpendicular to the direction of scanning is high, compared with conventional sintering.

The surface properties of laser sintered high-speed steel material inserts require more development work in order to obtain smoother surfaces for tooling inserts in a shorter time. Small powder particle sizes and thin layers to improve surface quality is required. In addition, it can be concluded that direct laser sintering of high-speed steel was not an

appropriate route for mould tooling. This approach (direct SLS) is likely to have greatest application in the direct manufacture of small components, with micro scale components a possibility.

References

Agarwala M. David Bourell, Beaman J.J, Marcus H. and Barlow J., "Direct Selective Laser Sintering of Metals," Rapid Prototyping Journal, Vol. 1 No. 1, pp. 26-36, 1995 a.

Agarwala M. K., David L. Bourell, Benny Wu, and Beaman J.J., "An Evaluation of the Mechanical Behavior of Bronze-NI Composites Produced by Selective Laser Sintering," Proceeding of the Solid Freeform Fabrication Symposium, The University of Texas at Austin, Austin, Texas, pp. 193-203, 1993.

Agarwala M., Bourell D., Beaman J.J, Marcus H. and Barlow J., "Post-Processing of Selective Laser Sintered Metal Parts," Rapid Prototyping Journal, Vol. 1 No. 2, pp. 36-44, 1995 b.

ASM, "Mechanical Testing," Metals Handbook 9th Edition, 1984.

Badrinarayan B., and Barlow J. W., "Effect of Processing Parameters in SLS of Metal-Polymer Powders," Proceeding of the Solid Freeform Fabrication Symposium, The University of Texas at Austin, Austin, Texas, pp. 55-63, 1995.

Badrinarayan B., and Barlow J. W., "Manufacture of Injection Molds Using SLS", Proceeding of the Solid Freeform Fabrication Symposium, The University of Texas at Austin, Austin, Texas, pp. 371-378, 1994.

Badrinarayan B., and Barlow J. W., "Metal Parts From Selective Laser Sintering of Metal-Polymer Powders," Proceeding of the Solid Freeform Fabrication Symposium, The University of Texas at Austin, Austin, Texas, pp. 141-146, 1992.

Beaman J. J., Barlow J. W., Bourell D. L., Crawford R. H., Marcus H. L., and McAlea K. P., "Solid Freeform Fabrication: A New Direction in Manufacturing," Kluwer Academic Publishers Group, 1997.

Boivie Klas, "SLS Application of the Fe-Cu-C System for Liquid Phase Sintering," Proceeding of the Solid Freeform Fabrication Symposium, The University of Texas at Austin, Austin, Texas, pp. 141-149, 2000.

Bunnell D. E., Bourell D. L., and Murcus H. L., " Fundamentals of Liquid Phase Sintering Related to Selective Laser Sintering", Proceeding of the Solid Freeform Fabrication Symposium, The University of Texas at Austin, Austin, Texas, pp. 379-385, 1994.

Carter William T., and Jones M. G., "Direct Laser Sintering of Metals", Proceeding of the Solid Freeform Fabrication Symposium, The University of Texas at Austin, Austin, Texas, pp. 51-59, 1993.

Childs T. H. C., Ryder G. R., and Berzins M., "Experimental and Theoretical Studies of Selective Laser Sintering," Proceeding of the Solid Freeform Fabrication Symposium, The University of Texas at Austin, Austin, Texas, pp. 132-141, 1997.

Childs T.H.C., Berzins M., Ryder G.R., and Tontowi A., 'Selective Laser Sintering of an Amorphous Polymer - Simulations and Experiments'. Journal of Engineering Manufacture, Proceeding Part B, IMechE, Vol. 213, pp. 333-349, 1999.

Chua C. K., and Leong Kah Fai, "Rapid Prototyping: Principles and Applications in Manufacturing," John Wiley & Sons (Asia) Pte Ltd., Singapore, 1997.

Chua, C.K., Hong, K.H. and Ho, S.L., "Rapid Tooling Technology: Part 1 A Comparative study," International Journal of Advanced Manufacturing Technology, Vol. 15, pp. 604-608, 1999 a.

Chua C.K., Hong K.H., and Ho S. L., "Rapid Tooling Technology: Part 2 A Case study Using Arc Spray Metal Tooling," International Journal of Advanced Manufacturing Technology, Vol. 15, pp. 609-614, 1999 b.

Colton J., Blair B., "Experimental Study of Post-build Cure of Stereolithography Polymers for Injection Molds," Rapid Prototyping Journal, Vol. 5, No. 2, pp. 72-81 1999.

Comb J. W., Priedeman W. R., and Turley P. W., "FDM Technology Pro-cess Improvements", Proceedings of the Solid Freeform Fabrication Sym-posium, The University of Texas at Austin, Austin, Texas, August, pp. 42-49, 1994.

Crawford R. H., "Computer Aspects of Solid Freeform Fabrication: Geometry, Process Control, and Design", Proceeding of the Solid Freeform Fabrication Symposium, The University of Texas at Austin, Austin, Texas, pp. 102-112, 1993.

Cubital Homepage: http://www.cubital.com/cubital, 2001.

Dalgarno K. W., "Production Grade Tooling Via Layer Manufacture," Rapid Prototyping Journal, Vol. 7 No.4, pp. 203-206, 2001.

Dalgarno K. W., Childs T. H. C., Rowntree I., and Rothwell L., "Finite Element Analysis of Curl Development in the Selective Laser Sintering Process," Proceeding of the Solid Freeform Fabrication Symposium, The University of Texas at Austin, Austin, Texas, pp. 559-566, 1996.

Dalgarno K. W., Stewart T. D., and Childs T. H. C., "Production Tooling for Polymer Components Via the DTM RapidSteel Process," Proceeding of the Solid Freeform Fabrication Symposium, The University of Texas at Austin, Austin, Texas, pp. 559-566, 2000.

Dalgarno K. W., Stewart T. D., "Production Tooling for Polymer Moulding Using the RapidSteel Process," Rapid Prototype Journal, Vol. 7, No, 3, pp. 173-179, 2001.

Das S., Wohlert M., Beaman J.J. and Bourell D.L. "Direct Selective Laser Sintering and Containerless Hot Isostatic Pressing for High Performance Metal Components," Solid Freeform Fabrication Proceedings, The University of Texas, Austin, pp. 81-90, 1997.

Das, S., Wohlert M., Beaman J. J., and Bourell D. L., "Processing of titanium net shapes by SLS/HIP," Materials and Design 20. Elsevier Science Ltd. pp. 115-121, 1999.

Deckard L., and Dennis C. T., "Fabrication of Ceramic and Metal Matrix Composites From Selective Laser Sintered Ceramic Performs," Proceeding of the Solid Freeform Fabrication Symposium, The University of Texas at Austin, Austin, Texas, pp. 215-222, 1993.

Dowson Gordon, "Powder Metallurgy the Process and its Products," IOP publishing Lid 1990.

DTM. 'Guide to Materials: RapidSteel™ 2.0 Used to Produce Rapid Tool LR Mold Inserts' DTM Corporation, DCN: 8002-10001, August, 1998.

DTM. 'SinterStation 2000 System User's Guide: Part and Build Profile Parameter Definitions' DTM Corporation, DCN: 8010-00000-006, March, 1996.

DTM. 'The SinterStation 2000 System Selective Laser Sintering Service Manual' DTM Corporation, DCN: 8010-00000-006, February, 1995.

DTM. http://www.dtm-corp.com/products/slssystems/Hi_res/LASERF100High.pdf, 2002.

DTM. 'Tooling Users Group - Process Update' DTM Corporation. April 21, 1999.

Eric C. Whitney, Kenneth Meinert, Jr, Paul Howell, (Laser Free Form Fabrication of Nickel-Aluminum-Bronze," Advances in Powder Metallurgy & Particulate Materials Vol. 5 pp 31-38, 1999 a.

Eric Radstok, "Rapid Tooling," Rapid Prototyping Journal, Vol. 5 No.4, pp. 164-168, 1999.

Frank Petzoldt, Greul M., and Loffer H., "Direct Metal Laser Sintering-Different Applications/Different Material Concepts," Advances in Powder Metallurgy & Particulate Materials Vol. 5 pp 71-77, 1999.

Fuesting T., Brown L., Das S., Harlan N., Lee G. Beaman J. J., Barlow J. W., and Sargent K., "Development of Direct SLS Processing for Production of Cermet Composite Turbine Sealing Components," Proceeding of the Solid Freeform Fabrication Symposium, The University of Texas at Austin, Austin, Texas, pp. 39-55, 1996.

Fukai M., Horlkawa T., Nishiyama K., and Okumura K., "Application of Direct Metal Laser Sintering for Fabrication of Production Injection Molds," Proceeding of International Conference on Rapid Prototyping. Tokyo, Japan. pp. 407-412, 2000.

German R. M., "Liquid Phase Sintering," Plenum Press, New York 1985.

German R. M., "Powder Metallurgy of Iron and Steel," John Wiley & Sons, Inc., 1998.

German, R. M., "Powder Metallurgy Science," (2^{nd} Ed.). MPIF (Metal Powder Industries Federation), USA, 1994.

German, R. M., "Sintering Theory and Practice," John Wiley & Sons, Inc., 1996.

Gopalakrishna B. Prabhu and David L. Bourell, "Supersolidus Liquid Phase Selective Laser Sintering of Prealloyed Bronze Powder," Proceeding of the Solid Freeform Fabrication Symposium, The University of Texas at Austin, Austin, Texas, pp. 317-324, 1993.

GSI (General Scanning Inc.) XY Scan Head Series: X-Y Scan Head User Manual. GSI PN 12P-XY, Rev. B, 1991.

Hauser C., "Selective Laser Sintering of a Stainless Steel Powder," PhD Thesis, School of Mechanical Engineering, The University of Leeds, UK, 2002.

Childs T. H. C., Dalgarno K. W., and Eane R. B., "Atmospheric Control During Selective Laser Sintering of Stainless Steel 314S Powder," Proceeding of the Solid Freeform Fabrication Symposium, The University of Texas at Austin, Austin, Texas, pp. 265-272, 1999.

Hauser C., Childs T. H. C., and Dalgarno K. W., "Selective Laser Sintering of Stainless Steel 314S HC Processed Using Room Temperature Powder Beds," Proceeding of the Solid Freeform Fabrication Symposium, The University of Texas at Austin, Austin, Texas, pp. 273-280, 1999.

Helysis, Inc. Homepage: http://helisys.com, 2001.

Hilton P. D., and Jacobs P. F., " Rapid tooling: technologies and industrial applications," New York Marcel Dekker 2000.

Himmer T. Nakagawa T. and Noguchi H., "Stereolithography Of Ceramics", Proceedings of the Solid Freeform Fabrication Symposium, The University of Texas at Austin, Austin, TX, August 11-13, pp. 363-369, 1997.

Hoyle G., "High Speed Steel," Butterworths, 1988.

Hügel, H. & Dausinger, F., "Interaction phenomena and energy coupling in laser surface treatment," Eurolaser Academy. Institute für Strahlwerkzeuge, University of Stuttgart, Germany, 1996.

Jacobs P. F, "Rapid Prototyping & Manufacturing: Fundamentals of Stereolithography", 1st ed., Society of Manufacturing Engineers, Dearborn, MI, 1992.

Jacobs P. F., "Rapid Prototyping and Manufacturing: Fundamentals of StereoLithography. Society of Manufacturing Engineers", Dearborn, Michigan, 1996.

Karapatis N. P., Guidoux Y., Gygax P. E., and Glardon R., "Thermal Behavior of Parts Made Direct Metal Laser Sintering", Proceeding of the Solid Freeform Fabrication Symposium, The University of Texas at Austin, Austin, Texas, pp. 79-87, 1998.

Karunakaran K. P., Vivekananda Shanmuganathan P., Sanjay J.J., Prashant B., and Ashish P., "Rapid Prototyping of Metallic Parts and Moulds," Journal of Materials Processing Technology, Vol. 105, pp. 371-381, 2000.

Khaing M. W., Fuh J. Y. H., and Lu L., "Direct Metal Laser Sintering for Rapid Tooling: Processing and Characterisation of EOS Parts," Journal of Materials Processing Technology 113, pp. 269-272, 2001.

Klocke F., and Wirtz H., "Direct of Metal Prototypes and Prototype Tools," Proceeding of the Solid Freeform Fabrication Symposium, The University of Texas at Austin, Austin, Texas, pp. 141-147, 1996.

Klocke F., Celiker T., and Song Y.-A., "Rapid Metal Tooling," Rapid Prototyping Journal, Vol. 1 No. 3, pp. 32-42, 1995.

Klocke F., and Wirtz H., "Selective Laser Sintering of Zirconium Silicate", Proceeding of the Solid Freeform Fabrication Symposium, The University of Texas at Austain, Austin, Texas, pp. 605-612, 1998.

Kruth J. P., Peeters P., Smolderen T., Bonse J., Laoui T., and Froyen L., "Comparison between CO_2 and Nd:YAG lasers for use with selective laser sintering of Steel-Copper powders," Photonics applied to Mechanics and Environmental Testing Engineering European, Proceeding of the Workshop on Rapid Prototyping, 24-26 November, 1999.

Kruth J. P., Van der Schuren B., Bonse J., and Morren B., "Basic Powder Metallurgical Aspects in Selective Metal Powder Sintering", Annals of the CIRP, Vol. 45, No. 1, pp.183-186, 1996.

Kruth J. P., Peeters P., "Smolderen T., Bonse, J., Laoui T., & Froyen L., The Performance of CO_2 and Nd:YAG Lasers in the Selective Laser Sintering of Steel-Copper Powders," Proc. of the 7th Assises Européennes du prototypage Rapide, Paris, pp 15-27, 1998.

Laoui T., Heapel P., Kruth J. P., and Froyen L., "Process Optimization of WC-9CO Parts Made by Selective Laser sintering," Proceeding of International Conference on Rapid Prototyping. Tokyo, Japan. pp. 419-424, 2000.

Lauwers B., Kruth J. P., Froyen L., Bonse J., and Morren, B., "Hard metal parts by SLS," Prototyping Technology International, pp. 124-126, 1998.

Manthiram A., Bourell D. L., and Marcus H. L., "Nanophase Materials in Solid Freeform Fabrication," JOM, pp 66-70, November 1993.

Marcus H. L., Beaman J. J., Barlow J. W., and Bourell D. L., "From Computer to Component in 15 Minutes: The Integrated Manufacture of Three-Dimensional Objects," JOM, pp. 8-10, April 1990 a.

Marcus H. L., Beaman J. J., Barlow J. W., and Bourell D. L., " Solid Freeform Fabrication: Powder Processing," Ceramic Bulletin Vol. 69, No. 6, pp. 1030-1031, 1990 b.

McDonald J. A., Ryall C. J., and Wimpenny D. I., "Rapid Prototyping Casebook," The Cromwell Press, Trowbridge, Wiltshire, UK, 2001.

Metal Hand Book Vol. 7, "Powder Metallurgy," ASM International, Material Park, Ohio, 1984.

Metal Powder Industries Federation, "Standard Test Methods for Metal Powders and Powder Metallurgy Products," Metal Powder Industries Federation, 1991.

Miller, D., Deckard, C. and Williams, J. "Variable beam size SLS workstation and enhanced SLS Model," Rapid Prototyping Journal, Vol.3, No. 1, pp. 4-11, 1997.

Morgan R., Sutcliffe C. F., and O'Neill W., "Experimental Investigation of Nanosecond Pulsed Nd:YAG Laser Re-melted Pre-placed Powder Beds," Rapid Prototyping Journal, Vol. 7 No.3, pp. 159-172, 2001.

Nelson Christian, Jason Kepler, Rich Booth, and Phillip Conner, "Direct Injection Molding Tooling Inserts from the SLS Process with Copper Polyamide", Proceeding of the Solid Freeform Fabrication Symposium, The University of Texas at Austin, Austin, Texas, pp. 451-459, 1998.

Nelson J. C., "Selective Laser sintering: A Definition of the Process and an Empirical Sintering Model." Phd Thesis, the University of Texas at Austin, 1993.

Nelson C., Kevin McAlea, and Damien Gray, "Improvement in SLS Part Accuracy," Proceeding of the Solid Freeform Fabrication Symposium, The University of Texas at Austin, Austin, Texas, pp. 159-169, 1995.

Nelson J. C., Samuel Xue, Barlow J. W., Beaman J. J., Marcus H., and David L. Bourell, "Model of the Selective Laser Sintering of Bisphenol-A Polycarbonate," Ind. Eng. Chem. Res., Vol. 32, No. 10, pp.2305-2317, 1993.

Niu H. J., and Chang I. T. H., "Instability of Scan Tracks Selective Laser Sintering of High Speed Steel Powder", Scripta Materialia, Vol. 41, No. 11, pp. 1229-1234, 1999 a.

Niu H. J., and Chang I. T. H., "Liquid Phase Sintering of M3/2 High Speed Steel by Selective Laser Sintering", Scripta Materialia, Vol. 39, No. 1, pp. 67-72, 1998.

Niu H. J., and Chang I. T. H., "Selective Laser Sintering of Gas Atomized M2 High Speed Steel Powder", Journal of Materials Science, Vol. 35, No. 1, pp. 31-38, 2000.

Niu H. J., and Chang I. T. H., "Selective Laser Sintering of Gas and Water Atomized High Speed Steel Powders", Scripta Materialia, Vol. 41, No. 1, pp. 25-30, 1999 b.

Olli Nyrhila, Juha Kotila, Jan-Erik Lind, and Tatu Syvanen, " Industrial Use of Direct Metal Laser Sintering", Proceeding of the Solid Freeform Fabrication Symposium, The University of Texas at Austain, Austin, Texas, pp. 487-493, 1998.

O'Neill W., Sutcliffe C. J., Morgan R., and B Hon K. K., "Investigation of Short Pulse Nd:YAG Laser Interaction with Stainless Steel Powder Beds," Proceeding of the Solid Freeform Fabrication Symposium, The University of Texas at Austain, Austin, Texas, pp. 147-159, 1998.

O'Neill W., Sutcliffe C. J., Morgan R., Landsborough A., and B Hon K. K., "Investigation on Multi-Layer Direct Metal Laser Sintering of 316L Stainless Steel Powder Beds," Annals of the CIRP Vol. 48/1, pp 151-154, 1999.

Pham D. T., and Dimov S., "Rapid Manufacturing the Technologies and Applications of Rapid Prototyping and Rapid Tooling," Springer-Verlag London Limited, 2001.

Pham D. T., and Gault R. S. " A Comparison of Rapid Prototyping Technologies", International Journal of Machine Tools & Manufacture, Vol. 38, pp. 1257-1287, 1998.

Pham D. T. and Wang X., "Prediction and Reduction of Build Times for the Selective Laser Sintering Process," Proc Instn Mech Engrs Vol. 214 Part B, pp. 425, 2000.

Reeves P.E. and Cobb R.C., "The Finishing of Stereolithography Models Using Resin Based Coatings", Proceedings of the Solid Freeform Fabrication Symposium, The University of Texas at Austin, Austin, TX, August 7-9, pp. 96-106, 1995.

Rosochowski A., and Matuszak A., " Rapid Tolling: the State of the Art," Journal of Materials Processing Technology, Vol. 106, pp. 191-198, 2000.

Sachs Emanuel, Samuel Allen, Michael Cima, Edward Wylonis, Honglin Guo, "Production of Injection Molding Tooling with Conformal Cooling Channels using The Three Dimensional Printing Process," Solid Freeform Fabrication Proceedings, pp 448-467, 1995.

Shellabear, "Benchmark Study of Accuracy and Surface Quality in RP Models," Process Chains for Rapid Technical Prototypes (Raptec) Task 4.2, Report 2, 1999

Sih, S.S. and Barlow, J. W., "The Measurement of the Thermal Properties and Absorbtances of Powders Near Their Melting Temperatures," Solid Freeform Fabrication Proceedings, The University of Texas, Austin, pp. 131-140, 1992.

Simchi, A., Pohl, H. & Petzoldt, F. (2001), "A novel steel powder for rapid tooling using direct metal laser sintering", in Proc. uRapid 2001, conf. held in Amsterdam, Netherlands, 28-30th May 2001.

Spotts M. F., " Design of Machine Elements," 6th Ed., Prentice Hall, Englewood Cliffs, NJ 1985.

Steen, W. M., "Laser surface treatment. Laser Processing: Surface Treatment and Film Deposition,". Proceedings of the NATO Advanced Study Institute on Laser Processing. Kluwer Academic Press. Netherlands. pp. 1-19, 1996.

Steen, W. M., "Laser material processing," Second Edition. Springer - Verlag, London, 1998.

Stewart T. D., Dalgarno K. W., and Childs T. H. C., "Strength of DTM RapidSteel ™ 1.0 Material", Materials & Design Vol. 20, pp. 133-138, 1999.

Stratasys, Inc., "Fast, Precise, Safe Prototypes with FDM", Proceedings of the 1991 Solid Freeform Fabrication Symposium, The University of Texas at Austin, Austin, Texas, August, pp. 115-122, 1991.

Stratasys, Inc., http://www.strarasys.com 2000.

Stucker B., Malhotra M., Qu X., Hardro P., and Mohanty H., "RapisSteel Part Accuracy," Proceedings of the 1991 Solid Freeform Fabrication Symposium, The University of Texas at Austin, Austin, Texas, August, pp. 133-140, 2000.

Suh, Y.S. and Wozny, M.J. 'Adaptive Slicing of Solid Freeform Fabrication Processes' Solid Freeform Fabrication Proceedings, The University of Texas, Austin, Texas, pp. 404-411, 1994.

Sun R. L., Yang D. Z., Guo L. X., and Dong S. L., "Laser Cladding of Ti-6Al-4V Alloy with TiC and TiC + NiCrBSi Powder," Surface and Coatings Technology, Vol. 135, pp. 307-312, 2001.

Thummler F., and Oberacker R., "An Introduction to Powder Metallurgy," The institute of Materials, 1 Carlton House Terrace London SW1Y 5DB, 1993.

Tobin J. R., Badrinaraya B., Barlow J. W., Beaman J. J., and Bourell D. L., "Indirect Metal Composite Part Manufacture Using the SLS Process," Proceeding of the Solid Freeform Fabrication Symposium, The University of Texas at Austin, Austin, Texas, pp. 303-307, 1993.

Tolochko, N.K., Laoui, T., Khlopkov, Y.V., Mozzharov, S.E., Titov, V.I and Ignatiev, M.B., "Absorbtance of powder materials suitable for laser sintering," Rapid Prototyping Journal, Vol.6, No.3, pp. 155-160, 2000.

Trent E. M., "Metal Cutting," Butterworth-Heinmann, Ltd, 1991.

Uday Hejmadi, and Kevin McAlea, "Selective Laser Sintering of Metal Molds: The RapidTool™ Process," Proceeding of the Solid Freeform Fabrication Symposium, The University of Texas at Austin, Austin, Texas, pp. 97-104, 1996.

Upadhyaya G. S., "Powder Metallurgy Technology," Cambridge International Science Publishing, Cambridge, UK, 1997.

Upadhyaya G. S., "Sintering Metallic and Ceramic Materials," John Wiley & Sons Ltd, 2000.

Volpato N., "Time-Saving and Accuracy Issues in Rapid Tooling by Selective Laser Sintering". PhD Thesis, School of Mechanical Engineering, The University of Leeds, UK, 2001.

Weaver T. J., Thomas J. A., Atre S. V., and German R. M., "Time Compressed Tooling-Production Tooling in 3 to 5 Days," Advances in Powder Metallurgy & Particulate Materials Vol. 5 pp 49-57, 1999.

Westin L., "Mechanical Properties of PM High-Speed Steels Related to Heat Treatment and Hardness," M.P.R. pp. 768-773 1989.

Wilkening, C. 'Fast Production of Technical Prototypes Using Direct Laser Sintering of Metals and Foundry Sand'. Solid Freeform Fabrication Proceedings, The University of Texas, Austin, pp. 133-140, 1996.

Williams John D., and Deckard C. R., "Advances in Modeling the Effects of Selected Parameters on the SLS Process," Rapid Prototyping Journal, Vol. 4 No.2, pp. 90-100, 1998.

Williams R. E., Komaragiri S. N., Melton V. L., and Bishu R. R., "Investigation of the Effect of Various Build Methods on the Performance of Rapid Prototyping (Stereolithography)," Journal of Materials Processing Technology, Vol. 61, pp 173-178, 1996.

Wright C. S., "Role of Molybdenum in Promoting Densification During Vacuum Sintering of T1 Grade High Speed Steel Powders," Powder Metallurgy Vol. 32, No.2, pp. 114-117, 1989.

Wright C. S., and Ogel B., "Supersolidus Liquid Phase Sintering of High Speed Steels, Part 1: Sintering of Molybdenum Based Alloys", Powder Metallurgy Vol. 36, No.2, pp. 213-217 1993.

Wright C. S., Youseffi M., Wronski A. S., Ansara I., Durand-Charre M., Mascarenhas J., Oliveira M. M., Lemoisson F., and Bienvenu Y., "Supersolidus Liquid Phase Sintering of High Speed Steels, Part 3: Computer Aided Design of Sinterable Alloys", Powder Metallurgy Vol. 42, No.2, pp. 131-146, 1999.

Wohlert, M., Das, S., Beaman, J. J. & Bourell, D. L. "Direct laser fabrication of high performance metal components via SLS/HIP". Proceeding of the Solid Freeform Fabrication Symposium. The University of Texas at Austin. Austin Texas. pp. 281-288, 1999.

Wronski A.S., Oliveira M.M., "Fracture Strength and Fracture Toughness of Powder Metallurgy Materials," Inzynieria Materiatowa, Vol 4, pp 1123-1130, 1998.

Yevko V., Park C. B., Zak G., Coyle T. W., and Benhabib B., "Cladding Formation in Laser-Beam Fusion of Metal Powder," Rapid Prototyping Journal, Vol. 4 No.4, pp. 168-184, 1998.

Yule Andrew J., and Dunkley John J., "Atomization of Metals for Powder Production and Spray Deposition", Oxford University Press Inc., New York, 1994.

Zhou Jack G., Daniel Herscovici , and Calvin C. Chen, "Parametric process optimisation to improve the accuracy of rapid prototyped stereolithography parts," International Journal of Machine Tools & Manufacture Vol. 40, pp. 363–379, 2000

Appendices

Appendix A

Density and volume report of some infiltrated samples of RapidSteel 2.0 cut horizontally

AccuPyc 1330 V1.04
Serial Number: 585
Density and Volume Report

Sample ID: A1
Number of Purges: 20
Cell Volume: 12.1718 cc

Sample Weight: 9.0630 g
Equilibration Rate: 0.0050 psig/min
Expansion Volume: 8.7054 cc

Run#	Volume cc	Deviation cc	Density g/cc	Deviation g/cc
1*	1.1274	-0.0006	8.0387	0.0039
2*	1.1265	-0.0015	8.0452	0.0104
3*	1.1271	-0.0009	8.0410	0.0062
4*	1.1275	-0.0005	8.0381	0.0033
5*	1.1297	0.0018	8.0223	-0.0125
6*	1.1279	-0.0001	8.0355	0.0008
7*	1.1263	-0.0017	8.0468	0.0120
8	1.1278	-0.0002	8.0363	0.0015
9	1.1274	-0.0005	8.0385	0.0038
10	1.1290	0.0010	8.0276	-0.0072
11	1.1277	-0.0003	8.0370	0.0022
12	1.1280	0.0000	8.0345	-0.0003

Average Volume: 1.1280 cc
Average Density: 8.0348 g/cc

Standard Deviation: 0.0006 cc
Standard Deviation: 0.0043 g/cc

AccuPyc 1330 V1.04
Serial Number: 585
Density and Volume Report

Sample ID: B2
Number of Purges: 20
Cell Volume: 12.1718 cc

Sample Weight: 8.8753 g
Equilibration Rate: 0.0050 psig/min
Expansion Volume: 8.7054 cc

Run#	Volume cc	Deviation cc	Density g/cc	Deviation g/cc
1*	1.1179	0.0000	7.9396	-0.0003
2*	1.1174	-0.0004	7.9427	0.0028
3	1.1170	-0.0008	7.9460	0.0060
4	1.1175	-0.0003	7.9422	0.0022
5	1.1182	0.0004	7.9369	-0.0031
6	1.1185	0.0007	7.9348	-0.0051
7	1.1178	0.0000	7.9398	-0.0001

Average Volume: 1.1178 cc
Average Density: 7.9399 g/cc

Standard Deviation: 0.0006 cc
Standard Deviation: 0.0044 g/cc

AccuPyc 1330 V1.04
Serial Number: 585
Density and Volume Report

Sample ID: C3
Number of Purges: 20
Cell Volume: 12.1718 cc

Sample Weight: 8.3473 g
Equilibration Rate: 0.0050 psig/min
Expansion Volume: 8.7054 cc

Run#	Volume cc	Deviation cc	Density g/cc	Deviation g/cc
1*	1.0673	-0.0011	7.8211	0.0083
2*	1.0690	0.0006	7.8087	-0.0041
3*	1.0675	-0.0009	7.8194	0.0066
4*	1.0697	0.0013	7.8035	-0.0093
5*	1.0668	-0.0017	7.8249	0.0121
6	1.0686	0.0002	7.8111	-0.0017
7	1.0688	0.0004	7.8101	-0.0027
8	1.0680	-0.0004	7.8157	0.0029
9	1.0687	0.0003	7.8108	-0.0020
10	1.0679	-0.0005	7.8163	0.0035

Average Volume: 1.0684 cc
Average Density: 7.8128 g/cc

Standard Deviation: 0.0004 cc
Standard Deviation: 0.0030 g/cc

AccuPyc 1330 V1.04
Serial Number: 585
Density and Volume Report

Sample ID: D4
Number of Purges: 20
Cell Volume: 12.1718 cc

Sample Weight: 9.1032 g
Equilibration Rate: 0.0050 psig/min
Expansion Volume: 8.7054 cc

Run#	Volume cc	Deviation cc	Density g/cc	Deviation g/cc
1	1.1356	-0.0003	8.0164	0.0024
2	1.1357	-0.0003	8.0158	0.0018
3	1.1362	0.0003	8.0119	-0.0021
4	1.1359	-0.0000	8.0143	0.0003
5	1.1363	0.0003	8.0116	-0.0024

Average Volume: 1.1359 cc
Average Density: 8.0140 g/cc

Standard Deviation: 0.0003 cc
Standard Deviation: 0.0022 g/cc

Appendix B

Time Predictor Program Using Pascal Language

```
program  Predicting_of_Build_Time (input,output);
uses crt;
var
  S_Speed,S_Spacing,Beam_Diameter,Layer_Thickness,Length,Width,Height,
  n1,n2,scan_spc,length_l,length_w,beam_dia,No_of_Lines,time,salam,
  Total_timelayer,Delay_time_of_line,Delay_time_of_layer,
  Scan_ time,Number_Layer,Number_lines:real;
  i,k,j,one,number_Layers:integer;
  speed:array [1..50] of real;
  path_name,output:string;
Begin
   Writeln('');
   Writeln('** This Program to Calculate the Building Time of Sintering Part **');
   Writeln('');
   Writeln('');
   Writeln('********** Enter The Dimensions Of The Shape,Scan Speed,*******');
   Writeln('     ********** Scan Spacing, And Layer Thickness ******* ');
   Writeln('');
   Writeln('');
   Writeln('Input Data for Length L');
   Readln(length);
   Writeln('');
   Writeln('');
   Writeln('Input Data for Width W');
   Readln(width);
   Writeln('');
   Writeln('');
   Writeln('Input Data for Height H');
   Readln(Height);
   Writeln('');
   Writeln('');
   Writeln('Input Data for Scan Speed');
   Readln(S_Speed);
   Writeln('');
   Writeln('');
   Writeln('Input Data for Scan Spacing');
   Readln(S_Spacing);
   Writeln('');
   Writeln('');
   Writeln('Input Data for Beam Diameter');
   Readln(Beam_Diameter);
   Writeln('');
   Writeln('');
   Writeln('Input Data for Delay_Time_of _One_Line');
   Readln(Delay_time_of_line);
   Writeln('');
   Writeln('');
   Writeln('Input Data for Delay_Time_of _One_Layer');
   Readln(Delay_time_of_layer);
   Writeln('');
   Writeln('');
```

```
    Writeln('Input Data for Layer_Thickness');
    Readln(layer_thickness);
 Writeln('');
 Writeln('');
  number_layer:=Height/Layer_thickness;
  Number_layers:=round(number_layer); {No of layers}
  Writeln('');
  writeln('You Have',Number_layer,'Layers');   writeln('Are the Scan Speed of These Layers
  the   Same ?!!!! (1) or (2)  ');
  Writeln('');
  writeln(' (1) If Scan Speeds Are the Same, or (2) If Not');
  Readln(one);
  Writeln('');
  writeln('No of layer=',Number_layers);
  Time:=0;
   If one=1 then
 begin
     writeln('Enter the layer thickness');
     readln(Layer_thickness);

time:=((((length/s_speed)+Delay_time_of_line)*(width/s_spacing))+Delay_time_of_layer)*(heigh
t/layer_thickness);
     time:=time/60;
     writeln('Total Time (per min)=',time, 'Min.');
     time:=time/60;
     writeln('Total Time (per hour)=',time, 'Hour');
  end;
     if one= 2 then
 begin
    for i:=1 to Number_layers do
 begin
    writeln('Enter scan speed in layer ', i);
    readln(s_speed);
    Speed[i]:=s_speed
 end;
    for i:=1 to Number_layers do
    begin
    writeln('thickness of layer ', i);
    writeln(speed[i]);
    end;
    for i:=1 to number_layers do
 begin
  Time:=time+(((length/speed[i])+Delay_time_of_line)*(width/s_spacing))
          +Delay_time_of_layer;
   time:=time/60;
   writeln('Total Time (per min)=',time, 'Min.');
   time:=time/60;
   writeln('Total Time (per hour)=',time, 'Hour');
   end;
   writeln('Total Time=',time);
   readln(salam);
end;
end.
```

Appendix C

A CAD Program to Control the Laser Beam (as a Tool) to Build a Different Shape Geometries Using Pascal Language

```
Program  Main_Program_For_Different _shaps (input,output,fout);
uses crt;
var
  n1,n2,scan_spc,length_l,length_w,beam_dia,No_of_Lines,
  q1_x,q1_y,q2_x,q2_y,q3_x,q3_y,q4_x,q4_y,point1_x,point1_y,
  point2_x,point2_y,con,dat_y,dat_x,p1x,p2x,p3x,p4x,p1y,p2y,p3y,p4y,
  point3_x,point3_y, point4_x,point4_y,cf1,cf2,cn,cm:real;
 i,k,j,mon:integer;
  mona:integer;
  fout:text;
  path_name,output:string;
 label
1,2,3,4,5,6,7,8,9,10,11,12,13,14,15,16,17,18,19,20,21,22,23,24,25,26,27,28,29,30,31,32,33,34,
35,36,100,200,300,400,500,600;
Begin  {For the Program}
  Writeln('************************** Main Menu ***************************');
         Writeln('   (1)  Single Lines in X Direction  ');
         Writeln('   (2)  Single Lines in Y Direction ');
         Writeln('   (3)  One Rectangle in X Direction  ');
         Writeln('   (4)  One Rectangle in Y Direction ');
         Writeln('   (5)  Two Rectangles in X Direction ');
         Writeln('   (6)  Three Rectangles in X Direction ');
         Writeln('   (7)  One Rectangle 45 Degree from Left to Right ');
         Writeln('   (8)  One Rectangle 45 Degree from Right to Left ');
         Writeln('   (9) Two Rectangles 45 Degree from up to down ');
         Writeln('   (10) One Rectangle with Zigzag strategy ');
         Writeln;Writeln;Writeln;
          repeat
         writeln( 'select line');
         Readln(mon);
         until((mon>0) and (mon<11));
         if mon=1 then
         begin {For part one}
         writeln('Selected to Do Single Lines Sintering in X Direction');
   Writeln('   ************************** Calibration Factor ***************************');
         Writeln('    A calibration number is required that depends on the working ');
         Writeln('    distance between scanning mirrors and powder bed.');
         Writeln;Writeln;Writeln;
         Writeln('         (1). Plate Scanning  (171).');
         writeln('         (2). Bed Scanning    (153).');
         writeln;writeln;writeln;
         Write('    Enter Choice (Or Input own Calibration Number) >.. ');
         Read(con);
               If con = 1 then goto 1 else goto 2;
               1: Con:=con+170;
               2: If con = 2 then goto 3 else goto 4;
               3: con:=con+151;
               4: con:=con;
          {Begin sub program for specified number of rasters}
     Writeln('          ************************** Data Offset **************************');
```

```
                Writeln;writeln;writeln;writeln;
                Writeln('          This option allows the aliignment of the mirrors if the laser');
                writeln('          spot is not alligned to the centre of the bed.');
                Writeln;Writeln;Writeln;
                Write('     X Offset > ');
                Read(Dat_x);
                Writeln;Writeln;
                Write('     Y Offset > ');
                Read(Dat_y);
    Writeln('Input the No of lines');
    Readln(No_of_Lines);
       Writeln('Input data for Scan Spacing');
    Readln(scan_spc);
    Writeln('Input data for Beam Diameter');
    Readln(beam_dia);
    length_l:=length_l*con;
    scan_spc:=(scan_spc*beam_dia)*con;
    beam_dia:=beam_dia*con;
    i:=1;
  k:=round(No_of_Lines);
 write('Enter New Path_Name>');
 readln(path_name);
          {writes heading statements for specified raster scans}
output:=path_name;
assign(fout,output);
rewrite(fout);
Writeln(fout,'  .(;  .I81;;17:  .N;19:IN;SC;PU;PU;SP7;LT;VS36');
         Writeln(fout,'PU;');
         Writeln(fout,'SP',1,';');
  for i:=1 to k do
 begin   {for (for) to part 1}
  Writeln('Input data for length');
  ReadLn (length_l);
  Length_l:=length_l*con;
  length_l:=length_l-((-0.0602*length_l)-(0.646*con));
  point1_x:=-(Length_l/2);
  point1_y:=i*scan_spc;
  point1_y:=point1_y-((k*scan_spc/2)+(scan_spc/2));
  point1_y:=point1_y-((-0.1303*point1_y)-(0.4158*con));
  point2_x:=(Length_l/2);
  point2_y:=i*scan_spc;
  point2_y:=point2_y-((k*scan_spc/2)+(scan_spc/2));
  point2_y:=point2_y-((-0.1303*point2_y)-(0.4158*con));
   {begin}
      write(fout,'PA',point1_x:1:0);
         writeln(fout,',',point1_y:1:0,';');
         writeln(fout,'PD;');
         write(fout,'PA',point2_x:1:0);
         writeln(fout,',',point2_y:1:0,';');
         writeln(fout,'PU;');
  end; {for (for)}
 end; {part 1}
 { close(fout);}
{ end; }
          if mon=2 then
          begin
          writeln('Selected to Do Single Lines Sintering in Y Direction');
Writeln('   ************************** Calibration Factor **************************');
```

```
        Writeln('    A calibration number is required that depends on the working ');
        Writeln('    distance between scanning mirrors and powder bed.');
        Writeln;Writeln;Writeln;
        Writeln('         (1). Plate Scanning  (171).');
        writeln('         (2). Bed Scanning    (153).');
        writeln;writeln;writeln;
        Write('    Enter Choice (Or Input own Calibration Number) >.. ');
        Read(con);
              If con = 1 then goto 5 else goto 6;
              5: Con:=con+170;
              6: If con = 2 then goto 7 else goto 8;
              7: con:=con+151;
              8: con:=con*1;
         {Begin sub program for specified number of rasters}
   Writeln('          ************************* Data Offset *************************');
               Writeln;writeln;writeln;writeln;
               Writeln('          This option allows the allignment of the mirrors if the laser');
               writeln('          spot is not alligned to the centre of the bed.');
               Writeln;Writeln;Writeln;
               Write('     X Offset > ');
               Read(Dat_x);
               Writeln;Writeln;
               Write('     Y Offset > ');
               Read(Dat_y);
   Writeln('Input the No of lines');
   Readln(No_of_Lines);
   Writeln('Input data for Scan Spacing');
   Readln(scan_spc);
   Writeln('Input data for Beam Diameter');
   Readln(beam_dia);
   scan_spc:=(scan_spc*beam_dia)*con;
   beam_dia:=beam_dia*con;
  i:=1;
  k:=round(No_of_Lines);
 write('Enter New Path_Name>');
 readln(path_name);
     {writes heading statements for specified raster scans}
output:=path_name;
assign(fout,output);
rewrite(fout);
Writeln(fout,'  .(;  .I81;;17:   .N;19:IN;SC;PU;PU;SP7;LT;VS36');
        Writeln(fout,'PU;');
        Writeln(fout,'SP',1,';');
 J:=1;
 for i:=1 to k do
  begin
  Writeln('Input data for length');
   ReadLn (length_l);
   Length_l:=length_l*con;
   length_l:=length_l-((-0.1303*length_l)-(0.4158*con));
   point1_x:=i*scan_spc;
   point1_x:=point1_x-((k*scan_spc/2)+(scan_spc/2));
   point1_x:=point1_x-((-0.0602*point1_x)-(0.646*con));
   point1_y:= -(Length_l/2);
   point2_x:=point1_x;
   point2_y:= (Length_l/2);
begin
        write(fout,'PA',point1_x:1:0);
```

```
        writeln(fout,',',point1_y:1:0,';');
        writeln(fout,'PD;');
        write(fout,'PA',point2_x:1:0);
        writeln(fout,',',point2_y:1:0,';');
        writeln(fout,'PU;');
end;
        if mon=3 then
        begin
      writeln('Selected to Do One Rectangle in X Direction');
      Writeln('************************Calibration-Factor-************************');
      Writeln('    A calibration number is required that depends on the working ');
      Writeln('    distance between scanning mirrors and powder bed.');
      Writeln;Writeln;Writeln;
      Writeln('         (1). Plate Scanning  (171).');
      writeln('         (2). Bed Scanning    (153).');
      writeln;writeln;writeln;
      Write('    Enter Choice (Or Input own Calibration Number) >.. ');
        Read(con);
            If con = 1 then goto 9 else goto 10;
            9: Con:=con+170;
            10: If con = 2 then goto 11 else goto 12;
            11: con:=con+151;
            12: con:=con*1;
        {Begin sub program for specified number of rasters}
    Writeln('          ************************** Data Offset **************************');
            Writeln;writeln;writeln;writeln;
            Writeln('          This option allows the allignment of the mirrors if the laser');
            writeln('          spot is not alligned to the centre of the bed.');
            Writeln;Writeln;Writeln;
            Write('     X Offset > ');
            Read(Dat_x);
            Writeln;Writeln;
            Write('     Y Offset > ');
            Read(Dat_y);
   Writeln('');
   Writeln('');
   Writeln('Input Data for First Rectangler');
   Writeln('');
   Writeln('');
   Writeln('Input data for Length L');
   Readln(length_l);
   Writeln('Input data for Length W');
   Readln(length_w);
   Writeln('Input data for Scan Spacing');
   Readln(scan_spc);
   Writeln('Input data for Beam Diameter');
   Readln(beam_dia);
   length_l:=length_l*con;
   length_w:=length_w*con;
   scan_spc:=(scan_spc*beam_dia)*con;
   beam_dia:=beam_dia*con;
  CN:=LENGTH_W;
  CN:=CN;
  n1:=(CN)/scan_spc; {No of Sean Lines in First Zone}
  CM:=LENGTH_L;
  CM:=CM;
  q1_x:=-length_w;
  q1_y:=-scan_spc*n1;
```

```
  q2_x:=length_w;
  q2_x:=q2_x;
  q2_y:=q1_y;
  i:=1;
  k:=round(n1);
 write('Enter New Path_Name>');
 readln(path_name);
     {writes heading statements for specified raster scans}
output:=path_name;
assign(fout,output);
rewrite(fout);
Writeln(fout,'  .(;  .I81;;17:  .N;19:IN;SC;PU;PU;SP7;LT;VS36');
         Writeln(fout,'PU;');
         Writeln(fout,'SP',1,';');
 J:=1;
 for i:=0 to k do
  begin
   point1_x:=cm-cm;
   point1_y:=-i*scan_spc;
   point2_x:=cm;
   point2_y:=-i*scan_spc;
   if j=1 then
    begin
         write(fout,'PA',point1_x:1:0);
         writeln(fout,',',point1_y:1:0,';');
         writeln(fout,'PD;');
         write(fout,'PA',point2_x:1:0);
         writeln(fout,',',point2_y:1:0,';');
         writeln(fout,'PU;');
         j:=2;
     end
   else
     begin
         write(fout,'PA',point2_x:1:0);
         writeln(fout,',',point2_y:1:0,';');
         writeln(fout,'PD;');
         write(fout,'PA',point1_x:1:0);
         writeln(fout,',',point1_y:1:0,';');
         writeln(fout,'PU;');
         j:=1
     end;
 end;
           end;
           if mon=4 then
        begin {for part 4}
          writeln('Selected to Do One Rectangle in Y Direction');
Writeln('   ************************** Calibration Factor **************************');
         Writeln('    A calibration number is required that depends on the working ');
         Writeln('    distance between scanning mirrors and powder bed.');
         Writeln;Writeln;Writeln;
         Writeln('         (1). Plate Scanning  (171).');
         writeln('         (2). Bed Scanning    (153).');
         writeln;writeln;writeln;
         Write('    Enter Choice (Or Input own Calibration Number) >.. ');
         Read(con);
               If con = 1 then goto 13 else goto 14;
               13: Con:=con+170;
               14: If con = 2 then goto 15 else goto 16;
```

```
                15: con:=con+151;
                16: con:=con*1;
          {Begin sub program for specified number of rasters}
 Writeln('          ************************* Data Offset *************************');
                 Writeln;writeln;writeln;writeln;
                 Writeln('          This option allows the allignment of the mirrors if the laser');
                 writeln('          spot is not alligned to the centre of the bed.');
                 Writeln;Writeln;Writeln;
                 Write('     X Offset > ');
                 Read(Dat_x);
                 Writeln;Writeln;
                 Write('     Y Offset > ');
                 Read(Dat_y);
    Writeln('');
  Writeln('');
  Writeln('Input Data for  Rectangler');
  Writeln('');
  Writeln('');
  Writeln('Input data for Length L');
   Readln(length_l);
   Writeln('Input data for Length W');
   Readln(length_w);
   Writeln('Input data for Scan Spacing');
   Readln(scan_spc);
   Writeln('Input data for Beam Diameter');
   Readln(beam_dia);
   length_l:=length_l*con;
   length_w:=length_w*con;
   scan_spc:=(scan_spc*beam_dia)*con*1.0769;
   beam_dia:=beam_dia*con;
  CN:=LENGTH_W;
  CN:=CN;
  n1:=(CN)/scan_spc; {No of Sean Lines in First Zone}
  CM:=LENGTH_L;
  CM:=CM;
  q1_x:=-length_w;
  q1_y:=-scan_spc*n1;
  q2_x:=length_w;
  q2_x:=q2_x;
  q2_y:=q1_y;
  i:=1;
  k:=round(n1);
          {writes heading statements for specified raster scans}
 J:=1;
for i:=0 to k do
 begin {for (for)}
  point1_x:=(length_w-length_w)+i*scan_spc;
  point1_y:=length_l-length_l;
  point2_x:=+i*scan_spc;
  point2_y:=-length_l;
  if j=1 then
    begin {for if }
         write(fout,'PA',point1_x:1:0);
         writeln(fout,',',point1_y:1:0,';');
         writeln(fout,'PD;');
         write(fout,'PA',point2_x:1:0);
         writeln(fout,',',point2_y:1:0,';');
         writeln(fout,'PU;');
```

```
        j:=2;
      end {for if}
    else
      begin
        write(fout,'PA',point2_x:1:0);
        writeln(fout,',',point2_y:1:0,';');
        writeln(fout,'PD;');
        write(fout,'PA',point1_x:1:0);
        writeln(fout,',',point1_y:1:0,';');
        writeln(fout,'PU;');
        j:=1
      end;
  end; {for (for)}
    close(fout);
end. {for part 4}
          if mon=5 then
       Begin {for part 5}
          writeln('Selected to Do Two Rectangles in X Direction');
   Writeln('   ************************** Caiibration Factor **************************');
          Writeln('    A calibration number is required that depends on the working ');
          Writeln('    distance between scanning mirrors and powder bed.');
          Writeln;Writeln;Writeln;
          Writeln('          (1). Plate Scanning  (171).');
          writeln('          (2). Bed Scanning    (153).');
          writeln;writeln;writeln;
          Write('    Enter Choice (Or Input own Calibration Number) >.. ');
          Read(con);
                If con = 1 then goto 17 else goto 18;
                17: Con:=con+170;
                18: If con = 2 then goto 19 else goto 20;
                19: con:=con+151;
                20: con:=con*1;
           {Begin sub program for specified number of rasters}
       Writeln('          ************************** Data Offset **************************');
                Writeln;writeln;writeln;writeln;
                Writeln('          This option allows the allignment of the mirrors if the laser');
                writeln('          spot is not alligned to the centre of the bed.');
                Writeln;Writeln;Writeln;
                Write('     X Offset > ');
                Read(Dat_x);
                Writeln;Writeln;
                Write('     Y Offset > ');
                Read(Dat_y);
    Writeln('');
   Writeln('');
   Writeln('Input Data for First Rectangler');
   Writeln('');
   Writeln('');
   Writeln('Input data for Length L');
   Readln(length_l);
   Writeln('Input data for Length W');
   Readln(length_w);
   Writeln('Input data for Scan Spacing');
   Readln(scan_spc);
   Writeln('Input data for Beam Diameter');
   Readln(beam_dia);
   length_l:=length_l*con;
   length_w:=length_w*con;
```

```
    scan_spc:=(scan_spc*beam_dia)*con;
    beam_dia:=beam_dia*con;
  CN:=LENGTH_W;
  CN:=CN-((-0.1303*CN)-(1.36*con));
  CN:=CN;
  n1:=(CN)/scan_spc; {No of Sean Lines in First Zone}
  CM:=LENGTH_L;
  CM:=CM-((-0.0602*CM)-(1.121*con));
  CM:=CM;
  q1_x:=-length_w;
  q1_y:=-scan_spc*n1;
  q2_x:=length_w;
  q2_x:=q2_x;
  q2_y:=q1_y;
  i:=1;
  k:=round(n1);
 write('Enter New Path_Name>');
 readln(path_name);
     {writes heading statements for specified raster scans}
output:=path_name;
assign(fout,output);
rewrite(fout);
Writeln(fout,'  .(;  .I81;;17:  .N;19:IN;SC;PU;PU;SP7;LT;VS36');
         Writeln(fout,'PU;');
         Writeln(fout,'SP',1,';');
 J:=1;
 for i:=0 to k do
  begin {for (for)}
   point1_x:=-cm/2;
   point1_y:=-i*scan_spc;
   point2_x:=cm/2;
   point2_y:=-i*scan_spc;
   if j=1 then
     begin {for if}
         write(fout,'PA',point1_x:1:0);
         writeln(fout,',',point1_y:1:0,';');
         writeln(fout,'PD;');
         write(fout,'PA',point2_x:1:0);
         writeln(fout,',',point2_y:1:0,';');
         writeln(fout,'PU;');
         j:=2;
       end {for if}
    else
       begin
         write(fout,'PA',point2_x:1:0);
         writeln(fout,',',point2_y:1:0,';');
         writeln(fout,'PD;');
         write(fout,'PA',point1_x:1:0);
         writeln(fout,',',point1_y:1:0,';');
         writeln(fout,'PU;');
         j:=1
  end;
  end; {for (for)}
    Writeln('');
    Writeln('');
    Writeln('Input Data for Second Rectangler');
    Writeln('');
    Writeln('');
```

```
  Writeln('Input data for Length L');
   Readln(length_l);
   Writeln('Input data for Length W');
   Readln(length_w);
   Writeln('Input data for Scan Spacing');
   Readln(scan_spc);
   Writeln('Input data for Beam Diameter');
   Readln(beam_dia);
   length_l:=length_l*con;
   length_w:=length_w*con;
   scan_spc:=(scan_spc*beam_dia)*con*1.0769;
   beam_dia:=beam_dia*con;
  CN:=LENGTH_W;
 CN:=CN-((-0.1303*CN)-(1.408*con));
 CN:=CN;
 n1:=(CN)/scan_spc; {No of Sean Lines in First Zone}
 CM:=LENGTH_L;
 CM:=CM-((-0.0602*CM)-(1.6113*con));
 CM:=CM;
 q1_x:=-length_w;
 q1_y:=-scan_spc*n1;
 q2_x:=length_w;
 q2_x:=q2_x;
 q2_y:=q1_y;
 i:=1;
 k:=round(n1);
   {writes heading statements for specified raster scans}
J:=1;
for i:=0 to k do
 begin {for (for)}
 point1_x:=-cm/2;
 point1_y:=-i*scan_spc+50*con;
 point2_x:=cm/2;
 point2_y:=-i*scan_spc+50*con;
 if j=1 then
   begin {for if}
        write(fout,'PA',point1_x:1:0);
        writeln(fout,',',point1_y:1:0,';');
        writeln(fout,'PD;');
        write(fout,'PA',point2_x:1:0);
        writeln(fout,',',point2_y:1:0,';');
        writeln(fout,'PU;');
        j:=2;
     end {for if}
  else
     begin
        write(fout,'PA',point2_x:1:0);
        writeln(fout,',',point2_y:1:0,';');
        writeln(fout,'PD;');
        write(fout,'PA',point1_x:1:0);
        writeln(fout,',',point1_y:1:0,';');
        writeln(fout,'PU;');
        j:=1
     end;
 end; {for (for)}
 close(fout);
end. {for part 5}
      if mon=6 then
```

```
      Begin
     writeln('Selected to Do Three Rectangles in X Direction');
Writeln('   ************************** Calibration Factor **************************');
        Writeln('    A calibration number is required that depends on the working ');
        Writeln('    distance between scanning mirrors and powder bed.');
        Writeln;Writeln;Writeln;
        Writeln('         (1). Plate Scanning  (171).');
        writeln('         (2). Bed Scanning    (153).');
        writeln;writeln;writeln;
        Write('    Enter Choice (Or Input own Calibration Number) >.. ');
        Read(con);
            If con = 1 then goto 21 else goto 22;
            21: Con:=con+170;
            22: If con = 2 then goto 23 else goto 24;
            23: con:=con+151;
            24: con:=con*1;
         {Begin sub program for specified number of rasters}
    Writeln('          ************************** Data Offset **************************');
            Writeln;writeln;writeln;writeln;
            Writeln('          This option allows the allignment of the mirrors if the laser');
            writeln('          spot is not alligned to the centre of the bed.');
            Writeln;Writeln;Writeln;
            Write('     X Offset > ');
            Read(Dat_x);
            Writeln;Writeln;
            Write('     Y Offset > ');
            Read(Dat_y);
   Writeln('');
   Writeln('');
   Writeln('Input Data for First Rectangler');
   Writeln('');
   Writeln('');
   Writeln('Input data for Length L');
   Readln(length_l);
   Writeln('Input data for Length W');
   Readln(length_w);
   Writeln('Input data for Scan Spacing');
   Readln(scan_spc);
   Writeln('Input data for Beam Diameter');
   Readln(beam_dia);
   length_l:=length_l*con;
   length_w:=length_w*con;
   scan_spc:=(scan_spc*beam_dia)*con;
   beam_dia:=beam_dia*con;
  CN:=LENGTH_W;
  CN:=CN-((-0.1303*CN)-(0.41508*con));
 CN:=CN;
 n1:=(CN)/scan_spc; {No of Sean Lines in First Zone}
 CM:=LENGTH_L;
 CM:=CM-((-0.0602*CM)-(0.646*con));
 CM:=CM;
 q1_x:=-length_w;
 q1_y:=-scan_spc*n1;
 q2_x:=length_w;
 q2_x:=q2_x;
 q2_y:=q1_y;
 i:=1;
 k:=round(n1);
```

```
 write('Enter New Path_Name>');
 readln(path_name);
     {writes heading statements for specified raster scans}
output:=path_name;
assign(fout,output);
rewrite(fout);
Writeln(fout,'  .(;  .I81;;17:  .N;19:IN;SC;PU;PU;SP7;LT;VS36');
          Writeln(fout,'PU;');
          Writeln(fout,'SP',1,';');
  J:=1;
 for i:=0 to k do
  begin
   point1_x:=-cm/2;
   point1_y:=-i*scan_spc-6*con;
   point2_x:=cm/2;
   point2_y:=-i*scan_spc-6*con;
   if j=1 then
     begin
          write(fout,'PA',point1_x:1:0);
          writeln(fout,',',point1_y:1:0,';');
          writeln(fout,'PD;');
          write(fout,'PA',point2_x:1:0);
          writeln(fout,',',point2_y:1:0,';');
          writeln(fout,'PU;');
          j:=2;
      end
    else
      begin
          write(fout,'PA',point2_x:1:0);
          writeln(fout,',',point2_y:1:0,';');
          writeln(fout,'PD;');
          write(fout,'PA',point1_x:1:0);
          writeln(fout,',',point1_y:1:0,';');
          writeln(fout,'PU;');
          j:=1
      end;
  end;
   Writeln('');
     Writeln('');
     Writeln('Input Data for Second Rectangler');
     Writeln('');
     Writeln('');
    Writeln('Input data for Length L');
     Readln(length_l);
     Writeln('Input data for Length W');
     Readln(length_w);
     Writeln('Input data for Scan Spacing');
     Readln(scan_spc);
     Writeln('Input data for Beam Diameter');
     Readln(beam_dia);
     length_l:=length_l*con;
     length_w:=length_w*con;
     scan_spc:=(scan_spc*beam_dia)*con;
     beam_dia:=beam_dia*con;
   CN:=LENGTH_W;
   CN:=CN-((-0.1303*CN)-(0.41508*con));
   CN:=CN;
   n1:=(CN)/scan_spc; {No of Sean Lines in First Zone}
```

```
  CM:=LENGTH_L;
  CM:=CM-((-0.0602*CM)-(0.646*con));
  CM:=CM;
  q1_x:=-length_w;
  q1_y:=-scan_spc*n1;
  q2_x:=length_w;
  q2_x:=q2_x;
  q2_y:=q1_y;
  i:=1;
  k:=round(n1);
     {writes heading statements for specified raster scans}
J:=1;
for i:=0 to k do
 begin
  point1_x:=-cm/2;
  point1_y:=-i*scan_spc+28*con;
  point2_x:=cm/2;
  point2_y:=-i*scan_spc+28*con;
  if j=1 then
    begin
         write(fout,'PA',point1_x:1:0);
         writeln(fout,',',point1_y:1:0,';');
         writeln(fout,'PD;');
         write(fout,'PA',point2_x:1:0);
         writeln(fout,',',point2_y:1:0,';');
         writeln(fout,'PU;');
         j:=2;
     end
   else
     begin
         write(fout,'PA',point2_x:1:0);
         writeln(fout,',',point2_y:1:0,';');
         writeln(fout,'PD;');
         write(fout,'PA',point1_x:1:0);
         writeln(fout,',',point1_y:1:0,';');
         writeln(fout,'PU;');
         j:=1
     end;
    end;
   Writeln('');
   Writeln('');
   Writeln('Input Data for Third Rectangler');
   Writeln('');
   Writeln('');
  Writeln('Input data for Length L');
   Readln(length_l);
   Writeln('Input data for Length W');
   Readln(length_w);
   Writeln('Input data for Scan Spacing');
   Readln(scan_spc);
   Writeln('Input data for Beam Diameter');
   Readln(beam_dia);
   length_l:=length_l*con;
   length_w:=length_w*con;
   scan_spc:=(scan_spc*beam_dia)*con;
   beam_dia:=beam_dia*con;
  CN:=LENGTH_W;
  CN:=CN-((-0.1303*CN)-(0.41508*con));
```

```
 CN:=CN;
 n1:=(CN)/scan_spc; {No of Sean Lines in First Zone}
 CM:=LENGTH_L;
 CM:=CM-((-0.0602*CM)-(0.646*con));
 CM:=CM;
 q1_x:=-length_w;
 q1_y:=-scan_spc*n1;
 q2_x:=length_w;
 q2_x:=q2_x;
 q2_y:=q1_y;
 i:=1;
 k:=round(n1);
     {writes heading statements for specified raster scans}
J:=1;
for i:=0 to k do
 begin
  point1_x:=-cm/2;
  point1_y:=-i*scan_spc+65*con;
  point2_x:=cm/2;
  point2_y:=-i*scan_spc+65*con;
  if j=1 then
    begin
         write(fout,'PA',point1_x:1:0);
         writeln(fout,',',point1_y:1:0,';');
         writeln(fout,'PD;');
         write(fout,'PA',point2_x:1:0);
         writeln(fout,',',point2_y:1:0,';');
         writeln(fout,'PU;');
         j:=2;
     end
   else
     begin
         write(fout,'PA',point2_x:1:0);
         writeln(fout,',',point2_y:1:0,';');
         writeln(fout,'PD;');
         write(fout,'PA',point1_x:1:0);
         writeln(fout,',',point1_y:1:0,';');
         writeln(fout,'PU;');
         j:=1
     end;
 end;
 close(fout);
end.
          if mon=7 then
        Begin
          writeln('Selected to Do One Rectangle 45 Degree from Left to Right');
   Writeln('    ************************** Calibration Factor **************************');
          Writeln('    A calibration number is required that depends on the working ');
          Writeln('    distance between scanning mirrors and powder bed.');
          Writeln;Writeln;Writeln;
          Writeln('          (1). Plate Scanning  (171).');
          writeln('          (2). Bed Scanning    (153).');
          writeln;writeln;writeln;
          Write('    Enter Choice (Or Input own Calibration Number) >.. ');
          Read(con);
                If con = 1 then goto 25 else goto 26;
                25: Con:=con+170;
                26: If con = 2 then goto 27 else goto 28;
```

```
            27: con:=con+151;
            28: con:=con;
        {Begin sub program for specified number of rasters}
    Writeln('          ************************** Data Offset **************************');
            Writeln;writeln;writeln;writeln;
            Writeln('          This option allows the allignment of the mirrors if the laser');
            writeln('          spot is not alligned to the centre of the bed.');
            Writeln;Writeln;Writeln;
            Write('     X Offset > ');
            Read(Dat_x);
            Writeln;Writeln;
            Write('     Y Offset > ');
            Read(Dat_y);
  Writeln('Input data for Length L');
  Readln(length_l);
  Writeln('Input data for Length W');
  Readln(length_w);
  Writeln('Input data for Scan Spacing');
  Readln(scan_spc);
  Writeln('Input data for Beam Diameter');
  Readln(beam_dia);
  length_l:=length_l*con;
  length_w:=length_w*con;
  scan_spc:=(scan_spc*beam_dia)*con;
  beam_dia:=beam_dia*con;
 n1:=(length_w*cos(45))/scan_spc; {No of Sean Lines in First Zone}
 n2:=((length_l*cos(45)-scan_spc*n1)/scan_spc); {No of Scan Lines in Second Zone}
 q1_x:=-length_w*sin(45);
 q1_y:=-scan_spc*n1;
 q2_x:=length_w*sin(45);
 q2_y:=q1_y;
 q3_x:=(length_l*cos(45)-length_w*cos(45))+(q1_x);
 q3_y:=-scan_spc*(n1+n2);
 q4_x:=q3_x+2*length_w*sin(45);
 q4_y:=q3_y;
 i:=1;
 k:=round(n1);
write('Enter New Path_Name>');
readln(path_name);
        {writes heading statements for specified raster scans}
output:=path_name;
assign(fout,output);
rewrite(fout);
Writeln(fout,'  .(;  .I81;;17:  .N;19:IN;SC;PU;PU;SP7;LT;VS36');
        Writeln(fout,'PU;');
        Writeln(fout,'SP',1,';');
 J:=1;
for i:=0 to k do
 begin
  point1_x:=length_l-length_l;
  point1_y:=-length_w+(i*scan_spc)/cos(45);
  point2_x:=(i*scan_spc)/cos(45);
  point2_y:=-length_w;
  if j=1 then
begin
        write(fout,'PA',point1_x:1:0);
        writeln(fout,',',point1_y:1:0,';');
        writeln(fout,'PD;');
```

```
          write(fout,'PA',point2_x:1:0);
          writeln(fout,',',point2_y:1:0,';');
          writeln(fout,'PU;');
          j:=2;
 end
 else
 begin
        write(fout,'PA',point2_x:1:0);
          writeln(fout,',',point2_y:1:0,';');
          writeln(fout,'PD;');
          write(fout,'PA',point1_x:1:0);
          writeln(fout,',',point1_y:1:0,';');
          writeln(fout,'PU;');
          j:=1
end;
 end;
  k:=round(n2);
   p1x:=point1_x;
   p2x:=point2_x;
   p1y:=point1_y;
   p2y:=point2_y;
   j:=1;
 for i:= 1 to k do
  begin
   point1_x:=(p1x)+(scan_spc*i)/cos(45);
   point1_y:=length_l-length_l;
   point2_x:=(p2x)+(scan_spc*i)/cos(45);
   point2_y:=p2y;
   if j=1 then
begin
          write(fout,'PA',point1_x:1:0);
           writeln(fout,',',point1_y:1:0,';');
           writeln(fout,'PD;');
           write(fout,'PA',point2_x:1:0);
           writeln(fout,',',point2_y:1:0,';');
           writeln(fout,'PU;');
           j:=2;
  end
  else
  begin
       write(fout,'PA',point2_x:1:0);
          writeln(fout,',',point2_y:1:0,';');
          writeln(fout,'PD;');
          write(fout,'PA',point1_x:1:0);
          writeln(fout,',',point1_y:1:0,';');
          writeln(fout,'PU;');
                    j:=1
  end;
  end;
    k:=round(n1);
    p3x:=point1_x;
    p4x:=point2_x;
    p3y:=point1_y;
    p4y:=point2_y;
   j:=1;
 for i:=1 to k do
  Begin
   point1_x:=(p3x)+(scan_spc*i)/cos(45);
```

```
  point1_y:=length_l-length_l;
  point2_x:=(p4x);
  point2_y:=p4y+(i*scan_spc/cos(45));;
   if j=1 then
begin
        write(fout,'PA',point1_x:1:0);
         writeln(fout,',',point1_y:1:0,';');
         writeln(fout,'PD;');
         write(fout,'PA',point2_x:1:0);
         writeln(fout,',',point2_y:1:0,';');
         writeln(fout,'PU;');
         j:=2;
 end
 else
 begin
        write(fout,'PA',point2_x:1:0);
         writeln(fout,',',point2_y:1:0,';');
         writeln(fout,'PD;');
         write(fout,'PA',point1_x:1:0);
         writeln(fout,',',point1_y:1:0,';');
         writeln(fout,'PU;');
j:=1
end;
 end;
 close(fout);
 end.
          if mon=8 then
       Begin
          writeln('Selected to Do One Rectangle 45 Degree from Right to Left');
Writeln('   ************************** Calibration Factor **************************');
          Writeln('    A calibration number is required that depends on the working ');
          Writeln('    distance between scanning mirrors and powder bed.');
          Writeln;Writeln;Writeln;
          Writeln('         (1). Plate Scanning  (171).');
          writeln('         (2). Bed Scanning    (153).');
          writeln;writeln;writeln;
          Write('    Enter Choice (Or Input own Calibration Number) >.. ');
          Read(con);
                If con = 1 then goto 29 else goto 30;
                29: Con:=con+170;
                30: If con = 2 then goto 31 else goto 32;
                31: con:=con+151;
                32: con:=con;
           {Begin sub program for specified number of rasters}
      Writeln('          ************************* Data Offset *************************');
                Writeln;writeln;writeln;writeln;
                Writeln('          This option allows the allignment of the mirrors if the laser');
                writeln('          spot is not alligned to the centre of the bed.');
                Writeln;Writeln;Writeln;
                Write('     X Offset > ');
                Read(Dat_x);
                Writeln;Writeln;
                Write('     Y Offset > ');
                Read(Dat_y);
   Writeln('Input data for Length L');
   Readln(length_l);
   Writeln('Input data for Length W');
   Readln(length_w);
```

```
    Writeln('Input data for Scan Spacing');
    Readln(scan_spc);
    Writeln('Input data for Beam Diameter');
    Readln(beam_dia);
    length_l:=length_l*con;
    length_w:=length_w*con;
    scan_spc:=(scan_spc*beam_dia)*con;
    beam_dia:=beam_dia*con;
  n1:=(length_w*cos(45))/scan_spc; {No of Sean Lines in First Zone}
  n2:=((length_l*cos(45)-scan_spc*n1)/scan_spc); {No of Scan Lines in Second Zone}
  q1_x:=-length_w*sin(45);
  q1_y:=-scan_spc*n1;
  q2_x:=length_w*sin(45);
  q2_y:=q1_y;
  q3_x:=(length_l*cos(45)-length_w*cos(45))+(q1_x);
  q3_y:=-scan_spc*(n1+n2);
  q4_x:=q3_x+2*length_w*sin(45);
  q4_y:=q3_y;
  i:=1;
  k:=round(n1);
 write('Enter New Path_Name>');
 readln(path_name);
          {writes heading statements for specified raster scans}
output:=path_name;
assign(fout,output);
rewrite(fout);
Writeln(fout,'  .(;  .l81;;17:  .N;19:IN;SC;PU;PU;SP7;LT;VS36');
         Writeln(fout,'PU;');
         Writeln(fout,'SP',1,';');
 J:=1;
 for i:=0 to k do
  begin
  point1_x:=(i*scan_spc)/cos(45);
  point1_y:=length_l-length_l;
  point2_x:=length_l-length_l;
  point2_y:=-i*scan_spc/cos(45);
  if j=1 then
  begin
  100:    write(fout,'PA',point1_x:1:0);
        writeln(fout,',',point1_y:1:0,';');
        writeln(fout,'PD;');
        write(fout,'PA',point2_x:1:0);
        writeln(fout,',',point2_y:1:0,';');
        writeln(fout,'PU;');
        j:=2;
   end
   else
   begin
      write(fout,'PA',point2_x:1:0);
        writeln(fout,',',point2_y:1:0,';');
        writeln(fout,'PD;');
        write(fout,'PA',point1_x:1:0);
        writeln(fout,',',point1_y:1:0,';');
        writeln(fout,'PU;');
        j:=1
end;
 end;
  k:=round(n2);
```

```
   p1x:=point1_x;
   p2x:=point2_x;
   p1y:=point1_y;
   p2y:=point2_y;
   j:=1;
 for i:= 1 to k do
  begin
   point1_x:=(p1x)+(scan_spc*i)/cos(45);
   point1_y:=length_l-length_l;
   point2_x:=(p2x)+(scan_spc*i)/cos(45);
   point2_y:=p2y;
   if j=1 then
begin
       write(fout,'PA',point1_x:1:0);
          writeln(fout,',',point1_y:1:0,';');
          writeln(fout,'PD;');
          write(fout,'PA',point2_x:1:0);
          writeln(fout,',',point2_y:1:0,';');
          writeln(fout,'PU;');
          j:=2;
   end
   else
   begin
     400:   write(fout,'PA',point2_x:1:0);
          writeln(fout,',',point2_y:1:0,';');
          writeln(fout,'PD;');
          write(fout,'PA',point1_x:1:0);
          writeln(fout,',',point1_y:1:0,';');
          writeln(fout,'PU;');
                   j:=1
  end;
  end;
    k:=round(n1);
    p3x:=point1_x;
    p4x:=point2_x;
    p3y:=point1_y;
    p4y:=point2_y;
   j:=1;
 for i:=1 to k do
  Begin
   point1_x:=(p3x);
   point1_y:=( -i*scan_spc/cos(45));
   point2_x:=(p4x)+(i*scan_spc/cos(45));
   point2_y:=p4y;
    if j=1 then
begin
500:    write(fout,'PA',point1_x:1:0);
          writeln(fout,',',point1_y:1:0,';');
          writeln(fout,'PD;');
          write(fout,'PA',point2_x:1:0);
          writeln(fout,',',point2_y:1:0,';');
          writeln(fout,'PU;');
          j:=2;
   end
   else
   begin
      write(fout,'PA',point2_x:1:0);
          writeln(fout,',',point2_y:1:0,';');
```

```
          writeln(fout,'PD;');
          write(fout,'PA',point1_x:1:0);
          writeln(fout,',',point1_y:1:0,';');
          writeln(fout,'PU;');
j:=1
end;
 end;
 close(fout);
 end.
          if mon=9 then
         Begin
          writeln('Selected to Do One  Rectangle 45 Degree from up to down');
Writeln('    ************************** Calibration Factor **************************');
          Writeln('    A calibration number is required that depends on the working ');
          Writeln('    distance between scanning mirrors and powder bed.');
          Writeln;Writeln;Writeln;
          Writeln('          (1). Plate Scanning  (171).');
          writeln('          (2). Bed Scanning    (153).');
          writeln;writeln;writeln;
          Write('    Enter Choice (Or Input own Calibration Number) >.. ');
          Read(con);
                If con = 1 then goto 33 else goto 34;
                33: Con:=con+170;
                34: If con = 2 then goto 35 else goto 36;
                35: con:=con+151;
                36: con:=con*1;
           {Begin sub program for specified number of rasters}
    Writeln('          ************************** Data Offset **************************');
                 Writeln;writeln;writeln;writeln;
                 Writeln('          This option allows the allignment of the mirrors if the laser');
                 writeln('          spot is not alligned to the centre of the bed.');
                 Writeln;Writeln;Writeln;
                 Write('     X Offset > ');
                 Read(Dat_x);
                 Writeln;Writeln;
                 Write('     Y Offset > ');
                 Read(Dat_y);
      Writeln('');
    Writeln('');
    Writeln('Input Data for First Rectangler');
    Writeln('');
    Writeln('');
    Writeln('Input data for Length L');
    Readln(length_l);
    Writeln('Input data for Length W');
    Readln(length_w);
    Writeln('Input data for Scan Spacing');
    Readln(scan_spc);
    Writeln('Input data for Beam Diameter');
    Readln(beam_dia);
    length_l:=length_l*con;
    length_w:=length_w*con;
    scan_spc:=(scan_spc*beam_dia)*con;
    beam_dia:=beam_dia*con;
writeln('Enter New Path_Name>');
 readln(path_name);
          {writes heading statements for specified raster scans}
output:=path_name;
```

```
assign(fout,output);
rewrite(fout);
Writeln(fout,'  .(;  .I81;;17:  .N;19:IN;SC;PU;PU;SP7;LT;VS36');
          Writeln(fout,'PU;');
          Writeln(fout,'SP',1,';');
  CN:=LENGTH_W*COS(45);
  CN:=CN-((-0.1303*CN)-(0.4158*con));
  CN:=CN*1.2857;
  n1:=(CN)/scan_spc; {No of Sean Lines in First Zone}
  CM:=LENGTH_L*COS(45);
  CM:=CM-((-0.1303*CM)-(0.4158*con));
  CM:=CM*1.2857;
  n2:=((CM-CN)/scan_spc); {No of Scan Lines in Second Zone}
  q1_x:=-length_w*sin(45);
  q1_y:=-scan_spc*n1;
  q2_x:=length_w*sin(45);
  q2_x:=q2_x;
  q2_y:=q1_y;
  q3_x:=(length_l*cos(45)-length_w*cos(45))+(q1_x);
  q3_y:=-scan_spc*(n1+n2);
  q4_x:=q3_x+2*length_w*sin(45);
  q4_y:=q3_y;
  i:=1;
  k:=round(n1);
  J:=1;
for i:=0 to k do
 begin
  point1_x:=-(i*scan_spc);
  cf1:=((i*scan_spc)/cos(45))*sin(3.2);
  point1_x:=point1_x-cf1;
  point1_y:=-i*scan_spc;
  point2_x:=(i*scan_spc);
  point2_x:=point2_x;
  point2_y:=-i*scan_spc;
  if j=1 then
   begin
        write(fout,'PA',point1_x:1:0);
        writeln(fout,',',point1_y:1:0,';');
        writeln(fout,'PD;');
        write(fout,'PA',point2_x:1:0);
        writeln(fout,',',point2_y:1:0,';');
        writeln(fout,'PU;');
        j:=2;
    end
  else
    begin
        write(fout,'PA',point2_x:1:0);
        writeln(fout,',',point2_y:1:0,';');
        writeln(fout,'PD;');
        write(fout,'PA',point1_x:1:0);
        writeln(fout,',',point1_y:1:0,';');
        writeln(fout,'PU;');
        j:=1
    end
end;
  k:=round(n2);
   p1x:=point1_x;
   p2x:=point2_x;
```

```
  p1y:=point1_y;
  p2y:=point2_y;
  j:=1;
for i:= 1 to k do
 begin
  point1_x:=(p1x)+(scan_spc*i);
  point1_y:=(p1y-i*scan_spc);
  point2_x:=(p2x)+(scan_spc*i);
  point2_y:=p2y-i*scan_spc;
  if j=1 then
  begln
       write(fout,'PA',point1_x:1:0);
          writeln(fout,',',point1_y:1:0,';');
          writeln(fout,'PD;');
          write(fout,'PA',point2_x:1:0);
          writeln(fout,',',point2_y:1:0,';');
          writeln(fout,'PU;');
          j:=2;
    end
    else
 begin
      write(fout,'PA',point2_x:1:0);
         writeln(fout,',',point2_y:1:0,';');
         writeln(fout,'PD;');
         write(fout,'PA',point1_x:1:0);
         writeln(fout,',',point1_y:1:0,';');
         writeln(fout,'PU;');
                  j:=1
 end
 end;
   k:=round(n1);
   p3x:=point1_x;
   p4x:=point2_x;
   p3y:=point1_y;
   p4y:=point2_y;
  j:=1;
 for i:=0 to k do
  Begin
   point1_x:=(p3x)+(i*scan_spc);
   point1_y:=( -i*scan_spc+p3y);
   point2_x:=(p4x)-i*scan_spc;
   cf2:=((i*scan_spc)/cos(45))*sin(3.2);
   point2_x:=point2_x-cf2;
   point2_y:=-i*scan_spc+p4y;
    if j=1 then
begin
    write(fout,'PA',point1_x:1:0);
          writeln(fout,',',point1_y:1:0,';');
          writeln(fout,'PD;');
          write(fout,'PA',point2_x:1:0);
          writeln(fout,',',point2_y:1:0,';');
          writeln(fout,'PU;');
          j:=2;
    end
    else
begin
      write(fout,'PA',point2_x:1:0);
         writeln(fout,',',point2_y:1:0,';');
```

```
          writeln(fout,'PD;');
          write(fout,'PA',point1_x:1:0);
          writeln(fout,',',point1_y:1:0,';');
          writeln(fout,'PU;');
         j:=1
end
 end;
    Writeln('');
    Writeln('');
    Writeln('Input Data for Second Rectangler');
    Writeln('');
    Writeln('');
    Writeln('Input data for Length L');
    Readln(length_l);
    Writeln('Input data for Length W');
    Readln(length_w);
    Writeln('Input data for Scan Spacing');
    Readln(scan_spc);
    Writeln('Input data for Beam Diameter');
    Readln(beam_dia);
    length_l:=length_l*con;
    length_w:=length_w*con;
    scan_spc:=(scan_spc*beam_dia)*con*1.0769;
    beam_dia:=beam_dia*con;
  CN:=LENGTH_W*COS(45);
  CN:=CN-((-0.1303*CN)-(0.4158*con));
  CN:=CN*1.2857;
  n1:=(CN)/scan_spc; {No of Sean Lines in First Zone}
  CM:=LENGTH_L*COS(45);
  CM:=CM-((-0.1303*CM)-(0.4158*con));
  CM:=CM*1.2857;
  n2:=((CM-CN)/scan_spc); {No of Scan Lines in Second Zone}
  q1_x:=-length_w*sin(45);
  q1_y:=-scan_spc*n1;
  q2_x:=length_w*sin(45);
  q2_x:=q2_x;
  q2_y:=q1_y;
  q3_x:=(length_l*cos(45)-length_w*cos(45))+(q1_x);
  q3_y:=-scan_spc*(n1+n2);
  q4_x:=q3_x+2*length_w*sin(45);
  q4_y:=q3_y;
  i:=1;
  k:=round(n1);
          {writes heading statements for specified raster scans}
 J:=1;
 for i:=0 to k do
  begin
  point1_x:=-(i*scan_spc);
  cf1:=((i*scan_spc)/cos(45))*sin(3.2);
  point1_x:=point1_x-cf1;
  point1_y:=-i*scan_spc+50*con;
  point2_x:=(i*scan_spc);
  point2_x:=point2_x;
  point2_y:=-i*scan_spc+50*con;
  if j=1 then
    begin
        write(fout,'PA',point1_x:1:0);
        writeln(fout,',',point1_y:1:0,';');
```

```
        writeln(fout,'PD;');
        write(fout,'PA',point2_x:1:0);
        writeln(fout,',',point2_y:1:0,';');
        writeln(fout,'PU;');
        j:=2;
    end
  else
    begin
        write(fout,'PA',point2_x:1:0);
        writeln(fout,',',point2_y:1:0,';');
        writeln(fout,'PD;');
        write(fout,'PA',point1_x:1:0);
        writeln(fout,',',point1_y:1:0,';');
        writeln(fout,'PU;');
        j:=1
    end
end;
  k:=round(n2);
   p1x:=point1_x;
   p2x:=point2_x;
   p1y:=point1_y;
   p2y:=point2_y;
   j:=1;
for i:= 1 to k do
 begin
  point1_x:=(p1x)+(scan_spc*i);
  point1_y:=(p1y-i*scan_spc);
  point2_x:=(p2x)+(scan_spc*i);
  point2_y:=p2y-i*scan_spc;
  if j=1 then
  begin
      write(fout,'PA',point1_x:1:0);
        writeln(fout,',',point1_y:1:0,';');
        writeln(fout,'PD;');
        write(fout,'PA',point2_x:1:0);
        writeln(fout,',',point2_y:1:0,';');
        writeln(fout,'PU;');
        j:=2;
   end
   else
 begin
      write(fout,'PA',point2_x:1:0);
        writeln(fout,',',point2_y:1:0,';');
        writeln(fout,'PD;');
        write(fout,'PA',point1_x:1:0);
        writeln(fout,',',point1_y:1:0,';');
        writeln(fout,'PU;');
                j:=1
 end
 end;
   k:=round(n1);
   p3x:=point1_x;
   p4x:=point2_x;
   p3y:=point1_y;
   p4y:=point2_y;
  j:=1;
for i:=0 to k do
 Begin
```

```
  point1_x:=(p3x)+(i*scan_spc);
  point1_y:=( -i*scan_spc+p3y);
  point2_x:=(p4x)-i*scan_spc;
  cf2:=((i*scan_spc)/cos(45))*sin(3.2);
  point2_x:=point2_x-cf2;
  point2_y:=-i*scan_spc+p4y;
   if j=1 then
begin
    write(fout,'PA',point1_x:1:0);
         writeln(fout,',',point1_y:1:0,';');
         writeln(fout,'PD;');
         write(fout,'PA',point2_x:1:0);
         writeln(fout,',',point2_y:1:0,';');
         writeln(fout,'PU;');
         j:=2;
    end
    else
begin
      write(fout,'PA',point2_x:1:0);
         writeln(fout,',',point2_y:1:0,';');
         writeln(fout,'PD;');
         write(fout,'PA',point1_x:1:0);
         writeln(fout,',',point1_y:1:0,';');
         writeln(fout,'PU;');
        j:=1
end
 end;
 close(fout);
 end.
          if mon=10 then
        begin
          writeln('Selected to Do Two Rectangles 45 Degree from up to down');
 Writeln('    ************************** Calibration Factor **************************');
          Writeln('    A calibration number is required that depends on the working ');
          Writeln('    distance between scanning mirrors and powder bed.');
          Writeln;Writeln;Writeln;
          Writeln('          (1). Plate Scanning  (171).');
          writeln('          (2). Bed Scanning    (153).');
          writeln;writeln;writeln;
          Write('    Enter Choice (Or Input own Calibration Number) >.. ');
          Read(con);
                If con = 1 then goto 37 else goto 38;
                37: Con:=con+170;
                38: If con = 2 then goto 39 else goto 40;
                39: con:=con+151;
                40: con:=con*1;
           {Begin sub program for specified number of rasters}
     Writein('          ************************** Data Offset **************************');
                 Writeln;writeln;writeln;writeln;
                 Writeln('          This option allows the allignment of the mirrors if the laser');
                 writeln('          spot is not alligned to the centre of the bed.');
                 Writeln;Writeln;Writeln;
                 Write('     X Offset > ');
                 Read(Dat_x);
                 Writeln;Writeln;
                 Write('     Y Offset > ');
                 Read(Dat_y);
   Writeln('');
```

```
    Writeln('');
    Writeln('Input Data for  Rectangler');
    Writeln('');
    Writeln('');
   Writeln('Input data for Small Length L');
    Readln(length_l);
    Writeln('Input data for Long Length L');
    Readln(l_l);
    Writeln('Input data for Length W');
    Readln(length_w);
    Writeln('Input data for Scan Spacing');
    Readln(scan_spc);
    Writeln('Input data Big SS');
    Readln(S_S);
    Writeln('Input data for Beam Diameter');
    Readln(beam_dia);
    length_l:=length_l*con;
    length_w:=length_w*con;
    l_l:=l_l*con;
    S_S:=(S_S*beam_dia)*con;
    scan_spc:=(scan_spc*beam_dia)*con*1.0769;
    beam_dia:=beam_dia*con;
  CN:=LENGTH_W;
  CN:=CN;
  n1:=(CN)/scan_spc; {No of Sean Lines in First Zone}
  CM:=LENGTH_L;
  CM:=CM;
  q1_x:=-length_w;
  q1_y:=-scan_spc*n1;
  q2_x:=length_w;
  q2_x:=q2_x;
  q2_y:=q1_y;
  i:=1;
  k:=round(n1);
  m1:=l_l/s_s;
  p:=round (m1);
  f:=1;
  t:=0;
  rev:=0;
 write('Enter New Path_Name>');
 readln(path_name);
     {writes heading statements for specified raster scans}
output:=path_name;
assign(fout,output);
rewrite(fout);
Writeln(fout,'  .(;  .I81;;17:  .N;19:IN;SC;PU;PU;SP7;LT;VS36');
         Writeln(fout,'PU;');
         Writeln(fout,'SP',1,';');
         rev:=(0.25*scan_spc);
  for f:=1 to p do
    begin
    J:=1;
     for i:=0 to k do
       begin
         point1_x:=((length_w-length_w)+i*scan_spc)-(rev);
         point1_y:=(length_l-length_l)-t;
         point2_x:=(+i*scan_spc)-(rev);
         point2_y:=(-length_l)-t;
```

```
        if j=1 then
           begin
             write(fout,'PA',point1_x:1:0);
             writeln(fout,',',point1_y:1:0,';');
             writeln(fout,'PD;');
             write(fout,'PA',point2_x:1:0);
             writeln(fout,',',point2_y:1:0,';');
             writeln(fout,'PU;');
             j:=2;
           end
        else
           begin
             write(fout,'PA',point2_x:1:0);
             writeln(fout,',',point2_y:1:0,';');
             writeln(fout,'PD;');
             write(fout,'PA',point1_x:1:0);
             writeln(fout,',',point1_y:1:0,';');
             writeln(fout,'PU;');
             j:=1
           end;
     end;
    rev:=rev*(-1);
  t:=(t-s_s);
     end;
  close(fout);
end.
end. {For the Program}
```